CONTRACT NO. A932-079
FINAL REPORT
DECEMBER 1995

Characterization of Air Quality Data for the Southern California Air Quality Study

CALIFORNIA ENVIRONMENTAL PROTECTION AGENCY
AIR RESOURCES BOARD
Research Division

Characterization of Air Quality Data for the Southern California Air Quality Study

Final Report

Contract No. A932-079

Prepared for:

California Air Resources Board
Research Division
2020 L Street
Sacramento, California 95814

Prepared by:

Ken Underwood, John H. Seinfeld, Philip K. Hopke,
and Daniel Grosjean

AeroVironment Inc.
222 East Huntington Dr.
Monrovia, CA 91016

December 1995

EXECUTIVE SUMMARY

This report presents research based on data acquired during the Southern California Air Quality Study (SCAQS). SCAQS was an air pollution field measurement program that focused on development and improvement of our understanding of the most important factors affecting the production, transport, and deposition of acidic species in the South Coast Air Basin (SoCAB). In addition, the goal was to develop a comprehensive air quality and meteorology database that could be used to evaluate and improve elements of air quality simulation models for oxidants, fine and coarse particles, toxic air contaminants, and acidic species.

AeroVironment managed this project and received analytical contributions from Daniel Grosjean and Associates, Caltech, and Clarkson University.

Section 2 characterizes the SCAQS air quality data through graphical visualization and trajectory analyses.

The conclusions made from the visual analysis include the following:

- A good correlation between high SO_2 concentrations and high $SO_4^=$ levels was observed at Long Beach and Hawthorne, especially for relative humidities above 50%. However, at Rubidoux the relationship was not obvious, which means that phenomena other than chemistry and direct emissions could be responsible for the observed sulfate at the site; e.g., the transport from distant sources could be the major source of sulfates at that site.

- Increased levels of $SO_4^=$ corresponding to steady or decreased SO_2, or vice versa, were both observed in all of the episodes.

Section 3.1 summarizes the analysis of organic acids from the SCAQS database. The analysis contains:

- A review of available data, prior to SCAQS, regarding emissions, ambient levels, in situ formation and removal processes for organic acids in the SoCAB.

- An estimate of direct emissions, using ambient air data for organic acids and for a number of unreactive tracers including carbon monoxide, acetylene, Freon 113, and several chlorinated hydrocarbons.

- An estimate of in situ formation rates, using kinetic data, reaction mechanisms, and emission rates for olefins that produce organic acids in situ by reaction with ozone.

- An estimate of removal rates, with focus on dry deposition as the major atmospheric removal process for gas-phase organic acids.

- An attempt to reconcile ambient observations, production (direct emissions and in situ formation) and removal (mostly dry deposition) for gas-phase organic acids in the SoCAB.

The major findings are:

Emissions. Formic, acetic, and total organic acid emissions have been estimated using organic acid/carbon monoxide ratios. Emission rates of 6,500, 9,000, and 19,700 kg/day were estimated for formic, acetic, and total organic acids, respectively.

Atmospheric formation. The results of the study indicate that several reactions may produce organic acids in situ, three in the gas phase (the aldehyde-HO_2, phenol-OH, and ozone-olefin reactions) and one in the aqueous phase (oxidation of aldehyde in cloud and/or rainwater). Of these, the ozone-olefin reaction was deemed to be a major source of organic acids.

Removal processes. For the gas-phase organic acids, dry deposition far exceeds removal by rain and accounts for 95% (formic acid) and 91% (acetic acid)

of the organic deposition budget. Overall, dry deposition is estimated to be 14 times more important than the removal by rain, accounting for 92% of the total organic acid deposition budget.

Sections 3.2 through 3.7 present an analysis of physical and chemical processes that entail discussions of the following: aerosol size distribution and their relationship to the concentrations and deposition of acidic gases and particles; effects of fog formation on the production and deposition of acidic species and vertical distribution and chemistry of acidic species and precursors; and the role of upper air chemistry in producing acidic species. The results of the study are discussed below:

Aerosol size distribution and its relationship to the concentrations and deposition of acidic species. Mixing of droplets with different pHs that are undergoing Henry's Law equilibrium with the surrounding atmosphere always results in a bulk mixture that is supersaturated with weak acids like S(IV) and HCOOH, and bases like NH_3 with respect to the original atmosphere. The degree of supersaturation of the bulk liquid water sampling for a particular species depends on its dissociation constant, on the initial pH of the bulk droplet mixture, and on the distribution of the pH and of the liquid water over the droplet spectrum. High supersaturations result only when the pH of the bulk droplet mixture exceeds the pHa of the species, in which pH differences among droplets of different sizes lead to large deviations from Henry's Law for the bulk mixture.

Heterogeneous production of acidic species. Trajectory analysis suggests that high sulfate concentrations were associated with the arrival of air parcels at the receptor sites that passed through the fog layer the previous night. The trajectory gas-aerosol model successfully explained the sulfate levels in air parcels that did not pass through the fog layer, but underestimated the sulfate levels of the trajectories that passed through the fog by a factor of as much as 2.5. Sensitivity/uncertainty analysis indicated that the presence of excess sulfate (around 10 μgm^{-3}) cannot be attributed to uncertainties in the model parameters (e.g., initial conditions, emissions, mixing heights, deposition velocities). The episode was then simulated using a full gas- and aqueous-phase chemistry trajectory model and the analysis indicated that heterogeneous sulfate formation in

fog droplets under the conditions of the episode can indeed explain the observed excess sulfate.

Section 4 presents an analysis of receptor model techniques to SCAQS data, that includes the Target Transformation Factor Analysis, Multiple Regression Analysis, and Potential Source Contribution Function Analysis.

The results of the types of analysis conducted include:

Target Transformation Factor Analysis. This analysis is able to: (1) estimate the number of independent sources that contribute to the system; (2) determine the components of the elemental source profiles; and (3) calculate the contribution of each source to each sample. A five-factor model is derived to account for the source apportionment of samples collected at the Burbank site. Although the analysis resolves "five" sources, it is quite difficult to associate them with physically real emission sources. A four-factor model was used to describe the samples collected at the Claremont site. Source 1 contributes mainly PM-2.5 $SO_4^=$, NH_4^+L9, and a significant amount of $SO_4^=$ and NO_3^-L3. Source 3 contributes significant amounts of NO_3^-L9 and NH_4^+L9. The last source (4) contributes mainly NO_3^-L3. Sources 2, 3, and 4 do not include significant amounts of marine aerosols. A 3-factor model was obtained to account for the source apportionment of samples collected at Rubidoux. The first source involves large amounts of NH_4^+L5 and $SO_4^=$. The second source contributes significant amounts of NH_4^+L5, NO_3^-L3 and NO_3^-L9. All three sources contribute insignificant amounts of marine aerosols.

Multiple Regression Analysis. The results indicate that the atmospheric transport of the gaseous precursors and their conversion into particulate-phase acidic species tends to decouple them from the variations seen in any primary particles that might have been coemitted with SO_2 or NO_x. As a result, this method cannot be used for the identification of the sources of secondary acidic species.

Potential Source Contribution Function Analysis. In contrast to the other receptor techniques, the potential source contribution function analysis was able to identify possible locations of sources. Major sources are located along the coast. These sources produce SO_2 which reacts in the gas and the aqueous phases, thereby producing acidic species, as it is transported inland by the prevailing winds.

TABLE OF CONTENTS

ILLUSTRATIONS

LIST OF TABLES

1. INTRODUCTION

Acid deposition is the process by which atmospheric acidic substances—sulfuric, nitric, organic acids, and their salts—are deposited to the earth's surface. The main sources of these acidic species are anthropogenic activities, such as emissions of sulfur dioxide, nitrogen oxides, and hydrocarbons. The processes that lead to the formation, evolution, and removal of these acidic species are complicated and depend on transformation processes, such as photochemical activity, gas-to-particle conversion, droplet formation, droplet chemistry, particle dynamics, and both wet and dry deposition.

Acid deposition can damage trees, lakes, and crops. This concern is reflected in existing and pending legislation, such as Title V of the federal Clean Air Act, and in growing research interest on this subject.

In 1987, an air pollution field measurement program was performed as part of the Southern California Air Quality Study (SCAQS). The SCAQS program was funded by government agencies, industry groups, and individual corporate sponsors. The goal of SCAQS was to develop a comprehensive air quality and meteorology data base for the South Coast Air Basin (SoCAB) that can be used to evaluate and improve elements of air quality simulation models for oxidants, fine and coarse particles, toxic air contaminants, and acidic species. SCAQS also addressed specific technical questions about emission rates, transport, transformation, and deposition of pollutants.

This report presents research based on data acquired during the SCAQS program. The focus of this research was to develop and improve our understanding of the most important factors affecting the production, transport, and deposition of acidic species in the SoCAB. Some of the major research areas that are addressed in this report are:

- The distribution of acidic species among the three phases: gas, aerosol, and droplet.

- The role of atmospheric aerosol in nucleating fog and cloud droplets and those aerosols most important in droplet nucleation.

- The role of aqueous-phase chemistry in generating acidic species.

- The factors that determine the size of atmospheric liquid droplets and their aqueous-phase chemistry relationship.

- The rate of deposition for atmospheric gases, particles, and droplets.

- The relationship between primary gaseous and particulate species, and airborne and deposition acidity.

Section 2 of the report describes the "preliminary" analysis performed on the SCAQS data, using visualization and trajectory analysis. Section 3 describes the deterministic modeling approaches we used to determine the contribution of emissions, gas-phase chemistry, aqueous-phase chemistry, and removal processes to the observed concentrations of organic and inorganic acidic species. Section 4 presents the source-receptor relationships determined by various receptor modeling methods. Finally, Section 5 summarizes the results and conclusions from the study.

2. CHARACTERIZATION OF SCAQS AIR QUALITY DATA

2.1 PRELIMINARY ANALYSIS

2.1.1 Introduction

This section characterizes the air quality data through examination of geographical patterns, identification of source receptor relationships, and associated influences of meteorological conditions. Two methodologies have been used to characterize the data: a preliminary analysis and a trajectory analysis.

The preliminary analysis was a visual examination of the data. Figure 2.1.1 presents the spatial distribution of the stations used in this analysis. The trajectory analysis included the use of surface wind field generation and trajectory integration procedures.

2.1.2 Identification of Geographical Patterns, Source-Receptor Relationships, and Influences of Meteorological Conditions

The SCAQS data were examined graphically to highlight any geographical patterns, source-receptor relationships, and influences of meteorological conditions. The geographical patterns and relationships were examined to include relative humidity, sulfur dioxide (SO_2), and sulfates ($SO_4^=$).

The method used to study the data from the South Coast Air Basin (SoCAB) was visual examination of the graphical display of data. Time series plots are one method used in the visual examination and are presented for the June episode (Figure 2.1.2), the August episode (Figure 2.1.3), and the December episode (Figure 2.1.4). SO_2 and $SO_4^=$ are plotted in terms of sulfur concentration ($\mu g/m^3$); that is, $[SO_2]/2$ and $[SO_4^=]/3$. In general, $SO_4^=$ has a higher contribution to total sulfur than SO_2 in the June and August episodes. However, in the December episode, SO_2 has a higher fraction of the total sulfur than $SO_4^=$. The June episode stood out for the Burbank and Los Angeles sites with relatively high $SO_4^=$, accompanied by relatively low SO_2 concentrations. During all episodes, the Hawthorne and Long Beach sites were observed to exhibit

FIGURE 2.1.1. SCAQS network.

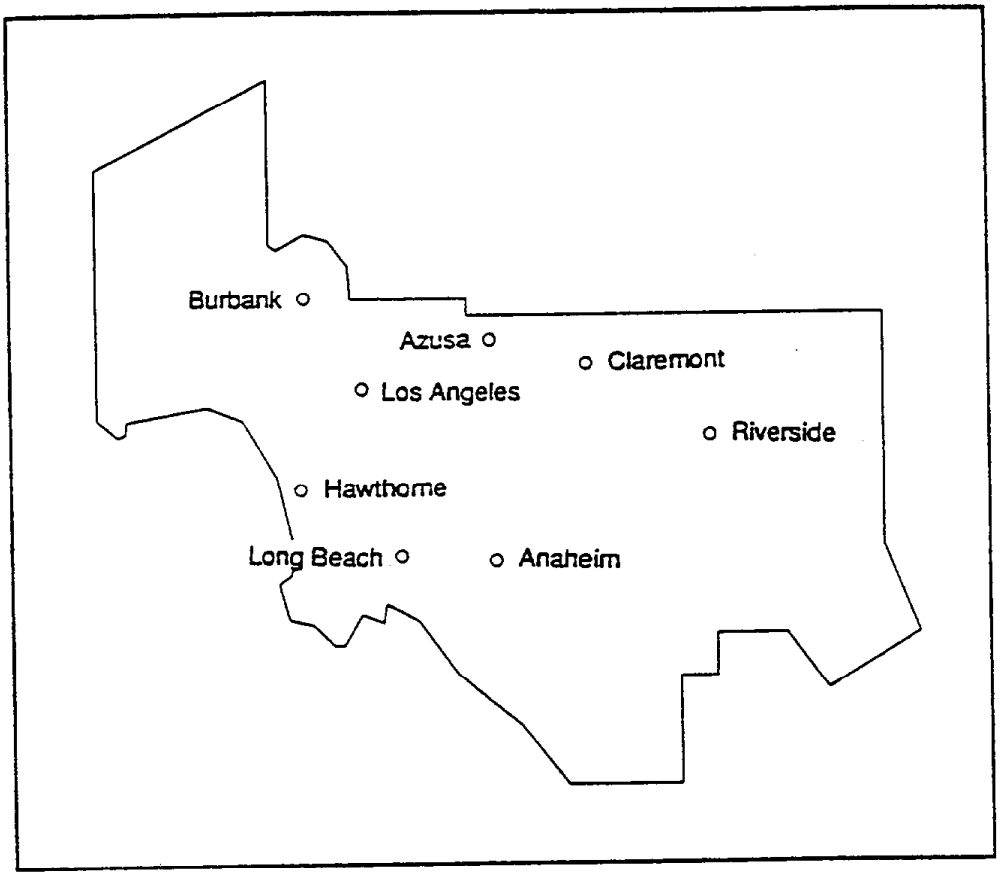

FIGURE 2.1.2. Time series plot (June 24-25, 1987).

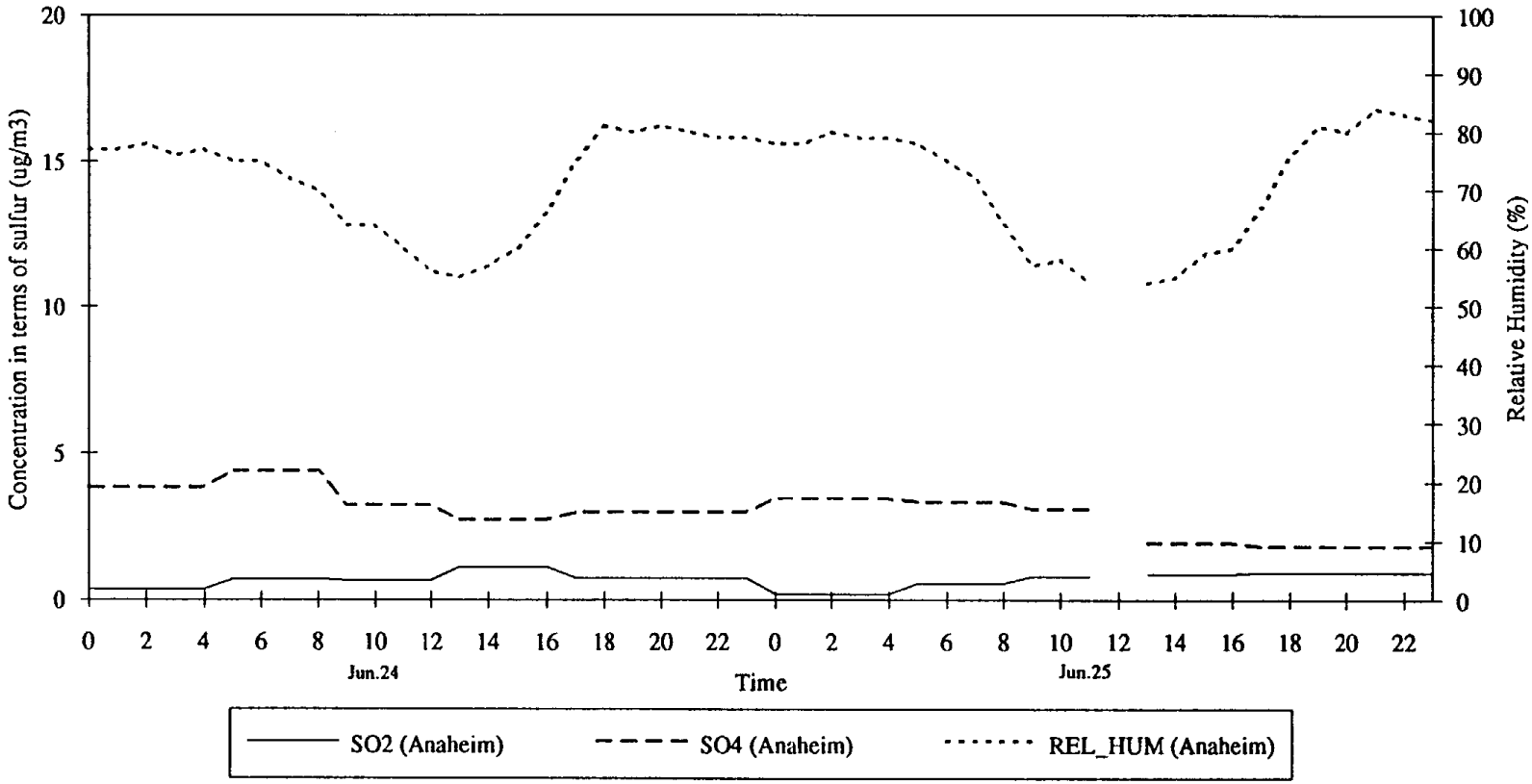

FIGURE 2.1.2 (continued)

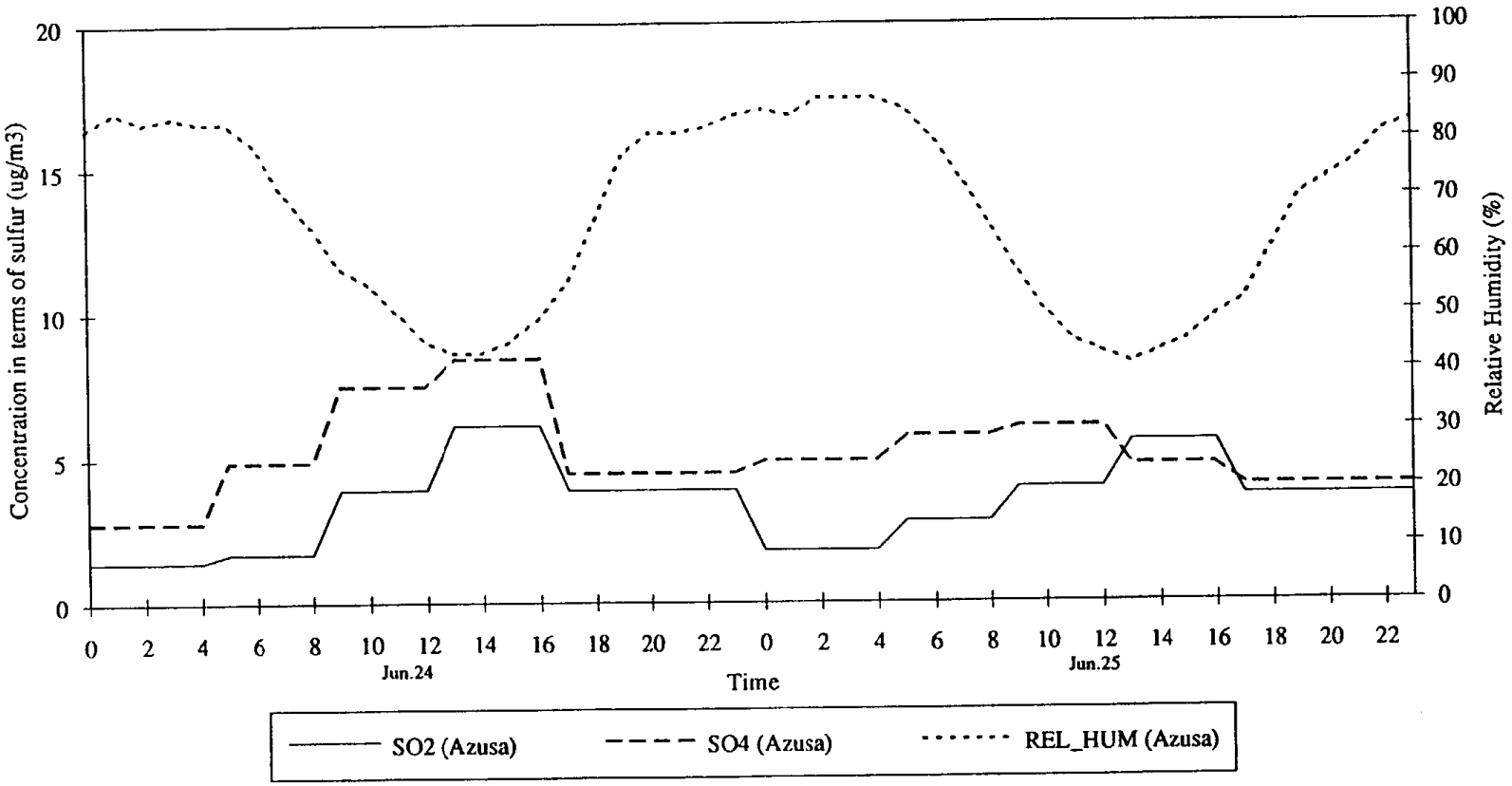

FIGURE 2.1.2 (continued)

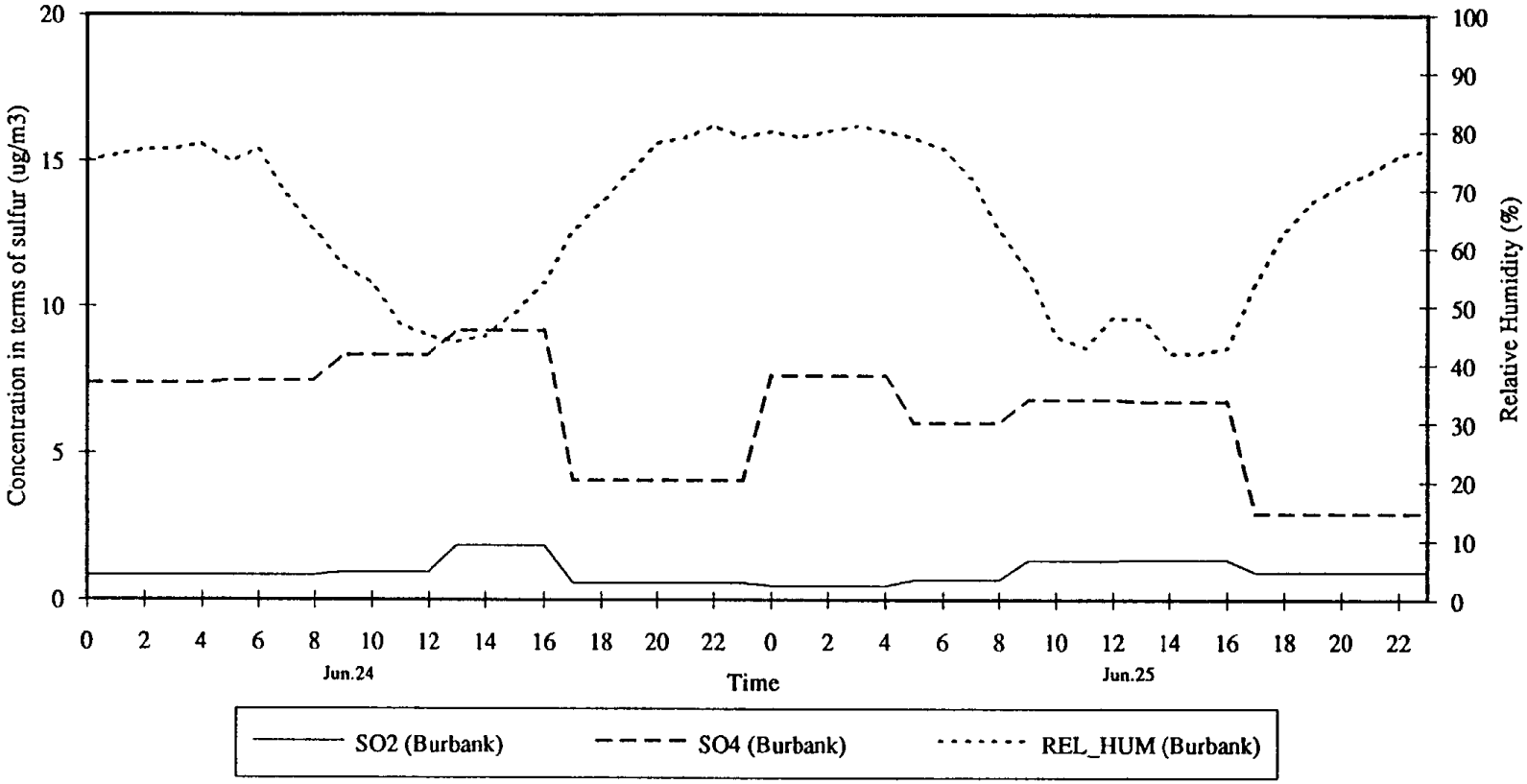

FIGURE 2.1.2 (continued)

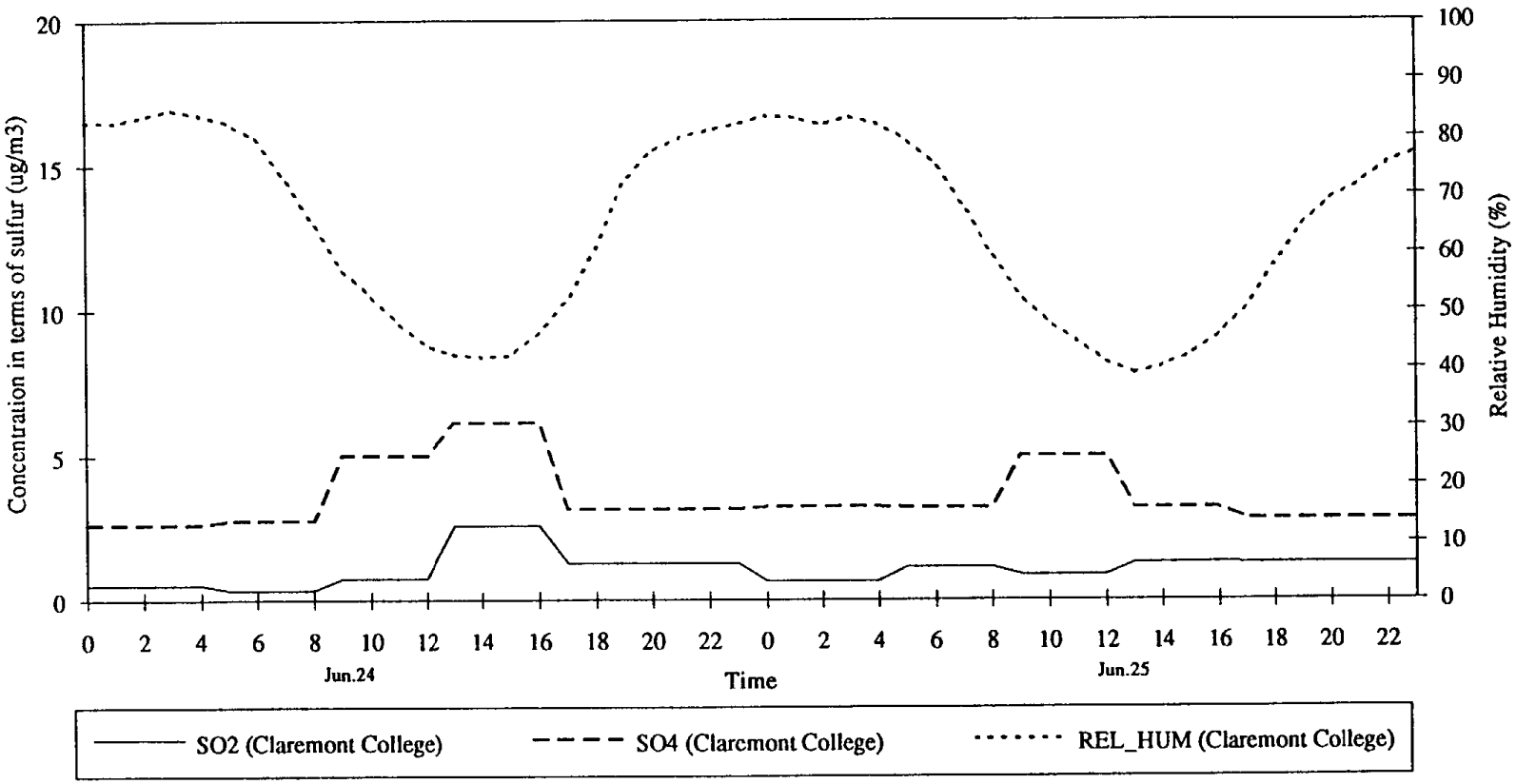

FIGURE 2.1.2 (continued)

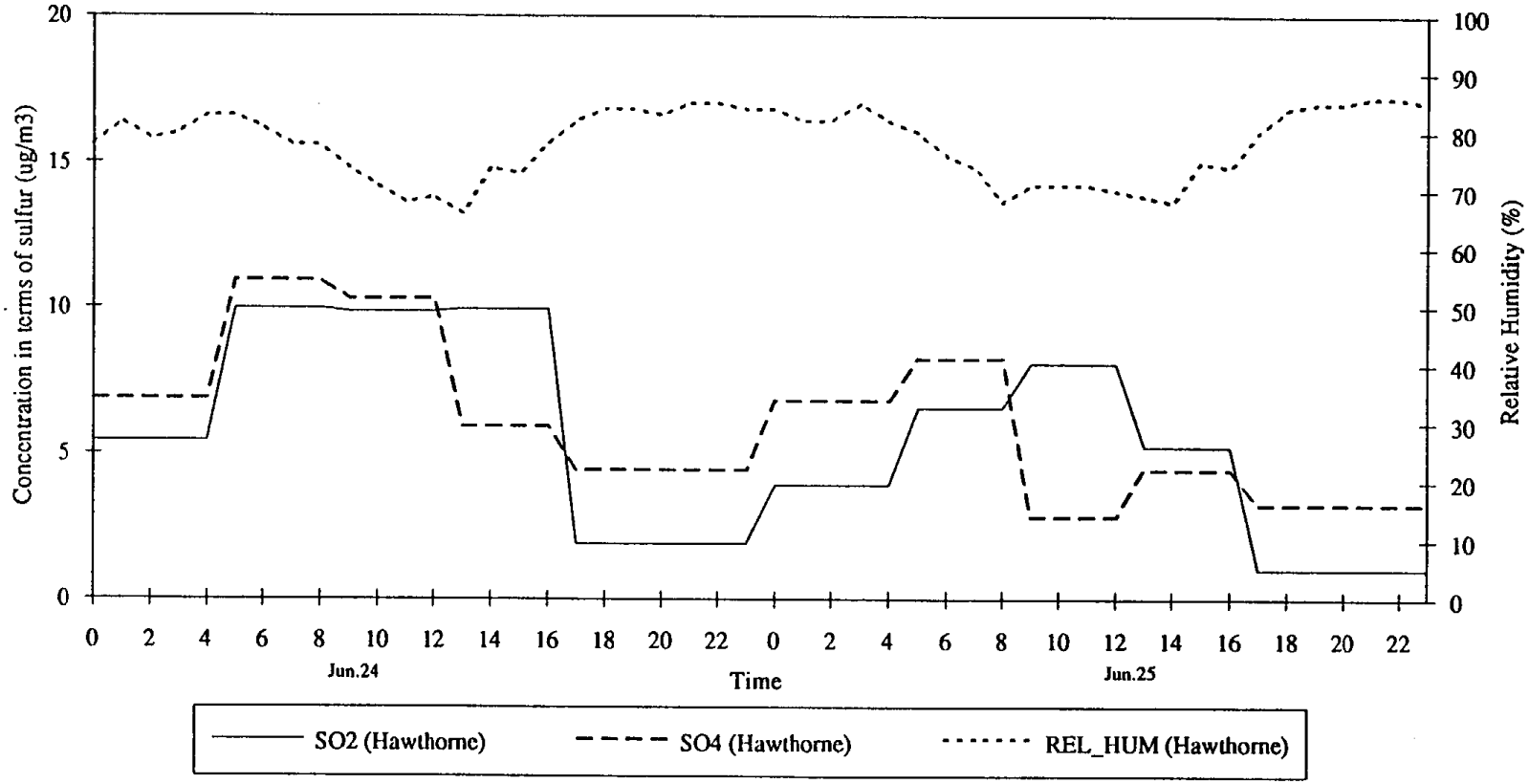

FIGURE 2.1.2 (continued)

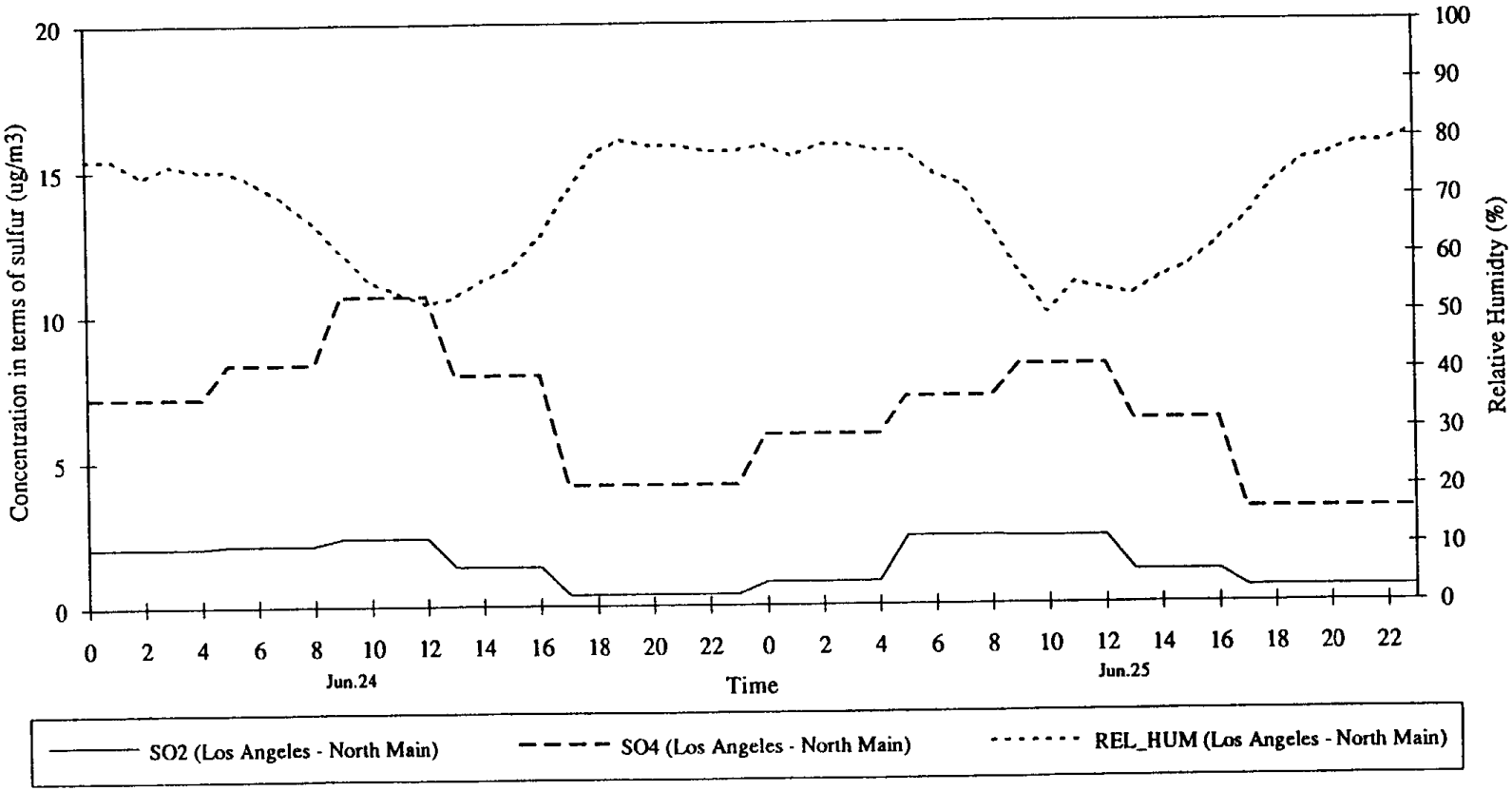

FIGURE 2.1.2 (continued)

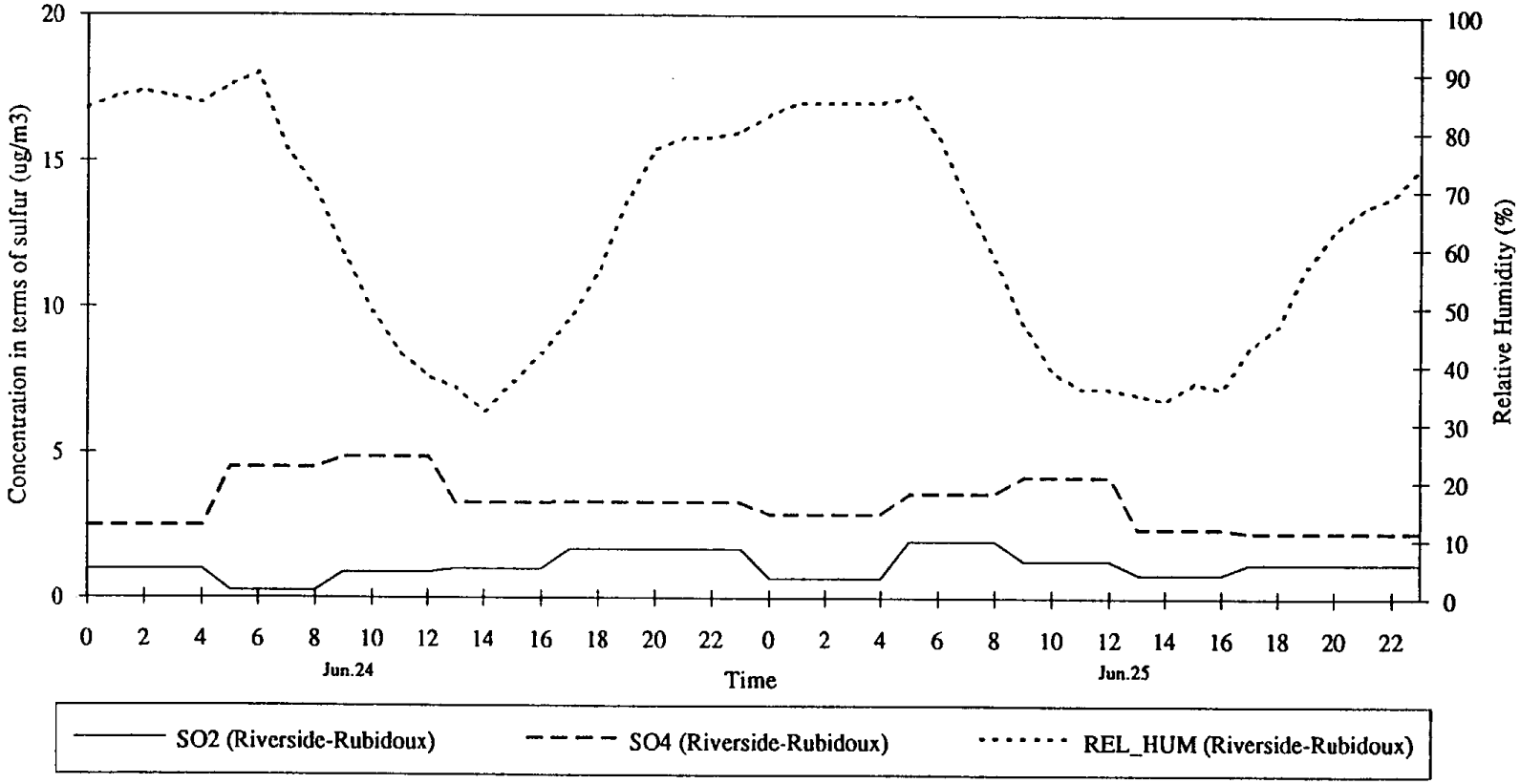

FIGURE 2.1.3. Time series plot (August 27-29, 1987)

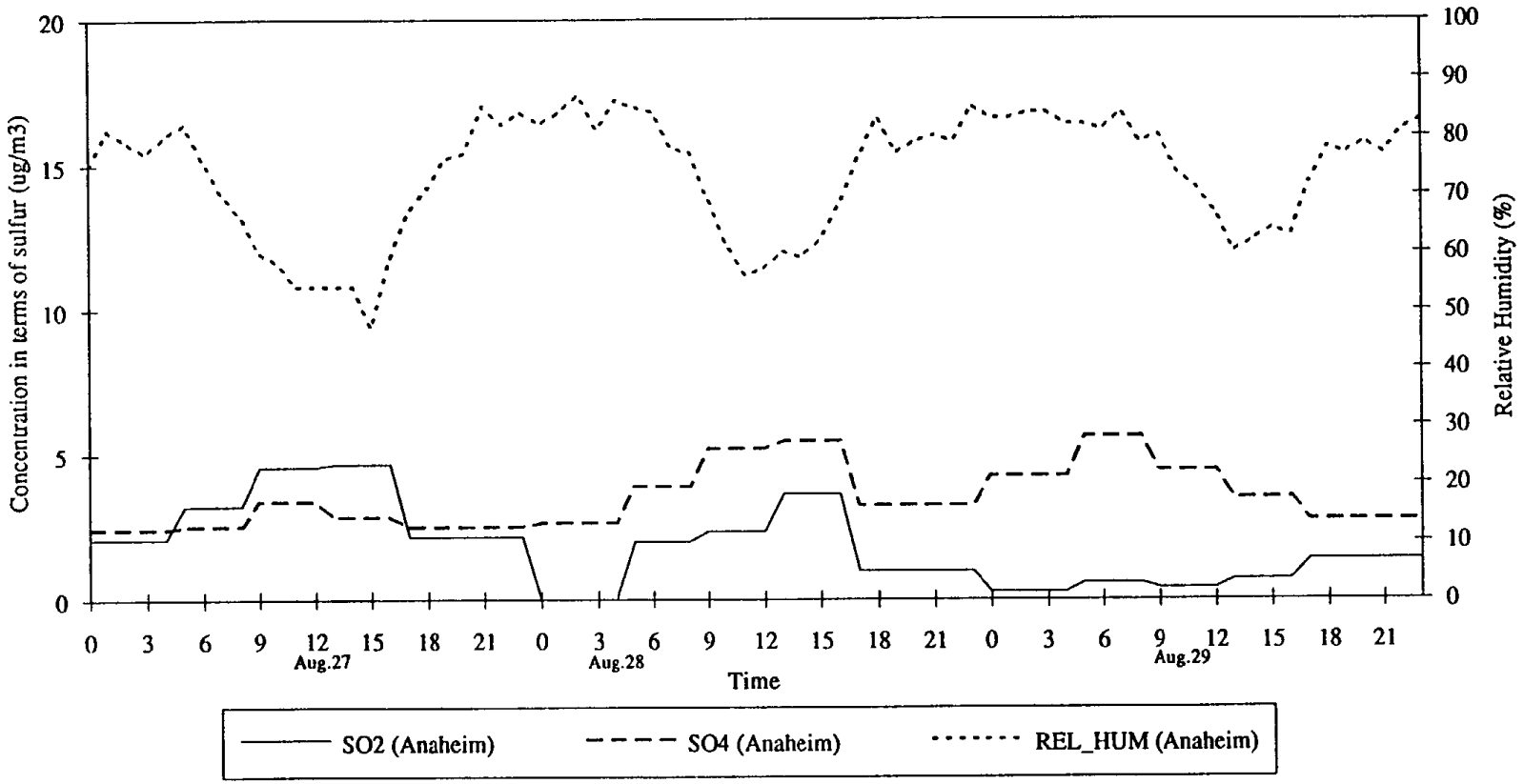

FIGURE 2.1.3 (continued)

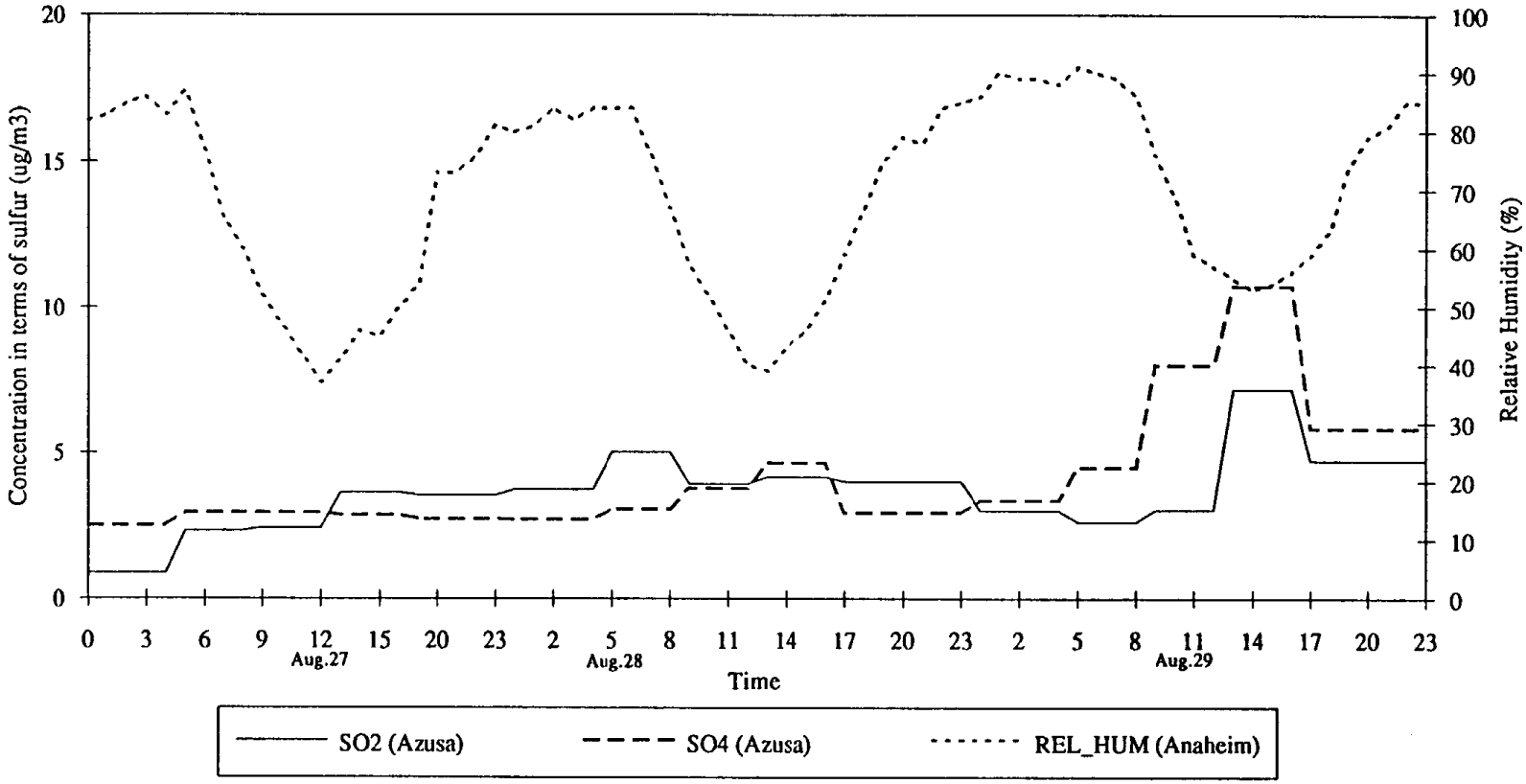

FIGURE 2.1.3 (continued)

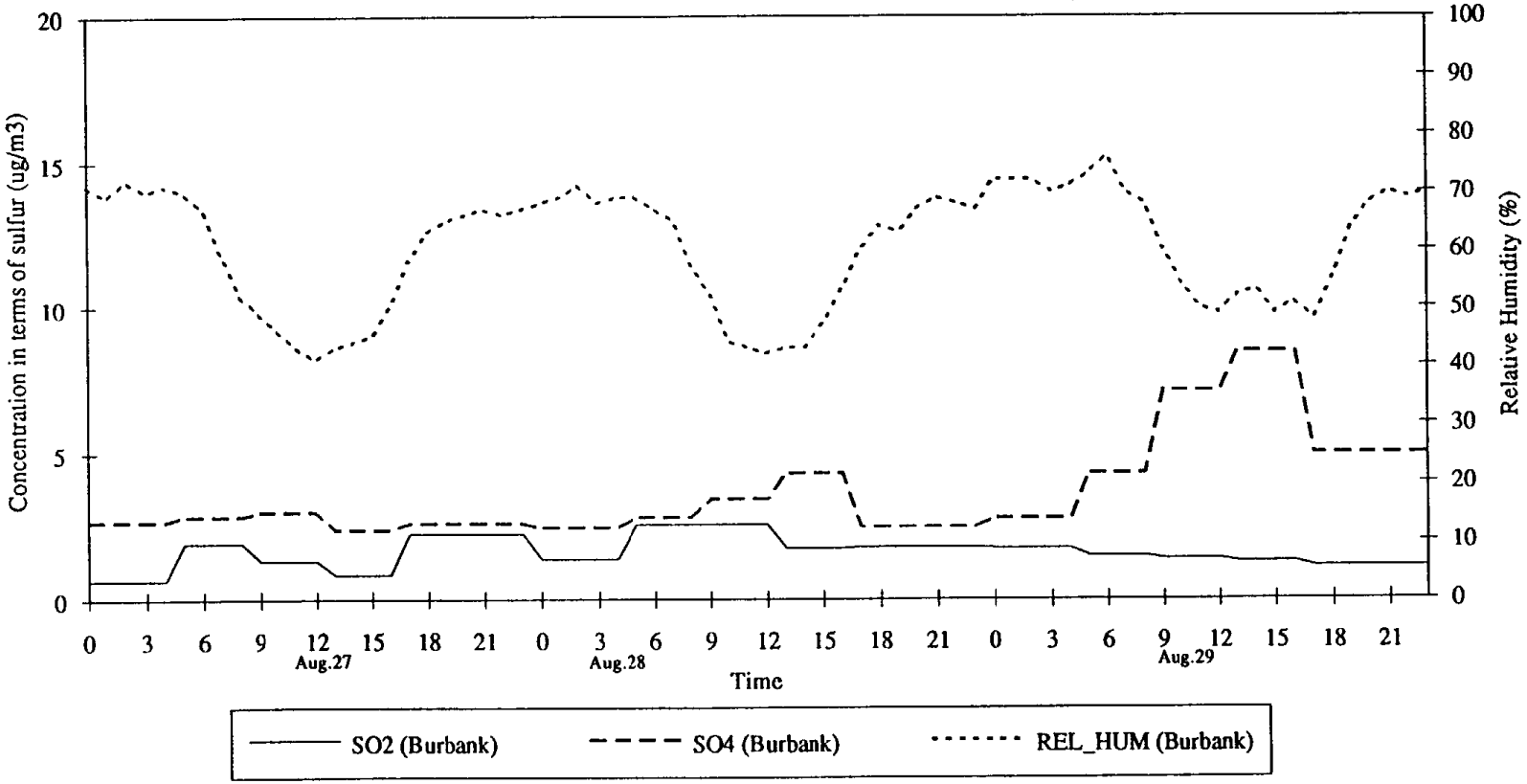

FIGURE 2.1.3 (continued)

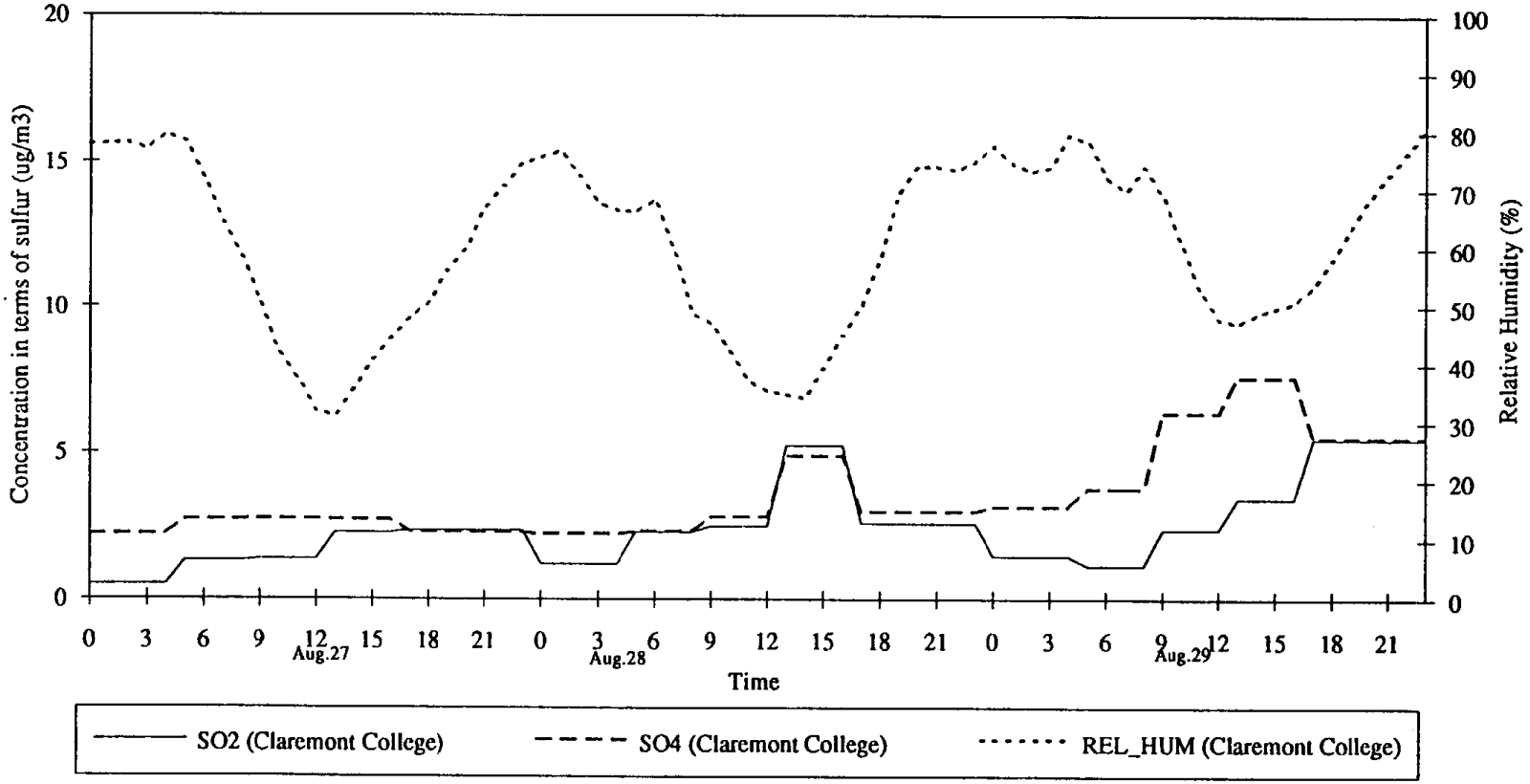

FIGURE 2.1.3 (continued)

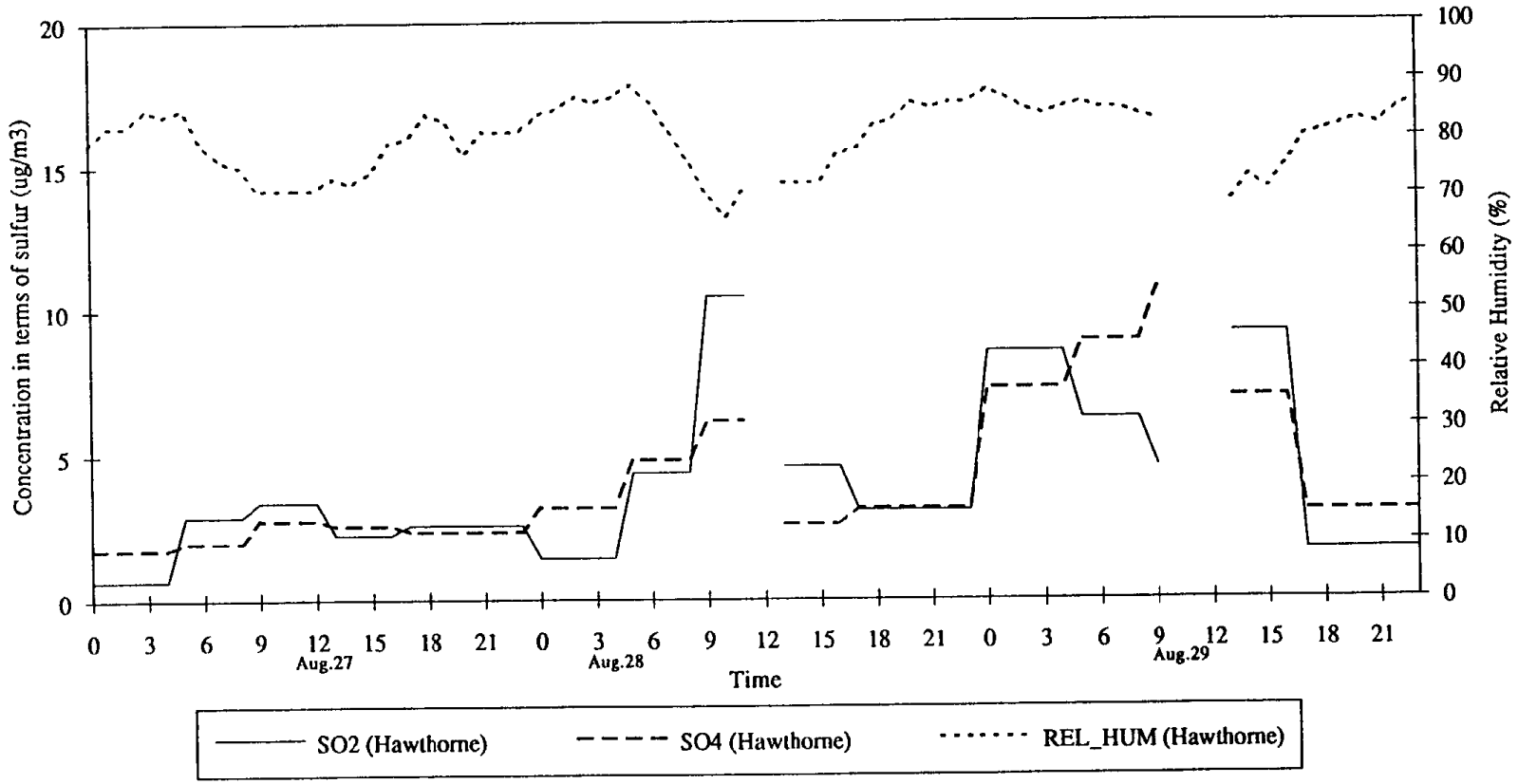

FIGURE 2.1.3 (continued)

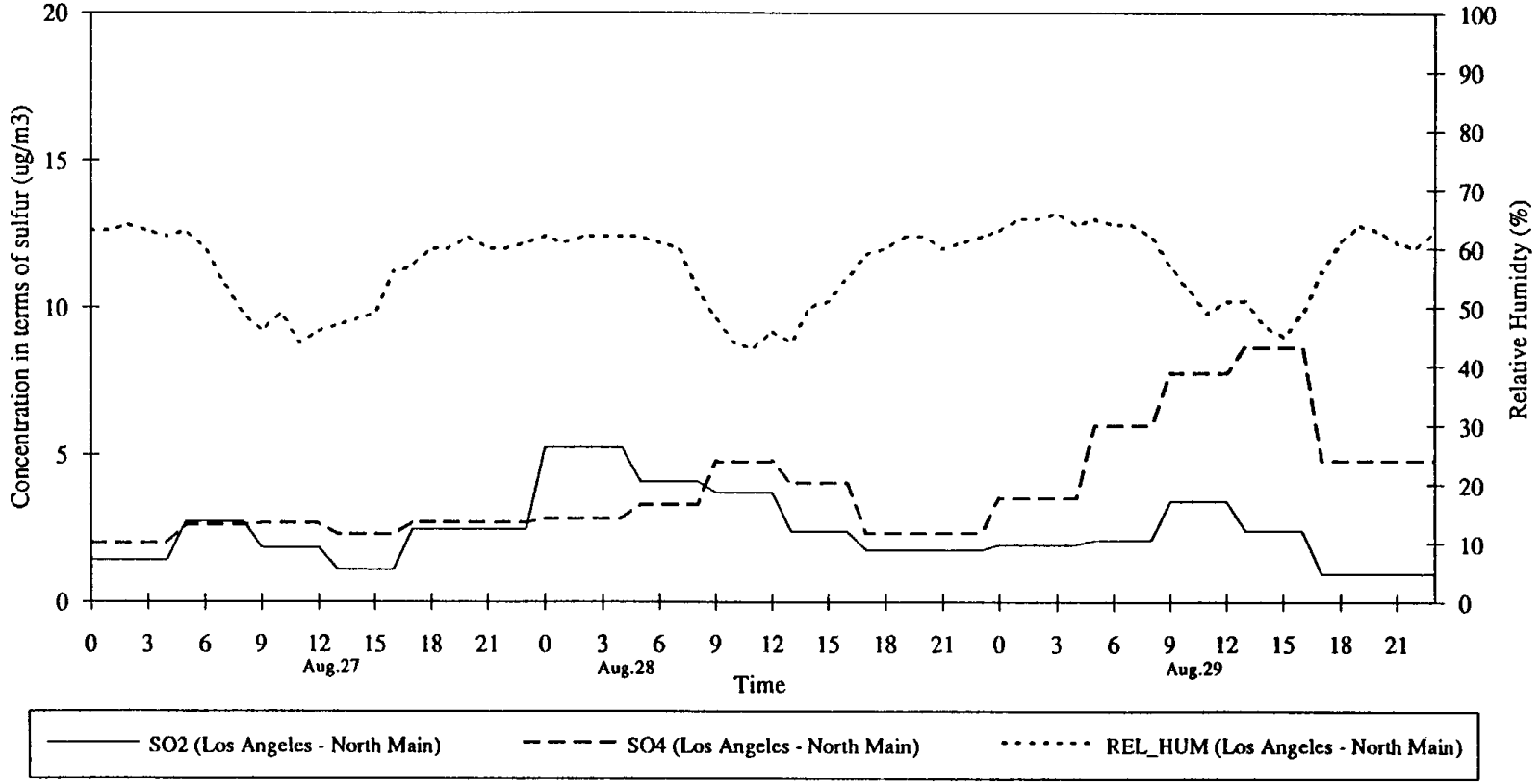

FIGURE 2.1.3. (continued)

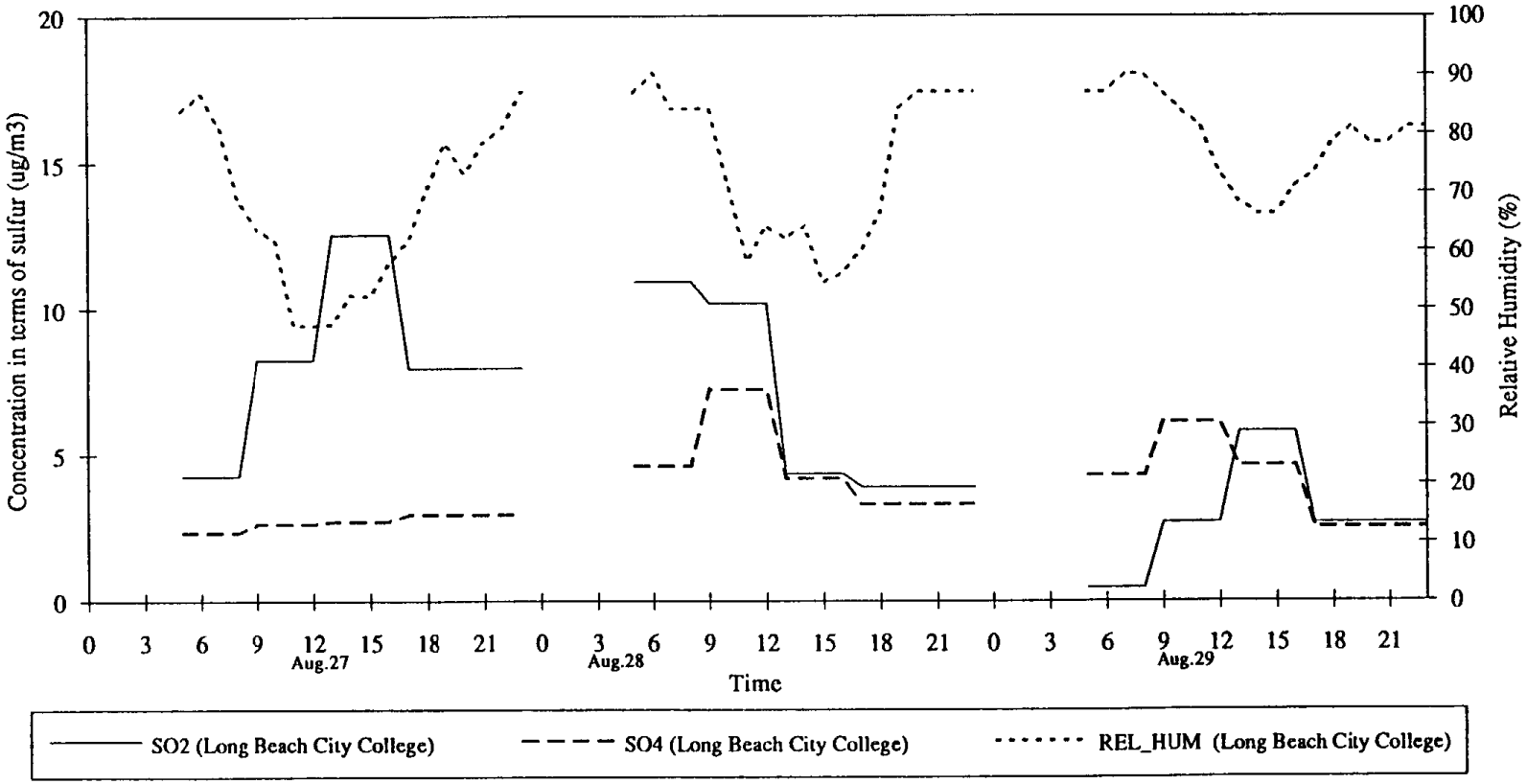

FIGURE 2.1.3 (continued)

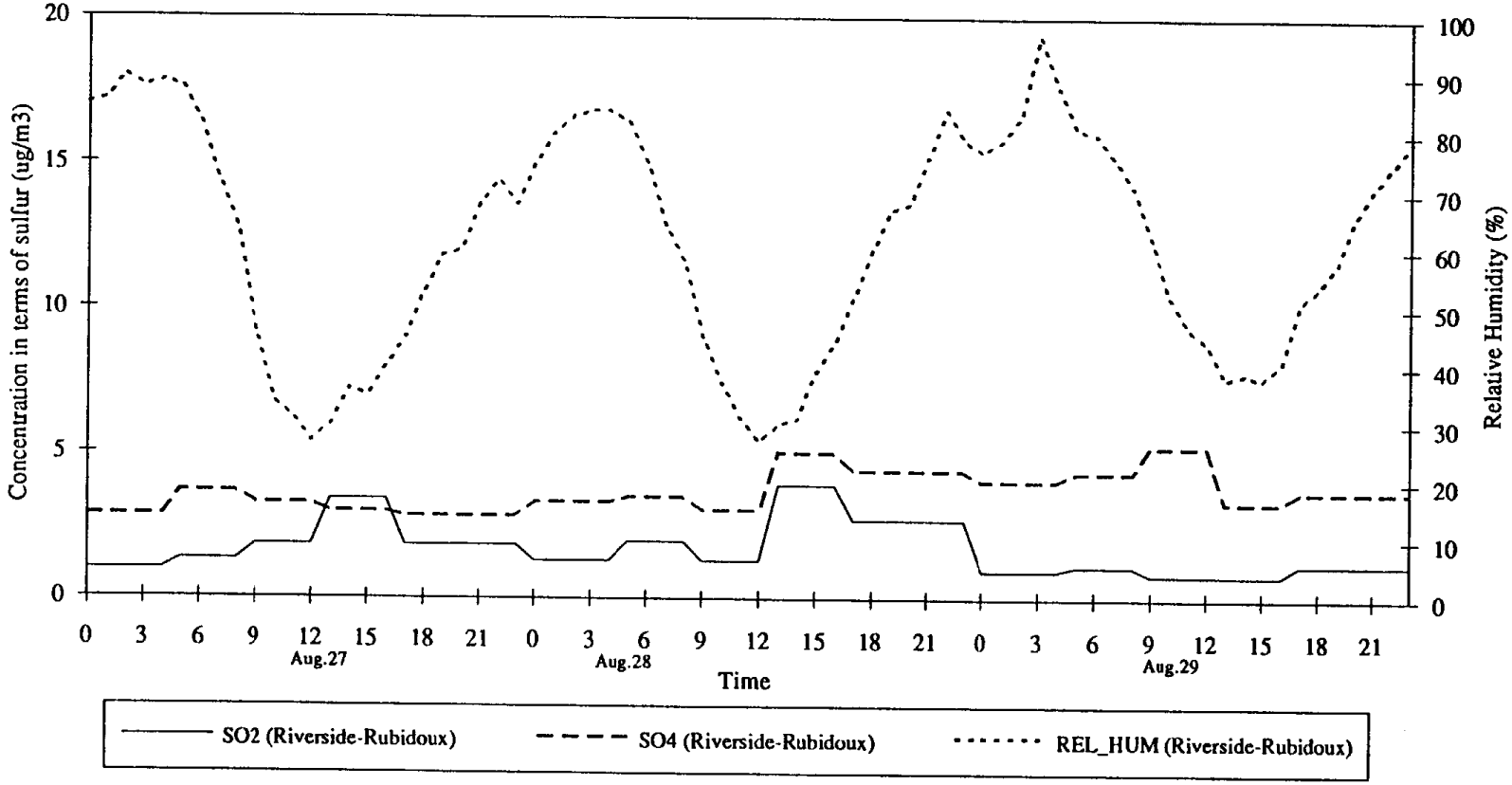

FIGURE 2.1.4. Time series plot (December 10 -11, 1987)

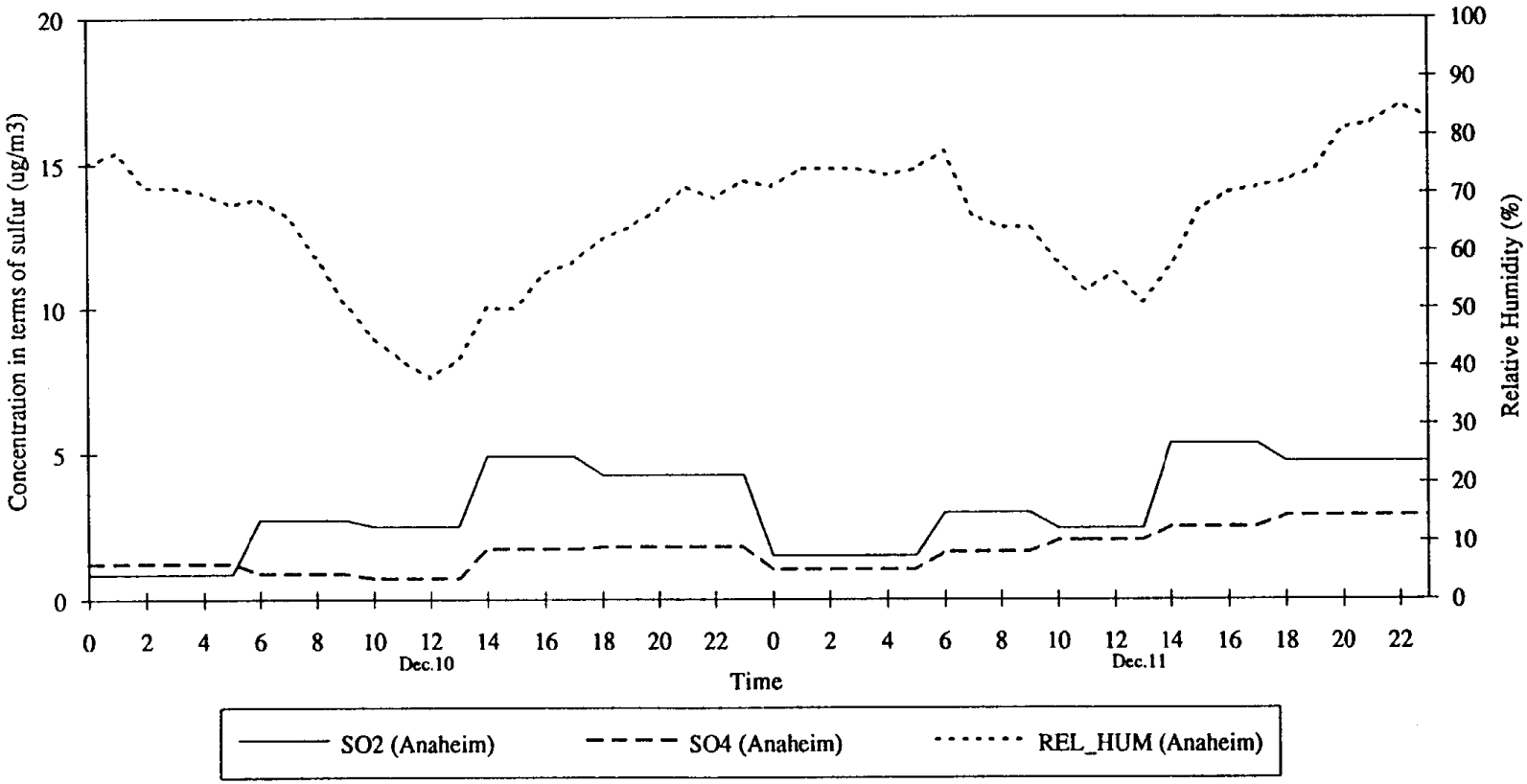

FIGURE 2.1.4 (continued)

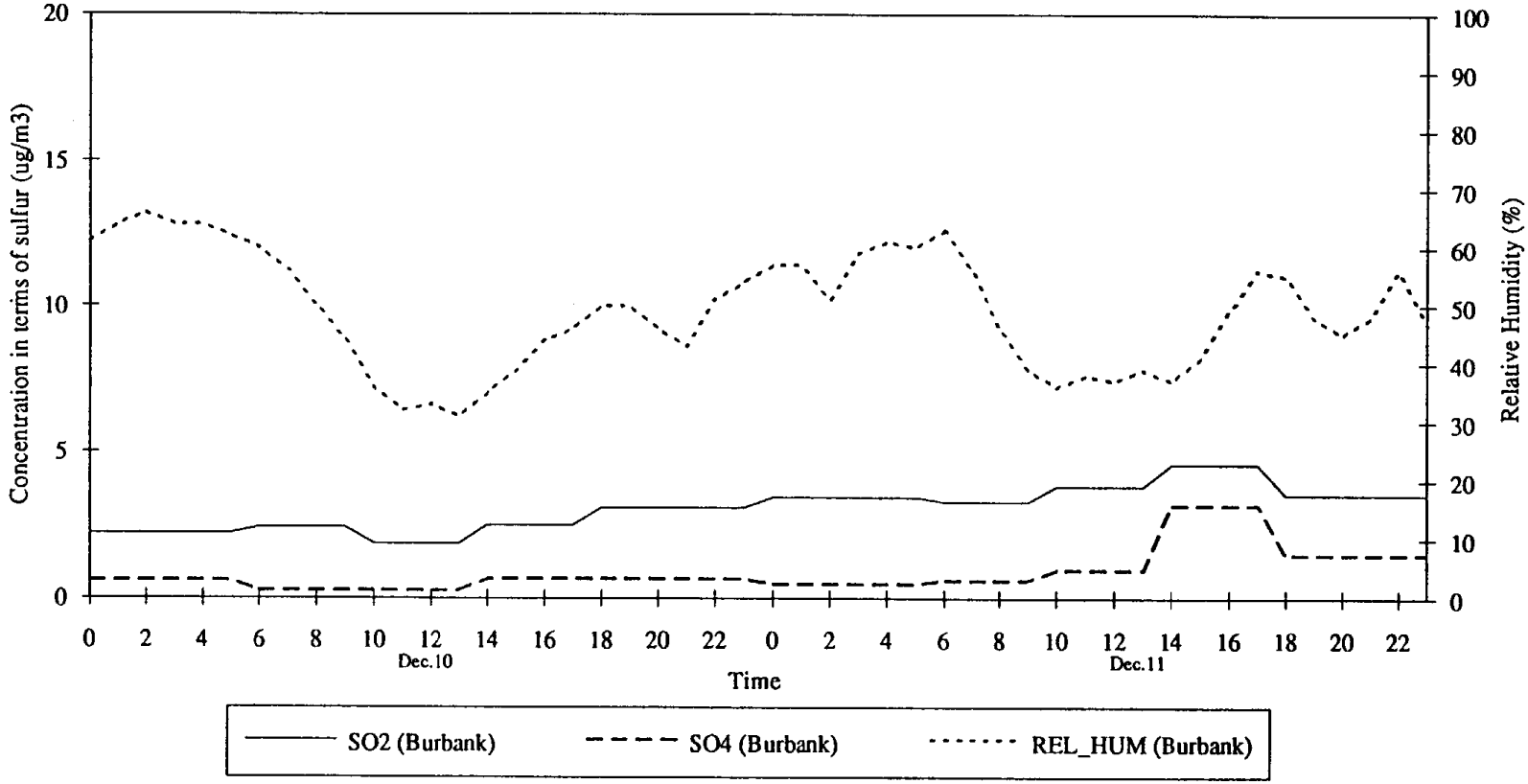

FIGURE 2.1.4 (continued)

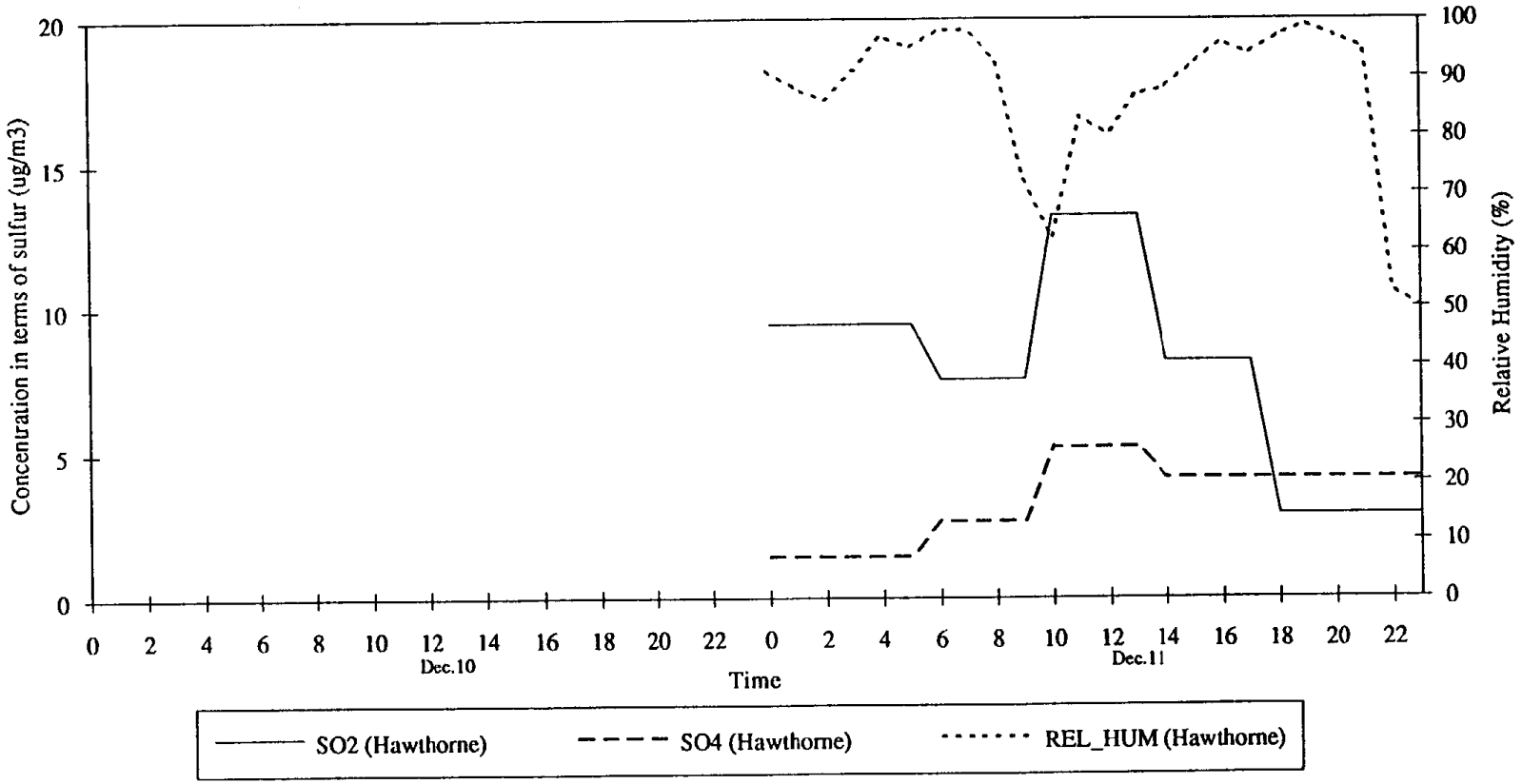

FIGURE 2.1.4 (continued)

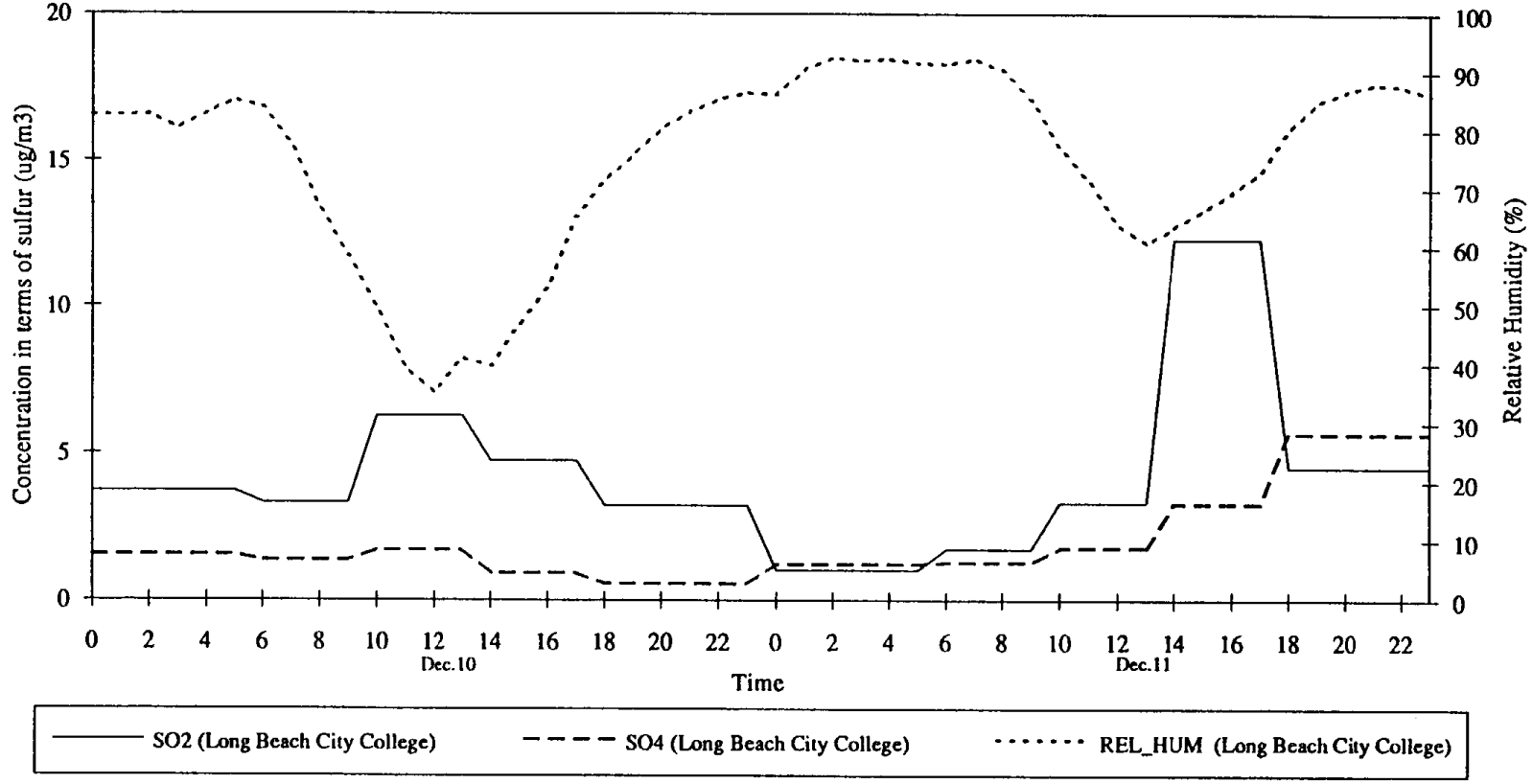

FIGURE 2.1.4. (continued)

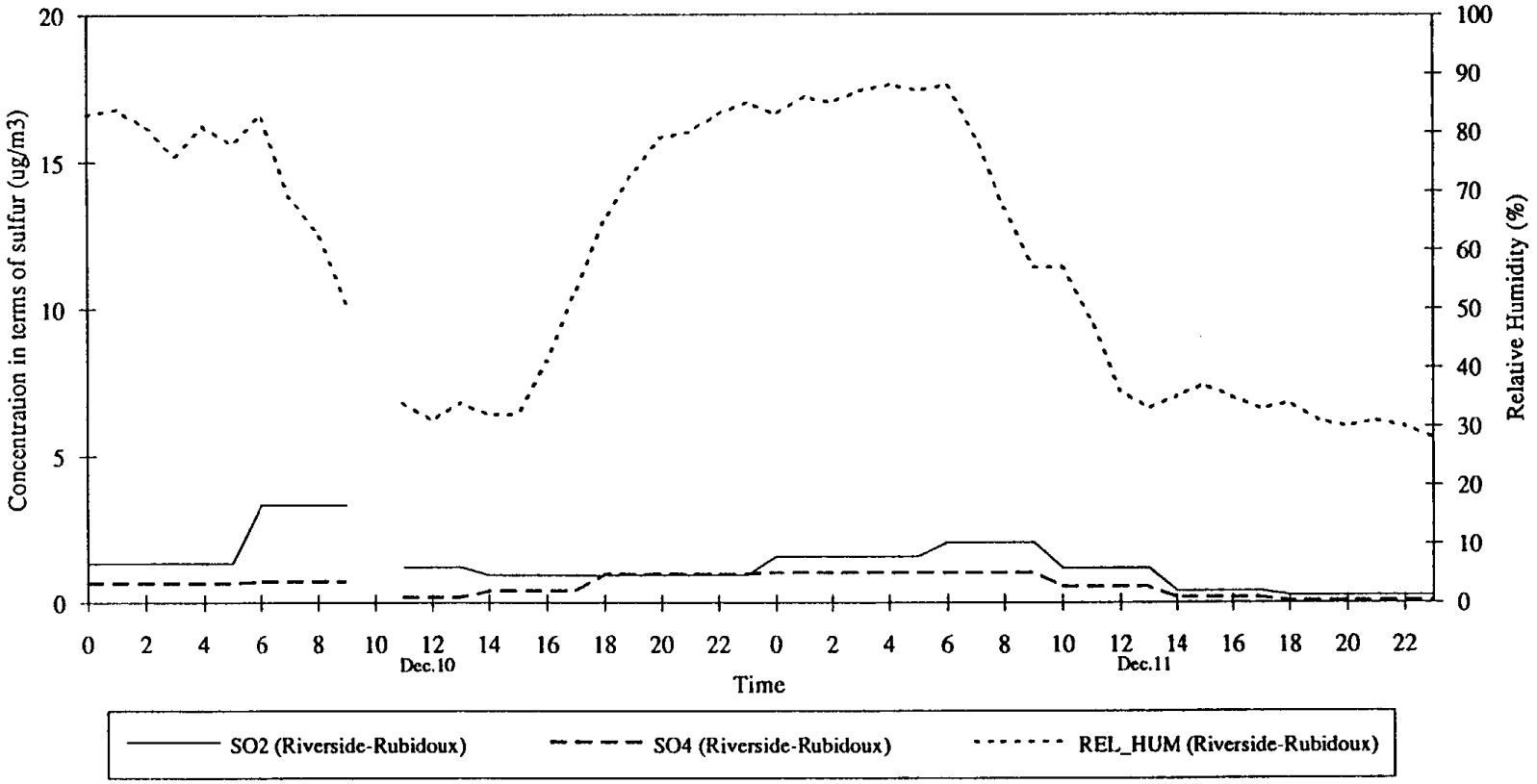

more pronounced $SO_4^=$ and SO_2 concentrations than the other sites. An increase of $SO_4^=$ concentrations and a steady value or decrease of SO_2 concentrations, or vice versa, were observed in all episodes. The following discussion provides more detailed descriptions of the observations for each episode.

During the June episode, the Azusa, Burbank, Hawthorne, and Los Angeles sites appeared to have higher $SO_4^=$ concentrations than the other sites. Almost all of the sites had relatively high sulfur contributions from $SO_4^=$ and relatively low sulfur contributions from SO_2 compared to other episodes. Increased $SO_4^=$ concentrations, accompanied by increased or steady SO_2 concentrations, were observed at the Azusa, Burbank, Claremont, Hawthorne, and Los Angeles sites. Decreased $SO_4^=$, accompanied by steady SO_2 concentrations, were observed at noon on June 24 at Hawthorne and decreased $SO_4^=$ accompanied by increased SO_2 were observed at 9 a.m. on June 25 at Hawthorne.

During the August episode, the Azusa, Long Beach, and Hawthorne sites appeared to have higher SO_2 concentrations than the other sites. The peak $SO_4^=$ and the second highest peak of $SO_4^=$ appeared at Hawthorne and Azusa sites, respectively. Often, increased $SO_4^=$ concentrations were observed in the afternoon with increased SO_2 concentrations. Photooxidation could explain the changes in the $SO_4^=$ concentrations.

During the December episode, the Hawthorne and Long Beach sites showed higher SO_2 and $SO_4^=$ concentrations. Increased $SO_4^=$ concentrations, accompanied by increased SO_2 concentrations, were observed at Hawthorne in the late morning and at Long Beach in the afternoon on December 11. An increase of $SO_4^=$, accompanied by a decrease of SO_2 concentrations were observed in the evening of December 11 at the Long Beach site.

Figure 2.1.5 presents three-dimensional plots of relative humidity, SO_2, and $SO_4^=$ concentrations. The plots were constructed using all data collected at each station during the study. As shown in this figure, high $SO_4^=$ concentrations are likely to occur during periods of high SO_2 concentrations and especially when relative humidities are above 50%. This behavior is clear at receptors near coastal source areas, such as Long Beach and Hawthorne, and may be due to a combination of emitted primary sulfuric acid (H_2SO_4) and local chemistry, both aqueous and gaseous.

FIGURE 2.1.5. Concentrations of PM-10 sulfates (SO_4) at SCAB monitoring sites.

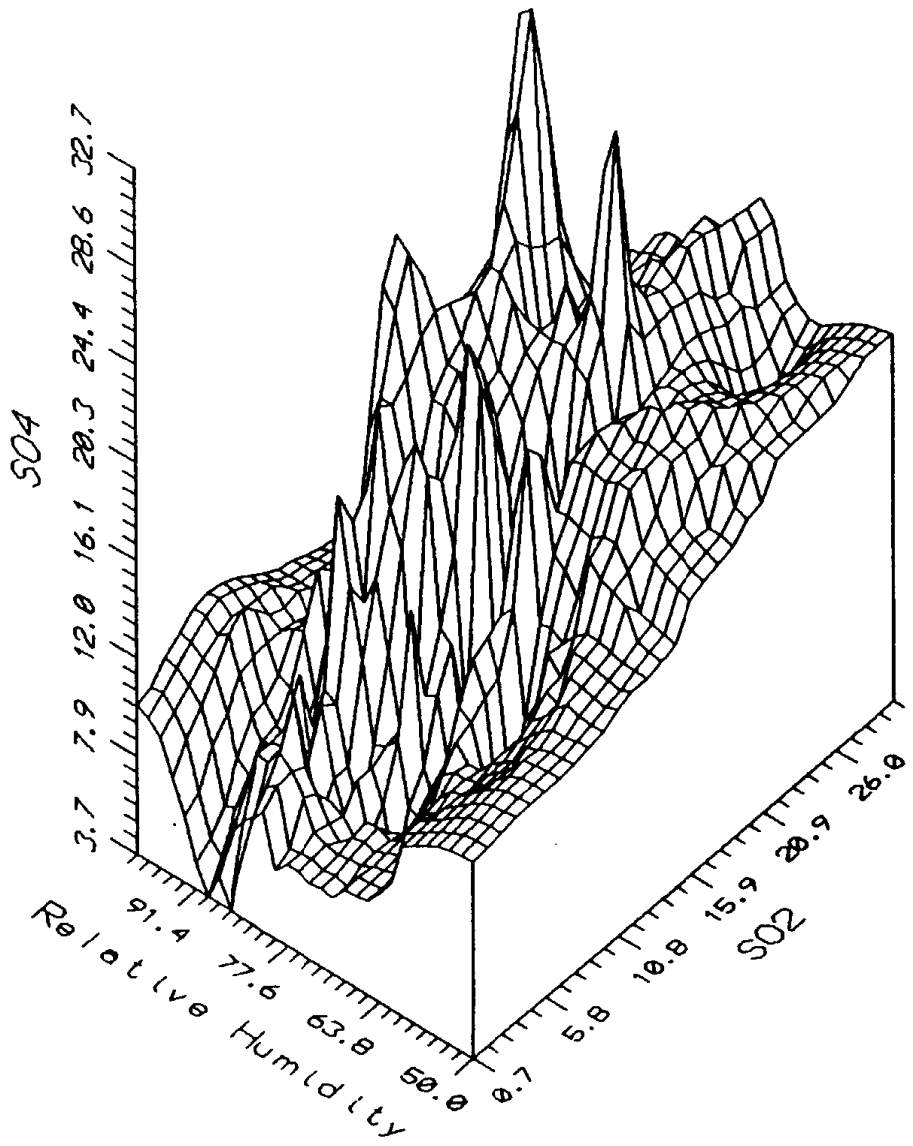

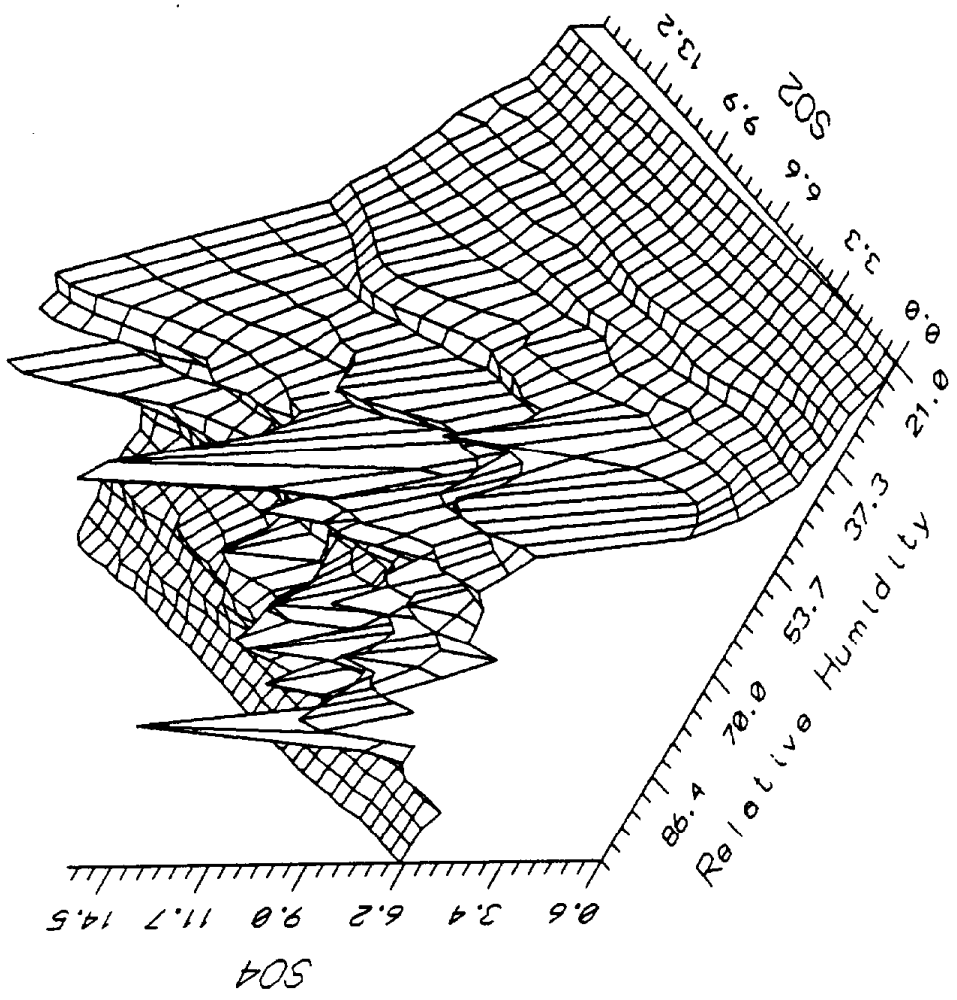

FIGURE 2.1.5 (continued)

Burbank

FIGURE 2.1.5 (continued)

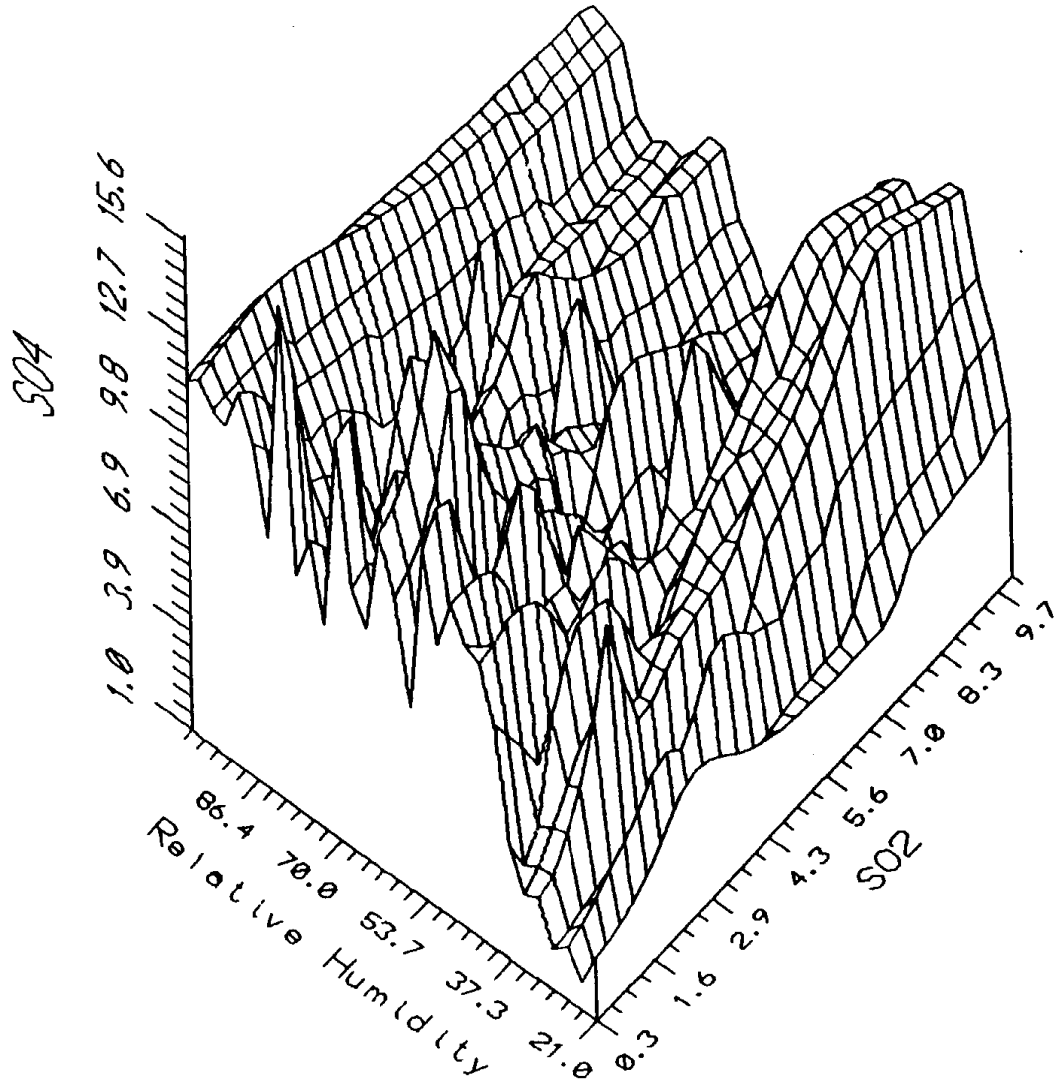

Rubidoux

FIGURE 2.1.5 (continued)

Los Angeles

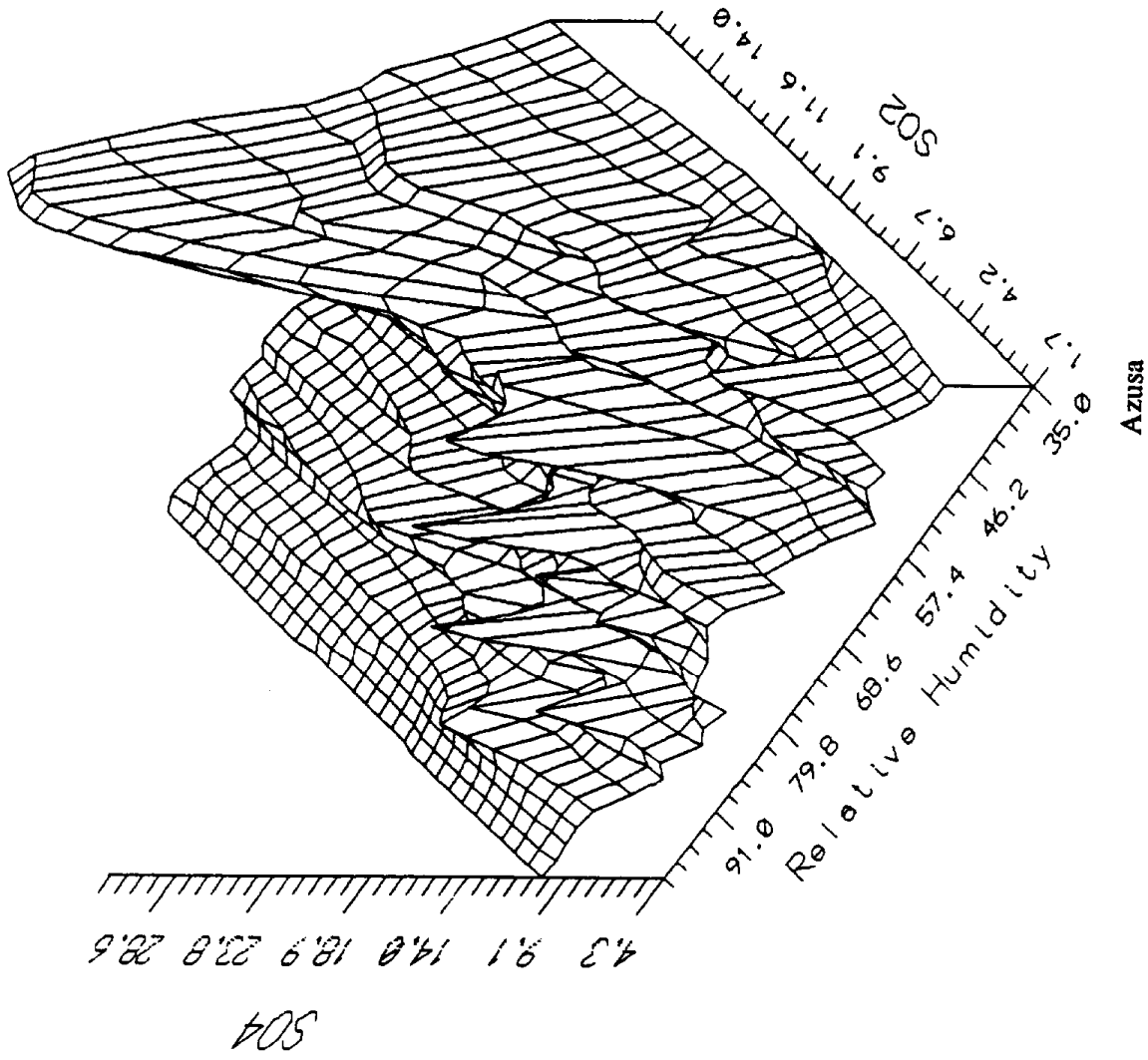

FIGURE 2.1.5 (continued)

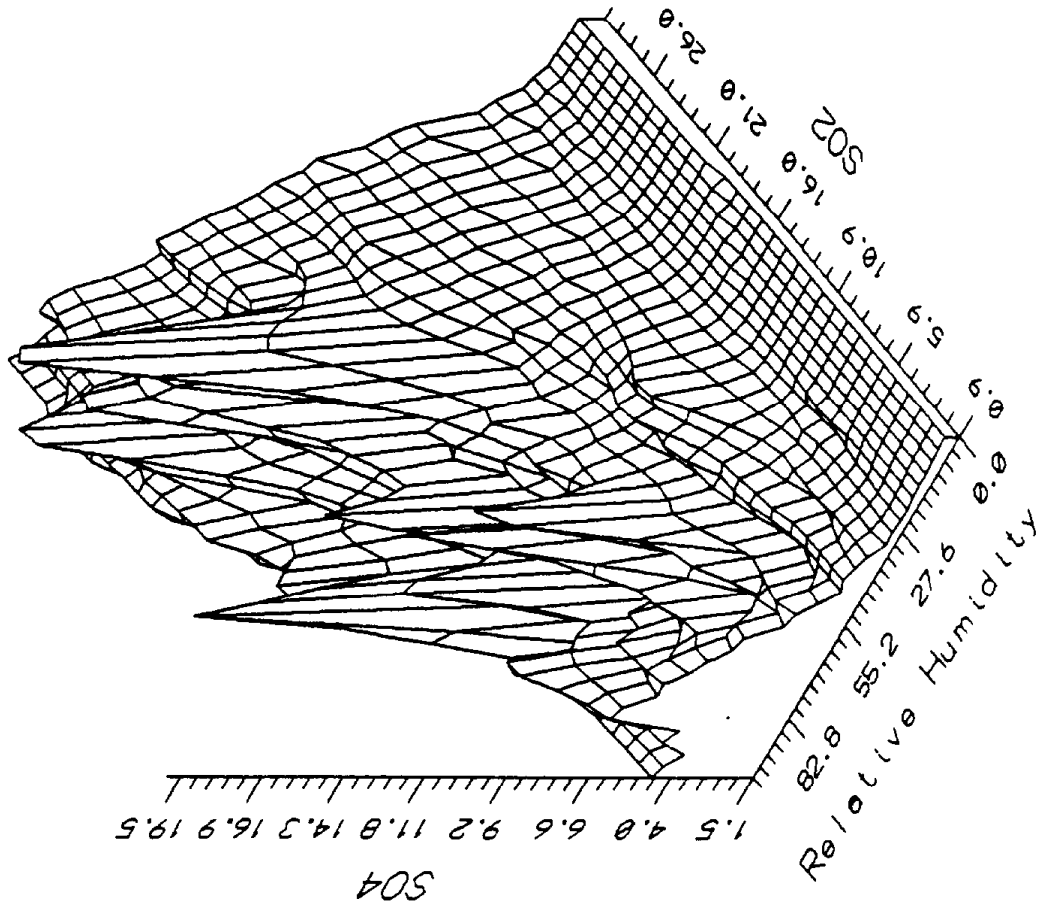

FIGURE 2.1.5 (continued)

Long Beach

FIGURE 2.1.5 (continued)

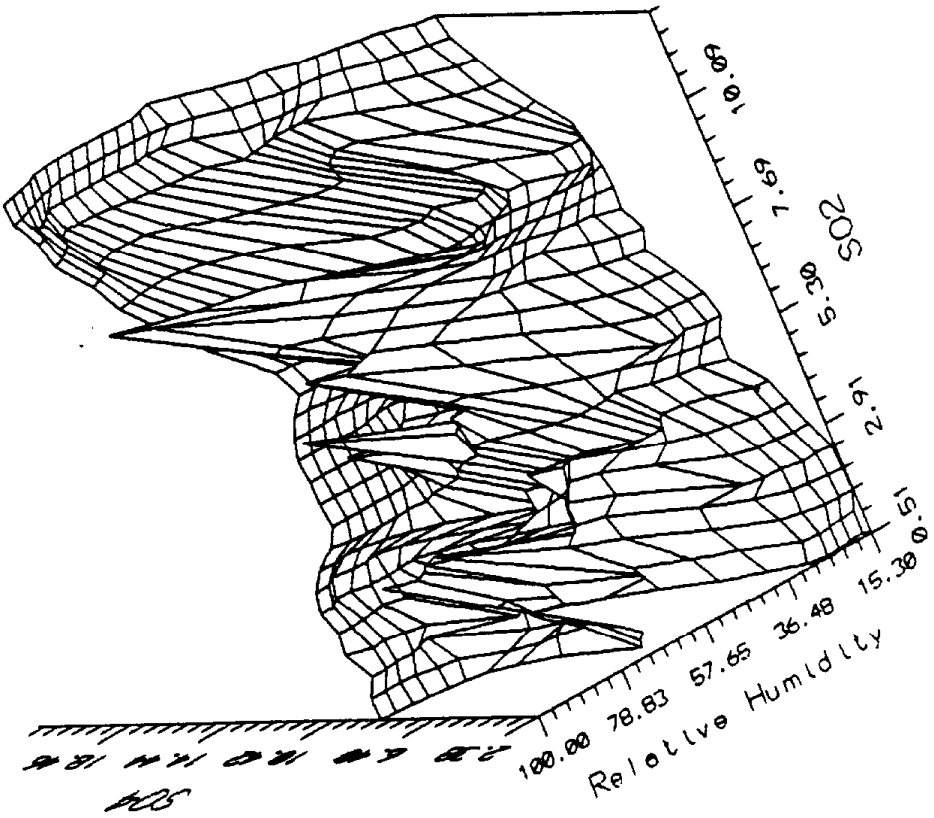

Claremont

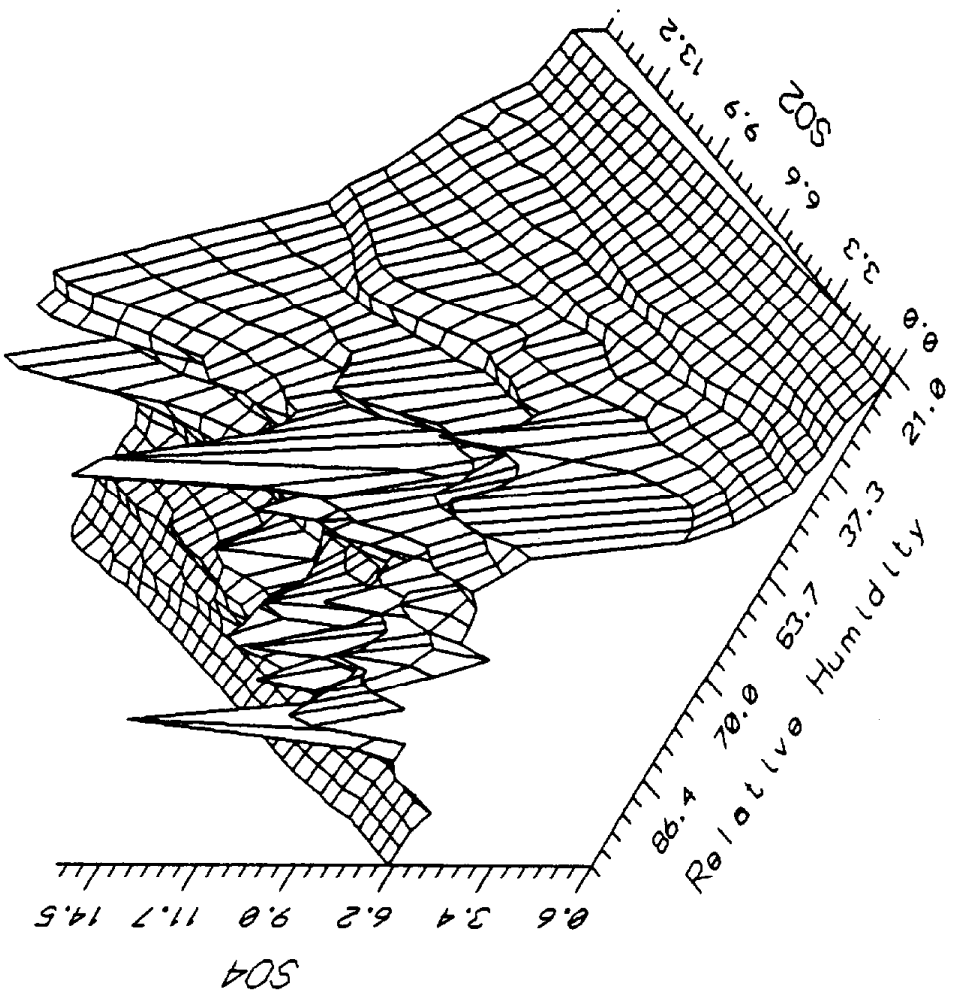

FIGURE 2.1.5 (continued)

Anaheim

FIGURE 2.1.6. SO2, SO4 concentration in terms of sulfur, total sulfur concentrations and relative humidity for June 24-25, measured at Hawthorne site.

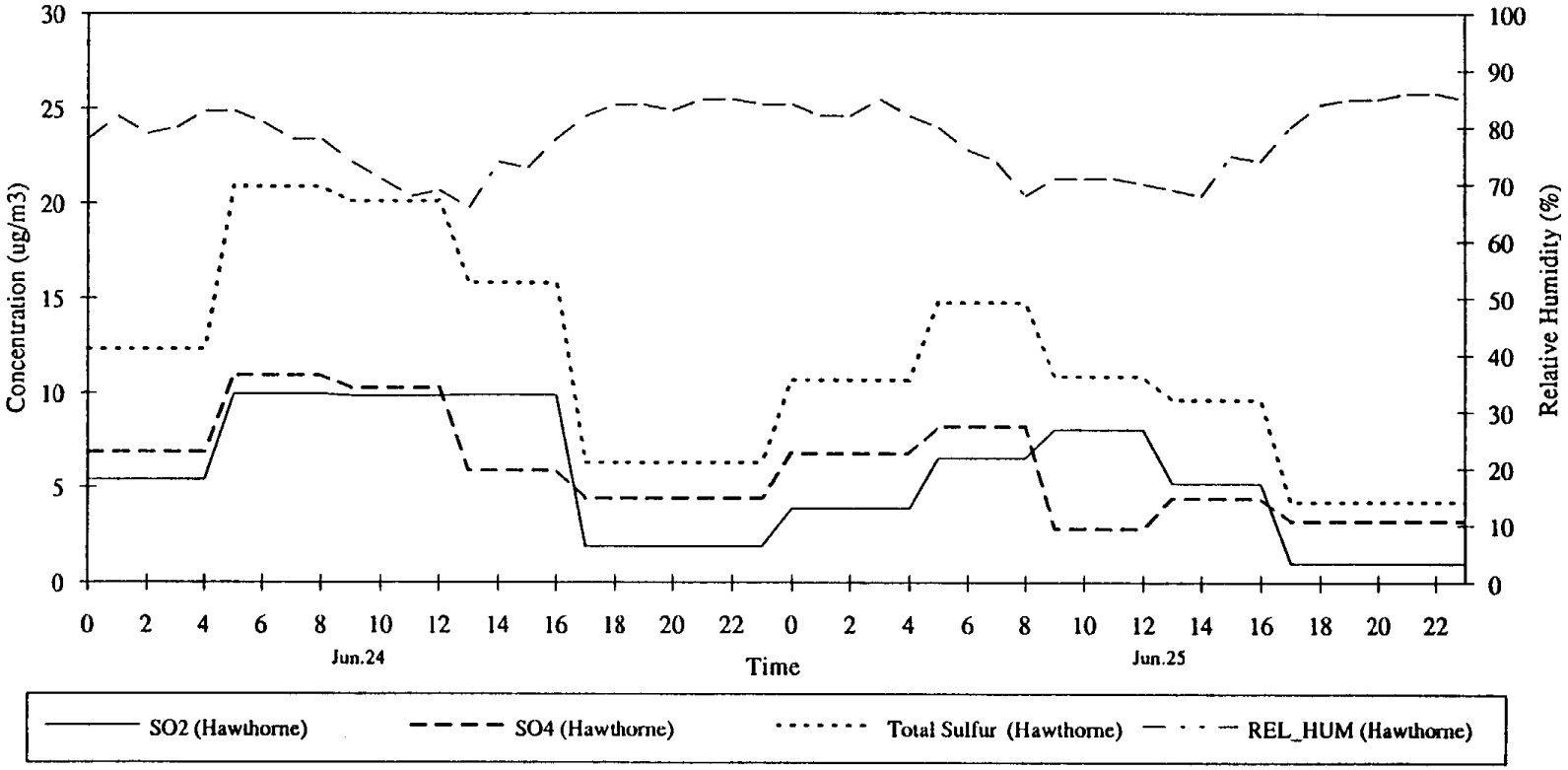

FIGURE 2.1.7. SO2, SO4 concentration in terms of sulfur, total sulfur concentrations and relative humidity for August 27-29, measured at Hawthorne site.

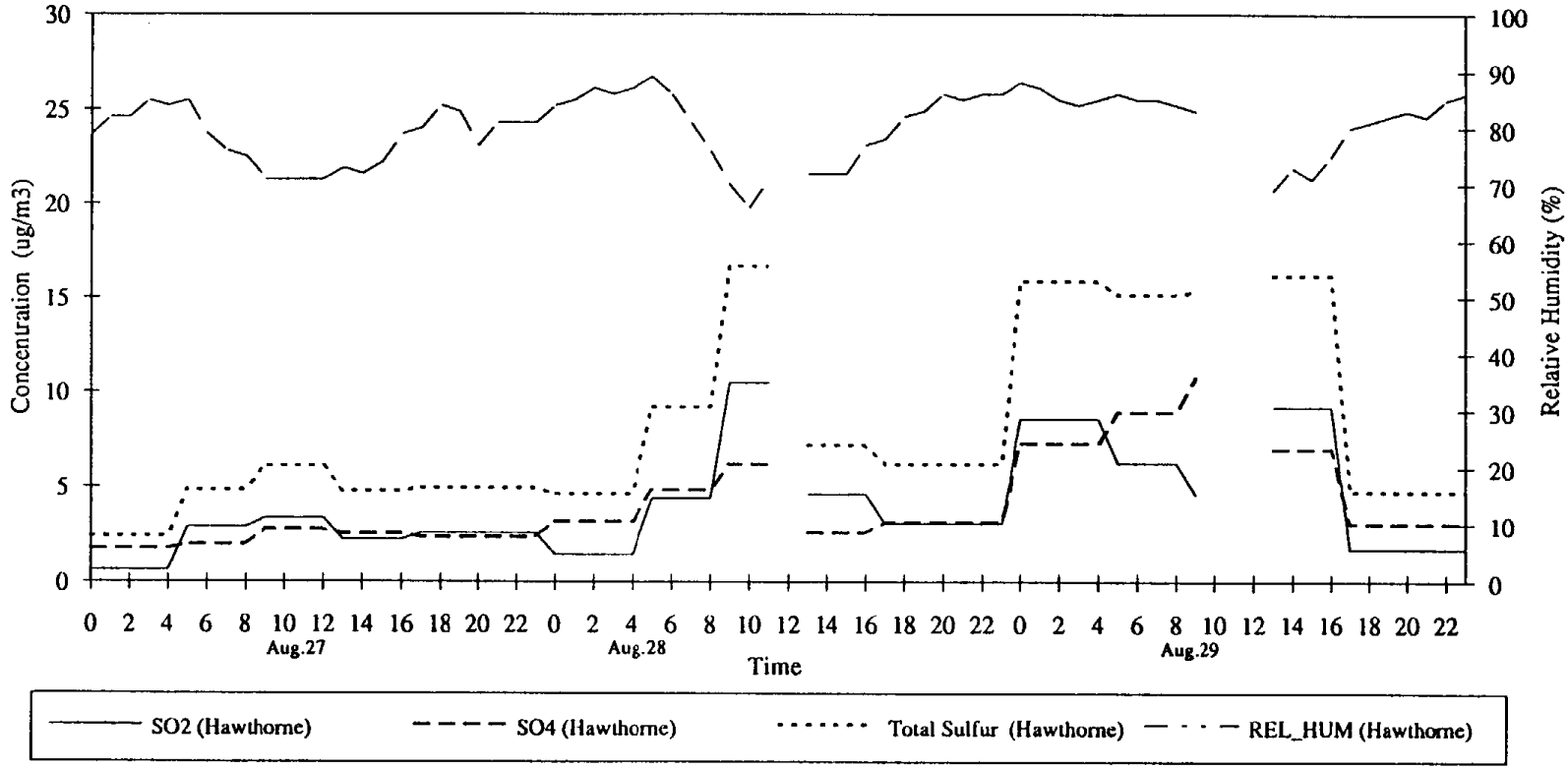

observed very early in the morning. If however, sulfates were produced locally by the reaction of

$$SO_2 + OH\bullet \xrightarrow{H_2O} H_2SO_4$$

then the maximum should occur after noon, or early in the evening. Another indication that aged parcels could cause the peaks in the sulfate concentration at Hawthorne is that the high sulfate concentrations are accompanied by high SO_2 concentrations, except at 1 p.m.-4 p.m. on June 24 and at 9 a.m.-noon on June 25. Similar behavior is also observed during the August 27-29 episode, except for the period from 10 a.m.-noon of the last day of the episode. However, the peak concentration appears around noon and may indicate the high transformation rate of photooxidation. For both episodes, the decrease of the $SO_4^=$ concentration corresponding to the steady or increased SO_2 concentration, or vice versa, indicates that direct emissions of sulfate and transformations which is associated with meteorological conditions, could be one of the important factors dominating $SO_4^=$ concentrations during that period.

To understand the overall sulfate concentrations in the SoCAB, and to identify the origins of the parcels that cause the high sulfate concentrations at the Hawthorne site, bar-graphs of SO_2 were plotted on a map of the SoCAB for each site, as were available data for $SO_4^=$ and relative humidity. The December and August episodes for the Hawthorne site were plotted.

For the December episode, only five of the eight sites have data available. As shown on Figure 2.1.8, both SO_2 and sulfate concentrations were low through December 10. However, on December 11, relatively high concentrations of SO_2 were observed at 2 a.m., 8 a.m., 12 noon, and 4 p.m. at Hawthorne and at 4 p.m. at Long Beach. Relatively high $SO_4^=$ was observed at 12 noon and 4 p.m. the same day at the Hawthorne site and at 8 p.m. at the Long Beach site.

As the day progressed on December 11, both SO_2 and $SO_4^=$ concentrations at Hawthorne increased substantially, while the corresponding concentrations at the rest of the sites remained relatively low. The cause of the high concentrations appearing at

FIGURE 2.1.8. SCAQS monitoring locations showing SO_2 and SO_4 concentrations and relative humidity during December episode.

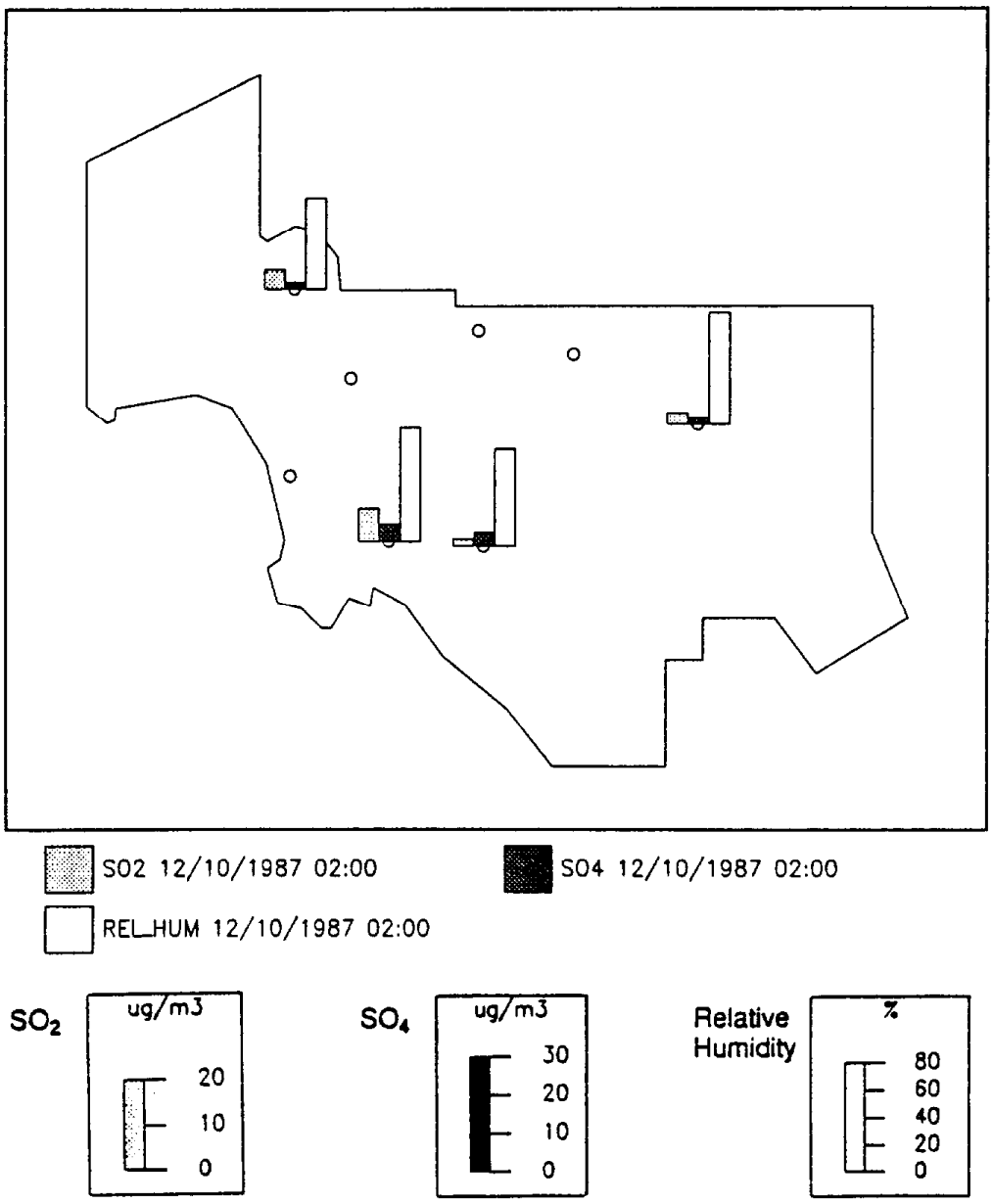

FIGURE 2.1.8 (continued)

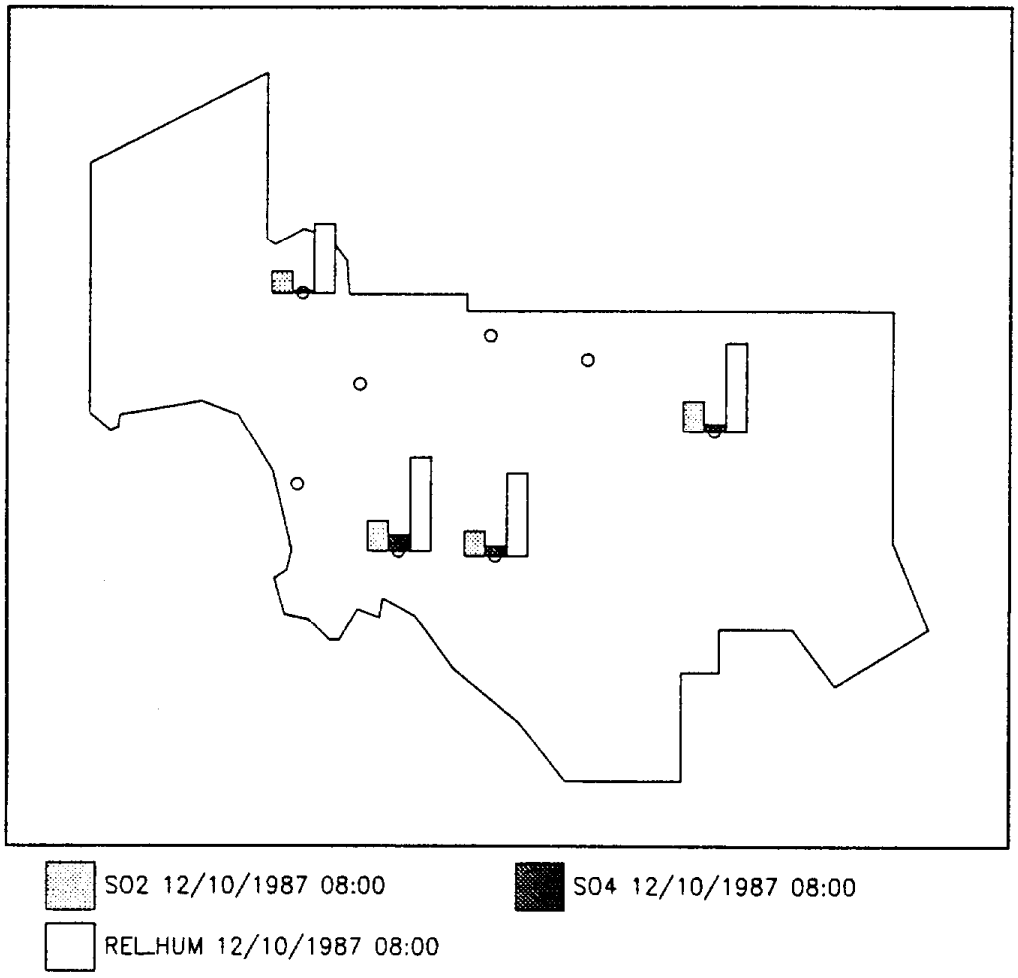

FIGURE 2.1.8 (continued)

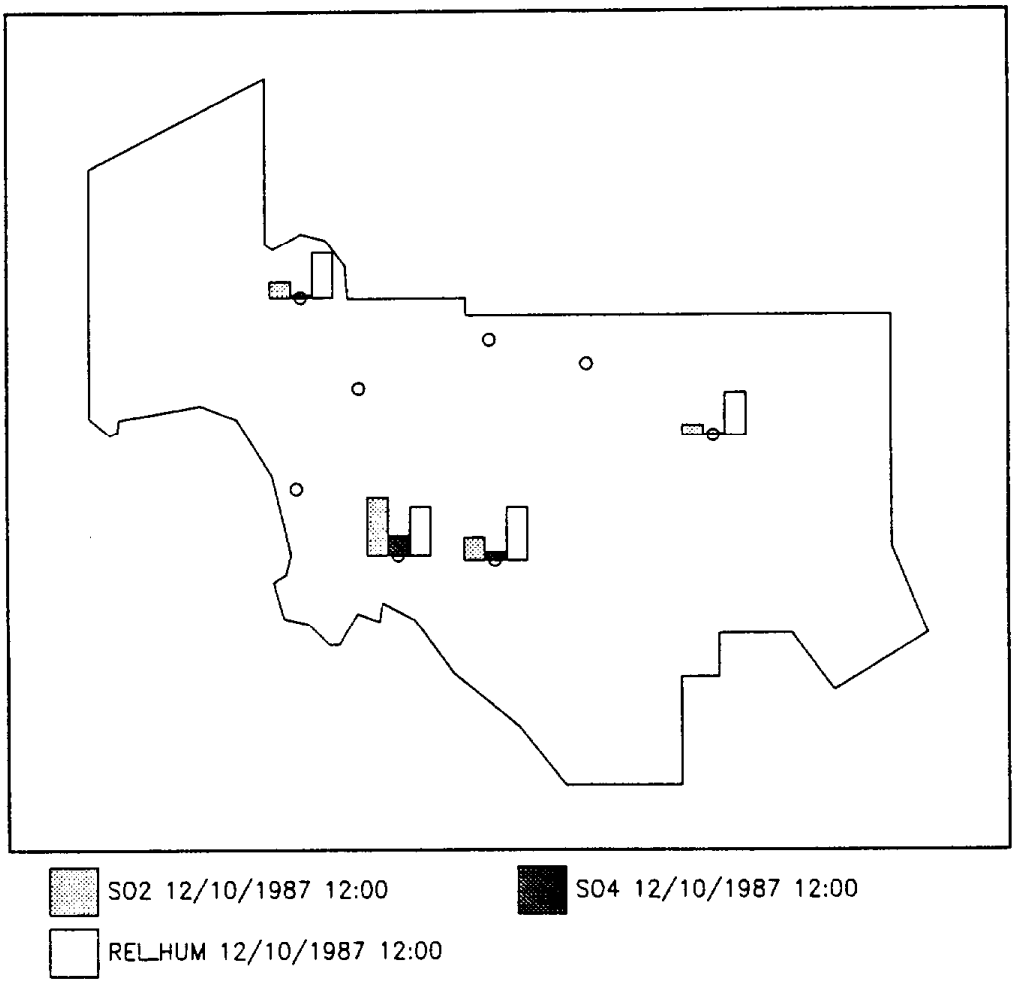

FIGURE 2.1.8 (continued)

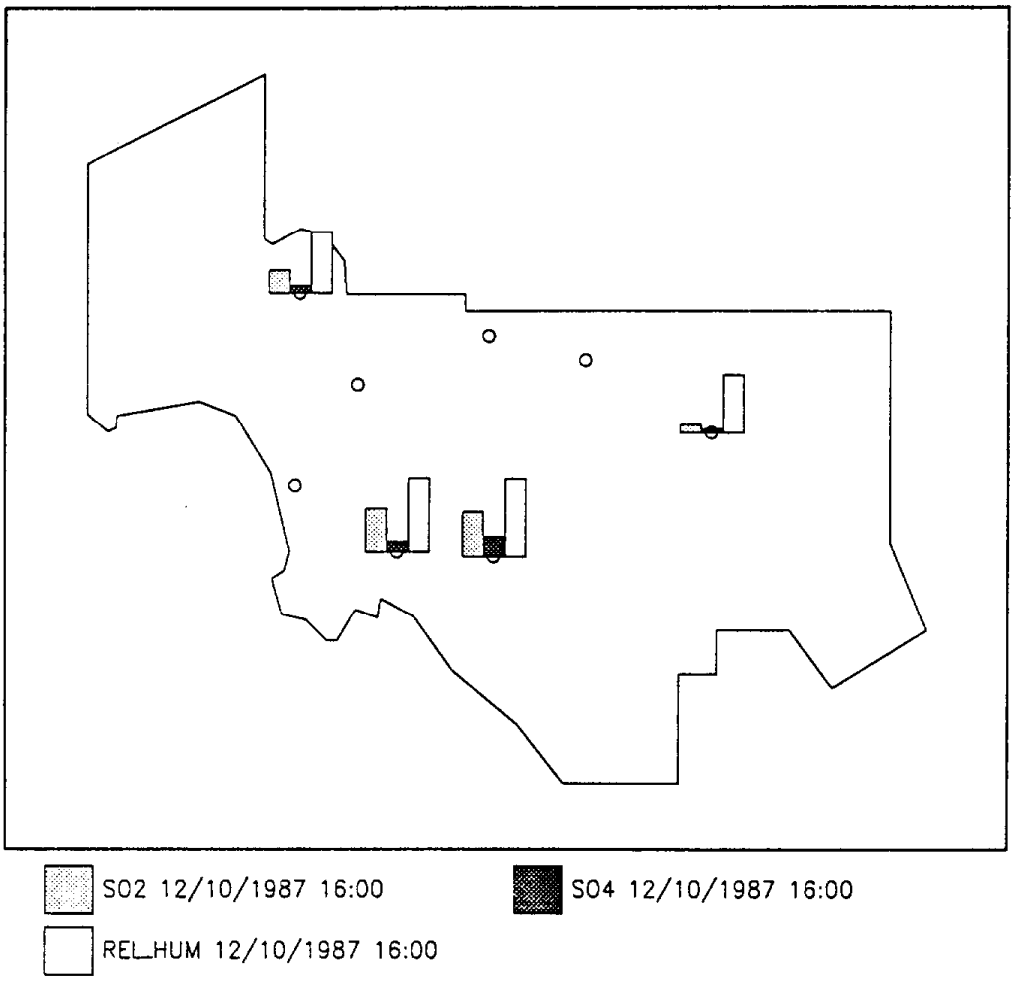

FIGURE 2.1.8 (continued)

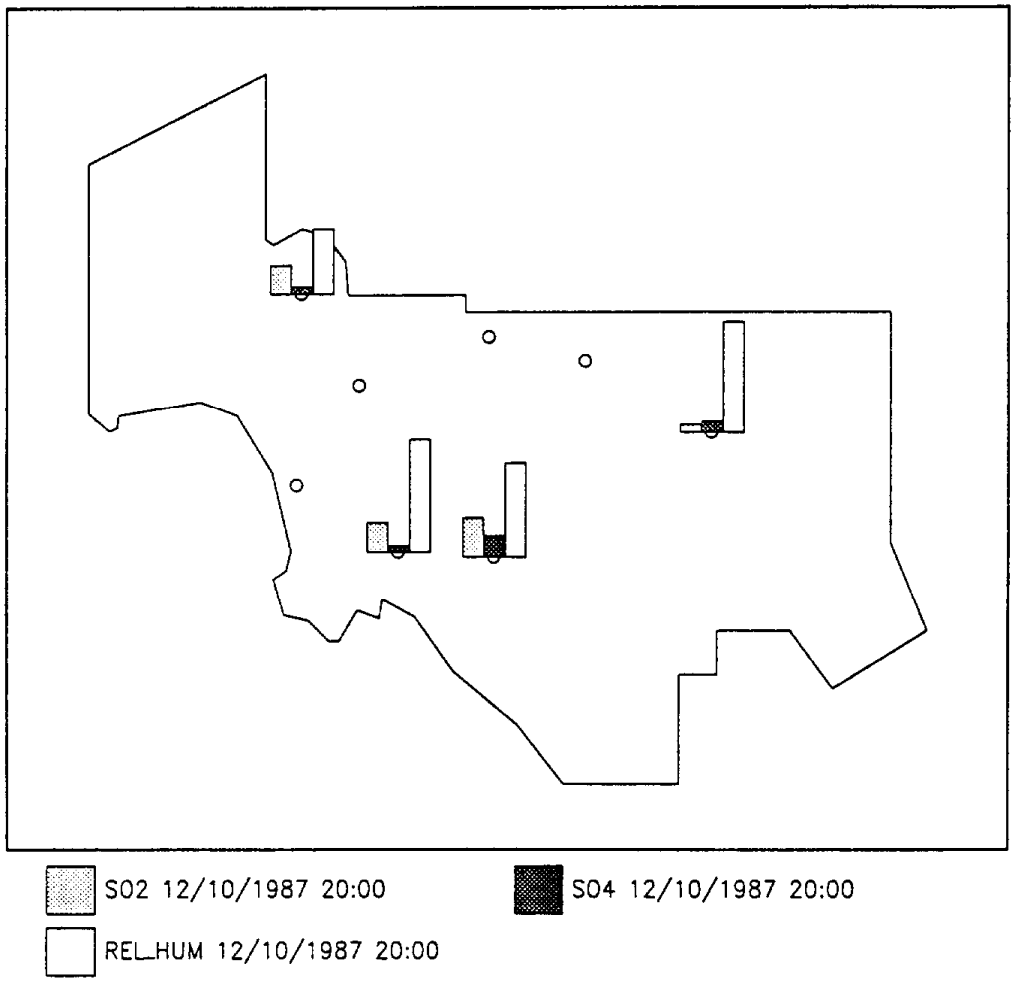

FIGURE 2.1.8 (continued)

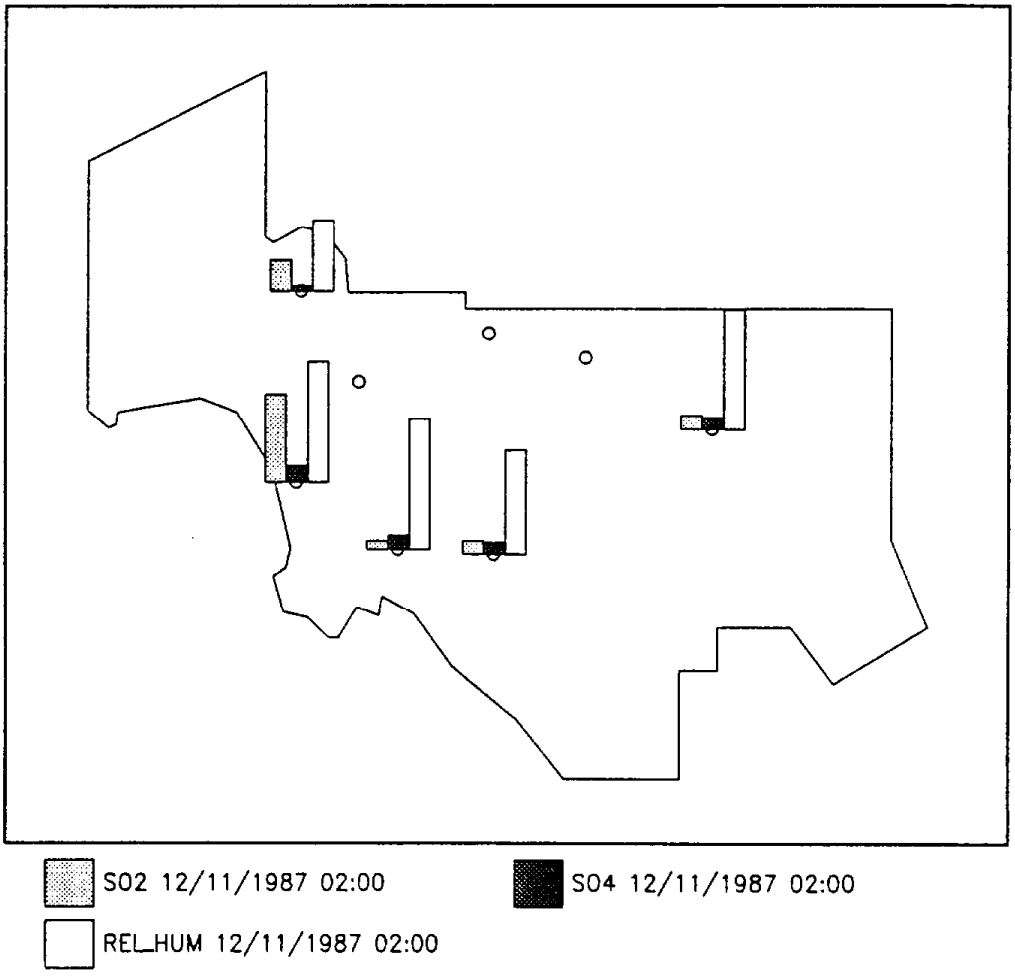

FIGURE 2.1.8 (continued)

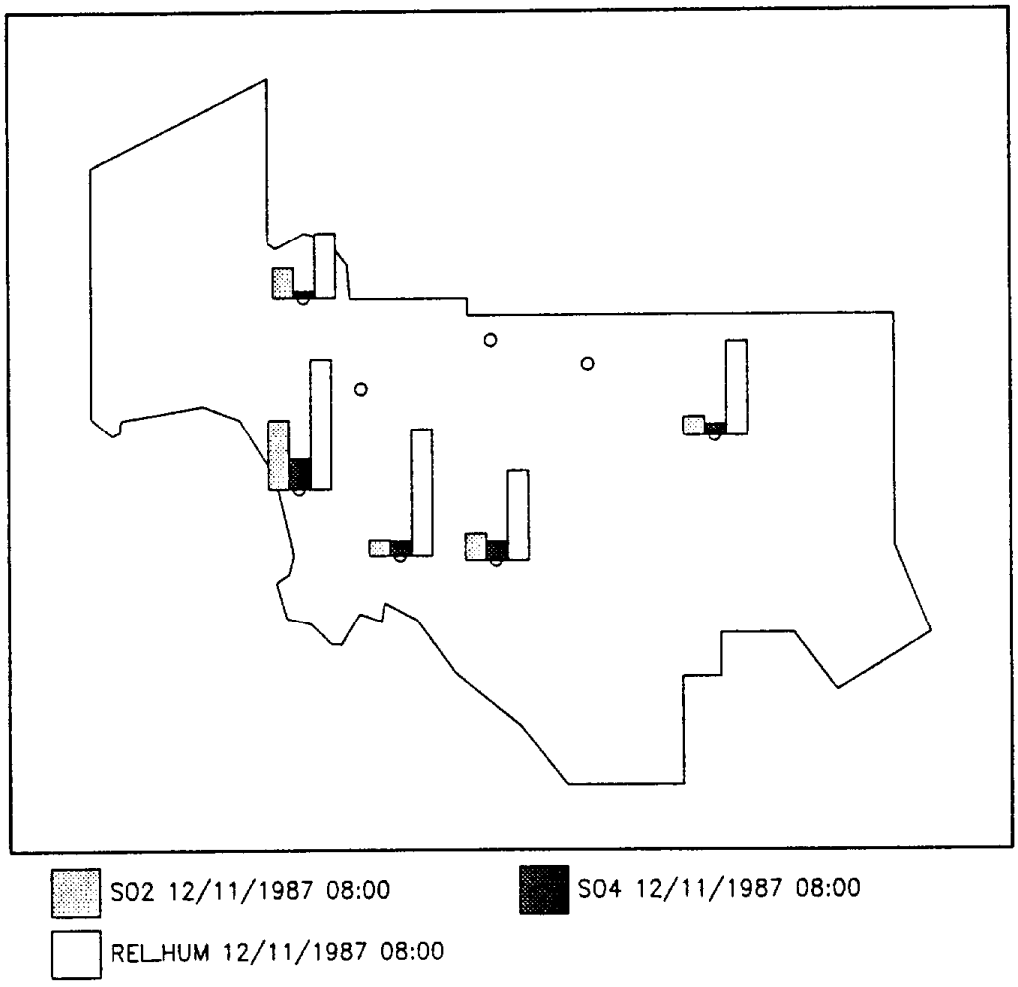

FIGURE 2.1.8 (continued)

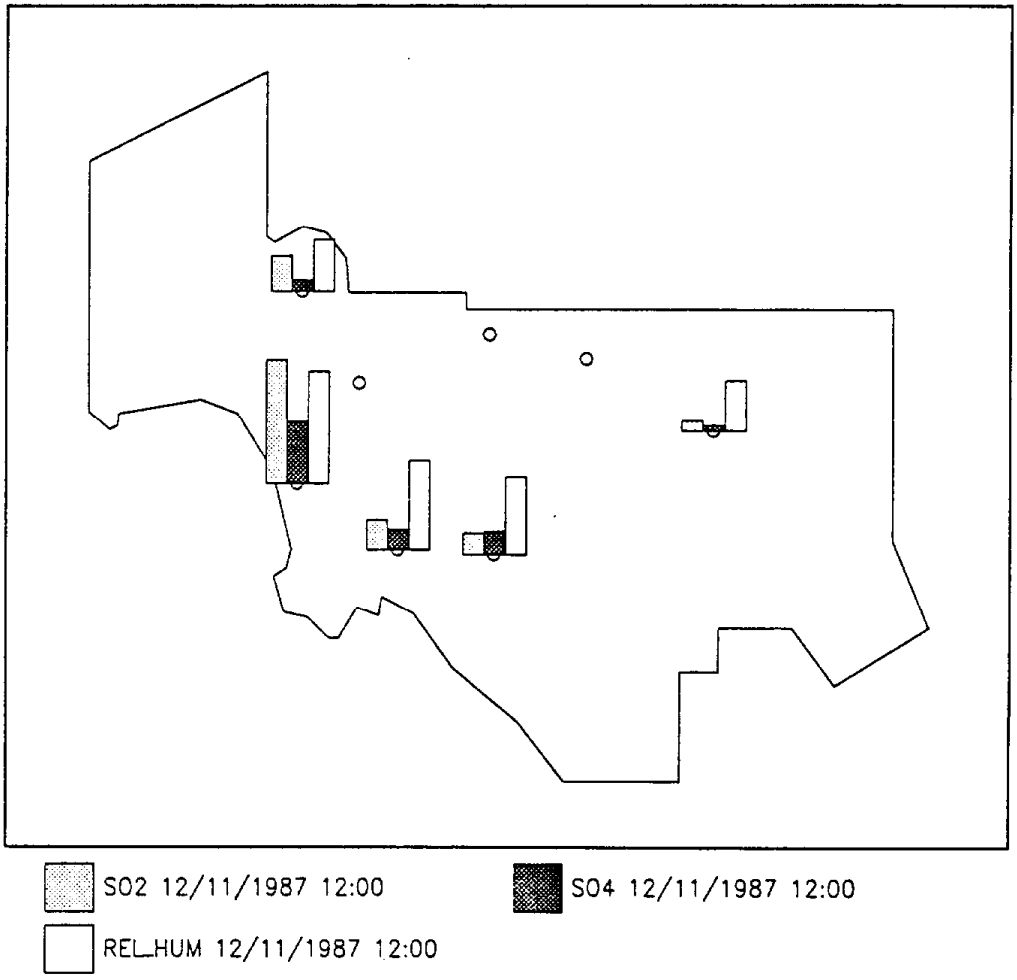

FIGURE 2.1.8 (continued)

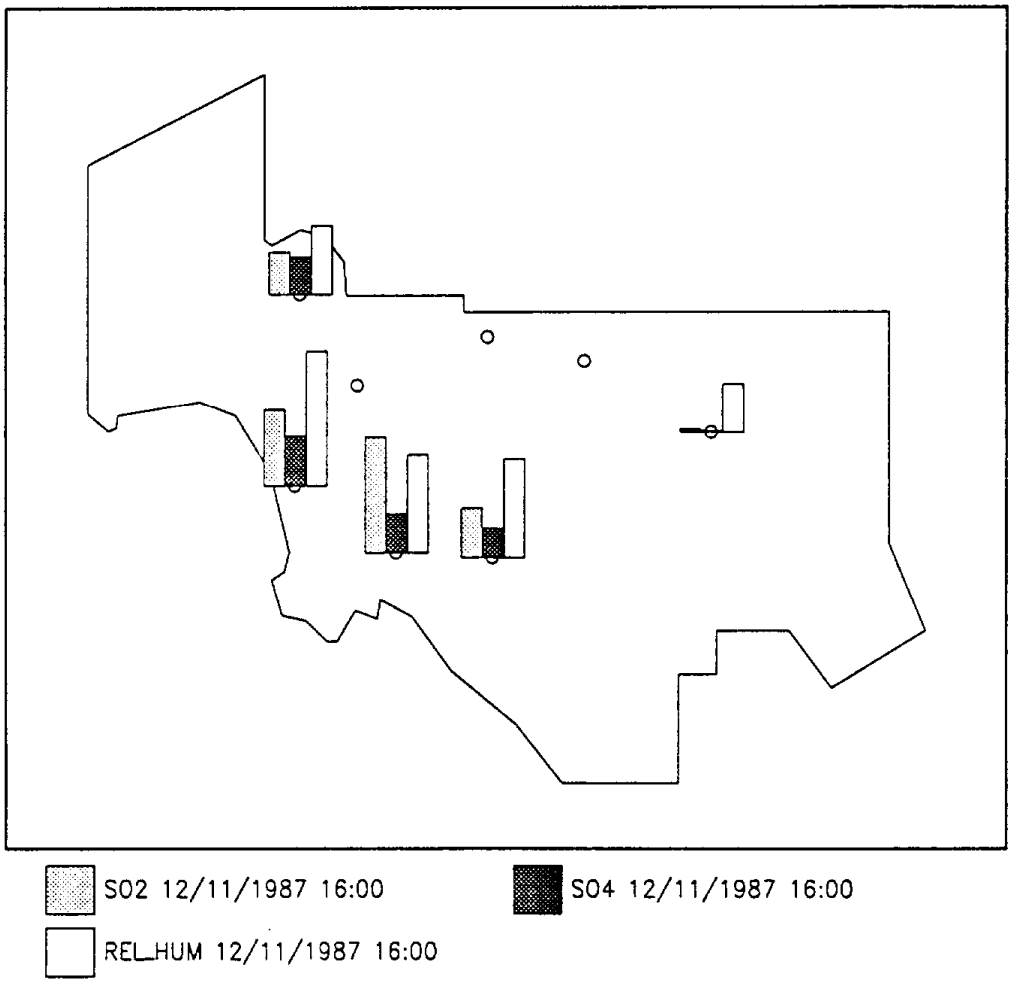

FIGURE 2.1.8 (continued)

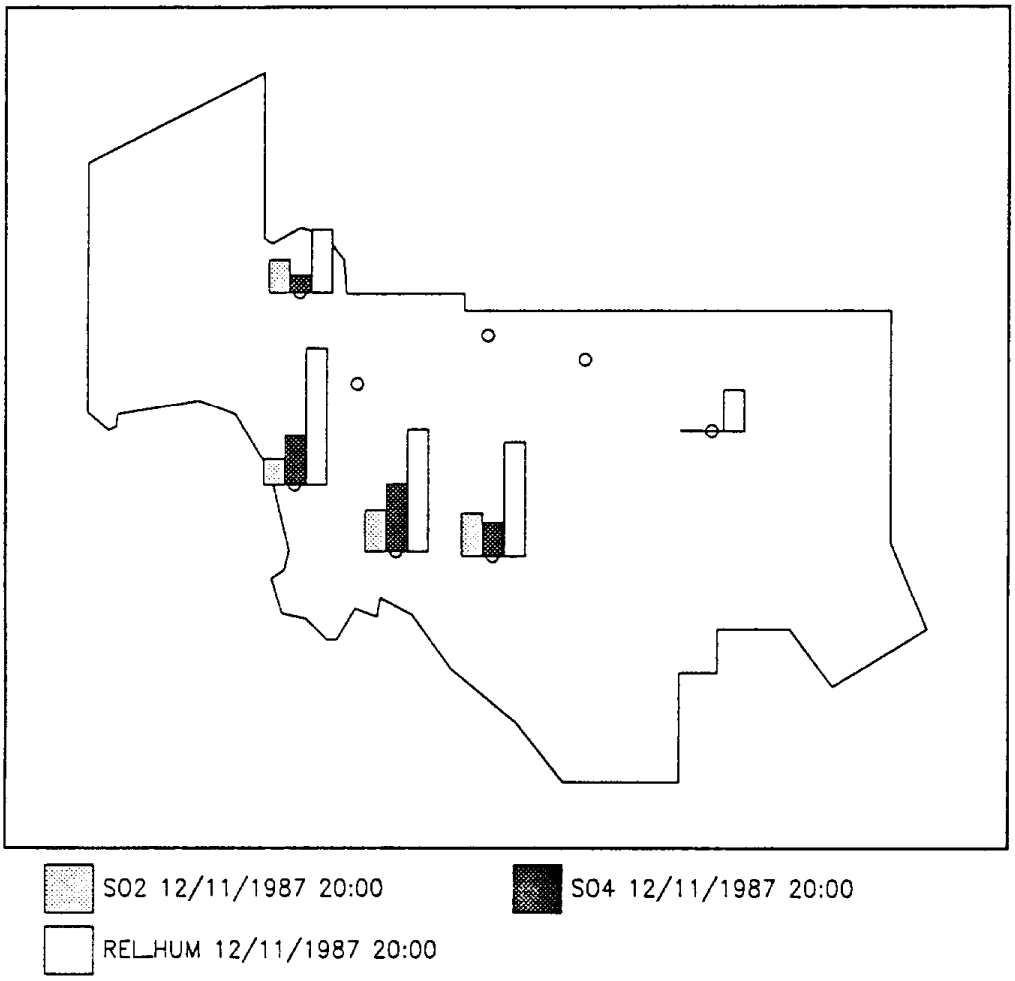

the Hawthorne site are not clear. Clarification could occur through deterministic modeling, which would assess the contribution of various sources of those peaks.

Figure 2.1.8 illustrates the increased concentration of $SO_4^=$ occurring at 4 p.m. on December 11 at the Anaheim, Burbank, and Long Beach sites. The increased $SO_4^=$ concentrations indicate that photochemical activity played a major role at that time. SO_2 concentrations at the Long Beach site also were much higher than the rest of the sites observed at that time. Later in the evening on December 11, while the SO_2 concentrations decreased substantially at the Long Beach site, the $SO_4^=$ concentrations increased by approximately 70%. The cause of the increase in $SO_4^=$ concentrations is unclear; however, the photochemically produced $SO_4^=$ from elsewhere could have moved to Long Beach, or local SO_2 could have oxidized in the aqueous phase (noting that the relative humidity was around 90%).

Figure 2.1.9 shows the August episode. At the beginning of the August episode, $SO_4^=$ was almost evenly distributed throughout the SoCAB. These concentrations were approximately 8 $\mu g/m^3$. Both the SO_2 and $SO_4^=$ concentrations remained at relatively low levels through August 27, with the exception of the SO_2 concentration at the Long Beach site, which reached 25 $\mu g/m^3$ at approximately noon. Because of the high relative humidity (around 80% during the night throughout the SoCAB) and warm temperature, it has been observed that photochemical activity is very intense during August. However, despite the high SO_2 concentrations and high relative humidity observed during this episode, no subsequent increase in the $SO_4^=$ concentrations was noticed on August 27.

On August 28, the concentrations of both pollutants followed similar behavior to those of August 27, 1987. On the morning of August 29, high $SO_4^=$ concentrations were observed throughout the SoCAB from all of the stations; Hawthorne measured highest at 6 a.m. At 2 p.m., the high concentrations were shifted inland. This phenomenon can be observed especially in the northeastern part of the SoCAB, which indicates that polluted air from the coastal areas moved inland and affected those areas. Later in the evening, the sulfate concentrations decreased substantially.

FIGURE 2.1.9. SCAQS monitoring locations showing SO_2 and SO_4 concentrations and relative humidity during August episode.

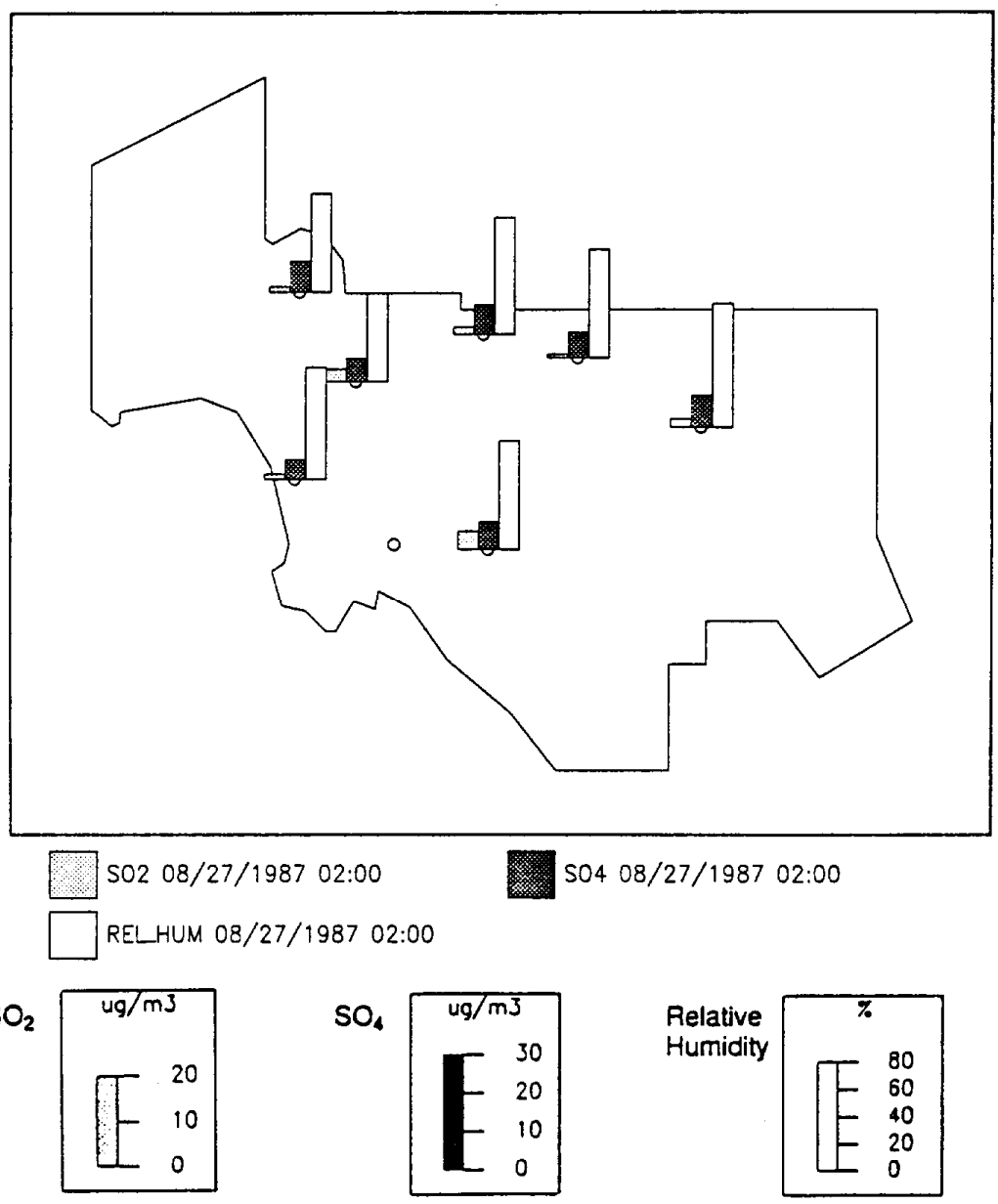

FIGURE 2.1.9 (continued)

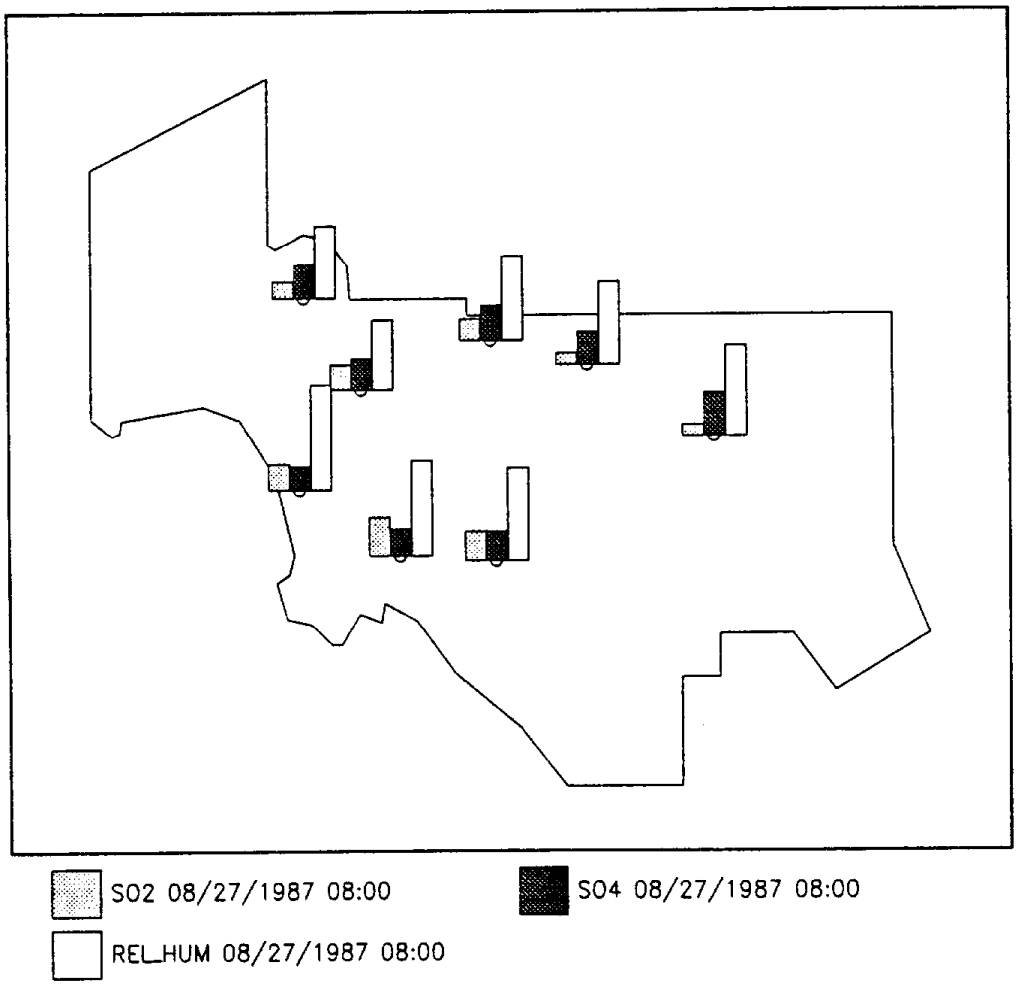

FIGURE 2.1.9 (continued)

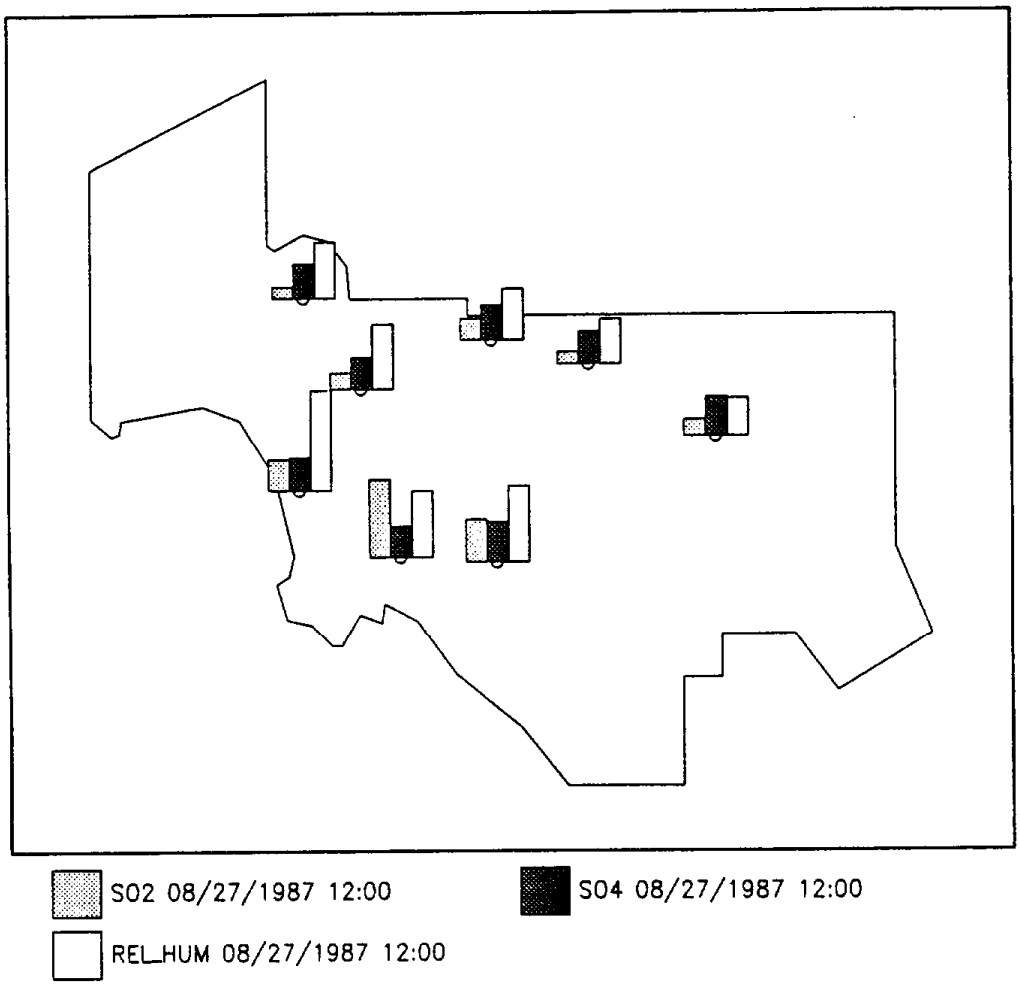

FIGURE 2.1.9 (continued)

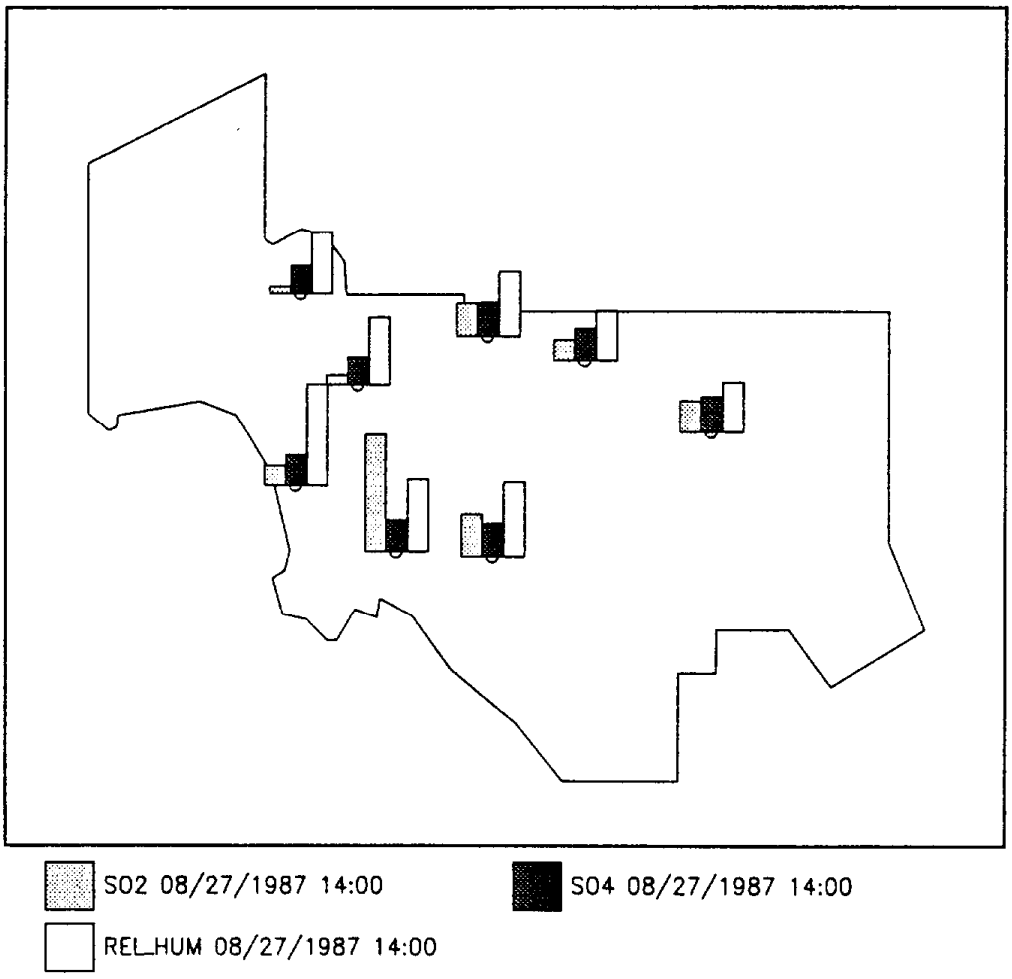

FIGURE 2.1.9 (continued)

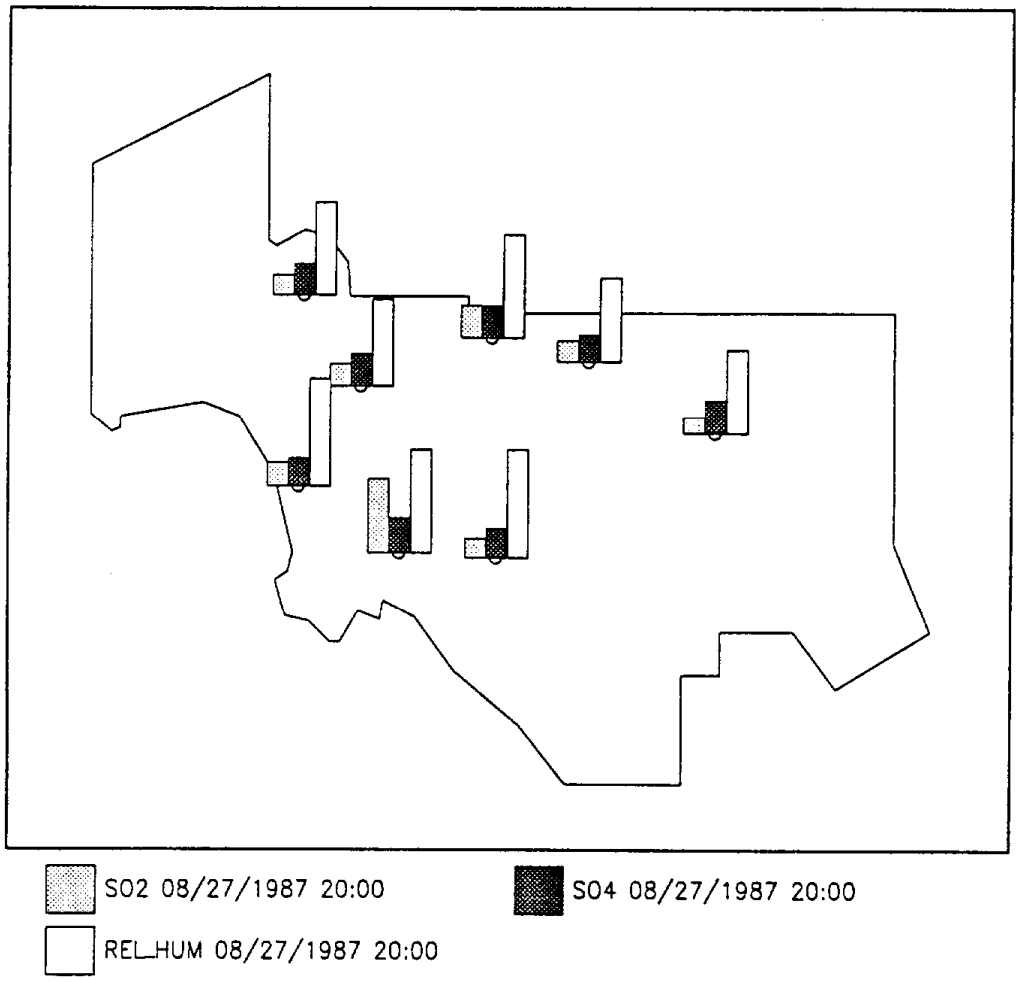

FIGURE 2.1.9 (continued)

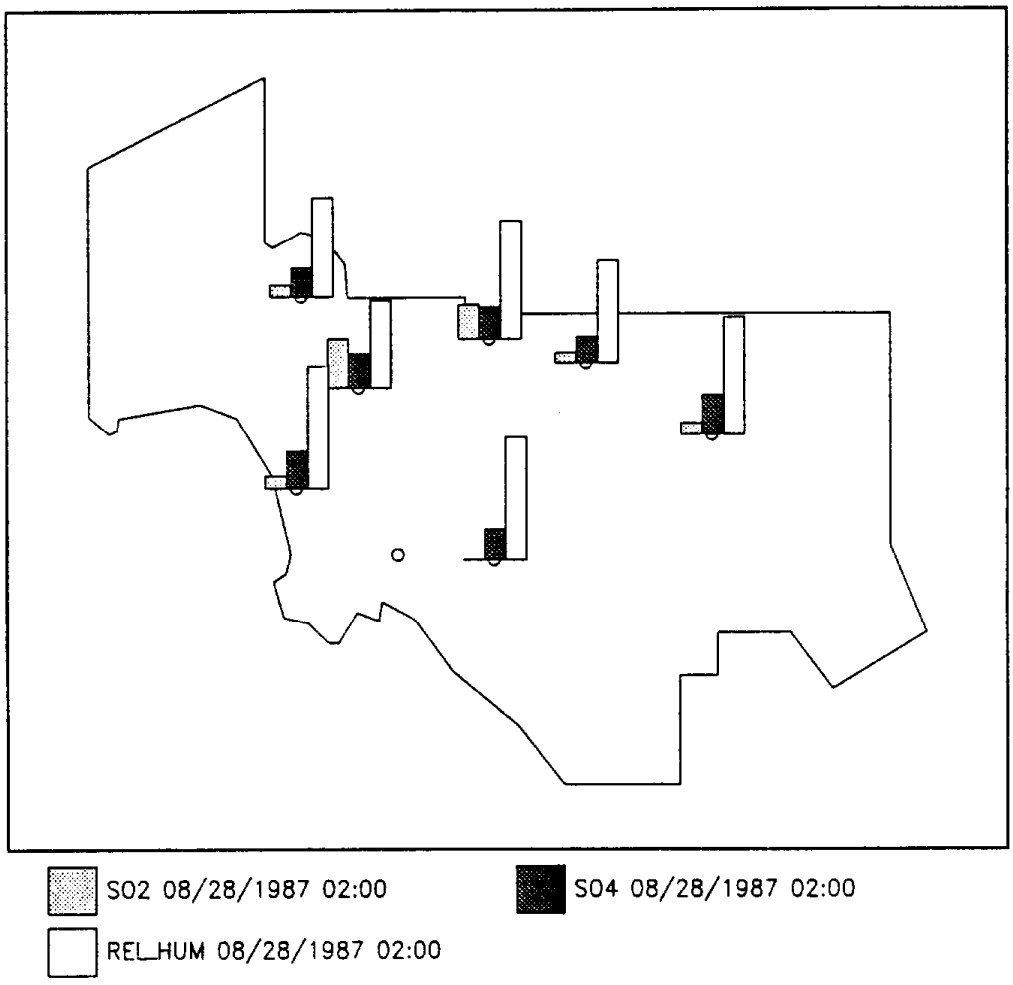

FIGURE 2.1.9 (continued)

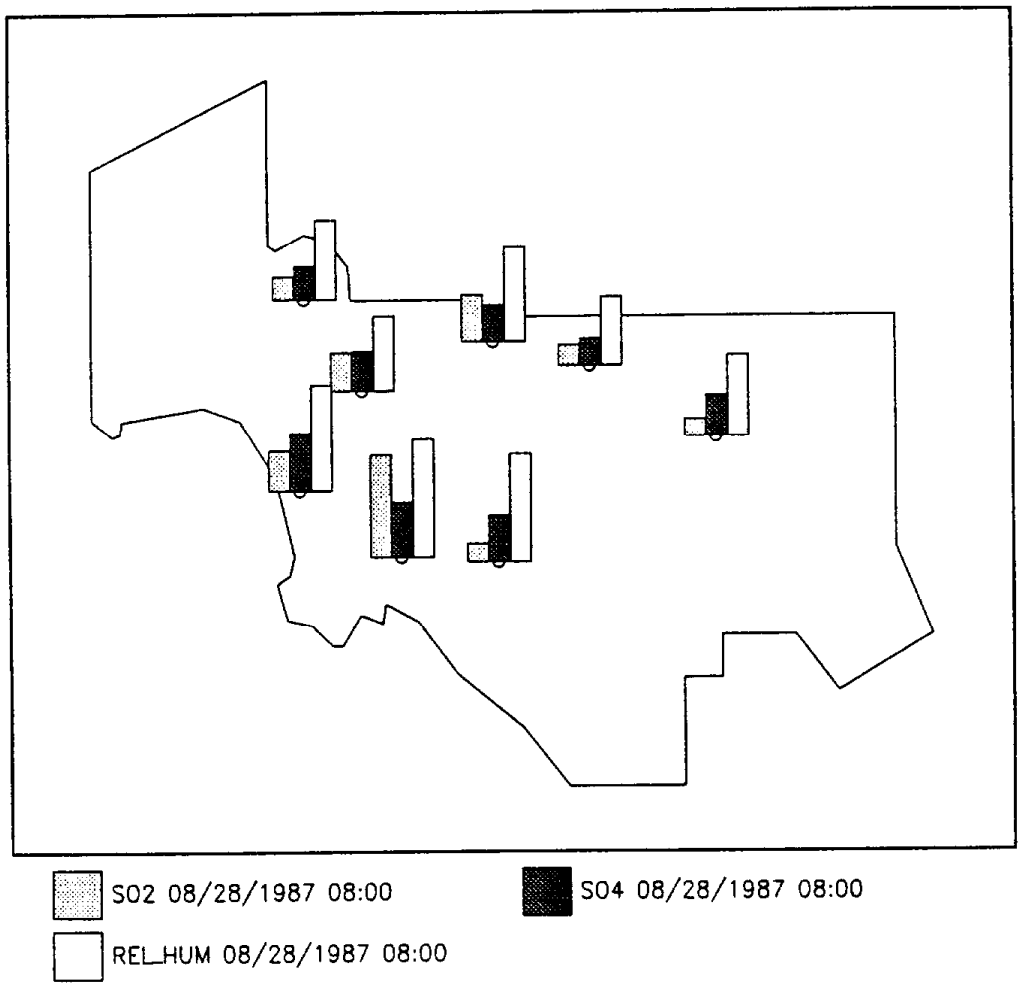

FIGURE 2.1.9 (continued)

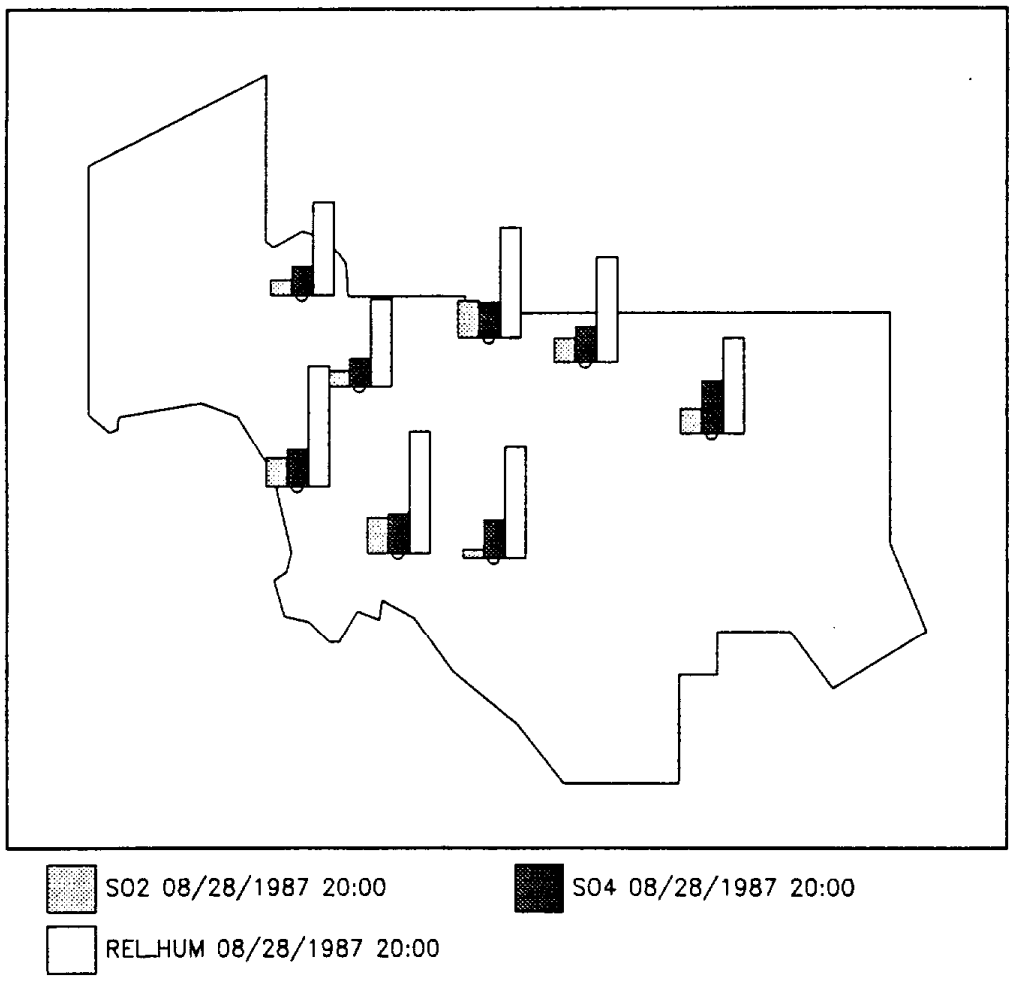

FIGURE 2.1.9 (continued)

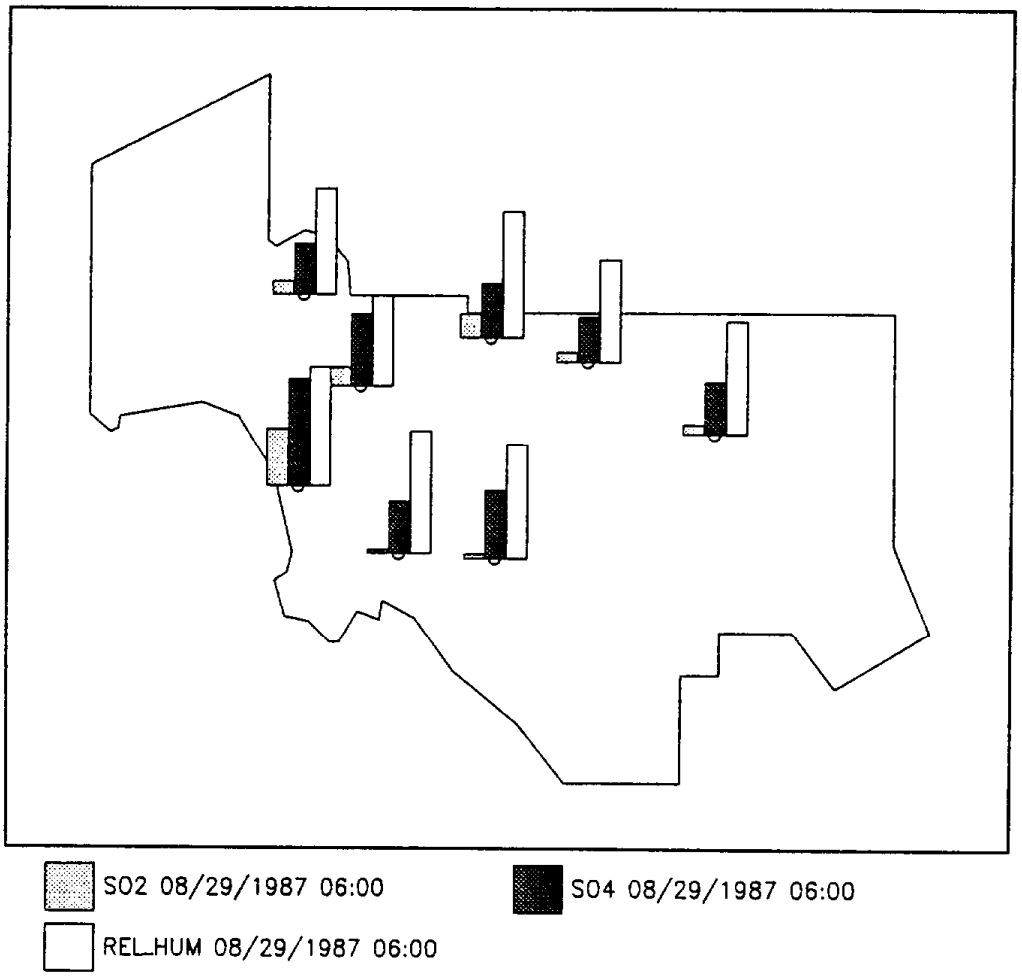

FIGURE 2.1.9 (continued)

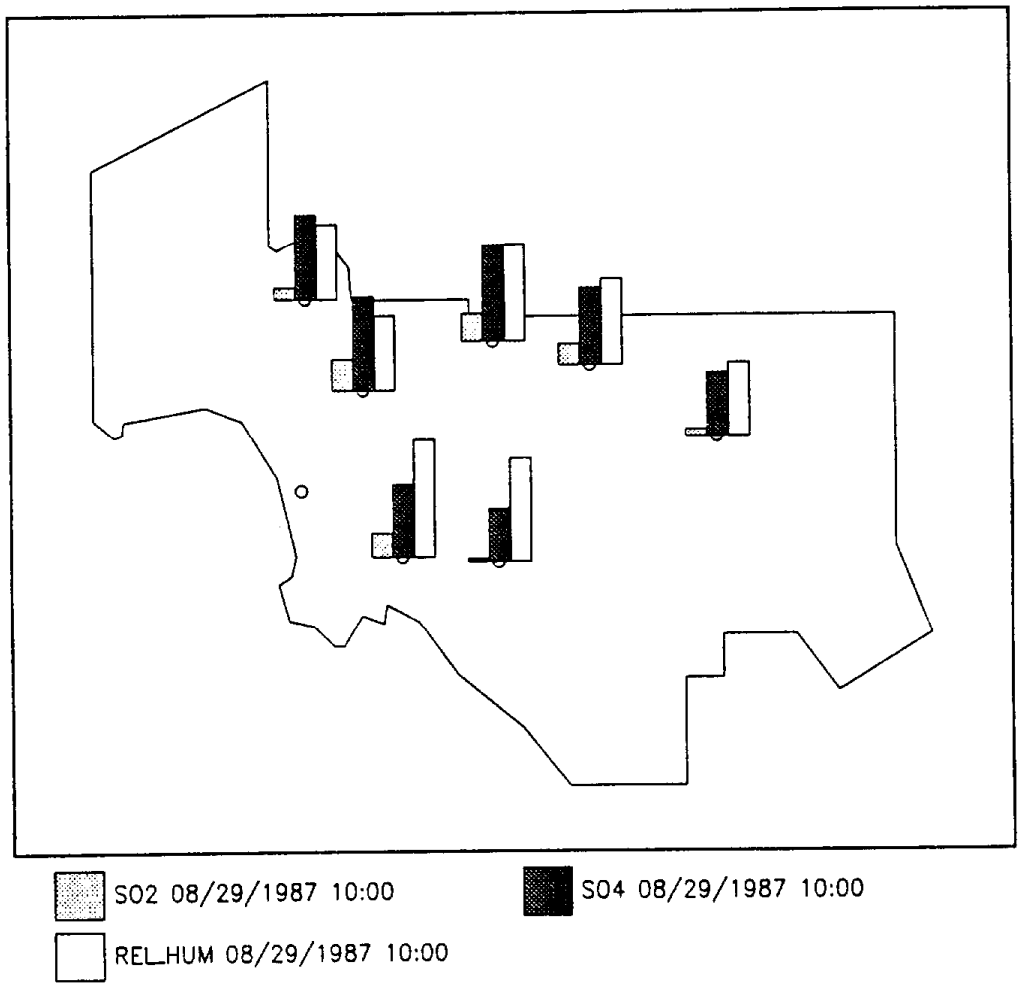

FIGURE 2.1.9 (continued)

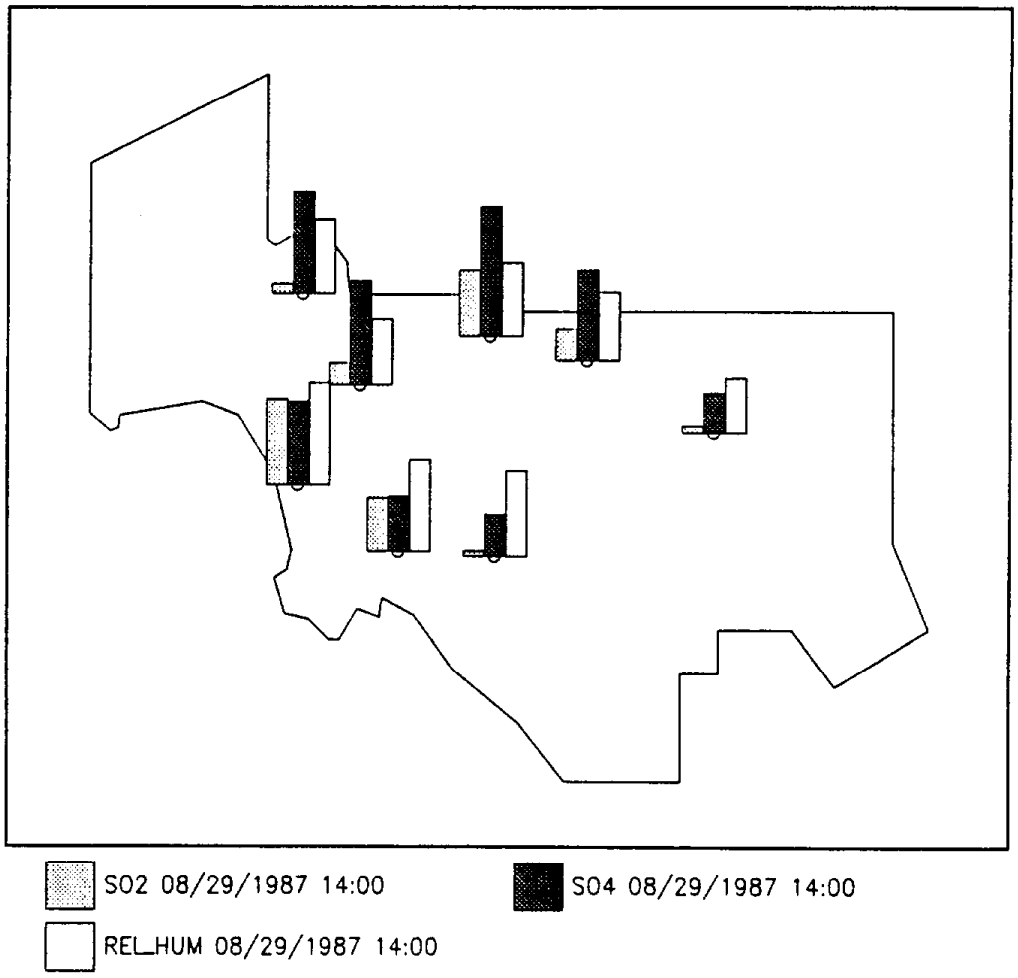

FIGURE 2.1.9 (continued)

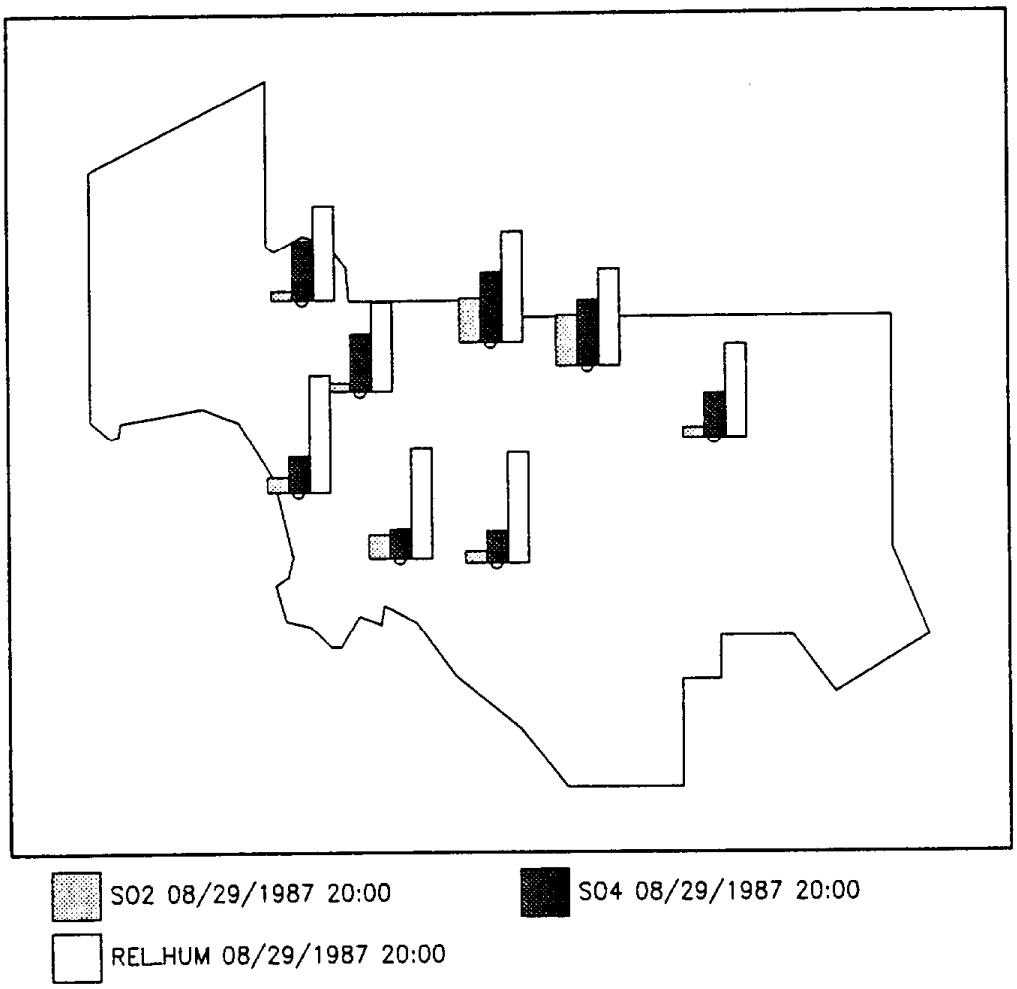

2.2 TRAJECTORY ANALYSIS

The trajectory analysis was performed to identify the source receptor relationship. The construction of the trajectories involved surface wind field generation and a trajectory integration procedure.

2.2.1 Surface Wind Field Generation

The surface wind field was constructed from the measured data by interpolation to the regular grid, using the method of Goodin et al., 1979. The influence of gross terrain features, like mountains, was accounted for by the use of barriers to wind flow during interpolation of the wind components. Following the interpolation procedure, a local terrain-adjustment technique, which involves the solution of Poisson's equation (Goodin et al., 1979), was used to adjust the wind field. The limitation of surface wind field generation is discussed in the papers written by Goodin, et al.

2.2.2 Trajectory Integration Procedure

Once the wind field has been established, the position of the air parcel at time "t" relative to the initial starting locations *x(0)* can be found (McRae et al., 1982).

$$x(t) = x(0) + u(x,t)dt$$

Where, *x(0)* is the initial coordinate of the air parcel; *u(x,t)* is the wind velocity at locations at *t* time; and *x(t)* is the coordinate of the air parcel at time *t*. Since the velocity field *u(x,t)* is usually only available at discrete locations, a distance-weighted mean of the wind field at the four nearest grid points was used.

Using the two-step procedure described previously, we developed hourly forward trajectories starting at Long Beach for the August and December episodes. The duration of the forward trajectories is 24 hours and is shown in Figures 2.2.1 to 2.2.48 (see Appendix A.1) and in Figures 2.2.49 to 2.2.72 (see Appendix A.2) for the August and December episodes, respectively.

As shown in Figures 2.2.1 to 2.2.48 (Appendix A.1), the trajectories starting at Long Beach followed an eastern-northeastern path throughout the August 27-29 episode, indicating that pollutants emitted in the coastal area near Long Beach were transported inland. There are many trajectories of interest in terms of modeling and analysis. For example, the trajectories that were scheduled between 1 p.m. and 3 p.m. on August 27 passed through Anaheim, and later, Riverside. Also, the air parcel that passed over Long Beach at 7 p.m. on August 27 reached Fontana the next evening. Similarly, most of the trajectories that started between 5 a.m. and 3 p.m. on August 28 passed through Fontana the next day. Finally, the only trajectory that was found to connect the two A-sites—Long Beach and Claremont—was the one that started at 4 p.m. on August 28 and reached Claremont around 12 noon the next day.

Figures 2.2.49 to 2.2.72 (Appendix A.2) shows the trajectories that began at Long Beach during the December episode. The meteorology was much different than that of August, with apparent strong stagnation. Most of the air parcels that started at Long Beach during the period showed no significant inland movement. Thus, it is very unlikely that pollutants emitted at the coastal areas affected receptor sites, like Rubidoux and Claremont, during the December episode. More importantly, the 12/10 trajectories from 0000-1100 passed over Anaheim the next day. This would show recirculation over the ocean and back to the land at a time when samples were being collected at Anaheim. Trajectories at the end of 12/10 arrived at Hawthorne late on 12/11—maybe too late to be sampled. Potentially important trajectories, in terms of modeling and analysis, are those that passed over Long Beach between 2 p.m. and 4 p.m. on December 10, because those trajectories reached Hawthorne the next day.

3. ANALYSIS OF PHYSICAL AND CHEMICAL PROCESSES IN THE SOUTH COAST ATMOSPHERE

3.1 ORGANIC ACIDS

3.1.1 Introduction

The overall objective of this project is to analyze and interpret atmospheric acidity data from the 1987 Southern California Air Quality Study (SCAQS), emphasizing understanding of the chemistry, sources and deposition of acidic gases and particles in the South Coast Air Basin (SoCAB). One important category of airborne acidic pollutants is organic acids (carboxylic acids).

Organic acids are ubiquitous in the urban atmosphere. Organic acids are emitted by mobile and stationary sources and are formed in situ by chemical reactions involving olefins and other hydrocarbons (Grosjean, 1989). Studies carried out before SCAQS (Grosjean, 1990a, and references therein) have shown that the two most abundant organic acids are formic acid (HCOOH) and acetic acid (CH_3COOH). These two acids are generally more abundant in southern California air than the most abundant inorganic acids; i.e., nitric acid (HNO_3) and hydrogen chloride (HCl). Likewise, organic acids are the leading contributors to acid dry deposition in the SoCAB (Pierson and Brachaczek, 1990).

While organic acids account for a major fraction of the total gas-phase acidity, our current knowledge of the sources, atmospheric formation and atmospheric removal of organic acids is very limited. Thus, the major objective of this study is to perform an interpretive analysis of the SCAQS data base to obtain more reliable estimates of emissions, in situ formation, and deposition of organic acids in the SoCAB. Accordingly, this report is organized into the following sections:

- a review of available data prior to SCAQS, regarding emissions, ambient levels, in situ formation and removal processes for organic acids in the SoCAB.

- an estimate of direct emissions, using ambient air data for organic acids and for a number of nonreactive tracers such as carbon monoxide, acetylene, Freon 113, and several chlorinated hydrocarbons.
- an estimate of in situ formation rates, using kinetic data, reaction mechanisms, and emission rates for olefins that produce organic acids in situ by reaction with ozone.
- an estimate of removal rates, focusing on dry deposition as the major atmospheric removal process for gas-phase organic acids.
- an attempt to reconcile ambient observations, production (direct emissions and in situ formation) and removal (mostly dry deposition) for gas-phase organic acids in the SoCAB.

3.1.2 Emissions, In Situ Formation, and Deposition of Organic Acids

Our current knowledge of the sources, transformations, and deposition of organic acids is limited. The SCAQS data base for organic acids, which includes information on spatial and seasonal behavior, offers an excellent opportunity to improve our knowledge of organic acids in the South Coast Air Basin (SoCAB). The objective of this section is to conduct an interpretive analysis of the SCAQS data base to construct more reliable estimates of emissions, in situ formation and deposition of organic acids, focusing on the two major compounds—formic acid and acetic acid.

3.1.3 Background: Review of Existing Data

Much of the research and regulatory efforts concerning acid deposition have focused in the past on inorganic acids, sulfuric and nitric, and on their respective precursors, sulfur dioxide and oxides of nitrogen. Organic acids have received much less attention. However, recent studies have shown that organic acids, including formic and acetic acids, are ubiquitous in the atmosphere (Andreae et al., 1988, Talbot 1988, and references therein) and that organic acids may account for a large fraction, up to 64%, of the total acidity in nonurban precipitation (Keene et al., 1983).

3.1.3.1 Ambient Observations in Southern California

In urban southern California, several studies have included reports of organic acids in engine exhaust, ambient air (gas-phase and particle-bound), and precipitation samples (Hanst et al., 1975, 1982, Tuazon et al., 1978, 1981, Grosjean et al., 1978, Kawamura et al., 1985, Grosjean 1988). Pierson and Brachaczek (1990) measured organic acids in dew collected at Glendora, California. Formate was the most abundant of all anions present—organic or inorganic.

In an ARB-sponsored study (August 12-21, 1986), Grosjean (1989) measured formic acid and acetic acid in Glendora, California. These two acids, by far the most abundant organic acids in ambient air, were present at levels exceeding those of the inorganic acids hydrogen chloride and nitric acid. During the 12-hour nighttime period 8 P.M. - 8 A.M., levels of organic acids also exceeded those of the photochemical oxidants ozone, peroxyacetyl nitrate (PAN) and nitric acid (Table 3.1.1).

During SCAQS, measurements of formic acid and acetic acid were performed at four locations: San Nicolas Island, Long Beach, Claremont, and Palm Springs (Grosjean, 1990b). The results, summarized in Table 3.1.2, displayed strong spatial and seasonal variations. Ambient levels of both acids increased from 0.6 ppb at the "control" site, San Nicolas Island, to up to 19 ppb at the inland locations. At the single location surveyed (Long Beach) as part of the Fall 1987 phase of SCAQS, ambient levels of organic acids were substantially higher during the fall than during the summer. The acetic acid/formic acid concentration ratio decreased from the coastal to the inland sites, and was higher during the fall than during the summer. These observations point to possible differences in direct emissions and in situ formation rates for the two acids (Grosjean, 1990b).

To our knowledge, only one study of ambient levels of organic acids has been carried out in southern California since the completion of SCAQS, namely a one-year study (from September 1988 to September 1989) of ambient formic acid at Upland. Twenty four-hour samples were collected every sixth day and yielded formic acid levels of 0.6-8 ppb, with fall and summer maxima and with a minimum during the winter months (Grosjean, 1991).

Table 3.1.1. Organic acids data summary, Glendora, California, August 12-21, 1986 (a).

	Time				
	8 - 12	12 - 16	16 - 20	20 - 24	0 - 8
Gas-phase concentration, ppb:					
formic acid	5.10	3.40	3.36	3.53	6.34
acetic acid	4.54	2.84	3.24	3.52	5.55
hydrogen chloride	1.55	1.39	1.04	1.03	0.50
nitric acid	1.72	6.48	3.84	0.82	0.42
ozone	48	171	89	3.5	5.1
Formic acid/acetic acid concentration ratio	1.12	1.20	1.04	1.00	1.14
Organic acid/CO ratio, ppb/ppm					
formic/CO	2.33	2.28	2.00	1.84	3.75
acetic/CO	2.07	1.91	1.93	1.83	3.28

(a) adapted from Grosjean (1989)

Table 3.1.2. Gas-phase concentrations of formic acid and acetic acid during SCAQS (a).

Location	Season	Sampling duration, hr	Maximum concentration, ppb		Mean ratios, acetic/formic
			formic acid	acetic acid	
San Nicolas Island	summer	one week	0.58	0.62	1.07
Long Beach	summer	4, 5 or 7	12	15	0.60 - 1.63
	fall	4 or 6	7	17	1.41 - 2.78
Claremont	summer	4, 5 or 7	19	13	0.53 - 0.93
Palm Springs	summer	4 or 6	13	11	0.47 - 0.62

(a) adapted from Grosjean, 1990b.

3.1.3.2 Emission Data

Emission data for organic acids are virtually nonexistent. On the basis of limited measurements, Grosjean (1989) attempted to construct an emission inventory for organic acids in the SoCAB. Using organic acid/carbon monoxide ratios and other relevant data, emission rates of 6,500, 9,000 and 19,700 kg/day were estimated for formic, acetic and total organic acids, respectively (Table 3.1.3). Large uncertainties were associated with these emission estimates.

3.1.3.3 Atmospheric Formation

In the same study (Grosjean, 1989), chemical reactions that produce organic acids in the atmosphere were examined, using kinetic data and information on organic acid precursors. Several reactions may produce organic acids in situ, three in the gas phase (the aldehyde-HO_2, phenol-OH, and ozone-olefin reactions) and one in the aqueous phase (oxidation of aldehydes in cloud and/or rainwater). Of these, the ozone-olefin reaction was deemed to be a major source of organic acids. Olefins, whose reaction with ozone lead to organic acids, are listed in Table 3.1.4 in order of decreasing emission rates. Of the 230×10^3 kg of olefins emitted every day, 190×10^3 kg (83%) yield formic acid, only 56×10^3 (24%) yield acetic acid, and the balance yields small amounts of higher molecular weight acids. Thus, predicted atmospheric formation rates for formic and acetic acids are in the ratio 3.4:1. This compares to ambient concentration ratios of only 1.1:1, see Table 3.1.1.

3.1.3.4 Removal Processes

With the exception of ketoacids, which photolyze rapidly (Grosjean, 1983), organic acids are not significantly removed from the atmosphere by gas-phase reactions. Their only removal pathway is by slow reaction with the hydroxyl radical. The corresponding reaction rate constants are 0.35-0.46, 0.73, 1.2, and 2.0×10^{-12} cm^3 $molecule^{-1}$ sec^{-1} for formic, acetic, propionic and isobutyric acid,

Table 3.1.3. Estimated emission inventory for organic acids in the SCAB (a).

Organic acid	Emission rate, kg/day	Organic Acid	Emission rate, kg/day
Aliphatic Monocarboxylic		*Aliphatic Dicarboxylic*	
formic	6500	oxalic	87
acetic	9000	malonic	52
propionic	1370	succinic	52
butyric	136	glutaric	52
isobutyric	136	adipic	52
valeric	158	C-C	75
iso valeric	158		
hexanoic	180		
heptanoic	200		
octanoic	222		
nonanoic	244		
decanoic	250		
Subtotal:	**18,418**	**Subtotal:**	**370**
Aromatic Acids			
benzoic	310		
phthalic	300		
phenylacetic	250		
toluic (3 isomers)	120		
Subtotal:	**980**	**Total:**	**19,768**

(a) Grosjean, 1989

Table 3.1.4. Olefins whose reaction with ozone leads to formic acid and acetic acid (a).

Olefin	*Reaction Product*			Olefin Emission rate for SCAB, 10 kg/day (d)
	Formic acid	*Acetic acid*	*Other acid (c)*	
Ethylene	+			71
Propene	+	+		20
3-Me-1-pentene (b)	+		iso C5	20
1-pentene	+		n C4	18
2-Me-2-butene		+		16
1,-3-butadiene	+			15
2-Me-1-butene	+			13
1-butene	+		C3	11
cis-2-butene		+		9
trans-2-butene		+		8
isobutene	+			7
cyclohexene			adipic	7
3-Me-1-butene	+		iso C4	5
Me-cyclopentene			Meglutaric	3
2, 3-di Me-1-butene	+			3
cis-2-pentene		+	C3	1.5
trans-2-pentene		+	C3	1.3
cis-3-hexene			C3	0.8
2-Me-2-pentene			C3	0.8
trans-3-Me-2-pentene		+		0.6
1 -hexene	+		C5	0.3
2-Et-1-butene	+			0.3

(a) Daniel Grosjean and Associates
(b) Me = methyl, Et = ethyl
(c) C3 = propionic acid, C4 = butyric acid, C5 = valeric acid
(d) From 1974 ARB emission inventory

respectively (Dagaut et al., 1988, and references therein). These rates correspond to atmospheric residence times of several weeks.

Physical processes for removal of atmospheric organic acids include scavenging by hydrometeors (cloud, fog, and rain) as well as dry deposition. Organic acids are soluble in water; indeed, there are numerous reports concerning organic acids in rainwater, snow, cloudwater, fog, and mist. Formate and acetate are the most abundant organic acids in hydrometeors. Their concentrations range from 10-30 μM in nonurban precipitation (e.g., Galloway et al., 1982) to several hundreds μM in urban fog samples collected in southern California (Jacob et al., 1986, Munger et al., 1989).

Removal of organic acids by dry deposition, including deposition to dew, has only recently received some attention. Pierson and Brachaczek (1990) have identified formate, acetate, propionate, oxalate and benzoate at concentrations of 118, 52, 2.8, 2.1 and 0.4 μM, respectively, in dew samples collected at Glendora. However, species observed in dew may not always be those actually deposited. For example, deposited formaldehyde may be oxidized to formic acid in dew. Indeed, the results of Grosjean (1989) for the same Glendora dew samples indicate high levels of aldehydes (Table 3.1.5), thus underlining the potential for production of organic acids in dew by aqueous-phase oxidation of the corresponding aldehydes. Thus, the dew concentrations given above are probably upper limits for the actual deposition of organic acids.

Dry deposition velocities of formic acid, acetic acid and other organic acids have not been determined. Talbot et al. (1988), Jacob and Wofsy (1988), and Pierson and Brachaczek (1990), suggest that a deposition velocity of 1 cm sec^{-1} is reasonable; i.e., organic acids are assumed to have deposition velocities comparable to that of nitric acid. For comparison, the dry deposition velocity of nitric acid on grass is 2.5 ± 0.9 cm sec^{-1} (Huebert and Robert, 1985).

Table 3.1.5. Polar organics in Glendora dew samples (a).

Date collected (1986).	Polar organic concentration, µg/mL		
	Formaldehyde	*Acetaldehyde*	*Formic acid (b)*
8 - 12 to 8 -13	6.7	12.2	17.2
	8.2	6.2	10.7
8 - 14 to 8 - 15	8.5	5.1	6.5
	4.2	4.5	5.2
8 -16 to 8 - 17	24.2	5.3	11.6
	12.6 (c)	8.4	11.4
	11.8 (d)	2.3	15
	15.5 (d)	9.6	8.1
	14.1 (d)	4.9	13.9
8 - 21	9.9	5.2	6.8
Average	11.6	6.4	10.6
Detection limit	0.37	0.12	0.44

(a) adapted from Grosjean, 1989
(b) measured as formate ion
(c) with added biocide
(d) three consecutive short-term samples

In the absence of data, Grosjean (1989) has assumed a value of 1.0 cm sec^{-1} for the dry deposition velocity of all gas-phase organic acids, and has estimated the contribution of dry deposition and wet deposition to the removal of organic acids in the SoCAB. Input data for these estimates are listed in Table 3.1.6. Organic acid concentrations in the gas phase and in rainwater were taken from midrange values of literature data. Oxalic acid was assumed to be associated with fine particles, with a deposition velocity of 0.1 cm sec^{-1}.

Results of the corresponding calculations are also given in Table 3.1.6. For the gas-phase organic acids, dry deposition far exceeds removal by rain and accounts for 95% (formic acid) and 91% (acetic acid) of the organic acid deposition budget. This probably holds true for all other gas-phase organic acids, some of which are present in the atmosphere at levels much lower than those of formic acid and acetic acid. For oxalic acid, and probably all other particle-bound organic acids, wet deposition is more important by virtue of the lower dry deposition velocity for fine particles. Overall, dry deposition is estimated to be 14 times more important than removal by rain, accounting for 92% of the total organic acid deposition budget. In turn, removal by rain is about twice that estimated for dew. The estimates given in Table 3.1.6 are highly dependent on the values assigned to dry deposition velocities. For example, a ten-fold decrease from 1.0 to 0.1 cm sec^{-1} would make dry deposition and removal by rain equally important. Actual measurements of dry deposition are obviously needed to refine the deposition budget of organic acids in the SoCAB.

3.1.3.5 Comparison of Emissions, In situ Formation and Removal Processes

A summary of the estimates presented by Grosjean (1989) are given in Table 3.1.7. In situ formation estimates are from extrapolation of diurnal variations in organic acid/CO concentration ratios. In situ formation may account for as much as direct emissions from mobile sources. As removal competes with atmospheric formation, the "net" in situ formation values given in Table 3.1.7 are lower limits for actual formation rates. Removal data are from wet and dry deposition fluxes given in Table 3.1.6 and assuming the SoCAB area to be 6 x 10^3 km^2 (120 x 50 km).

Table 3.1.6. Depostion fluxes for organic acids (a).

Input data for deposition calculations					
	Formic	*Acetic*	*Propionic*	*Oxalic*	
Rainwater concentration, µm	10	20	1	5	
Amount of rain, mm/year	300	300	300	300	
Gas-phase concentration, ppb	5	5	0.5	0	
Particulate-phase concentration, µg m-3	0	0	0	0.5	
Deposition velocity, cm sec	1	1	1	0.1	
Deposition flux, mmole/m^2/year					
	Formic	*Acetic*	*Propionic*	*Oxalic*	*Total*
Wet	3	6	0.3	1.5	10.8
Dry	64	64	6.4	0.18	134.6
Total	67	70	6.7	1.7	145.4
Dry deposition, percent of total	95	91	95	11	92.5

(a) adapted from Grosjean, 1989

Table 3.1.7. Summary of estimated emissions (a).

	Formic acid kg/day	*Acetic acid kg/day*	*All organic acids kg/day*
Emissions:			
- stationary sources	no data	no data	no data
- mobile sources	6,500 (b)	9,000 (c)	19,800
In-situ formation:			
- ozone-olefin reaction	+++	++	+
- HO2-aldehyde reaction	?	?	?
- OH-phenol reaction	0	0	small, ketoacids only
- aldehyde oxidation in clouds	?	?	?
- net, estimated from ambient RCOOH/CO data (d)	8,000	5,000	~15,000
Removal processes:			
- gas-phase reaction with OH	negligible	negligible	negligible
- photolysis	negligible	negligible	negligible except for ketoacids
- removal by rain	minor, 2,200	minor, 5,800	minor (e)
- dry deposition	major, 47,000	major, 61,600	major (e)

(a) Grosjean, 1989
(b) range 1,000 - 13,000
(c) range 3,000 - 15,000
(d) net = not corrected for loss by deposition which competes with in situ formation.
(e) except for particulate-phase organic acids

It is evident from Table 3.1.7 that removal estimates exceed production (emissions plus in situ formation) estimates by a factor of about 4; i.e., 3.4 for formic acid and 4.8 for acetic acid. Using the upper range values for emission rates and using the corresponding increase in atmospheric formation rates (formation and emission vary together with a fixed ratio), would bring the removal/production ratio down to about 2 (1.7 for formic acid, and 2.7 for acetic acid). The discrepancy still remaining may indicate an overestimate of dry deposition velocities, an underestimate of direct emissions (and the associated underestimate of in situ formation rates), or an underestimate of in situ formation relative to direct emissions.

3.1.4 EMISSION RATES

3.1.4.1 Approach and Tracer Selection

Emission inventories for the SoCAB do not include data for formic acid and acetic acid. Of the two ARB compilations of emission rates available prior to SCAQS, one includes daily emission rates for some 180 compounds for the year 1974 (California Air Resources Board, 1981), and the other includes some 220 compounds for the year 1982 on the basis of a 1979 forecast (e.g., Russell and Cass, 1986). No organic acids are included in the 1974 inventory, and the 1982 inventory includes only one organic acid, benzoic acid (12.0 kg/day).

In the absence of emissions data, we have followed and updated the approach of Grosjean (1989) and have attempted to estimate organic acid emission rates on the basis of ambient air quality data for compounds that can serve as indicators of mobile and stationary source emissions. The indicators selected include the following unreactive (or slowly reacting) compounds:

- carbon monoxide (CO) and acetylene (C_2H_2) as tracers for mobile sources.
- the fluorocarbon Freon 113 and the chlorinated hydrocarbons methyl chloroform (1,1,1 trichloroethane, CH_3CCl_3), tetrachloroethylene (C_2Cl_4) and methylene chloride (CH_2Cl_2) as overall tracers of urban pollution.

In selecting these compounds as nonreactive tracers of mobile and overall emissions, respectively, we neglect, in first approximation, the small contribution of stationary sources to CO and C_2H_2 emissions, the small but measurable photochemical formation of CO during air mass transport, and the slow photochemical removal of some of the more reactive chlorinated hydrocarbons due to their reaction with the hydroxyl radical. We further assume that organic acid/tracer ratios in ambient air reflect the corresponding emission ratios (e.g., at the vehicle traffic peak for the mobile sources tracers CO and C_2H_2); i.e., we neglect possible differences in short-term dry deposition rates.

3.1.4.2 Data Set Selection

With these assumptions in mind, we have employed the following SCAQS data subsets to estimate direct emission rates of organic acids:

- Organic acids (formic acid and acetic acid): the data of Grosjean (1990b), which consist of measurements made at the SCAQS "A" sites, Claremont (summer) and Long Beach (summer and fall). This data set is the only set of organic acid measurements acquired during SCAQS. The data of Grosjean (1990b) for Palm Springs could not be included in our analysis due to lack of tracer data for that location (acetylene, chlorinated hydrocarbons, etc.).
- Carbon monoxide: two sets of SCAQS data were obtained from the ARB, one involving CO measurements using continuous analyzers and the other involving "off-line" CO measurements derived from canister samples. In view of the differences in sampling time, sampling duration and reported concentrations among the two sets of CO measurements, we elected to treat these two data sets separately rather than compute their average.

- Acetylene, Freon 113 and CH_2Cl_2: one set of SCAQS data was available for each compound; i.e., that derived from canister samples.
- Tetrachloroethylene: one set of data was available, that derived from another ARB-sponsored study of air toxic measurements during SCAQS and involving round-the-clock, on-site measurements by electron capture gas chromatography, EC-GC (Hisham and Grosjean, 1990).
- Methyl chloroform: two sets of data were available, one obtained from the ARB and derived from SCAQS measurements using canisters, and the other from the on-site EC-GC study mentioned above (Hisham and Grosjean, 1990). As for CO, and for the same reasons (see above), the two sets of data for methyl chloroform were not averaged and were treated separately.

3.1.4.3 Data Formatting

Since organic acid and tracer data were obtained from data subsets with different sampling durations, the following averages were calculated in order to match tracer data to the corresponding organic acid sampling periods (see Table 3.1.8):

- CO (continuous): obtained from ARB as hourly averages, further averaged to match the organic acid sampling schedule.
- Methyl chloroform and tetrachloroethylene (EC-GC): compiled as instantaneous measurements from the original data set of Hisham and Grosjean (1990) with measurement frequencies of 30-60 minutes; all data entries were averaged over time increments that match the organic acid sampling schedule.
- CO, acetylene, Freon 113, methylene chloride, methyl chloroform (canister samples): obtained from ARB as one-hour duration samples collected at 4 A.M., 6 A.M., 8 A.M., 11 A.M., 1 P.M., and 3 P.M. (summer) and 5 A.M., 7 A.M., 9 A.M., 12 P.M., 2 P.M. and 4 P.M. (fall). These samples were assigned to the corresponding organic acid sampling periods shown (see Table 3.1.9). This required us to compute the average of two consecutive canister samples for two of the organic acid sampling periods, and resulted in no tracer data being available for organic acid samples collected at night.

Table 3.1.8. Sampling duration, frequency, and data averaging method (a).

Parameter	Sampling duration in original data set	Sampling frequency (samples per day)	Averaging method
Formic acid	4, 5 and 7 hr (summer) 4 and 6 hr (fall)	5 (b) 5 (c)	none none
Acetic acid	4, 5 and 7 hr (summer) 4 and 6 hr (fall)	5 (b) 5 (c)	none none
CO (continuous)	1 hr	24	average of hourly values to match organic acid sampling schedule
CH_3CCl_3, C_2Cl_4 (EC-GC)	instantaneous, round the clock every 30 to 60 min	24 to 48	average of all individual entries within each organic acid sampling period
CO, acetylene, Freon 113, CH_2Cl_2, CH_3CCl_3 (canister)	1 hr	6	assign data from one or two canister samples to the corresponding organic acid sampling period, see Table 3.1.9

(a) Grosjean, 1989
(b) summer: 1 - 6, 6 - 10, 10 - 14, 14 - 18, 18 - 01 PST
(c) fall: 0 - 6, 6 - 10, 10 - 14, 14 - 18, 18 - 24 PST

Table 3.1.9. Matching of canister samples data to organic acids sampling period (a).

	SAMPLING PERIOD	
	Organic acid sampling period (PST)	*Canister sample*
Summer	1 - 6	4 PST
	6 - 10	average of 6 PST and 8 PST
	10 - 14	average of 11 PST and 13 PST
	14 - 18	15 PST
	18 - 01	none (a)
Fall	0 - 6	5 PST
	6 - 10	average of 7 PST and 9 PST
	10 - 14	12 PST
	14 - 18	average of 14 PST and 16 PST
	18 - 24	none (b)

(a) Grosjean, 1989
(b) no canister sample collected during this period

Concentration averages for each organic acid sampling period are provided in Table 3.1.10 according to three data subsets; i.e., Claremont summer, Long Beach summer, and Long Beach fall. Next, we calculated the corresponding organic acid/tracer concentration ratios. Finally, we calculated emission rates for formic acid and acetic acid using the organic acid/tracer ratios for the 6-10 A.M. vehicle traffic peak sampling period and the following emission rates, in units of kg/day:

carbon monoxide:	6,246,753
acetylene:	38,960
methylene chloride:	10,000
Freon 113:	10,960
methyl chloroform:	33,713
tetrachloroethylene:	32,900

Emission rates for CO, C_2H_2, CH_2Cl_2, Freon 113 and CH_3CCl_3 were obtained from the ARB (personal communication from C. Pilinis, AeroVironment, Inc., 1991). The ARB emission rate for methyl chloroform is slightly lower than, but consistent with, that of 35,600 kg/day reported by Hisham and Grosjean (1990) from examination of earlier literature data (Shikiya et al., 1987). The emission rate for tetrachloroethylene was not available from the ARB. Following Hisham and Grosjean (1990), we use the value of 32,900 kg/day published prior to SCAQS (Shikiya et al., 1987). For the purpose of our calculations, we rounded up the emission rates listed above to (in units of metric tons/day) 6.25×10^3 for CO, 39 for C_2H_2, 11 for Freon 113, 34 for CH_3CCl_3, and 33 for C_2Cl_4.

Table 3.1.10. Composite diurnal variations for organic acids and selected parameters during SCAQS (a).

Parameter	Location	Sampling period, PST				
	(a)	0 - 6 (b)	6 - 10	10 - 14	14 - 18	18 - 24 (b)
Formic acid (ppb)	CL,S	4.7	4.5	9.5	5.9	4.1
	LB, S	2.1	1.8	2.2	2	2.9
	LB, F	2.7	2.6	3.4	5.2	3.6
Acetic acid (ppb)	CL,S	2.5	2.8	5.1	3.3	3.9
	LB, S	2.1	2.9	3.5	2.9	1.9
	LB, F	4.9	4.6	9.4	7.4	6.5
Carbon monoxide (continuous, ppm)	CL,S	1.3	1.8	1.2	1	1
	LB, S	1	1.7	1.3	0.9	0.8
	LB, F	6.8	5.5	2.5	2.6	5.4
Carbon monoxide (canister, ppm)	CL,S	1.7	2.2	1.3	1.3	ND
	LB, S	0.6	1.2	0.8	0.8	ND
	LB, F	1	6.6	2.1	2.3	ND
Acetylene (ppbC)	CL,S	16	20.3	12.3	12.6	ND
	LB, S	13.8	13.5	10.9	8.9	ND
	LB, F	0	30.5	19.6	7.5	ND
Methyl chloroform (canister, ppbC)	CL,S	4.2	4.8	5.7	6.3	ND
	LB, S	6.4	8.9	10.2	5.7	ND
	LB, F	21.7	15.3	13.9	16	ND
Methyl chloroform (EC-GC, ppb)	CL,S	4.4	5.1	6.3	7.4	5.4
	LB, S	6	12.5	13.1	10	7.3
	LB, F	9.6	8	5.7	5.7	5
Freon 113 (ppbC)	CL,S	1.1	1.5	1.1	1.5	ND
	LB, S	1.2	1.3	1.1	0.7	ND
	LB, F	6.8	4.6	1.5	1.5	ND
Methylene chloride (ppbC)	CL,S	1.9	2	1.3	1.8	ND
	LB, S	3.5	14.3	29.6	17.7	ND
	LB, F	15.8	10.3	21.7	19.6	ND
Tetrachloroethylene (ppbC)	CL,S	0.6	1.2	1.1	1.1	0.8
	LB, S	0.6	0.9	1.5	1.1	0.7
	LB, F	2.3	2.2	1.3	1.7	0.8
Ozone (ppb)	CL,S	6.1	29.1	126.8	163.3	19.6
	LB, S	23.1	29.1	65.8	49.8	29.6
	LB, F	3.7	5.9	36.6	29.7	7.7

Table 3.1.10. Composite diurnal variations for organic acids and selected parameters during SCAQS (a).

Continued

Parameter	Location	Sampling period, PST				
	(b)	0 - 6 (c)	6 - 10	10 - 14	14 - 18	18 - 24 (b)
Peroxyacetyl nitrate (ppb)	CL,S	2.2	3.7	8.5	9.9	3.2
	LB, S	0.9	2.3	3.7	1.7	1.1
	LB, F	0.5	1.8	5.4	4.3	0.6
Formaldehyde (ppbC)	CL,S	7.1	8.9	11.2	13.5	ND
	LB, S	4.3	6.4	7.1	5.3	ND
	LB, F	15.3	16.1	13.9	14	ND
Acetaldehyde (ppbC)	CL,S	8.1	12.3	19.7	22.9	ND
	LB, S	5.4	8.1	12.9	7.5	ND
	LB, F	9	12.7	18.2	16.2	ND
Ethylene (ppbC)	CL,S	23.7	28.2	12.9	14.5	ND
	LB, S	14.6	21.8	13.5	13.1	ND
	LB, F	0	41	23.6	9.7	ND
Propene (ppbC)	CL,S	7.2	8.5	2.2	2.4	ND
	LB, S	6.1	9.7	5.1	6.1	ND
	LB, F	0	15.6	6.3	3.5	ND
Isoprene (ppbC)	CL,S	0.6	2.3	3.9	3.6	ND
	LB, S	0.3	1.6	1.6	0.5	ND
	LB, F	4	3.1	0.6	0.9	ND
Temperature (C)	CL,S	17.1	21.5	28.6	33.5	19.3
	LB, S	17.2	19.5	22.9	22.5	18
	LB, F	13.7	15	21.3	20.2	15.7
Humidity (%)	CL,S	72	60.2	41.2	43.7	69.1
	LB, S	85.9	83.1	64	61.3	80.3
	LB, F	79.6	71.2	49.4	54.7	78.6

(a) Grosjean, 1989

(b) CL = Claremont, LB = Long Beach, S = summer, F = fall

(c) 1 - 6 and 18 - 01 PST during summer

3.1.4.4 Emission Rate Estimates

Organic acid emission rates estimated from eight sets of organic acid/tracer ratios are listed in Table 3.1.11. These estimates vary substantially from one tracer to the next; e.g., methyl chloroform and methylene chloride are consistently on the "low" side, and acetylene and tetrachlorethylene are consistently on the "high" side for both acids, both locations, and both seasons. These differences may reflect, in addition to the assumptions discussed earlier, systematic discrepancies in measured tracer concentrations and/or in the corresponding emission rates. For the two tracers for which independent sets of measurements are available, CO (canister and continuous) and CH_3CCl_3 (canister and on-site EC-GC), the reported ambient concentrations agree well for CO and are generally within a factor of 2 for CH_3CCl_3. Since these two tracers give organic acid emission rates that are on the "high" and "low" side, respectively, of the range of estimates, the uncertainty in organic acid emission rates is likely to reflect, to a large extent, uncertainties in tracer emission rates.

While individual estimates vary from one tracer to the next as discussed above, these estimates are, overall, reasonably consistent for all tracers at both locations and for both seasons. For formic acid, the higher estimate obtained for Claremont as compared to Long Beach is likely to reflect in situ photochemical formation during air mass transport inland (see following section). For acetic acid, which has a much less important in situ formation component than formic acid (see following section), estimated emission rates for Claremont and Long Beach are in agreement. Estimates for both acids are higher (by 60-70%) during the summer than during the fall. This may reflect seasonal variations in tracer emissions, in organic acid/tracer emission rate ratios, or in organic acid/tracer loss rate ratios; for example, faster rates of removal of organic acids by dry deposition under the more stagnant conditions prevailing during the fall.

A brief comparison of the data given in Table 3.1.11 with earlier literature data is of interest. First, our estimates indicate that emission rates for acetic acid are higher than those for formic acid, with acetic acid/formic acid ratios of 2:1 - 2:3 (Long Beach).

Table 3.1.11. Estimated organic acids, emission rates (metric tons/day) (a).

Tracer	Tracer emission rate, metric tons/day	Formic acid			Acetic acid		
		Claremont, summer	Long Beach, summer	Long Beach, fall	Claremont, summer	Long Beach, summer	Long Beach, fall
CO, canister	6,250	20.9	14.9	4	16.9	31.7	9.1
CO, continuous	6,250	25.8	10.8	4.7	20.7	22.9	11
C2H2	39	30.4	18.2	11.6	24.5	38.9	26.8
Freon 113	11	15.8	7.3	3	12.7	15.5	6.9
CH3CCl3, EC-GC	34	10.4	1.7	3.8	8.4	3.6	8.8
CH3CCl3, canister	34	21.8	4.7	4	17.6	10.1	9.2
CH3Cl	10	24.3	1.3	2.7	19.8	2.9	6.3
CCl4	33	35.5	17.6	10.7	28.7	37.5	24.6
	Average:	**23.1**	**9.6**	**5.6**	**18.7**	**20.4**	**12.8**

(a) Grosjean, 1989

Indeed, limited measurements of acids in automobile exhaust and in a highway tunnel (see Section 3.1.2 Background: Review of Existing Data), also showed higher emissions of acetic acid, with acetic acid/formic acid ratios of 2:6 (tunnel) and 4:3 (car exhaust). Second, the organic acid emission rates given in Table 3.1.11 are consistent with, but somewhat higher than, those estimated earlier by Grosjean (1989) from CO data for two southern California locations: Claremont in 1985 and Glendora in 1986.

3.1.5 In Situ Formation of Organic Acids in the Atmosphere

Chemical reactions that produce organic acids in the atmosphere include the gas-phase reaction of ozone with olefins, the gas-phase reaction of aldehydes with the HO_2 radical, the gas-phase reaction of phenols with the hydroxyl radical (to produce ketoacids), and the aqueous-phase oxidation of aldehydes in cloudwater. These reactions have been discussed in detail by Grosjean (1989). In addition, Madronich et al. (1990) have recently suggested that acetic acid may form in the troposphere by reaction of the peroxy radicals CH_3CO_3 and HO_2. The relevance of this reaction to acetic acid production in urban air is unknown. Thus, with respect to in situ formation of gas-phase formic acid and acetic acid during SCAQS, we assume that two of the above reactions may be of importance: the ozone-olefin reaction and the aldehyde-HO_2 reaction. These two reactions are discussed below.

3.1.5.1 Aldehyde-HO_2 Reaction

Organic acid formation in the atmosphere may involve the reaction of aldehydes with the hydroperoxy radical HO_2 (Su et al., 1979; Veyret et al., 1982) as is shown below for formic acid:

$$HO_2 + HCHO \rightarrow O_2CH_2OH \quad (R1)$$
$$O_2CH_2OH + NO \rightarrow NO_2 + OCH_2OH \quad (R2)$$
$$OCH_2OH + O_2 \rightarrow HO_2 + HCOOH \quad (R3)$$

During daytime, aldehydes photolyse rapidly and also react rapidly with the OH radical. As a result, their conversion to organic acids by reaction with HO_2 is probably of negligible importance. At night, aldehydes are removed by reaction with the nitrate radical to form products other than organic acids:

$$HCHO + NO_3 \rightarrow HNO_3 + HCO \quad (R4)$$
$$HCO + O_2 \rightarrow HO_2 + CO \quad (R5)$$

However, removal of aldehydes at night by reaction with the nitrate radical is not as rapid as their daytime removal by reaction with OH and by photolysis. Therefore, the HO_2-aldehyde reaction may be of some importance at night. Examination of the SCAQS aldehyde data base, more specifically formaldehyde and acetaldehyde (see composite averages in Table 3.1.10) indicates sampling period-averaged aldehyde concentrations of 10-20 ppb at the Claremont and Long Beach locations. Thus, ambient levels of aldehydes were generally high enough for the aldehyde-HO_2 reaction to be of importance. With a rate constant of 8×10^{-14} cm^3 $molecule^{-1}$ sec^{-1} or reaction R1 (Carter, 1990) and setting [HCHO] = 10 ppb, a formic acid production rate of, for example, 2 ppb per hour, would require HO_2 concentrations of about 8×10^8 molecules cm^{-3}. Unfortunately, direct measurements of HO_2 were not made during SCAQS, and more precise kinetic calculations cannot be carried out. Therefore, the importance of the HO_2-aldehyde reaction as a pathway for organic acid formation is uncertain at this time.

3.1.5.2 Olefin-Ozone Reaction

Organic acids are formed in the reaction of ozone with olefins. This reaction proceeds by electrophilic addition of ozone on the unsaturated carbon-carbon bond and yields two carbonyls (aldehydes or ketones) and two Criegee biradicals:

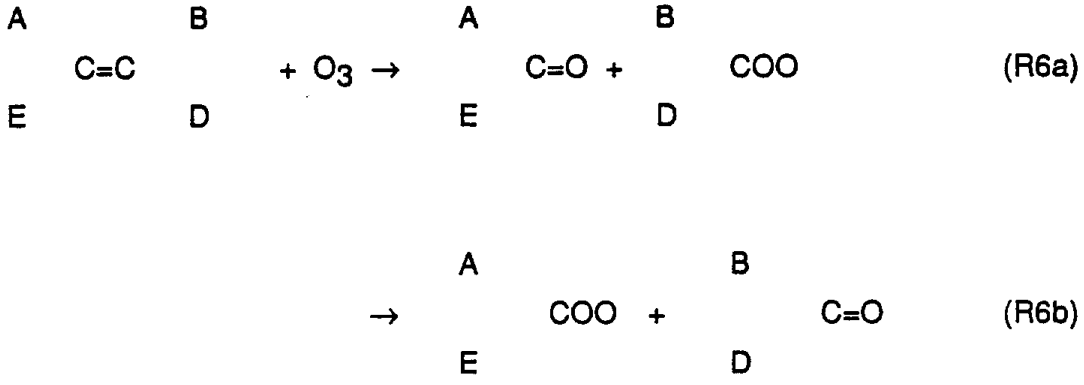

where A, B, D and E are substituents including H, CH_3, C_2H_5, etc. The energy-rich Criegee biradicals may decompose to yield small products including free radicals, or may be stabilized and isomerize to yield the corresponding carboxylic acid, as is shown below for E = H:

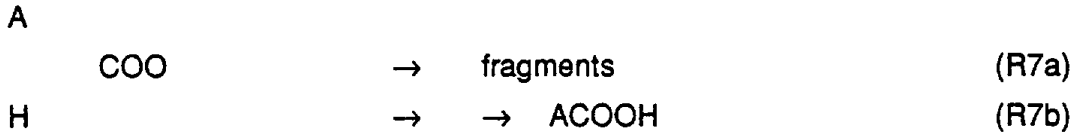

In the absence of more detailed product studies, it has been assumed in recent computer kinetic models (Carter, 1990) that the initial reaction with ozone results in a 50:50 split for all olefins; i.e., $k_{R6a} = k_{R6b}$, and that the organic acid yield from the Criegee biradical, i.e., $k_{R7b} / k_{R7a} + k_{R7b}$, is 37% for the H_2COO Criegee biradical

(e.g., ethylene) 20% for the $CH_3C(H)OO$ biradical (e.g., propene) and also 20% for other RC(H)OO biradicals (e.g., 1-butene, R = C_2H5). These two assumptions may not be valid if, as expected from theoretical considerations, the Criegee biradicals are increasingly more stable as the substituent size increases. If this is the case, the initial reaction R6 may proceed preferentially via the pathway; e.g., R6b, that leads to the Criegee biradical which contains the larger substituents. In addition, the yield of organic acid, i.e. the relative importance of reaction R7b, would also increase with substituent size.

In the absence of data, we have adopted the assumptions of Carter (1990) in the following calculations. Thus, the ozone-ethylene reaction is assumed to yield 37% formic acid, the ozone-propene reaction is assumed to yield 0.5 x 37% = 18.5% formic acid and 0.5 x 20% = 10% acetic acid, and so on (see Table 3.1.12). We realize that these assumptions are likely to result in an underestimate of the organic acid yield from higher molecular weight olefins.

A second important consideration when attempting to estimate organic acid production rates in the ozone-olefin reaction is that olefins also react with the hydroxyl radical and with the nitrate radical. These two reactions, which compete with the ozone-olefin reaction, lead to products other than organic acids. The relative importance of the three reactions is given by:

$$-\frac{d(\text{olefin})}{dt} = [\text{olefin}]\,(k_{OH}[OH] + k_{O3}[O_3] + k_{NO3}[NO_3])$$

where [OH], $[O_3]$ and $[NO_3]$ are ambient concentrations and k_{OH}, k_{O3} and k_{NO3} are the corresponding reaction rate constants. Since removal by OH is essentially a daytime process (OH levels are very low at night) and since removal by NO_3 is essentially a nighttime process (NO_3 photolyzes rapidly in sunlight), the above equation simplifies to:

$$-\frac{d(\text{olefin})}{dt} = [\text{olefin}]\,(k_{OH}[OH] + k_{O3}[O_3]) \quad \text{(daytime)}$$

$$= [\text{olefin}]\,(k_{NO3}[NO_3] + k_{O3}[O_3]) \quad \text{(nighttime)}$$

Table 3.1.12. Estimated organic acid yields in the ozone-olefin reaction (a).

Olefin	Yield of organic acid product			
	Formic acid	Acetic acid	Propionic acid	Other acid (b)
ethylene	0.37			
propene	0.185	0.10		
3-methyl-1-pentene	0.185			0.10 (isovaleric)
1-pentene	0.185			0.10 (n-butyric)
2-methyl-2-butene		0.10		
1,3-butadiene	0.37			
2-methyl-1-butene	0.185			
1-butene	0.185		0.10	
cis-2-butene		0.20		
trans-2-butene		0.20		
isobutene	0.185			
cyclohexene				0.20 (adipic)
3-methyl-1-butene	0.185			0.10 (isobutyric)
methyl cyclopentene				0.20 (methyl glutaric)
2,3-dimethyl-1-butene	0.185			
cis-2-pentene		0.10	0.10	
trans-2-pentene		0.10	0.10	
cis-3-hexene			0.20	
2-methyl-2-pentene			0.10	
trans-3-methyl-2-pentene		0.10		
1-hexene	0.185			0.10 (valeric)
2-ethyl-1-butene	0.185			

(a) Grosjean, 1989

(b) estimated yields for these acids are probably lower limits, see text for discussion of acid yields from olefins with larger substituents.

We have assumed two simple scenarios: one daytime scenario with O_3 = 100 ppb, OH = 10^6 molecules cm^{-3}, and NO_3 = O, and one nighttime scenario with O_3 = 10 ppb, OH = O and NO_3 = 10 ppt. Our selection of daytime and nighttime ozone concentrations is based on the actual data given in Table 3.1.3. Our selection of concentrations for the OH and NO_3 radicals is arbitrary, but consistent with earlier literature data.

For these two scenarios, we have estimated, for most olefins measured during SCAQS, and for which emission rates are available, the fractional removal is due to reaction with ozone (see Table 3.1.13). The reaction rate constants used in the calculations are also listed in Table 3.1.13. These rate constants are from recent literature data (Atkinson, 1990 and Carter, 1990), or, when no data were available, have been estimated from structure-reactivity relationships (Grosjean, 1990c) or from data for structural homologues, see footnotes in Table 3.1.13 for details. For the daytime scenario, the ozone-olefin reaction increases in importance relative to the OH-olefin reaction with increasing olefin reactivity, from 22-33% for the less reactive olefins such as ethylene and butadiene to 85-97% for the more reactive olefins such as the 2-butene and 2-pentene isomers. The reverse is generally observed for the nighttime scenario, where the ozone-olefin reaction is often more important, relative to the NO_3-olefin reaction, for the less reactive olefins including ethylene.

Finally, we have calculated organic acid formation rates due to in situ formation in the ozone-olefin reaction for both daytime and nighttime scenarios. These formation rates were obtained, for each olefin and each scenario, by multiplying the olefin emission rate by the organic acid yield given in Table 3.1.12 and the fractional olefin removal due to reaction with ozone given in Table 3.1.13. For ethylene and propylene, emission rates were obtained from the ARB (C. Pilinis, personal communication, AeroVironment, 1991) and are 74,623 kg/day and 34,575 kg/day, respectively (these values were rounded to 74.6 and 34.6 metric tons/day). For the other olefins, emission rates from the 1974 ARB inventory as compiled by Grosjean (1989) were adjusted using the more recent propylene emission rate of 34.6 metric tons/day as a reference.

Estimated organic acid production rates from the ozone-olefin reaction are given in Table 3.1.14 for both daytime and nighttime scenarios. During the day, an estimated

Table 3.1.15. Fractional removal by ozone (a).

	Daytime (b)			Nightime (c)	
	k(d)	k(e)	ozone removal, %	k(f)	ozone removal, %
ethylene	0.85	1.7	0.33	0.21	0.89
propene	2.63	11.3	0.52	9.4	0.55
3-methyl-1-pentene	3.14 (h)	10.7 (h)	0.46	30.9 (h)	0.26
1-pentene	3.14	10.7	0.46	30.9 (g)	0.26
2-methyl-2-butene	6.89	423	0.94	9,300	0.04
1,3-butadiene	6.66	7.5	0.22	98	0.07
2-methyl-1-butene	6.10	12.1 (h)	0.33	170 (g)	0.07
1-butene	3.14	11	0.47	11	0.48
cis-2-butene	5.64	130	0.85	350	0.27
trans-2-butene	6.40	200	0.89	390	0.34
isobutene	5.14	12.1	0.37	310	0.04
cyclohexene	6.77	100	0.79	530	0.16
3-methyl-1-butene	3.18	11.0 (h)	0.46	29.5 (g)	0.27
methyl cyclopentene	6.70 (h)	400 (h)	0.94	460 (h)	0.47
2,3-dimethyl-1-butene	5.55 (g)	12.1 (h)	0.35	246 (g)	0.05
cis-2-pentene	6.50	209	0.89	282 (g)	0.43
trans-2-pentene	6.70	315	0.92	282 (g)	0.53
cis-3-hexene	6.28 (g)	130 (h)	0.84	427 (g)	0.23
2-methyl-2-pentene	6.89 (h)	423 (h)	0.94	9,300 (h)	0.04
trans-3-methyl-2-pentene	9.44 (g)	1,160 (h)	0.97	2,690 (g)	0.30
1-hexene	3.70	11.7	0.44	427 (g)	0.03
2-ethyl-1-butene	5.61 (g)	12.1 (h)	0.35	257 (g)	0.04

(a) Grosjean ,1989

(b) O = 100 ppb, OH = 1.0 x 10 molecules cm, NO = O

(c) O = 10 ppb, OH = O, NO = 10 ppt

(d) units: 10cm-molecule-sec

(e) units: 10-cm-molecule-sec

(f) units: 10-cm-molecule-sec

(g) estimated from structure-reactivity relationships (Grosjean 1990c)

(h) assumed to be the same as for structural homologue indicated in parentheses as follows: 3-methyl-1-pentene (1-pentene); 2-methyl-1-butene (isobutene); 3-methyl-1-butene (1-butene); methyl cyclopentene (cyclopentene); 2, 3-dimethyl-1-butene (isobutene); cis-3-hexene (cis-2-butene); 2-methyl-2-pentene (2-methyl-2-butene); trans-3-methyl-2-pentene (2, 3-dimethyl-2-butene); 2-ethyl-1-butene (isobutene)

TABLE 3.1.14. Organic acid production from ozone-olefin reaction (a).

Olefin	Organic acid production rate, metric tons per day					
	DAYTIME			NIGHTTIME		
	Formic	*Acetic*	*Other*	*Formic*	*Acetic*	*Other*
ethylene	9.1	-	-	24.6	-	-
propene	3.3	1.8	-	3.5	1.9	-
3-methyl-1-pentene	2.9	-	1.6	1.7	-	0.9
1-pentene	2.6	-	1.4	1.5	-	0.8
2-methyl-2-butene	-	2.6	-	-	0.1	-
1,3-butadiene	2.1	-	-	0.7	-	-
2-methyl-1-butene	1.4	-	-	0.3	-	-
1-butene	1.6	-	0.9	1.7	-	0.9
cis-2-butene	-	2.6	-	-	0.8	-
trans-2-butene	-	2.5	-	-	1.0	-
isobutene	0.8	-	-	0.1	-	-
cyclohexene	-	-	1.9	-	-	0.4
3-methyl-1-butene	0.7	-	0.4	0.4	-	0.2
methyl cyclopentene	-	-	1.0	-	-	0.5
2,3-dimethyl-1-butene	0.4	-	-	0.05	-	-
cis-2-pentene	-	0.3	0.3	-	0.4	0.4
trans-2-pentene	-	0.2	0.2	-	0.1	0.1
cis-3-hexene	-	-	0.2	-	-	0.1
2-methyl-2-pentene	-	-	0.1	-	-	0.0
trans-3-methyl-2-pentene	-	0.1	-	-	-	0.03
1-hexene	0.04	-	0.04	0.0	-	0.0
2-ethyl-1-butene	0.03	-	-	0.0	-	-
TOTAL:	**25.0**	**10.1**	**8.0**	**34.5**	**4.3**	**3.4**

(a) Grosjean, 1989

25.0 metric tons/day of formic acid, 10.1 metric tons/day of acetic acid, and 8.0 metric tons/day of higher molecular weight organic acids (including 1.7 tons/day of propionic acid) are produced in situ by the olefin-ozone reaction. At night, estimated production rates are 34.5, 4.3 and 3.4 metric tons per day for formic, acetic, and higher acids, respectively. While daytime and nighttime production rates are similar for the sum of all organic acids, 43.1 vs 42.2 metric tons/day, more formic acid and less acetic acid are produced at night. The major olefinic precursors of formic acid are ethylene, propene and 3-methyl-1-pentene, which together account for 61% (daytime) and 86% (nighttime) of the total formic acid produced. Propene, cis and trans-2-butene, and 2-methyl-2-butene (daytime only) account for most of the acetic acid produced; i.e., 94% during the day and 86% at night.

The ozone-olefin reaction produces more formic acid than acetic acid, with formic/acetic production rate ratios of 2.5 during the day and 8.0 at night. Since the reverse is true for direct emissions, see preceding section, the ambient concentrations ratio for the two acids in the SCAQS domain can be used as an indicator of the relative importance of direct emissions (low formic/acetic acid ratios; e.g., Long Beach, fall, nighttime and early morning samples) and photochemistry (high formic/acetic acid ratios; e.g., Claremont, summer, mid-day samples that also coincide with the peak ozone and PAN concentrations).

3.1.6 Removal Processes

3.1.6.1 General Considerations

With the exception of ketoacids as discussed before, organic acids are not significantly removed from the atmosphere by gas-phase reactions. Their only gas-phase removal pathway is by slow reaction with the hydroxyl radical. The OH-organic acid reaction rate constants are 0.35-0.46, 0.73, 1.2 and 2.0 x 10^{-12} cm^3 $molecule^{-1}$ sec^{-1} for formic, acetic, propionic, and isobutyric acid, respectively (Dagaut et al., 1988). These rates correspond to atmospheric residence times of several weeks against removal by reaction with OH. For example, taking formic acid = 10 ppb, OH = 10^6 molecules cm^{-3}, and k_{OH} = 0.46 x 10^{-12} cm^3 $molecule^{-1}$ sec^{-1}, the

removal rate of formic acid by reaction with OH is only 0.017 ppb per hour. For an air mass transport time of 12 hours (e.g., from Downtown Los Angeles to Palm Springs and beyond), this rate is equivalent to only 0.2 ppb of formic acid (or 0.32 ppb acetic acid) being removed by gas-phase chemical reaction.

As discussed in Section 3.1.2, other removal processes for airborne organic acids include dry and wet deposition. The calculations of Grosjean (1989) for deposition scenarios relevant to southern California (see Table 3.1.6 for details) indicate that dry deposition is the major loss process for gas-phase organic acids, and accounts for 95, 91 and 95% of the total deposition budget for formic, acetic and propionic acid, respectively. Thus, we assume here that wet deposition of organic acids was essentially negligible during SCAQS and that dry deposition was the only removal process of importance for organic acids. Dry deposition velocities for organic acids have not been measured. Following Talbot et al. (1988), Jacob and Wofsy (1988), Pierson and Brachaczek (1990), and Grosjean (1989) has assumed a deposition velocity of 1 cm sec^{-1} for all gas-phase organic acids. Recent conversations with scientists with expertise in dry deposition measurements also indicate that, in the absence of experimental data, a value of 1 cm sec^{-1} appears indeed reasonable (C. Davidson, personal communication, 1991). Of course, actual deposition velocities for organic acids in the SCAQS domain are expected to vary with the nature of the ground cover (concrete buildings, asphalt parking lots, grass and other vegetation, etc.) and perhaps also with time of day (day vs night), temperature, humidity and season (plant growing season and other factors).

3.1.6.2 Dry Deposition Fluxes and Removal Rates

For the purpose of calculating dry deposition fluxes of organic acids during SCAQS, we have taken the formic acid and acetic acid concentrations to be their actual averaged concentrations during SCAQS; i.e., 5.5 ppb (Claremont, summer), 2.3 ppb (Long Beach, summer), and 3.5 ppb (Long Beach, fall) for formic acid and 3.6 ppb (Claremont, summer), 2.5 ppb (Long Beach, summer) and 6.5 ppb (Long Beach, fall).

Dry deposition fluxes for formic acid and acetic acid are given in Table 3.1.15 for three values of the dry deposition velocity, 0.5, 1.0 and 2.0 cm sec $^{-1}$. Also listed in Table 3.1.15 are the organic acid dry deposition removal rates calculated from the corresponding fluxes and taking the area of the SCAQS domain to be 6.0 x 10^9 m^2 (120 x 50 km). Dry deposition removal rates obviously follow the corresponding average ambient air concentrations and are highest in Claremont (summer) for formic acid and in Long Beach (fall) for acetic acid. Both fluxes and removal rates are consistent with, but somewhat higher than, those calculated by Grosjean (1989) from measurements made in 1986 in Glendora.

3.1.6.3 Comparison of Direct Emissions, In situ Formation, and Dry Deposition Removal Rates

Finally, a comparison of direct emissions, in situ formation, and dry deposition removal rates is given in Table 3.1.16. Production of formic acid is seen to be dominated by in situ formation. The reverse is true for acetic acid, for which direct emissions predominate. Overall, production and removal rates are consistent within a factor of two or less, a significant improvement over the three-fold to five-fold discrepancies noted by Grosjean (1989). This uncertainty is commensurate with those for the input parameters used, including direct emission rates and dry deposition velocities. For formic acid, production and removal terms are in good agreement for Claremont (summer) and Long Beach (fall). Estimated production exceeds estimated removal by 57% of their mean value in Long Beach (summer). For acetic acid, removal exceeds production in all three cases (although only to a small extent for the Long Beach summer data), thus suggesting that the actual dry deposition velocity of acetic acid may be lower than the value of 1.0 cm sec^{-1} we assigned to both formic acetic and acetic acid. Conversely, the production terms for acetic acid may need to be adjusted

Table 3.1.15. Removal of organic acids by dry deposition (a).

	Ambient concentration, ppb	Dry deposition flux, mmoles/m^2/day			Removal rate due to dry deposition, metric ton/day		
		Dry deposition velocity, cm/sec			Dry deposition velocity, cm/sec		
		0.5	1	2	0.5	1	2
Formic Acid							
Claremont, summer	5.5	0.096	**0.193**	0.386	26.2	**52.4**	104.8
Long Beach, summer	2.3	0.041	**0.083**	0.166	10.9	**21.9**	43.8
Long Beach, fall	3.5	0.061	**0.123**	0.246	16.7	**33.4**	66.8
Acetic Acid							
Claremont, summer	3.6	0.063	**0.126**	0.252	22.9	**45.8**	91.6
Long Beach, summer	2.5	0.044	**0.088**	0.176	15.9	**31.8**	63.6
Long Beach, fall	6.5	0.114	**0.228**	0.456	41.3	**82.6**	165.2

(a) Grosjean, 1989

Table 3.1.16. Comparison of organic acid production and removal rates (a).

	Formic acid metric tons/day	Acetic acid metric tons/day
Direct Emissions		
Claremont, summer	23.1	18.7
Long Beach, summer	9.6	20.4
Long Beach, fall	5.6	12.8
In Situ Formation (Ozone-olefin reaction)		
Day	25	10.1
Night	34.5	4.3
Average	29.7	7.2
Total Production		
Claremont, summer	52.8	25.9
Long Beach, summer	39.3	27.6
Long Beach, fall	35.3	20
Dry Deposition Removal		
Claremont, summer	52.4	45.8
Long Beach, summer	21.9	31.8
Long Beach, fall	33.4	82.6
Differences, Production-Removal		
Claremont, summer	0.4	<19.9>
Long Beach, summer	17.4	<4.2>
Long Beach, fall	1.9	<62.6>

(a) Grosjean, 1989

upward, but this is less likely since production terms for formic and acetic acids, with the former being in good agreement with its removal counterpart, were derived from mutually consistent assumptions and calculations.

3.2 THE SMOG-FOG-SMOG CYCLE AND ACID DEPOSITION

3.2.1 Introduction

Historically, urban fogs have been interconnected with severe pollution episodes (Wilkins, 1954). A cyclical relationship between the occurrence of smog and fog in the Los Angeles basin has been proposed by Munger et al. (1983) and was termed the smog-fog-smog cycle. A polluted atmosphere with high aerosol concentration assists the formation of late night and early morning fogs which appear to enhance smog production, visibility reduction, and aerosol sulfate levels during the following day.

Fogs can be viewed as a physiochemical processor of the ambient aerosol and of various gaseous pollutants. As the relative humidity of an air parcel in contact with the ground increases, water condenses on the aerosol particles in accordance with water vapor equilibrium. If the relative humidity of the parcel reaches a critical supersaturation, the value of which depends on the size and chemical composition of the aerosol present, the particles become activated, grow freely by vapor diffusion, and a fog forms. The growth of the aerosol particles to liquid droplets leads to the acceleration of particle removal from the atmosphere, decreasing the aerosol concentration. Soluble gaseous species such as nitric acid, sulfur dioxide, and ammonia are transferred to the aqueous phase and their deposition is also giving products that remain in the aerosol phase after the fog dissipates, for example the dissolution of SO_2, its ionization and its subsequent oxidation to sulfate. These species can attract additional gaseous species; e.g., ammonia and water, into the aerosol phase; therefore, a fog may also increase the aerosol mass.

Cass and Shair (1984) reported a correlation between high aerosol sulfate concentrations in the Los Angeles basin and the occurrence of fog episodes. However, as noted in their findings, the quantitative effects of the fogs on the concentration of the major aerosol species are not yet fully understood. Pandis et al. (1990) and Hegg and Larson (1990) suggested that sulfate production is not uniformly distributed over the droplet spectrum. Therefore, it is necessary to investigate not only the effects of fogs on

bulk aerosol concentration, but also the possible effects on the aerosol size/composition distribution.

A rigorous theoretical investigation of the smog-fog-smog cycle requires a mathematical model to describe the thermodynamics and dynamics of multicomponent aerosols, the microphysics of the condensational growth of a droplet distribution, the droplet removal processes, and the gas- and aqueous-phase chemical processes occurring in a fog.

Such a model enables us to provide answers to several additional questions associated with the urban fog life cycle. These problems include the aerosol scavenging efficiencies of urban fogs, the uncertainties introduced by measuring in bulk a polydisperse fog droplet distribution, the difference in deposition velocities of different ionic species during fog episodes, and expression of the liquid water flux as a function of the liquid water content for fog models that do not include explicit treatment of droplet microphysics.

We begin with a short discussion of the distinction between aerosol and droplets. A brief description of the mathematical model employed in this study follows with a presentation of the representative fog episode that will be simulated. Next, the effects of fogs on aerosol concentration and aerosol size/composition distribution are investigated. Predictions for the aerosol scavenging efficiency of urban fogs are then compared with field measurements. The possible problems posed by the differences in chemical composition of fog droplets of different sizes on fog sampling and on calculations of deposition velocities are presented next. Suggestions for a more accurate calculation of liquid water deposition flux in fog models follow. Finally, a possible explanation is presented for the reported differences among the deposition velocitities of different ionic species.

3.2.2 Aerosol or Droplet?

There have been different approaches in the literature concerning the distinction between aqueous droplets and interstitial aerosol. In principle, this distinction appears

unnecessary because the same physicochemical processes (mass transfer, chemical reactions, etc.) take place in both aerosol and droplets. However, the difference in size between aerosol and droplets and the subsequent difference in the characteristic times of the respective processes has led previous investigators to separate these particles into aerosol and droplets, using different definitions and creating some confusion.

In several studies, a size cut is selected more or less arbitrarily and all the particles larger than this size are named droplets, while all particles smaller than that are considered aerosol. A second definition, used in cloud physics, is based on the fundamental droplet microphysics. For every particle there is a corresponding critical diameter d_c and a critical supersaturation s_c corresponding to the maximum of the Köhler equations (Pruppacher and Klett, 1980). If the environment reaches a supersaturation equal to, or larger than s_c, that particle is said to be activated. In the usual description of the activation process the larger particles are activated first, and as the supersaturation increases, smaller and smaller particles are successively activated. In cloud physics, a particle is not considered to be a droplet unless its diameter exceeds its critical diameter. In this case, however, because of mass transfer limitations, the larger particles may not be able to follow the changes of relative humidity (Hänel, 1987) and they may not be able to reach their critical radius. Nevertheless, these large particles carry a significant amount of the liquid water of the cloud or fog and should be included in the droplet population.

To overcome the arbitrary nature of the first definition (everything larger than a certain size is a droplet), and the omission of the larger particles from the droplet population in the second definition because of mass transfer limitations (their diameter often never exceeds their critical diameter during a fog episode), we propose a third definition: A particle is described as a droplet when either the supersaturation of the environment exceeds its critical supersaturation or its diameter exceeds its critical diameter. When both of these criteria are not met, the particle will be referred to as interstitial aerosol.

In our model, the same differential equations will be applied to all particles inde-

pendently of their size and chemical composition. Later, the definition suggested above will be used to distinguish between droplets and aerosol, so that a direct comparison between our work and previous studies will be possible.

3.2.3 Model Description

The mathematical model employed in this study describes gas-phase chemistry, aerosol dynamics and thermodynamics, aqueous-phase chemistry, droplet microphysics, and wet deposition in a closed homogeneous volume of air in which a fog is formed and dissipated. The primary input to the model is the temperature of the system. This model is an extended version of that developed by Pandis et al. (1990). The main addition is the inclusion of the wet removal processes to those described in the original work.

The fog physics suggests that the fog life cycle should be divided into three simulation periods; namely, the conditioning period (relative humidity, RH, rises from the initial value to a threshold value RH_c close to saturation, chosen as 99%), the rapid growth period ($RH > RH_c$), and the dissipation period (RH drops under RH_c).

During the fog conditioning stage, the model simulates the gas-phase chemistry and the aerosol size/composition distribution evolution. Both aerosol dynamics and thermodynamics are considered (Pilinis and Seinfeld, 1988) and for computational purposes the continuous aerosol size distribution is discretized into n uniform sections (Warren and Seinfeld, 1985). The detailed SAPRC/ERT gas-phase chemical reaction mechanism (Carter et al., 1986) with the modifications and extensions of Carter and Atkinson (1988) is used for the calculation of the gas-phase reaction rates. This mechanism describes the complex chemical reactions of hydrocarbon/NO_x/ SO_2 mixtures in a polluted atmosphere, using 154 reactions and 62 species.

When the relative humidity of the system exceeds the threshold value RH_c, processes described by the model include gas-phase chemistry, aqueous-phase chemistry, microphysics of aerosol and droplets, and deposition. The droplet size distribution is discretized as before into n individual size sections, but because of the magnitude of

the size changes occurring, each droplet size section is now allowed to move in the time-diameter space increasing its diameter when water condensation is taking place and decreasing its size in case of evaporation.

The change of the mass concentration of species i in droplet size section l, q_{il}, is calculated by:

$$\frac{dq_{il}}{dt} = \left[\frac{\partial q_{il}}{\partial t}\right]_{cond./evap.} + R^a_{il}(q_{1l}, q_{2l}, ..., q_{nl}) - \frac{v_l}{H} q_{il} \qquad (1)$$

where $\left[\frac{\partial q_{il}}{\partial t}\right]_{cond./evap.}$ is the mass transfer rate of species i from the gas phase to the aqueous droplets in moving section l, R^a_{il} is the rate of change of species i in section l due to aqueous-phase reactions, v_l is the deposition velocity of droplets in section l, and H is the fog height. For the water mass transfer rate, the detailed growth equation derived by Pruppacher and Klett (1980) is used, and for the remainder of the volatile species the expression used by Pandis and Seinfeld (1989a) is applied. The use of the detailed growth equation for the multicomponent aqueous solution droplets enables us to describe the activation process exactly without the use of any further assumptions (Pruppacher and Klett, 1980). The reaction rates R^a_{il} are derived from the aqueous-phase chemical mechanism presented by Pandis and Seinfeld (1989a) which includes 49 individual aqueous-phase species, 17 aqueous-phase ionic equilibria and 109 aqueous-phase reactions. Field studies in fogs (Dollard and Unsworth, 1983) have indicated that for wind speeds less than 2 m s^{-1}, typical of radiation fogs, droplet sedimentation accounts for most of the droplet flux to the ground. Therefore, the deposition velocity of fog droplets is approximated by Stokes Law as long as the diameter of the droplets remains less than 50 μm.

Droplet coagulation is neglected and the number concentration of droplets in each section l, N_l, changes only due to droplet deposition and is described by

$$\frac{dN_l}{dt} = -\frac{v_l}{H} N_l \qquad (2)$$

The change in section diameter, D_l, is calculated by:

$$\frac{dD_l}{dt} = \frac{2}{N_l \rho_l \pi D_l^2} \sum_{i=1}^{Nv} \left[\frac{\partial q_{il}}{\partial t}\right]_{cond./evap.} \tag{3}$$

where ρ_l is the density of droplets in section l, and N_v is the number of volatile species.

The turbulence induced by the radiative cooling of the fog top and the entrainment of air in the fog layer have been neglected in this study.

3.2.4 Representative Fog Episode for Evaluation

Unfortunately, no complete data set exists, to the best of our knowledge, for a full evaluation of the present model. Such a data set should include aerosol size/composition distributions before and after the fog episode and droplet size/composition distributions during the episode. Direct comparison of the model predictions with observations is problematic not only because of the difficulty of the required experimental measurements, but also because in fog field studies samples are acquired in the same location and no attempt is made to follow the air parcel in which fog was created. Because of the above limitations the current work should be viewed primarily as a sensitivity study investigating phenomena that have not yet been elucidated by field studies.

The case that will be considered is a typical urban radiation fog episode in the Los Angeles basin roughly corresponding to the fog episode of November 23, 1981 in Pasadena, California (Munger et al., 1983). The first stage of the simulation starts in the late afternoon with relative humidity 50% and dry aerosol particles. The temperature drops to 14°C and the relative humidity increases reaching 95% one hour before midnight. The main simulation begins with both gas- and aqueous-phase chemical processes being taken into account at this time. The initial conditions used are shown in Table 3.2.1. The fog lasted roughly three hours with the temperature dropping to a minimum of 12.8°C at midnight (t = 60 min), increasing slowly to 13° C at t = 130 min, and to 14 °C at t = 170 min. A constant fog height of 200 m is assumed, typical of radiation fog episodes (Pandis and Seinfeld, 1989b). During the fog dissipation stage,

TABLE 3.2.1. Base case parameters and initial conditions.

Model Parameter	*Value*
Latitude	34.5
Time at start (full simulation)	23 : 00 PST
Relative humidity at start	95%
Fog Height	200 m

Gas – phase species	*Initial concentration (ppb)*
SO_2	10.0
NH_3	8.03
HNO_3	5.17
HCl	3.90
O_3	10.0
NO	50.0
NO_2	50.0
H_2O_2	1.0
HCHO	7.0
PAN	1.0
ETHE	85.0
Parafins	700.0
Olefins	45.0
Aromatics	150.0

Aerosol species	*Initial concentration* ($\mu g/m^3$)
Sulfate	3.93
Sodium	3.38
Fe^{3+}	0.2
Mn^{2+}	0.01

the chemistry is followed until the relative humidity again reaches 95% and then the aerosol is allowed to dry until the relative humidity reaches the 50% point. Gas-phase chemical processes are neglected in the first and last stages.

The model has been applied with seven logarithmically spaced sections covering initially the diameter range from 0.2 to 8 μm. This choice of section number represents a reasonable compromise between computational accuracy and keeping the required computing time at a reasonable level. Increasing the current number of sections causes an exponential increase in computing time without changing the conclusions reached in the present work. The initial sulfate and sodium have been distributed over these sections according to the measurements of Wall et al. (1988). The initial aerosol mass concentration distribution is calculated assuming thermodynamic equilibrium between the gas and aerosol phases for the sulfate, nitrate, chloride, sodium, ammonium, water system (Pilinis and Seinfeld, 1987).

3.2.5 Effects of Fogs on Aerosol Concentration

At the beginning of the simulation, the air parcel contains 26.4 μg m^{-3} dry aerosol particles consisting mainly of NH_4NO_3 (12.1 μg m^{-3}), Na_2SO_4 (5.9 μg m^{-3}) $NaNO_3$ (4.7 μg m^{-3}), and smaller quantities of NH_4Cl, NaCl and $(NH_4)_2SO_4$. As the relative humidity increases, the salts deliquesce, and as the liquid water increases, more and more material is transferred to the aerosol phase. When the relative humidity reaches 95%, the aerosol nitrate has increased from 12.8 to 13.5 μg m^{-3}, the aerosol ammonium from 3.6 to 5.5 μg m^{-3}, and the chloride from 2.3 to 5.8 μg m^{-3}. At this moment, the aerosol phase contains around 450 μg m^{-3} water. Twenty minutes later, the humidity exceeds 100% and the fog episode begins. At $t = 23$ min, the system supersaturation reaches its maximum value of 0.06% and starts decreasing slowly following the familiar pattern (Pandis et al., 1990).

Deposition and aqueous-phase chemistry have opposite effects on the aerosol mass, with the net effect of fogs on the total and individual species aerosol concentrations. These concentrations depend on several factors that will be discussed next. For the case

discussed here, the total concentrations of the major ionic species in the aerosol and aqueous phase are presented in Figure 3.2.1, for the period for which the relative humidity exceeds 95%. The reader is reminded that in Figure 3.2.1 a particle is described as a droplet at a certain moment, when either the supersaturation of the environment exceeds its critical supersaturation or its diameter exceeds its critical diameter. Because of the finite number of size sections used in the simulation, a discontinuity is created in the calculation of the aerosol mass every time the particles in a section are activated or deactivated and are transformed from aerosol particles to liquid particles or vice versa. These discontinuities appear as jumps in Figure 3.2.1 and in several of the following figures. The fog episode causes an increase of the sulfate aerosol concentration from 4.1 μg m^{-3} to 8.4 μg m^{-3}, but causes a decrease in the concentration of aerosol nitrate from 13.5 μg m^{-3} to 8.5 μg m^{-3}, of aerosol ammonium from 5.5 to 3.9 μg m^{-3}, and of aerosol chloride from 5.8 to 3.8 μg m^{-3}.

The increase in the sulfate concentration is mainly a result of the aqueous-phase production of S(VI) through oxidation of S(IV) by H_2O_2. During this fog episode, 6.8 μg m^{-3} of sulfate are produced while 2.5 μg m^{-3} are deposited to the ground. This increase in sulfate is in qualitative agreement with observations by Cass and Shair (1984) of high aerosol sulfate concentrations in the Los Angeles basin after fog episodes. The above conclusion should not necessarily be generalized, because fogs can easily lead to reduction of the aerosol sulfate. Even in the specific fog episode considered here, if the fog duration is prolonged from 2 h to 10 h, one observes that as the available H_2O_2 is depleted and the fog pH becomes lower than 5, the sulfate production rate decreases significantly while the deposition rate continues at the same level for the full 10 h. Therefore, after the fog dissipates, one actually finds a reduction of the sulfate levels below those present in the prefog aerosol. Such a scenario has been considered by Pandis and Seinfeld (1989b) who predicted a reduction of the aerosol sulfate concentration for the radiation fog episode that they studied.

Previous sensitivity studies have shown that there are no major pathways for the aqueous-phase production of nitrate, and no chemical pathways for the production of

FIGURE 3.2.1(a). Sulfate mass balances for the main ionic species for a simulated radiation fog episode.

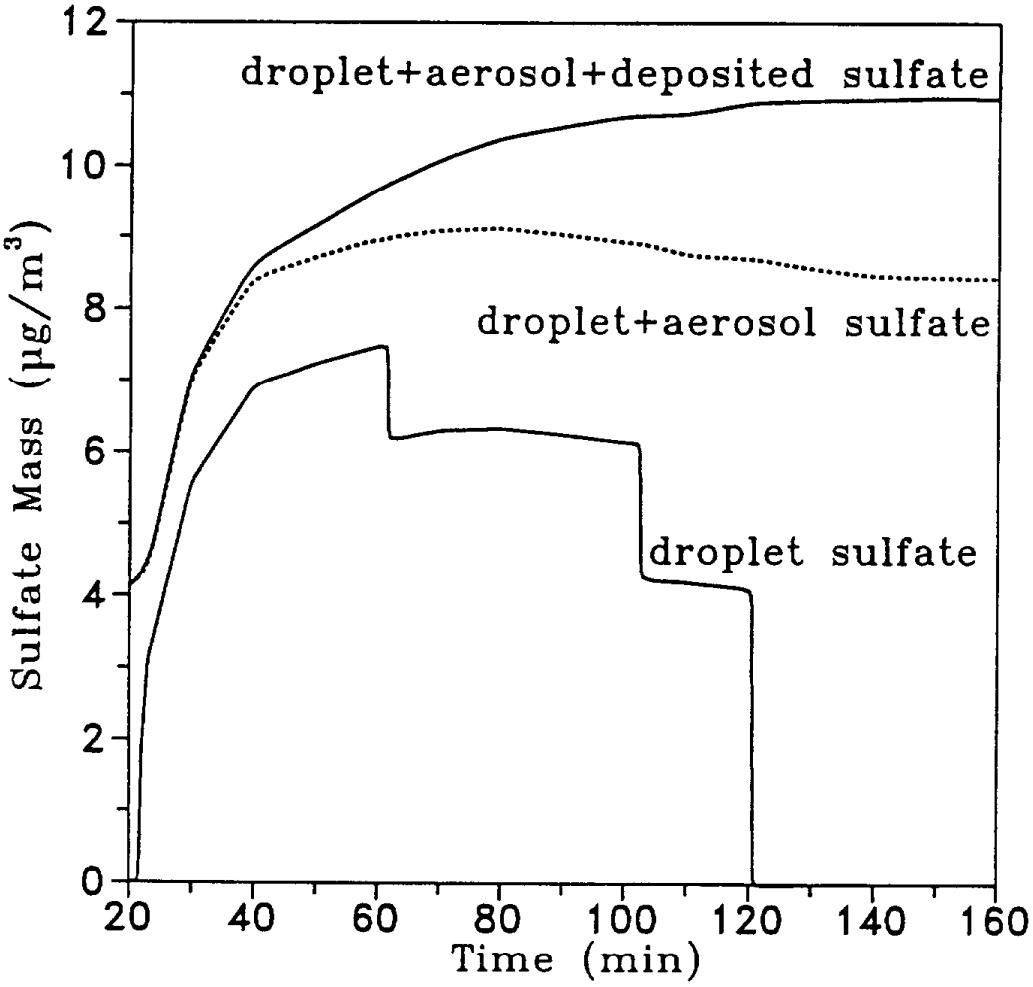

FIGURE 3.2.1(b). Ammonium (the gaseous NH_3 is not included) mass balances for the main ionic species for a simulated radiation fog episode.

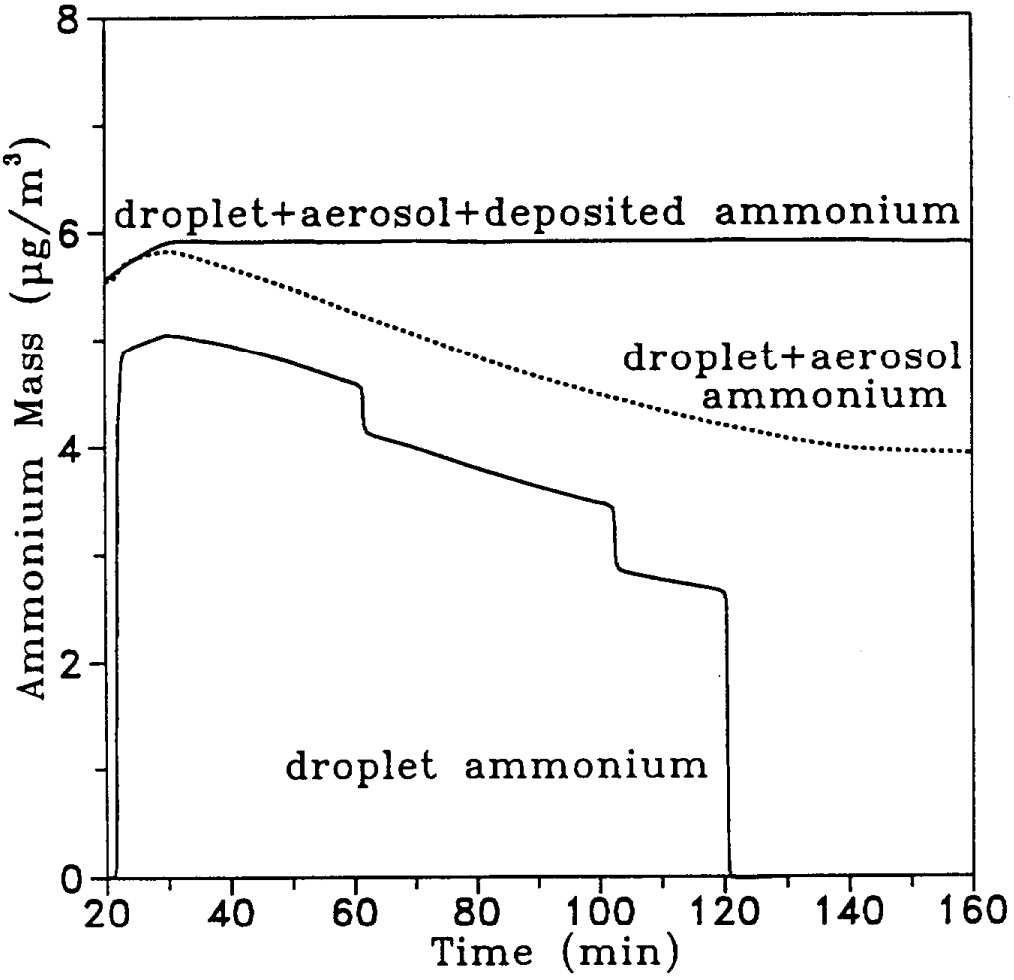

FIGURE 3.2.1(c). Nitrate mass balances for the main ionic species or a simulated radiation fog episode.

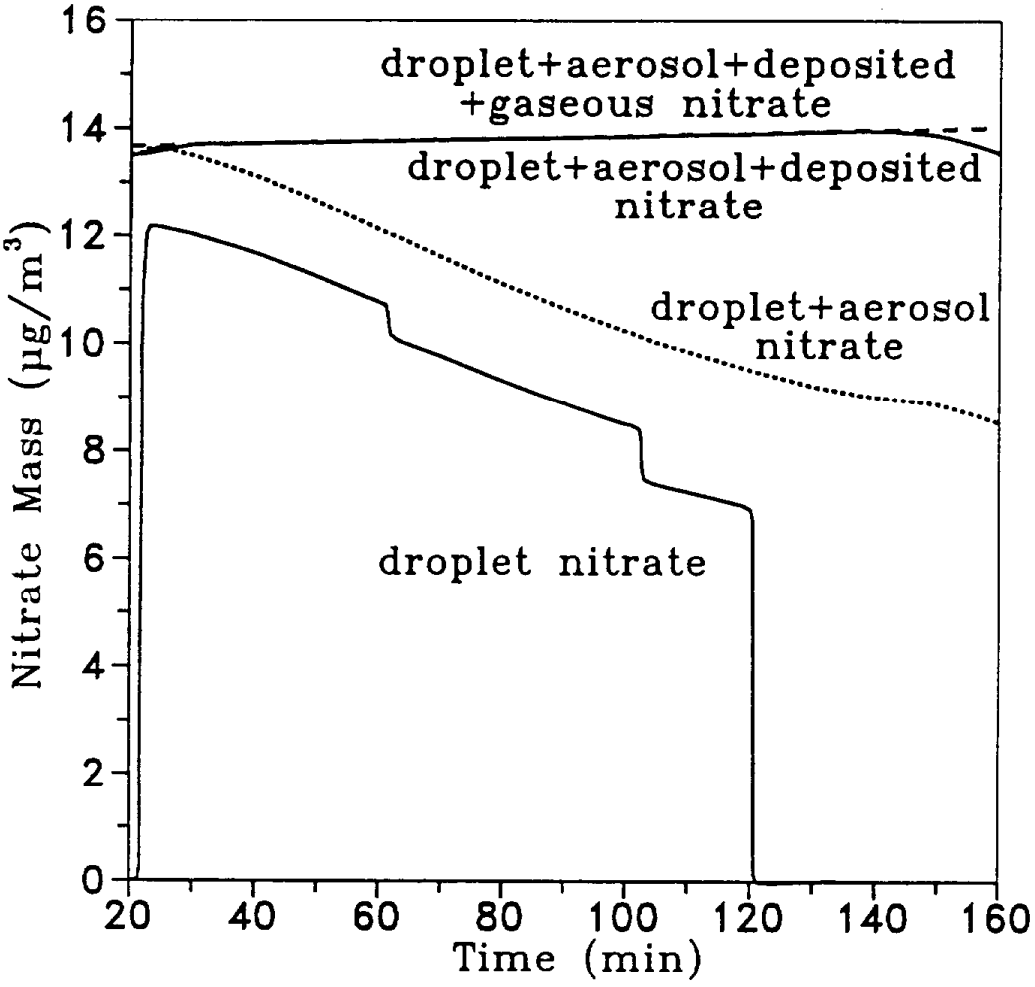

chloride or ammonium (Pandis and Seinfeld, 1989a). Therefore, the primary effect of fog is the reduction of the total concentrations of these species, gas plus aerosol, as a result of their removal to the ground. Existence of ammonia sources, or gas-phase production of nitric acid can reverse these effects, but this is independent of the fog occurrence.

After the fog has dissipated and the relative humidity has decreased back to 50%, the total aerosol mass has decreased from the initial 26.4 $\mu g\ m^{-3}$ to 19.7 $\mu g\ m^{-3}$. It consists of 7.8 $\mu g\ m^{-3}$ NH_4NO_3, 7.8 $\mu g\ m^{-3}$ Na_2SO_4 and 4.1 $\mu g\ m^{-3}$ $(NH_4)_2SO_4$. The mass of sulfate has increased by 95%, but the masses of aerosol ammonium, nitrate, sodium, and chloride have been reduced by 24%, 53%, 30%, and 100%, respectively.

The decrease of the total aerosol mass can be explained from the domination of the chemical production of the main ionic species. On the other hand, the decrease in the concentrations of all the aerosol species, except sulfate, is also due to the increase of the sulfate in the aerosol phase, sulfate that replaces volatile nitrate and chloride (Pilinis, 1989).

3.2.6 Effects of Fogs on Aerosol Size/Composition Distribution

Fogs cause changes in the aerosol concentration levels which are not uniform over the aerosol size distribution. During the smog-fog-smog cycle, the large aerosol particles are transformed to large fog droplets and then back to aerosol particles. Because of the greater deposition of larger fog droplets, the depositional losses of aerosol particles are mainly concentrated in the large size section of the aerosol distribution. On the other hand, most of the material that is produced by aqueous-phase reactions favors the droplet size that has access to most of the liquid water (Pandis and Seinfeld, 1990). The aerosol particles on which most of the liquid water condenses are determined by the aerosol distribution and by the cooling rate of the air parcel. Rapid cooling favors the small particles, while slow cooling favors the larger, transport limited particles (Pandis and Seinfeld, 1990).

In the case examined here, most of the fog liquid water content is predicted to

have condensed on the larger particles (Figure 3.2.2); therefore, both the positive and negative effects of the fog are concentrated in this size range. The bimodal distribution of the droplets at $t = 40$ min and $t = 120$ min is due to the initial aerosol size spectrum being bimodal. The dry aerosol distributions before and after the fog are presented in Figure 3.2.3. Most of the losses in mass are concentrated in the larger particle range, where the losses in mass of the >0.9 μm particles in diameter are around 50%. At the same time, most of the sulfate that is produced during the fog is also found in the larger particles. The sulfate content of the particles larger than 0.5 μm increases by 130%, while for the particles smaller than 0.5 μm, it increases by only 45%.

3.2.7 Aerosol Scavenging Efficiency

The aerosol scavenging efficiency of the fog determines the extent to which the fog droplet concentrations are influenced by the preexisting aerosol. This scavenging efficiency depends on the maximum supersaturation reached in the fog and on the preexisting aerosol size composition distribution.

Ten Brink et al. (1987) observed nearly complete scavenging of aerosol sulfate in clouds. Munger et al. (1990) reported aerosol scavenging ratios always lower than 100%, and depending on the method used, ratios ranged from 10% to 90%. In a theoretical study of wet removal of atmospheric pollutants, Jensen and Charlson (1984) calculated an average urban aerosol population nucleation scavenging efficiency is close to unity for convective clouds, but for stratiform clouds it decreases rapidly as the updraft velocity is lowered. Flossmann et al. (1985, 1987) reported calculated aerosol scavenging efficiencies equal to or larger than 90% in typical cloud environments.

The scavenging efficiencies for the fog episode under consideration are depicted in Figure 3.2.1. At $t = 20$ min, the relative humidity reaches 100%, and at $t = 23$ min a maximum supersaturation of 0.06% is reached. Even at this relatively low supersaturation, most of the aerosol mass gets activated and is dissolved in the fog droplets; namely, 70% of the sulfate, 80% of the nitrate and 85% of the ammonium. At the moment of maximum liquid water content ($t = 60$ min), the interstitial aerosol

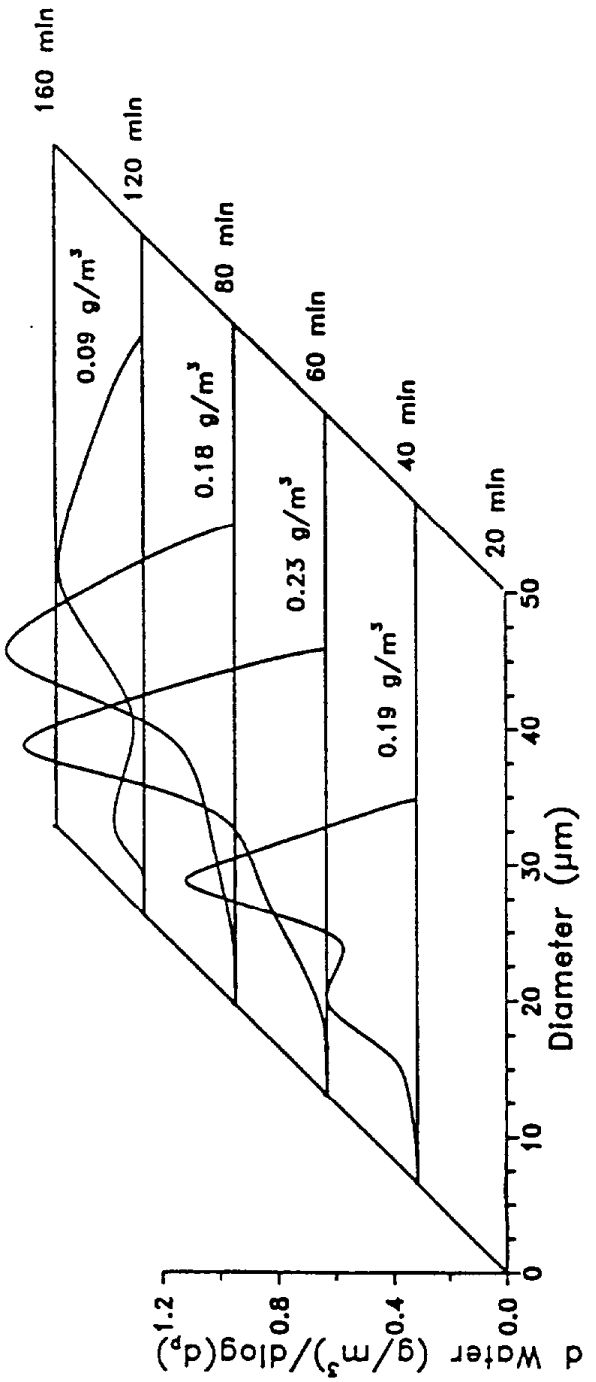

FIGURE 3.2.2. Evolution of the smoothed aqueous droplet mass distribution during the fog episode.

FIGURE 3.2.3(a). Comparison of the smoothed aerosol size/composition distributions at 50% relative humidity before the fog episode.

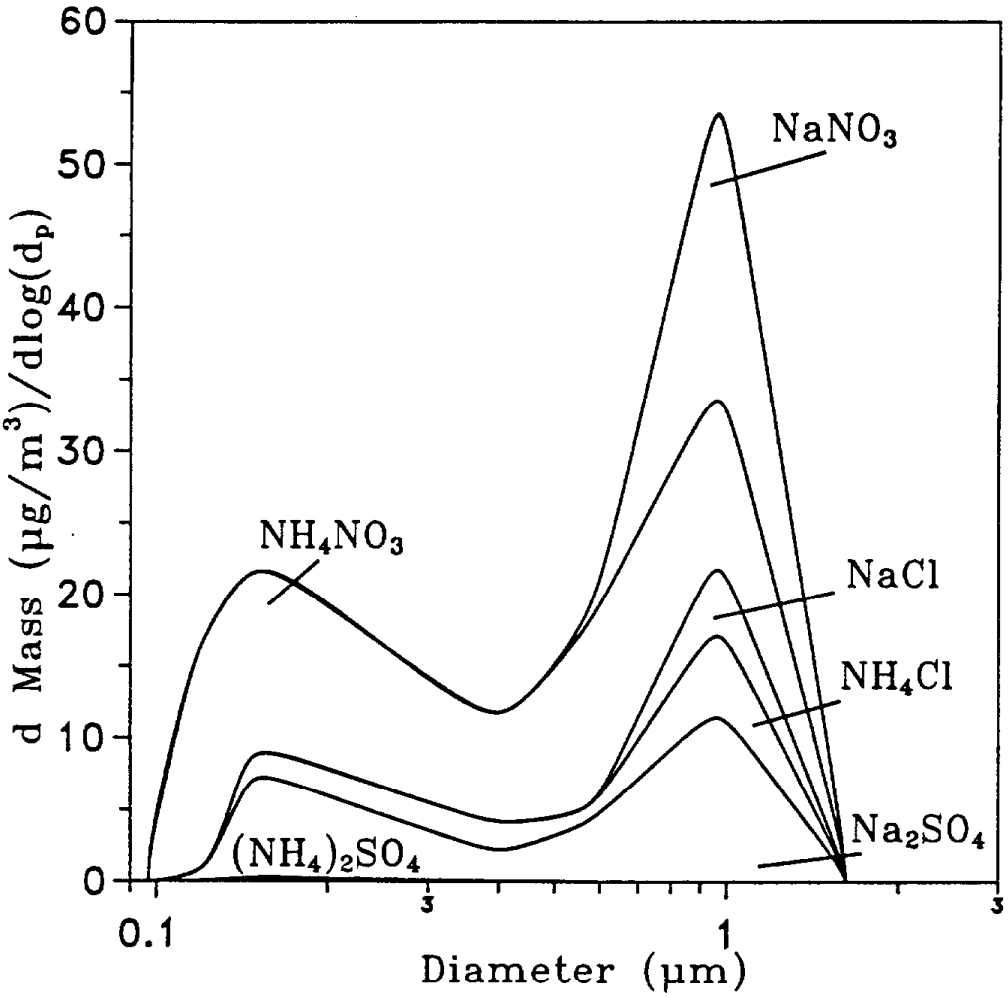

FIGURE 3.2.3(b). Comparison of the smoothed aerosol size/composition distributions at 50% relative humidity after the fog episode.

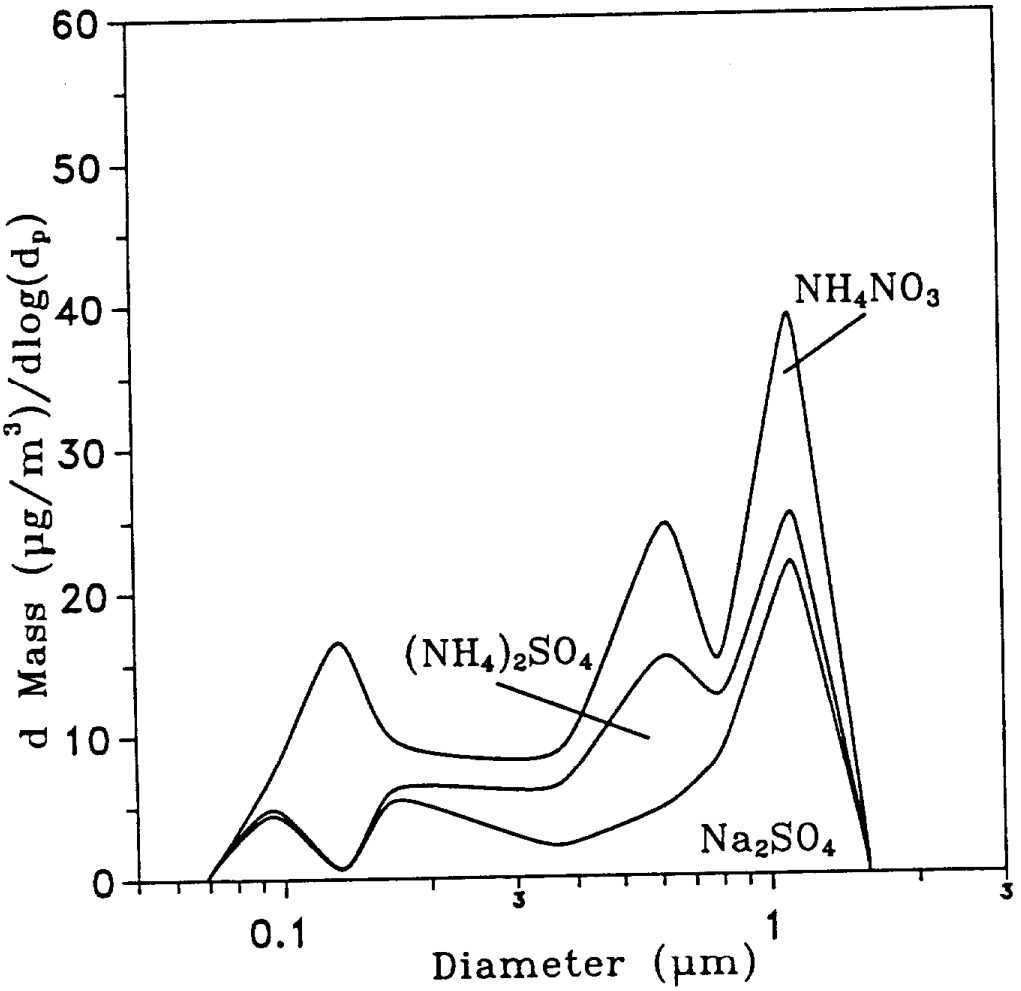

represents 16% of the sulfate, 11% of the nitrate and 12% of the ammonium. These interstitial aerosol concentrations will be even lower if one considers the coagulation of the aerosol particles with the fog droplets: a process that has been neglected in this study.

During the fog dissipation stage, the small droplets evaporate first, followed by the larger droplets, with the concentration of interstitial aerosol increasing significantly. For example, at $t = 120$ min the interstitial aerosol represents 53% of the total sulfate concentration, 27% of the total nitrate concentration and 37% of the total ammonium, with these percentages reaching 100% five minutes later.

The above results can be used to improve the assumptions used in fog models like the one developed by Pandis and Seinfeld (1989b). In that model, explicit droplet microphysics is not considered and the initial fogwater concentrations are calculated by assuming that all the preexisting aerosol is scavenged by the fog droplets. The evaluation of that model showed overprediction of the sulfate and ammonium concentrations for the first few hours of the fog episode. When no additional information is available, it seems preferable to assume in such models an 80% scavenging efficiency for the main ionic species instead of 100%, at least for polluted urban conditions.

3.2.8 Sampling a Polydisperse Fog Droplet Population

Pandis et al. (1990) suggested that significant solute concentration differences can occur in aqueous droplets inside a cloud or a fog. The same qualitative behavior is observed in this study (Figure 3.2.4 [a]) even if a different initial aerosol size distribution has been used compared to that used by Pandis et al. (1990). At the moment of maximum liquid water content ($t = 60$ min), the total solute concentration in the 25 μm diameter droplets is 2.5 times larger than that in the 15 μm droplets.

If one samples this fog droplet population with one of the routinely used fog samplers (Jacob et al., 1984, 1985; Waldman, 1986), one collects most particles larger than the instrument cutoff size, mixes them and then reports an average concentration. If the droplet concentrations differ considerably, then the measured concentration may

FIGURE 3.2.4(a). Total solute concentration for particles (aerosol and droplets) of different sizes during the fog growth period.

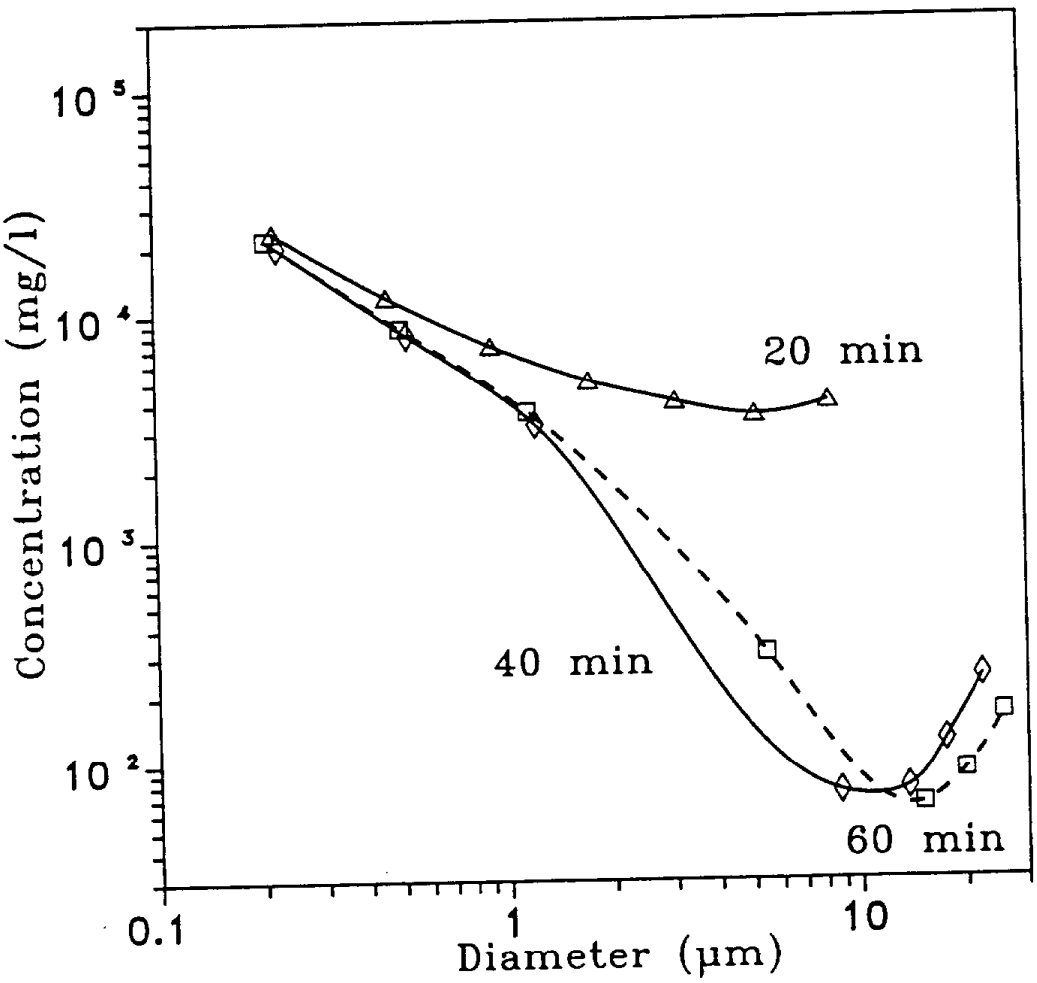

FIGURE 3.2.4(b). Total solute concentration for particles (aerosol and droplets) of different sizes during the fog dissipation period.

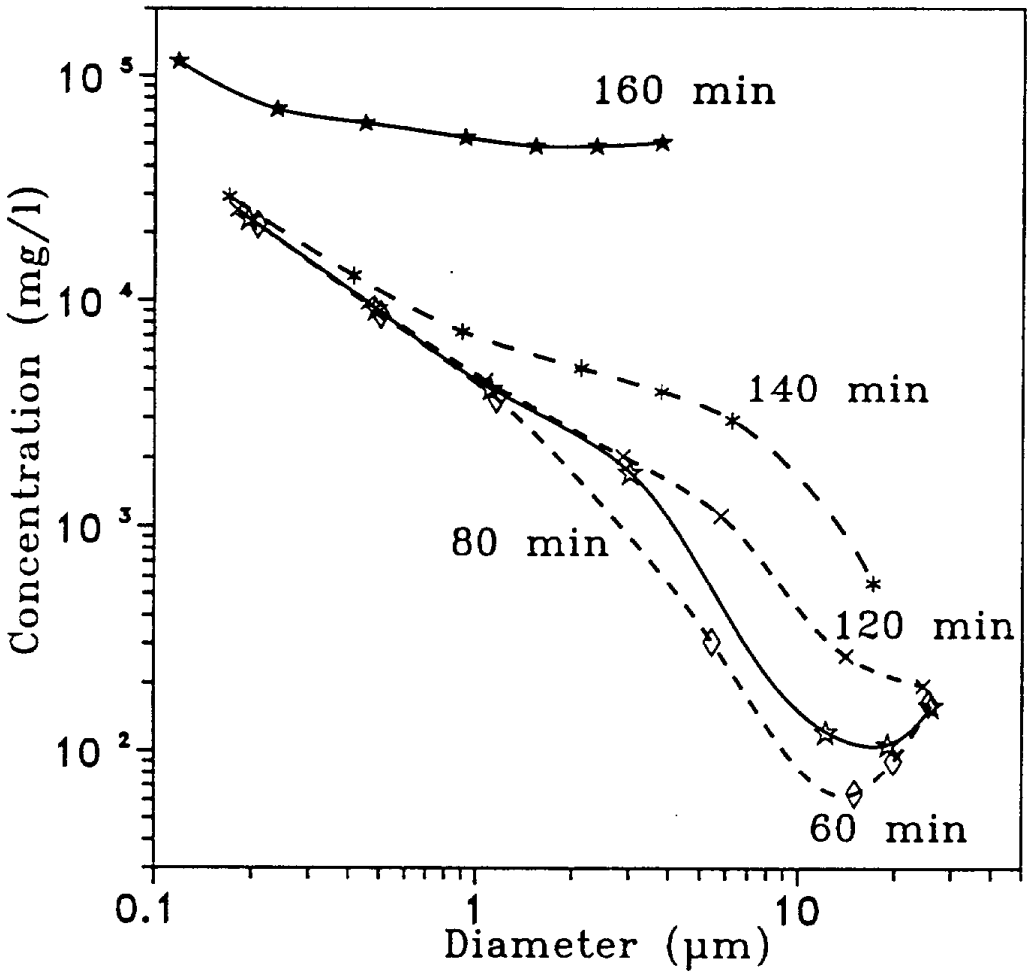

not be completely representative of the actual fogwater concentration. To investigate this, we assume that three fog samplers were used to sample the fog episode studied here. Each sampler was able to sample all droplets larger than their nominal cutoff size, 15 μm diameter for the first, 5 μm for the second, and the third sampler had zero cutoff and, therefore, was able to sample every droplet particle. The concentrations measured by these three idealized samplers were divided by the concentration of the larger droplet section to give the concentration ratio.

We have chosen the concentration of the larger droplet section as the fogwater reference composition because most of the fog liquid water content has condensed on these droplets (55% at the fog peak) and because these droplets are responsible for most of the wet deposition. This choice is not unique, but for any choice of the most representative concentration, the concentration ratio calculations are indicative of the possible complications in fog sampling. The concentration ratios for sulfate and ammonium are shown in Figure 3.2.5 [a] and 3.2.5 [b]. The discontinuities in the curves for the 5 and 15 μm samplers are also due to the finite number of sections used in this model application.

For this specific fog episode the 15 μm cutoff sampler collects droplets from the sixth and seventh sections. This sampler collects droplets only between $t = 25$ and $t = 142$ min and the concentration ratios cannot be defined outside this period. The largest deviation appears when the droplets of the sixth section start evaporating and the measured concentration is 20% higher than the representative sulfate concentration. The sulfate concentration measured is always close to the concentration of the largest droplets. Use of a finer resolution drop size spectrum would make this difference more pronounced. The sampler with the 5 μm cutoff in the growth period of the fog collects droplets from the 4th, 5th, 6th and 7th droplet sections and the measured average concentration is lower than the representative concentration, as the smaller droplets are less concentrated than the larger ones (Figure 3.2.4 [b]). During the dissipation stage, the smaller droplets evaporate first and their concentration becomes higher than that of the larger droplets. The sampler measures concentrations that are as much as

FIGURE 3.2.5(a). Concentration ratios (concentration measured by the samples over the concentration of the larger droplet section) for three idealized fog samplers for sulfate.

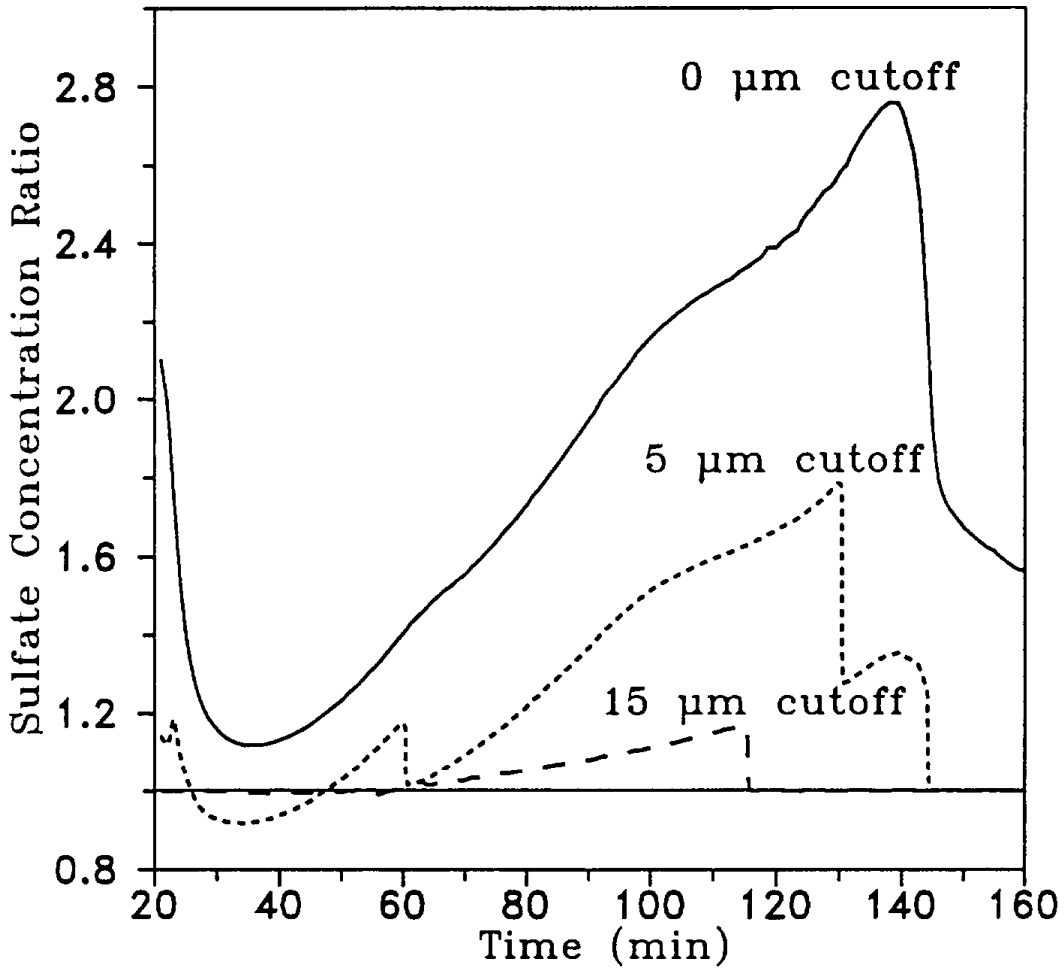

FIGURE 3.2.5(b). Concentration ratios (concentration measured by the samples over the concentration of the larger droplet section) for three idealized fog samplers for ammonium.

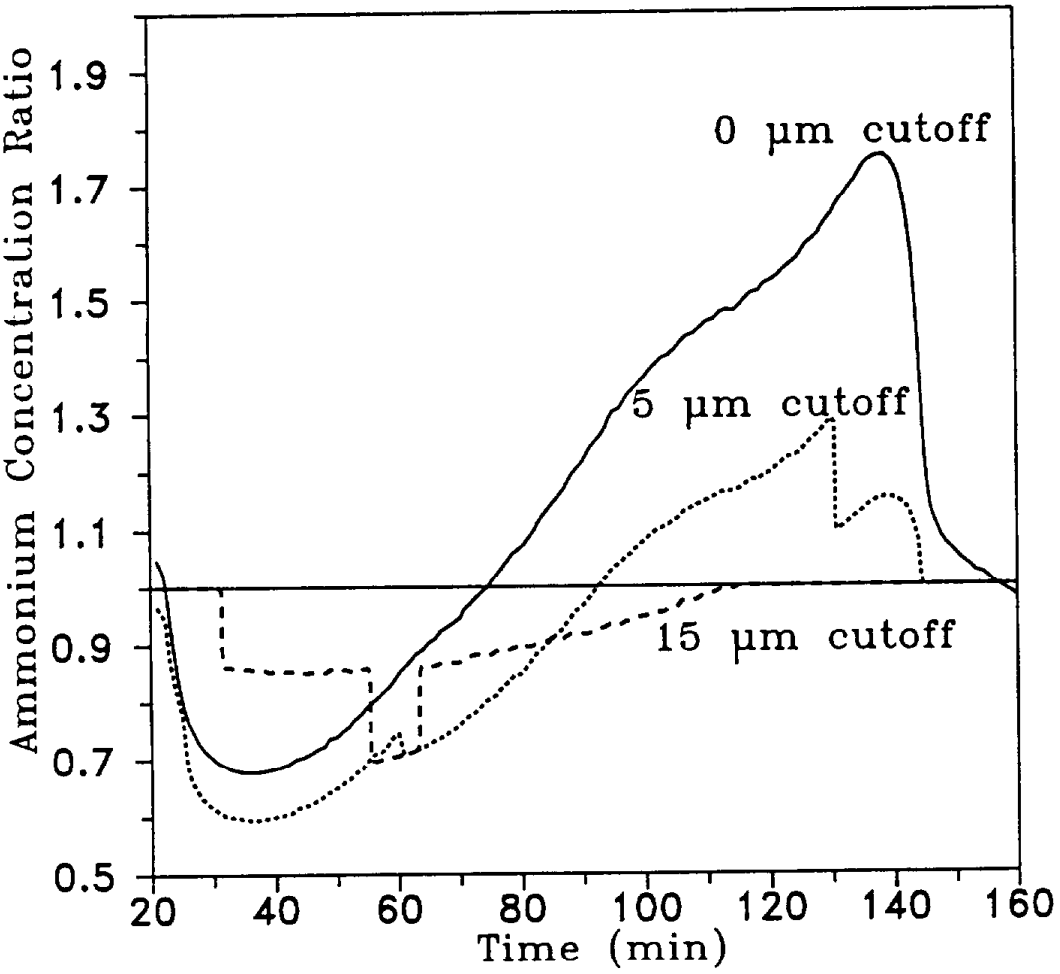

80% higher than the representative sulfate concentration. The total sampler collects all droplets and particles measuring average sulfate concentrations as much as a factor of 2.8 higher than the representative concentration.

The concentration ratio for ammonium (Figure 3.2.5 [b]) and the other major ionic species exhibit the same qualitative behavior as that for sulfate but with significantly lower values. The measured concentrations during the growth period can be as much as 40% lower than the representative ammonium concentration, and during the dissipation period as much as 80% higher. The lower values for the ammonium deposition ratio compared to sulfate are mainly due to the distribution of these species in the aerosol phase just before the onset of the fog. There is relatively more sulfate in the smaller droplets than ammonium, resulting in relatively low concentrations of sulfate in the larger droplets. For example at $t = 30$ min, the sulfate concentration is 560 μM for the 18.5 μm droplets and 450 μM for the 7.3 μm droplets (a ratio of 1:2). At the same time, the corresponding ammonium concentrations are 4060 μM and 890 μM (a ratio of 4:6). Therefore, during the growth period, the representative ammonium concentration is much higher than the concentration of the other droplets, resulting in concentration ratio values much lower than unity.

Generalization of the above results depends on the aerosol size/composition distribution before the fog episode as well as on the rates of temperature change in the fog. One conclusion is that sampling and mixing of fog droplets with different sizes can result in measured concentrations that are not completely representative of the actual fog composition. Furthermore, the measured concentrations can be very sensitive to the collection characteristics of the fog sampler. The choice of each representative aqueous-phase concentration is difficult and should depend on the goals of the study. If one is concerned about fogwater composition, one should chose the most representative concentration of the droplets; i.e., those that carry most of the liquid water. If one is concerned about acid deposition, one should concentrate on the droplets that are responsible for most of the deposited material. These are usually the larger droplets. If the representative concentration is in the small droplets, the measurement will usually

be higher than the actual value during the fog growth and lower during the fog dissipation. The opposite is true if the representative concentration is that of the larger droplets.

3.2.9 Fogs and Deposition

The depositional flux of species i, F_d^i (g m^{-2}) is usually expressed as

$$F_d^i = v_d^i c^i \tag{4}$$

where v_d^i (m s^{-1}) is the deposition velocity of species i and c_i (gm^{-3}), its ambient concentration. If the species i exists in all three phases (gas, aerosol and aqueous), then one can define three deposition velocities and get

$$F_d^i = v_{d,gas}^i c_g^i + v_{d,aer}^i c_{aer}^i + v_{d,aq}^i c_{aq}^i \tag{5}$$

or, define one deposition velocity for the condensed phases, $v_{d,cond}^i$ and express the depositional flux as

$$F_d^i = v_{d,gas}^i c_g^i + v_{d,cond}^i \left(c_{aer}^i + c_{aq}^i\right) \tag{6}$$

The size of the interstitial aerosol particles in a typical radiation fog is usually in the 0.1 to 1 μm diameter size range. For these particles, neither Brownian diffusion, nor gravitational settling, nor inertial impaction are efficient removal mechanisms (Seinfeld, 1986) and as the mass carried by these particles is small, one can, to a first order approximation, neglect the aerosol deposition flux inside a fog.

After this approximation, the expression (5) becomes quite simple, but has the major disadvantage that the value of the deposition velocity depends on what one considers as aqueous phase. The application of the expression (6) requires measurement of the total concentration of species i in the condensed phases, but fortunately is independent of what one defines as aerosol or droplet phase. The effect of the definition

of deposition velocity for sulfate is presented in Figure 3.2.6. Depending on the droplet size fraction sampled, quite a range of deposition velocities is calculated. The higher the cutoff size, the higher the calculated deposition velocity. These differences increase during the early and late stages of fog life. For example at $t = 25$, $t = 65$, and $t = 145$ min, the deposition velocity calculated with a cutoff size of 15 μm is, respectively, 170%, 30%, and 140% larger than the velocity calculated using a cutoff size of 5 μm. These results suggest that the best way of calculating deposition velocities is by using the sum of the species concentrations in the aerosol and droplet phases. If one uses the concentration in droplets larger than a certain size, then the deposition velocities can be very sensitive to the choice of this cutoff size.

3.2.10 Calculation of Liquid Water Deposition in Fog Models

In fog models where there is no explicit treatment of the microphysics, the gravitational flux of liquid water G (g m^{-2} s^{-1}) is expressed as a function of the liquid water content, w (g m^{-3}). Brown and Roach (1976) used

$$G = 0.078w^2 \tag{7}$$

for a 10 °C temperature, while Forkel et al. (1984) proposed the expression

$$G = 0.032w^{1.6} \tag{8}$$

and Pandis and Seinfeld (1989b) used

$$G = 0.120w^2 \tag{9}$$

and found that their model overpredicted the depositional fluxes of the major ionic species for the high liquid water values and underpredicted these fluxes during the fog dissipation stage.

The water deposition rates predicted by the model here have been plotted versus the fog liquid water content in Figure 3.2.7. These data suggest something that has

FIGURE 3.2.6. Calculated values of the sulfate deposition velocity for alternative definitions
a) deposition velocity of the condensed phase V_d, cond.,
b) deposition velocity of the aqueous - phase V_{aq}. Sampling cutoff 5μm,
c) deposition velocity of the aqueous - phase V_{aq}. Sampling cutoff 15μm.

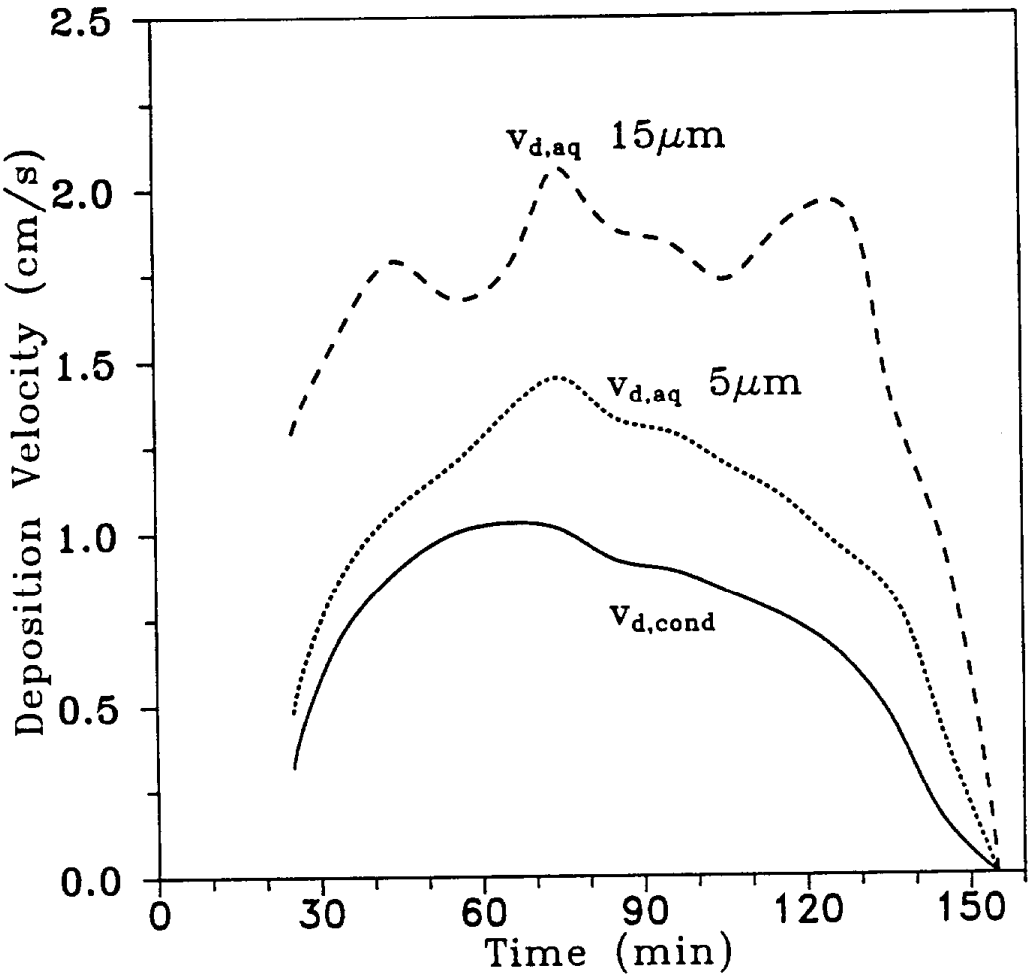

not been considered in the previous studies: different deposition rates correspond to the same liquid water content value depending on whether the fog is in a growth or dissipation period. This behavior is due to the fact that the smaller droplets can easily follow the changes of the relative humidity, so that during the fog growth period small droplets have access to considerable amounts of the liquid water, resulting in relatively slower deposition rates. On the contrary, during fog evaporation, the small droplets are the first to evaporate and most of the liquid water is left on the larger droplets, resulting in faster deposition.

Figure 3.2.7 suggests that two different expressions should be used for the growth and the dissipation period. The modeling results for this specific episode suggest

$$G = 0.027w^{1.67} \tag{10}$$

for the growth period and,

$$G = 0.018w^{1.08} \tag{11}$$

for the dissipation period.

For the period of almost constant liquid water content, the deposition rate appears to increase from the value suggested by equation 10 to the value corresponding to equation 11. Comparison of the expressions used in previous studies with the present results suggests that, at least for this fog episode, expressions 7 to 9 overpredict deposition for the growth and the constant liquid water period and underpredict deposition for the dissipation period. Equations 10 and 11 were derived using an urban radiation fog episode and a relatively crude resolution of the particle size distribution; therefore, their application, as well as the application of equations 7 to 9 to other fog episodes, should be conducted with caution.

3.2.11 Deposition Velocity of Major Ionic Species

Field measurements have indicated that fog deposition velocities of different ionic species can be quite different (Waldman, 1986). One of the possible explanations for this

FIGURE 3.2.7. Water deposition rates versus fog liquid water content.

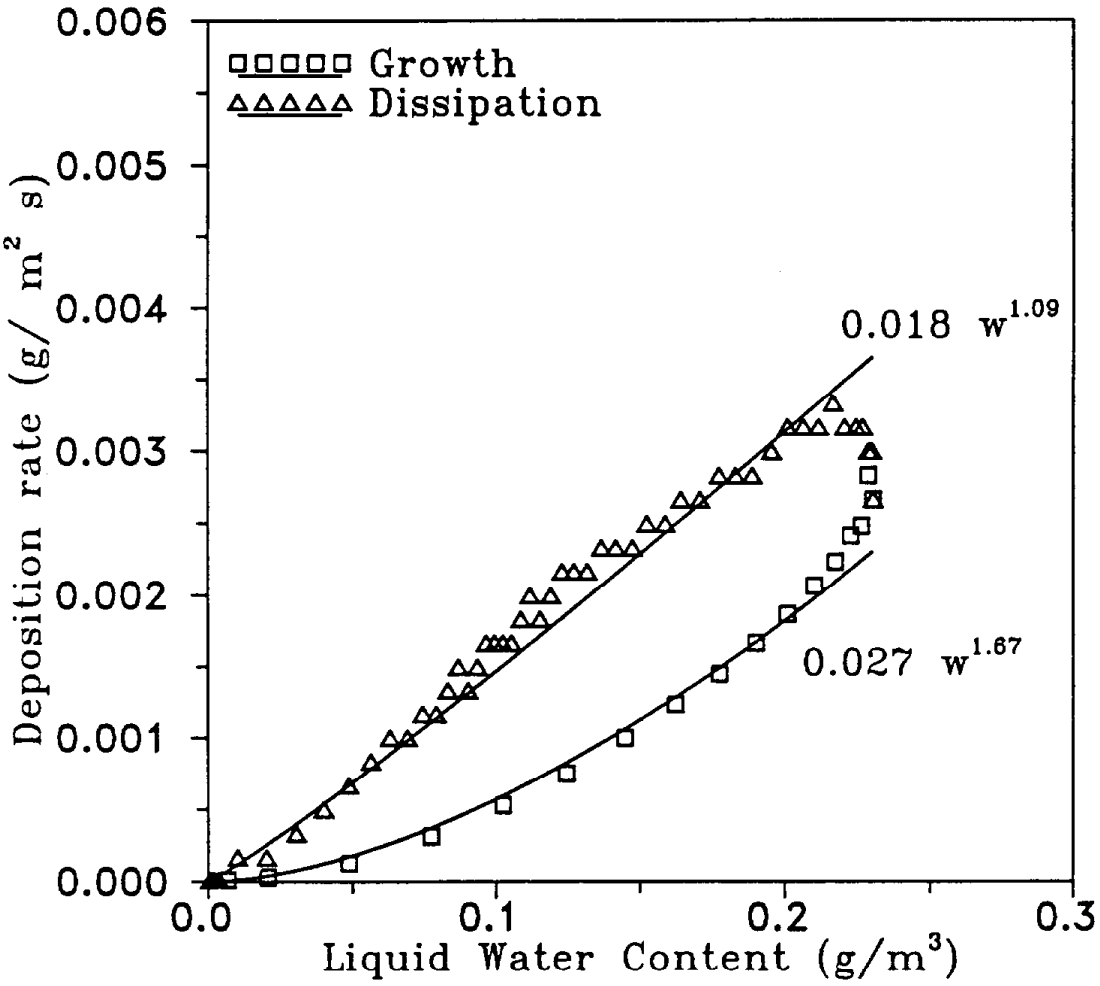

phenomenon is the manner in which solute mass is distributed within the fog droplet spectrum. To investigate this, we calculated the condensed phase deposition velocities for the major ionic species and water (Figure 3.2.8). The deposition velocities of all species exhibit the same qualitative behavior, but have, in certain periods, significantly different absolute values.

To explain these differences one can define the species average diameter, $\overline{D}_i$, for a sectional particle distribution as

$$\overline{D}_i = \left(\frac{\sum_j m_{ij} d_j^2}{\sum_j m_{ij}}\right)^{\frac{1}{2}} \tag{12}$$

where m_{ij} is the mass concentration per volume of air of species i in the j particle size section and d_j is the diameter of this section. If, in a homogeneous fog, the only deposition mechanism is a fog droplet, gravitational settling and all particles have the same density. One can show that the deposition velocity of species i is given by

$$v_i = C\overline{D}_i^2 \tag{13}$$

where C is a constant depending on the particle density and temperature. Because all these variables are practically constant during the fog episode, C remains constant throughout the simulation and the deposition velocities of all species can be represented by the same curve (Figure 3.2.9). Therefore, the difference of the species deposition velocities (Figure 3.2.8) can be quantitatively explained by calculating the average diameter of each species as a function of time.

At the beginning of the fog episode, a considerable fraction of the aerosol sulfate exists on the small particles resulting in a small initial sulfate average diameter and in a relatively small deposition velocity. Even if most of the sulfate production takes place in the large droplets, sulfate has the smallest average diameter among the major ionic species, therefore, the smallest deposition velocity. On the contrary, in this fog episode, most of the nitrate is found in the large particles and the maximum deposition velocity of nitrate is almost 50% larger than the corresponding sulfate deposition velocity. The

FIGURE 3.2.8. Condensed phase deposition velocities for major species in fogwater. (Deposition Velocity) = (Deposition Flux)/[(aerosol concentration) + (droplet concentration)].

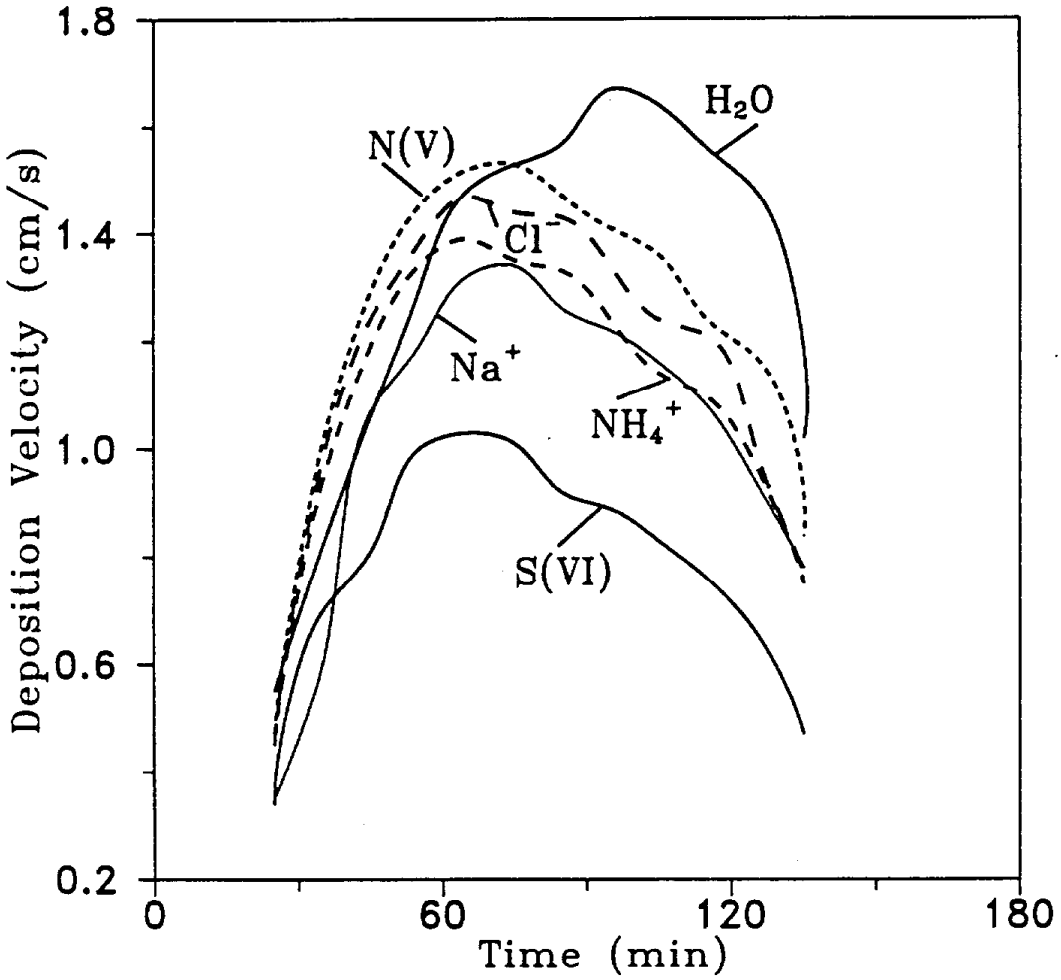

FIGURE 3.2.9. Calculated deposition velocity of selected species in fog as a function of their average diameter.

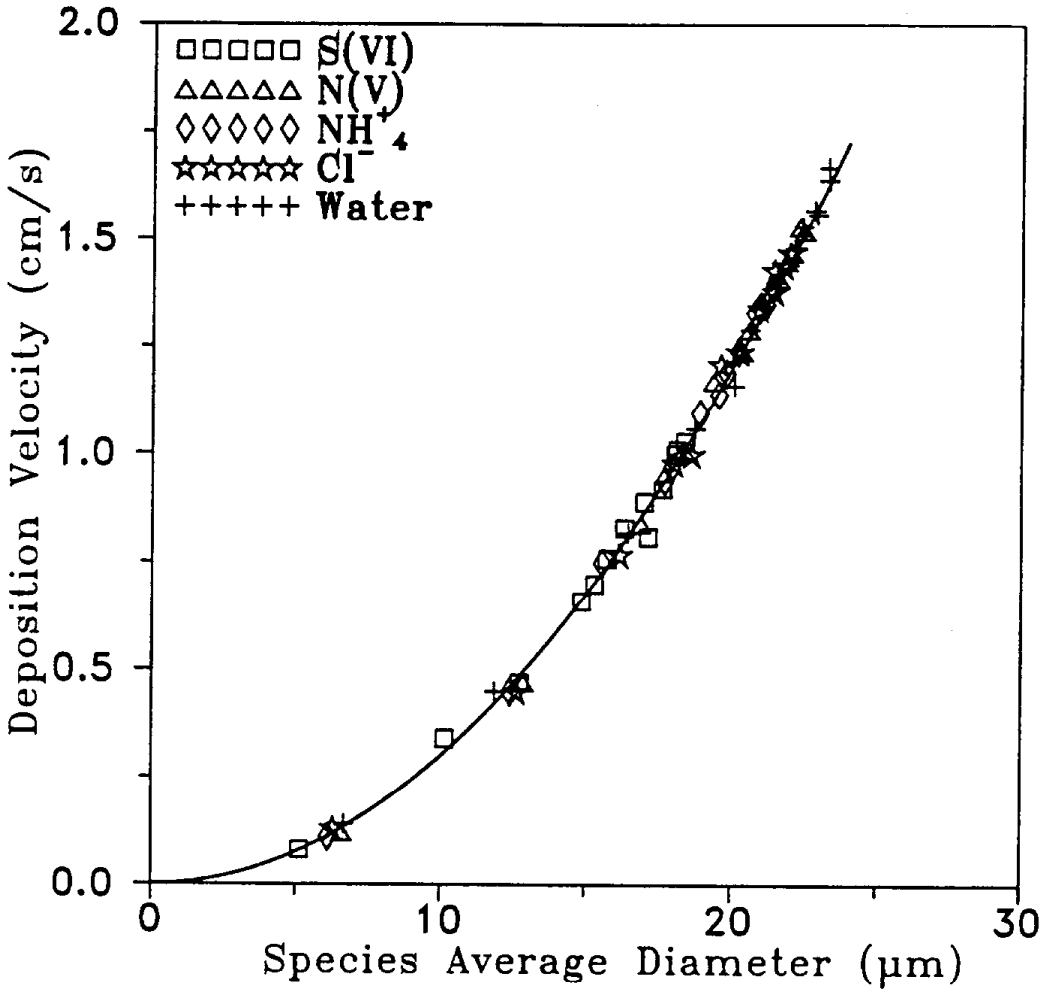

water deposition velocity reaches its maximum 30 minutes later than the major ionic species during the fog dissipation stage. Even if the total fog liquid water decreases, the losses are located in the small droplet size range and the average water diameter increases for the first 30 minutes of the fog dissipation stage.

3.3 SHOULD BULK CLOUDWATER OR FOGWATER SAMPLES OBEY HENRY'S LAW ?

3.3.1 Introduction

Henry's Law is routinely used to describe the partition of species between gas and aqueous phases in the atmosphere (Schwartz, 1986; Seinfeld, 1986) and has been employed in calculations in various studies of aqueous-phase chemistry (Richards et al., 1983; Hoffmann and Jacob, 1984; Kelly et al., 1985; Munger et al., 1990). In the majority of the atmospheric studies where both the gas-and the bulk aqueous-phase concentrations of a species have been measured, significant deviations from Henry's Law have been observed for species like S(IV), NH_3 and HCOOH (Richards et al., 1983; Munger et al., 1983, 1986, 1990; Waldman, 1986; Winiwarter et al., 1988).

Several possible explanations can be proposed for the observed deviations, including the formation of adducts of S(IV) with formaldehyde, glyoxal, methylglyoxal, etc., and the concentration changes occurring during the long periods required for the acquisition of aqueous- and some gas-phase samples, etc. (for example, Munger et al. [1984, 198])) explained part of the apparent excess of S(IV) in the aqueous phase compared to the predictions of Henry's Law by the formation of the hydroxymethanesulfonate ion (HMSA), the HSO_3^- adduct of HCHO. Their measurements and calculations, as well as the calculations of Richards et al. (1983), indicated however, that HMSA formation could account for only a part of the observed S(IV) concentration excess. An additional explanation of the observed behavior is presented in this work, based solely on our fundamental knowledge of the system, that together with the above phenomena (or similar processes) could completely explain the observed deviations.

Significant solute concentration differences can occur among droplets of different sizes inside clouds or fogs. Noone et al. (1988) sampled droplets from a marine stratus cloud and calculated that the volumetric mean solute concentration of the 9- to 18-μm droplets was a factor of 2.7 smaller than that in the 18- to 23-μm droplets. Munger et al. (1989) compared the ionic concentrations in two size-segregated fractions of cloudwater

and reported a large difference between the average composition of the smaller droplets and that of the larger droplets. Ogren et al. (1989) and Heintzenberg et al. (1989) reported that total solute concentration increases with droplet size by roughly a factor of 3 over the diameter ranges 10-18 μm and 8-22 μm. Pandis et al. (1990a, 1990b), using a model that included descriptions of aerosol and droplet microphysics, and gas- and aqueous-phase chemistry and deposition, found that during the development stage of a fog, the solute concentration in droplets larger than 10 μm diameter increased with size, with the 20 μm droplets being 3.6 times more concentrated than the 10 μm droplets. Hegg and Larson (1991) proposed that sulfate produced inside clouds was not uniformly distributed over the droplet spectrum.

The fact that the mixing of cloud or fog droplets of different compositions has implications associated with Henry's Law and the estimation of aqueous-phase reaction rates has been generally overlooked in most previous studies with the following two exceptions. Liljestrand (1985) proposed that averaging the nonconservative hydrogen ion concentration yields erroneously low mean pH values and presented algorithms for the determination of the average pH for a combination of samples. Purdue and Beck (1988) suggested that the mixing of droplets of different pH and acid-neutralizing capacity that occurs when bulk samples of cloud, fog, and rainwater are collected, yields solutions that are not in equilibrium with the atmosphere in which the droplets were originally equilibrated. Lack of a general theory and lack of knowledge of the magnitude of the composition differences in the droplet spectra has precluded the estimation of the mixing effect on the deviations from Henry's Law.

In this work, we prove that mixing of droplets with different pH, that are individually in Henry's Law equilibrium with the surrounding atmosphere, always results in a mixture that is supersaturated with weak acids like S(IV), HCOOH and bases like NH_3 with respect to the original atmosphere. After establishing the direction of this deviation from Henry's Law, a general method is developed for the estimation of the magnitude of this deviation under typical atmospheric conditions. The method is then applied to available experimental data in an effort to explain the observed dis-

crepancies from Henry's Law. The consequences of the findings of the present work to atmospheric water sampling and to the estimation of aqueous- and gas-phase reaction rates are discussed.

3.3.2 Bulk Cloudwater/Fogwater/Rainwater Samples and Henry's Law

Each droplet in a population of droplets (cloud, fog, or rain) is expected to be in Henry's Law equilibrium with the surrounding atmosphere. Let us assume that the droplet population consists of n droplet groups the ith of which has liquid water content w_L^i. All droplets in the same group have the same pH and the same acid neutralizing capacity (ANC) defined as the difference between the strong base cation concentrations and the strong acid anion concentrations. The chemical system that will be examined is similar to the one described by Pandis and Seinfeld (1989) in their model of atmospheric aqueous-phase chemistry, but our conclusions can be easily extended to any similar chemical system. Therefore:

$$\mathrm{ANC} = [\mathrm{Na^+}] + 3\,[\mathrm{Fe^{3+}}] + 2\,[\mathrm{Mn^{2+}}] + 2\,[\mathrm{Ca^{2+}}] - 2\,[\mathrm{SO_4^{2-}}] - [\mathrm{NO_3^-}] - [\mathrm{Cl^-}].$$

Assume that one samples the above droplet population and isolates the resulting liquid sample from the atmosphere. Let us begin our analysis by assuming that our sampler collects only the first two droplet groups and that the gas- and aqueous-phase concentrations of the species concerned remain practically constant during the sampling period. Hence, the first droplet group (liquid water content w_L^1, acid neutralizing capacity ANC_1, and hydrogen ion concentration $\mathrm{H^+}_1$) is mixed with the second droplet group (liquid water content w_L^2, acid neutralizing capacity ANC_2, and hydrogen ion concentration $\mathrm{H^+}_2$) to produce a mixture (liquid water content w_L^m, acid neutralizing capacity ANC_m, and hydrogen ion concentration $\mathrm{H^+}_m$). Both the initial droplet populations and the final mixture will satisfy the electroneutrality relation ($i = 1, 2, m$):

$$\mathrm{ANC}_i + [\mathrm{NH_4^+}]_i + [\mathrm{H^+}]_i = [\mathrm{OH^-}]_i + [\mathrm{HSO_3^-}]_i + 2[\mathrm{SO_3^{2-}}]_i + [\mathrm{NO_2^-}]_i + [\mathrm{HCOO^-}]_i$$
$$+[\mathrm{HCO_3^-}]_i + 2[\mathrm{CO_3^{2-}}]_i \qquad (1)$$

To avoid unnecessary complications due to the existence of the second dissociation products SO_3^{2-} and CO_3^{2-}, we initially restricted our analysis to acidic solutions (pH<6.5) where these species can be neglected in the electroneutrality equation.

No exhange between the liquid sample and the atmosphere is allowed; therefore, the liquid water content, the acid neutralizing capacity and the total concentrations of the weak acids and bases are conserved,

$$w_L^m = w_L^1 + w_L^2 \quad \text{or} \quad 1 = w_1 + w_2 \tag{2}$$

where $w_1 = w_L^1/w_L^m$ and $w_2 = w_L^2/w_L^m$ are the liquid water fractions of the droplet groups in the mixture. Also:

$$\begin{aligned}
\mathrm{ANC}_m &= w_1 \mathrm{ANC}_1 + w_2 \mathrm{ANC}_2 \\
[\mathrm{NH_3}]_m^T &= w_1 [\mathrm{NH_3}]_1^T + w_2 [\mathrm{NH_3}]_2^T \\
[\mathrm{S(IV)}]_m &= w_1 [\mathrm{S(IV)}]_1 + w_2 [\mathrm{S(IV)}]_2 \\
[\mathrm{HNO_2}]_m^T &= w_1 [\mathrm{HNO_2}]_1^T + w_2 [\mathrm{HNO_2}]_2^T \\
[\mathrm{HCOOH}]_m^T &= w_1 [\mathrm{HCOOH}]_1^T + w_2 [\mathrm{HCOOH}]_2^T \\
[\mathrm{CO_2}]_m^T &= w_1 [\mathrm{CO_2}]_1^T + w_2 [\mathrm{CO_2}]_2^T
\end{aligned} \tag{3}$$

with

$$\begin{aligned}
[\mathrm{NH_3}]_i^T &= [\mathrm{NH_3 \cdot H_2O}]_i + [\mathrm{NH_4^+}]_i \\
[\mathrm{S(IV)}]_i &= [\mathrm{SO_2 \cdot H_2O}]_i + [\mathrm{HSO_3^-}]_i \\
[\mathrm{HNO_2}]_i^T &= [\mathrm{HNO_2}]_i + [\mathrm{NO_2^-}]_i \\
[\mathrm{HCOOH}]_i^T &= [\mathrm{HCOOH}]_i + [\mathrm{HCOO^-}]_i \\
[\mathrm{CO_2}]_i^T &= [\mathrm{CO_2 \cdot H_2O}]_i + [\mathrm{HCO_3^-}]_i .
\end{aligned} \tag{4}$$

The second dissociation products, $[SO_3^{2-}]_i$ and $[CO_3^{2-}]_i$, have been neglected in the above definitions of $[S(IV)]_i$ and $[CO_2]_i^T$.

The two droplet groups satisfy Henry's Law and therefore for $i = 1, 2$ neglecting the second dissociation of $SO_2 \cdot H_2O$ and $CO_2 \cdot H_2O$,

$$
\begin{aligned}
[NH_3]_i^T &= H_{NH_3} G_{NH_3} (1 + K_{NH_3} H^+{}_i) \\
[S(IV)]_i &= H_{SO_2} G_{SO_2} (1 + \frac{K_{SO_2}}{H^+{}_i}) \\
[HNO_2]_i^T &= H_{HNO_2} G_{HNO_2} (1 + \frac{K_{HNO_2}}{H^+{}_i}) \\
[HCOOH]_i^T &= H_{HCOOH} G_{HCOOH} (1 + \frac{K_{HCOOH}}{H^+{}_i}) \\
[CO_2]_i^T &= H_{CO_2} G_{CO_2} (1 + \frac{K_{CO_2}}{H^+{}_i})
\end{aligned} \tag{5}
$$

with H_j the Henry's Law constant, G_j the gas-phase concentration and K_j the first dissociation constant ($j = HNO_2, HCOOH, CO_2$ and S(IV)). Also in the above equations, $K_{NH_3} = K_{NH_3 \cdot H_2O}/K_w$, where $K_{NH_3 \cdot H_2O}$ is the dissociation constant for $NH_3 \cdot H_2O$ and K_w, is the water dissociation constant.

Both the initial droplet populations and the final mixture satisfy ionization equilibria

$$
\begin{aligned}
[NH_4^+]_i &= \frac{K_{NH_3} H^+{}_i}{1 + K_{NH_3} H^+{}_i} [NH_3]_i^T \\
[HSO_3^-]_i &= \frac{K_{SO_2}}{K_{SO_2} + H^+{}_i} [S(IV)] \\
[NO_2^-]_i &= \frac{K_{HNO_2}}{K_{HNO_2} + H^+{}_i} [HNO_2]_i^T \\
[HCO_3^-]_i &= \frac{K_{CO_2}}{K_{CO_2} + H^+{}_i} [CO_2]_i^T \\
[HCOO^-]_i &= \frac{K_{HCOOH}}{K_{HCOOH} + H^+{}_i} [HCOOH]_i^T
\end{aligned} \tag{6}
$$

3.3.2.1 Henry's Law pH, pH_H

After the mixing, the bulk liquid sample is removed from contact with the atmosphere and its aqueous-phase concentration can be calculated from the mass balances of equation (3). We define the Henry's Law pH for a species, pH_H, as the hypothetical pH of the bulk mixture for which the gas-phase and the mixed aqueous-phase concentrations of the species satisfy Henry's Law. We shall demonstrate that generally this pH is not equal to the pH of the mixture, pH_m.

For ammonia, the Henry's Law pH can be calculated from:

$$[NH_3]_m^T = H_{NH_3} G_{NH_3} (1 + K_{NH_3} H^+{}_H) \tag{7}$$

where $H^+{}_H$ is the hypothetical hydrogen ion concentration that would be needed for the bulk mixture to be in equilibrium with the gas-phase concentration. Using the mass balance for NH_3 (equation 3) and substituting $[NH_3]_i$ with the expressions given by Henry's Law (equation 5) one finds that

$$H^+{}_H = w_1 H^+{}_1 + w_2 H^+{}_2 \quad \text{for } NH_3 \tag{8}$$

where $H^+{}_1$ and $H^+{}_2$ are the hydrogen ion concentrations of the two droplet groups that are mixed. Thus, the Henry's Law hydrogen ion concentration for NH_3 is the weighted arithmetic mean of the hydrogen ion concentrations of the individual droplets with the liquid water fractions used as weighting factors.

The same procedure can be repeated for the weak acids and where one finds that Henry's Law pH is independent of the species (as long as it dissociates only once) and is equal to the weighted harmonic mean of the hydrogen ion concentrations of the individual droplets:

$$\frac{1}{H^+{}_H} = \frac{w_1}{H^+{}_1} + \frac{w_2}{H^+{}_2} \quad \text{or} \quad H^+{}_H = \frac{H^+{}_1 H^+{}_2}{w_1 H^+{}_2 + w_2 H^+{}_1} \quad \text{for weak acids.} \tag{9}$$

Henceforth, we shall use separate symbols for the Henry's Law hydrogen ion concentrations for weak acids and weak bases, H^+_{arith} for the arithmetic mean (bases), and H^+_{harm} for the harmonic mean (acids). The weighted arithmetic mean is always larger or equal to the weighted harmonic mean

$$H^+_{harm} \leq H^+_{arith} \tag{10}$$

and the equality is valid only when the two droplet populations have the same pH.

3.3.2.2 pH of the mixture, pH_m

After mixing the two droplet populations, the mixture has a pH equal to pH_m, satisfying the electroneutrality equation (1). One can substitute equations (3) to (6) in the electroneutrality equation and arrive at an equation of the form $f(H^+) = 0$ for which H^+_m is the only real root:

$$f(H^+) = K_{SO_2} G_{SO_2} H_{SO_2} \left[\frac{H^+(w_1 H^+_2 + w_2 H^+_1) - H^+_1 H^+_2}{H^+_1 H^+_2 (H^+ + K_{SO_2})}\right]$$

$$+K_{CO_2} G_{CO_2} H_{CO_2} \left[\frac{H^+(w_1 H^+_2 + w_2 H^+_1) - H^+_1 H^+_2}{H^+_1 H^+_2 (H^+ + K_{CO_2})}\right]$$

$$+K_{HCOOH} G_{HCOOH} H_{HCOOH} \left[\frac{H^+(w_1 H^+_2 + w_2 H^+_1) - H^+_1 H^+_2}{H^+_1 H^+_2 (H^+ + K_{HCOOH})}\right]$$

$$+K_{HNO_2} G_{HNO_2} H_{HNO_2} \left[\frac{H^+(w_1 H^+_2 + w_2 H^+_1) - H^+_1 H^+_2}{H^+_1 H^+_2 (H^+ + K_{HNO_2})}\right] + K_w \left(\frac{w_1}{H^+_1}\frac{w_2}{H^+_2} - \frac{1}{H^+}\right)$$

$$+(H^+ - w_1 H^+_1 - w_2 H^+_2) + K_{NH_3} G_{NH_3} H_{NH_3} \left[\frac{H^+ - w_1 H^+_1 - w_2 H^+_2}{1 + K_{NH_3} H^+}\right] = 0 \quad .(11)$$

The mixing of two solutions with different pH results in a new solution with a unique pH and therefore H^+_m is the only real root of the above equation. Assume without any loss of generality that $H^+_1 \leq H^+_2$. One can show that:

$$f(H^+_1) = -K_{SO_2} G_{SO_2} H_{SO_2} \left[\frac{(H^+_2 - H^+_1) w_2}{H^+_2 (H^+_1 + K_{SO_2})}\right] - K_{CO_2} G_{CO_2} H_{CO_2}$$

$$\left[\frac{(H^+_2 - H^+_1)w_2}{H^+_2(H^+_1 + K_{CO_2})}\right] - K_{HCOOH}G_{HCOOH}H_{HCOOH}\left[\frac{(H^+_2 - H^+_1)w_2}{H^+_2(H^+_1 + K_{HCOOH})}\right]$$

$$-K_{HNO_2}G_{HNO_2}H_{HNO_2}\left[\frac{(H^+_2 - H^+_1)w_2}{H^+_2(H^+_1 + K_{HNO_2})}\right] - \frac{K_w w_2(H^+_2 - H^+_1)}{H^+_1 H^+_2}$$

$$-w_2(H^+_2 - H^+_1) - K_{NH_3}G_{NH_3}H_{NH_3}\left[\frac{w_2(H^+_2 - H^+_1)}{1 + K_{NH_3}H^+_1}\right] \qquad (12)$$

. Note that all the terms are nonpositive, and therefore $f(H^+_1) \leq 0$ with the equality satisfied only when $H^+_1 = H^+_2$.

Using the same procedure for H^+_2 one finds that:

$$f(H^+_2) = K_{SO_2}G_{SO_2}H_{SO_2}\left[\frac{(H^+_2 - H^+_1)w_1}{H^+_1(H^+_2 + K_{SO_2})}\right] + K_{CO_2}G_{CO_2}H_{CO_2}$$

$$\left[\frac{(H^+_2 - H^+_1)w_1}{H^+_1(H^+_2 + K_{CO_2})}\right] + K_{HCOOH}G_{HCOOH}H_{HCOOH}\left[\frac{(H^+_2 - H^+_1)w_1}{H^+_1(H^+_2 + K_{HCOOH})}\right]$$

$$+K_{HNO_2}G_{HNO_2}H_{HNO_2}\left[\frac{(H^+_2 - H^+_1)w_1}{H^+_1(H^+_2 + K_{HNO_2})}\right] + \frac{K_w w_1(H^+_2 - H^+_1)}{H^+_1 H^+_2}$$

$$+w_1(H^+_2 - H^+_1) + K_{NH_3}G_{NH_3}H_{NH_3}\left[\frac{w_1(H^+_2 - H^+_1)}{1 + K_{NH_3}H^+_2}\right] \qquad (13)$$

In this case, all the terms are nonnegative and therefore $f(H^+_2) \geq 0$ with the equality satisfied only when $H^+_1 = H^+_2$. Because $f(H^+)$ is a continous function of H^+, and H^+_m is its only non-negative root,

$$H^+_1 \leq H^+_m \leq H^+_2. \qquad (14)$$

Also, because of continuity and the existence of only one root, for any point H^+ between H^+_1 and H^+_m $f(H^+) < 0$ and also for any point between H^+_m and H^+_2 $f(H^+) > 0$. These properties of the function $f(H^+)$ allow one to make the comparison between the hydrogen ion concentration of the mixture H^+_m, and the hydrogen concentration predicted by Henry's Law: H^+_{harm} for acids and H^+_{arith} for bases. Substituting H^+_{harm} (equation 9) into equation (11) one gets

$$f(H^+_{harm}) = -\frac{w_1 w_2 (H^+_2 - H^+_1)^2}{w_1 H^+_2 + w_2 H^+_1}\left[1 + \frac{K_{NH_3} G_{NH_3} H_{NH_3}}{1 + K_{NH_3} H^+_{harm}}\right] \quad .(15)$$

Because $f(H^+_{harm}) \leq 0$ one concludes that

$$H^+_{harm} \leq H^+_m \quad (16)$$

or, in other words, the hydrogen ion concentration required for Henry's Law equilibration of a weak acid between the bulk sample and the gas phase is always less than or equal to the actual hydrogen ion concentration of the mixture.

Repeating the same procedure for the H^+_{arith} given by equation (8) one finds that:

$$f(H^+_{arith}) = K_{SO_2} G_{SO_2} H_{SO_2} \frac{w_1 w_2 (H^+_2 - H^+_1)^2}{H^+_1 H^+_2 (H^+_{arith} + K_{SO_2})} + K_{HNO_2} G_{HNO_2} H_{HNO_2}$$

$$\frac{w_1 w_2 (H^+_2 - H^+_1)^2}{H^+_1 H^+_2 (H^+_{arith} + K_{HNO_2})} + K_{CO_2} G_{CO_2} H_{CO_2} \frac{w_1 w_2 (H^+_2 - H^+_1)^2}{H^+_1 H^+_2 (H^+_{arith} + K_{CO_2})}$$

$$+K_{HCOOH} G_{HCOOH} H_{HCOOH} \frac{w_1 w_2 (H^+_2 - H^+_1)^2}{H^+_1 H^+_2 (H^+_{arith} + K_{HCOOH})} + K_w \frac{w_1 w_2 (H^+_2 - H^+_1)^2}{H^+_1 H^+_2 H^+_{arith}} \quad .(17)$$

In this case, $f(H^+_{arith}) \geq 0$ and therefore:

$$H^+_m \leq H^+_{arith} \quad (18)$$

or, in other words, the hydrogen ion concentration required for Henry's Law equilibration of a weak base between the bulk sample and the gas phase is always greater than or equal to the actual hydrogen ion concentration of the mixture.

3.3.2.3 Restriction and Generalization of the Proof

In our analysis, we have assumed only two droplet groups. The generalization of the proof to a collection of n droplet groups is straightforward. The validity of this generalization can be seen by imagining a device that samples and mixes the different droplet groups sequentially; e.g., mixes groups one and two forming a new group, mixes

this group with group three, etc. The harmonic and arithmetic mean of the hydrogen ion concentrations are defined as

$$H^+_{arith} = \sum_{i=1}^{n} w_i H^+_i, \quad \frac{1}{H^+_{harm}} = \sum_{i=1}^{n} \frac{w_i}{H^+_i}$$

and the pH of the mixture satisfies equations (16) and (18).

Until now, our analysis until now has focused on the weak acids and on ammonia. To simplify our derivation, we have implicitly assumed that the aqueous-phase concentrations of the strong acids (HNO_3 and HCl) do not change with the change of pH. One can very easily see that everything discussed until now applies to the strong acids (e.g., one can substitute HNO_2 by HNO_3 in all the equations). One should also keep in mind that these acids inside a cloud or a fog reside almost exclusively in the aqueous phase. For example, if there is 1 ppb of HNO_3 in the gas phase in the precloud or prefog atmosphere, and a cloud or a fog of pH=5 and liquid water content of 0.2 g m^{-3} is created, 0.99996 ppb will be dissolved in the aqueous phase and only 4×10^{-5} ppb will remain in the gas phase as $HNO_3(g)$. Also, the concentration of these acids dissolved in the aqueous-phase is not particularly sensitive to the pH, so if the pH drops to 4, the concentration of nitrate in the aqueous-phase will decrease by only 0.04%.

An assumption that could limit the generality of our results is the neglect of the second dissociation of $SO_2 \cdot H_2O$ and $CO_2 \cdot H_2O$. The product of the second dissociation of CO_2, CO_3^{2-}, represents less than 0.1% of the dissolved $[CO_2]^T$ for pH$<$ 10 and therefore does not restrict, in any practical way, the generality of our findings. On the other hand, SO_3^{2-} exceeds 20% of the total S(IV) for pHs higher than 7. Because most atmospheric droplets will tend to be acidic, our findings are virtually exact for the pH range of atmospheric interest. The fact that the neglect of the second dissociation is not valid for high pH does not necessarily mean that our conclusions do not apply in that range, but simply that the proof becomes too cumbersome to carry out in this pH range.

3.3.3 Definition of Henry's Law Ratios

The variables that one can measure in the field include the gas-phase concentration of species j, G_j, its aqueous-phase concentration in the bulk mixture, C_j, and the hydrogen ion concentration of the mixture ${H^+}_m$. Combining these quantities and using Henry's Law, one can define various additional variables that are, in a sense, hypothetical as they differ from the quantities that one actually measures.

We define the Henry's Law aqueous-phase concentration of species j, C_{Hj} as

$$C_{Hj} \equiv H_j^*({H^+}_m)G_j \tag{19}$$

where H_j^* is the effective Henry's Law constant for species j, a function of the pH of the solution. The Henry's Law hydrogen ion concentration ${H^+}_H$ has already been defined above from

$$C_j \equiv H_j^*({H^+}_H)G_j \tag{20}$$

and it has also been shown that for acids dissociating once ${H^+}_H = {H^+}_{harm}$ while for NH_3, ${H^+}_H = {H^+}_{arith}$.

One can also define the Henry's Law gas-phase concentration G_{Hj} from

$$C_j \equiv H_j^*({H^+}_m)G_{Hj} \tag{21}$$

and the observed Henry's Law constant H_j^{*m} as

$$C_j \equiv H_j^{*m}G_j. \tag{22}$$

Note that $H_j^{*m} = H_j^*({H^+}_H)$.

The degree of deviation from Henry's Law can be determined by defining the ratios of the measured concentrations to those that are calculated by assuming Henry's Law for the bulk mixture. These ratios also express the magnitude of the error committed

when one incorrectly assumes Henry's Law equilibrium between the bulk mixture and the original gas phase. These ratios are:

$$R_H \equiv \frac{{H^+}_m}{{H^+}_H}, \quad R_K \equiv \frac{H_j^*({H^+}_m)}{H_j^{*m}} = \frac{H_j^*({H^+}_m)}{H_j^*({H^+}_H)}, \quad R_{aq} \equiv \frac{C_j}{C_{Hj}}, \quad R_G \equiv \frac{G_j}{G_{Hj}} \qquad (23)$$

One can easily show that the last three ratios are related by

$$R_{aq} = \frac{1}{R_K} = \frac{1}{R_G}. \qquad (24)$$

Also, the ratio of the aqueous-phase concentrations depends on the hydrogen concentration ratio, on the species dissociation constant K_j, and on the pH of the mixture. For an acid

$$R_{aq} = \frac{{H^+}_m + K_j R_H}{{H^+}_m + K_j}, \qquad (25)$$

and for a base

$$R_{aq} = \frac{1 + (K_j {H^+}_m / R_H)}{1 + K_j {H^+}_m}. \qquad (26)$$

We have already shown that $R_H \geq 1$ for acids and $R_H \leq 1$ for bases. This results in

$$R_{aq} \geq 1, \quad R_K \leq 1, \quad R_G \leq 1 \qquad (27)$$

for both acids and bases.

Mixing therefore, results in a supersaturation R_{aq} of the aqueous phase compared to that predicted on the basis of Henry's Law, or an undersaturation of the gas phase equal to R_G.

3.3.4 Aqueous-phase Concentration Ratio, R_{aq}

It has been shown that under practically all conditions of atmospheric interest R_{aq} exceeds unity. Some reasonable questions arise at this point. What parameters

influence the value of R_{aq}? Under typical atmospheric conditions, is R_{aq} expected to be much larger that unity or is it sufficiently close to unity so that the effect can be neglected? These questions will now be addressed.

3.3.4.1 Parameters Influencing R_{aq}

For a species i, the ratio of the aqueous-phase concentrations, R_{aq}, depends on the pH of the bulk mixture, on the ratio of the hydrogen ion concentrations, R_H, and on the dissociation constant of the species, K_i (equations 25 and 26).

R_{aq} for HCOOH and S(IV) is shown as a function of the pH of the mixture, pH_m, and the ratio of the hydrogen ion concentrations, R_H, in Figure 3.3.1. Formic acid has a dissociation constant K_{HCOOH} equal to 1.78×10^{-4} M at 298 K (Martell and Smith, 1977) corresponding to a pK_a ($=-\log_{10}K_i$) value of 3.7. For pHs significantly lower than its pK_a value, the acid does not dissociate, and therefore the mixing of droplets of different composition do not cause deviations from Henry's Law. Therefore, R_{aq} is practically unity for any value of the hydrogen concentration ratio when the pH of the bulk mixture is lower than 2.5 (Figure 3.3.1a). For pHs between 2.5 and 5, the R_{aq} for formic acid depends strongly on the pH, while for pH higher than 5, it is practically equal to R_H. The same behavior is observed in Figure 3.3.1b for S(IV) with the difference that S(IV) has a much smaller pK_a, equal to 1.9 at 298 K (Smith and Martell, 1976) and mixing causes deviations from Henry's Law for almost any pH_m. The dissociation of ammonia is practically complete over the entire pH range of interest; therefore, R_{aq} is equal to $1/R_H$.

The above analysis indicates that the calculation of R_H is necessary for the determination of the magnitude of the expected deviations from Henry's Law under typical atmospheric conditions. R_H has been defined as the ratio of the measured bulk mixture hydrogen ion concentration to the hydrogen ion concentration determined from Henry's Law, ${H^+}_H$. ${H^+}_H$ is equal to the harmonic mean of the hydrogen ion concentrations for the acids and equal to their arithmetic mean for ammonia.

FIGURE 3.3.1(a). Ratio, R_{aq}, of the measured aqueous phase concentration to the concentration calculated from Henry's law as a function of pH of the bulk mixture, pH_m, and the ratio of the hydrogen concentration R_H for formic acid.

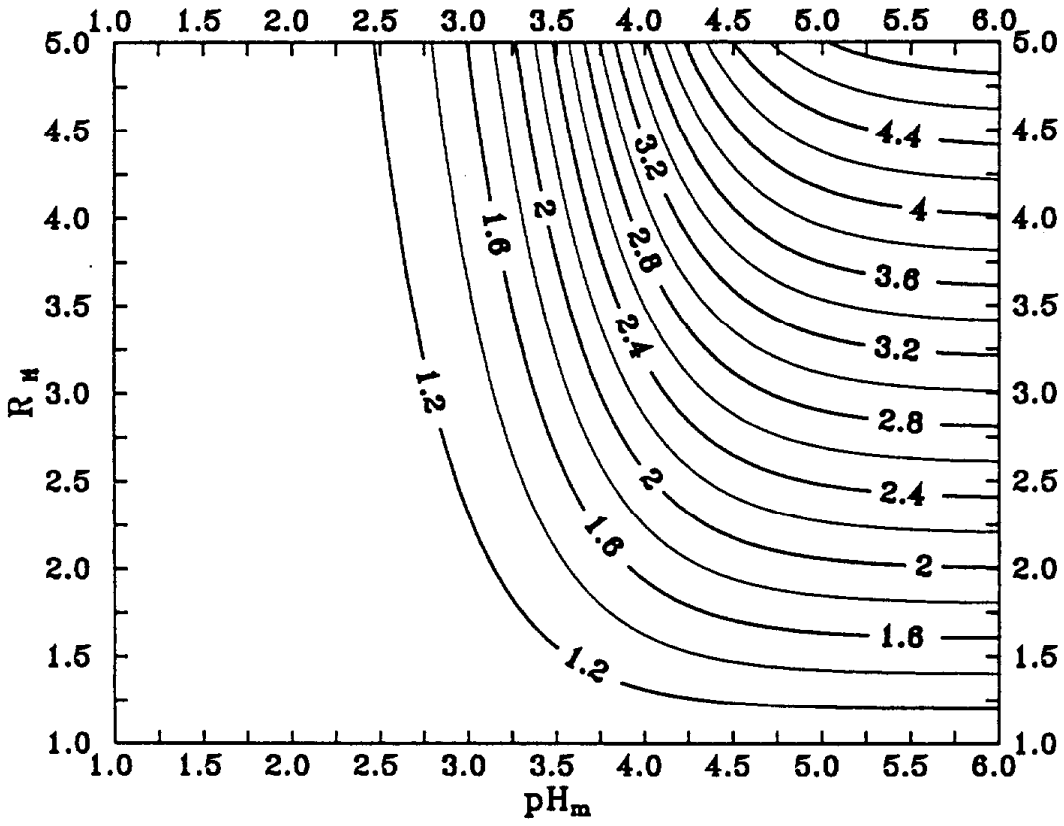

FIGURE 3.3.1(b). Ratio, R_{aq}, of the measured aqueous phase concentration to the concentration calculated from Henry's law as a function of pH of the bulk mixture, pH_m, and the ratio of the hydrogen concentration R_H for S(IV).

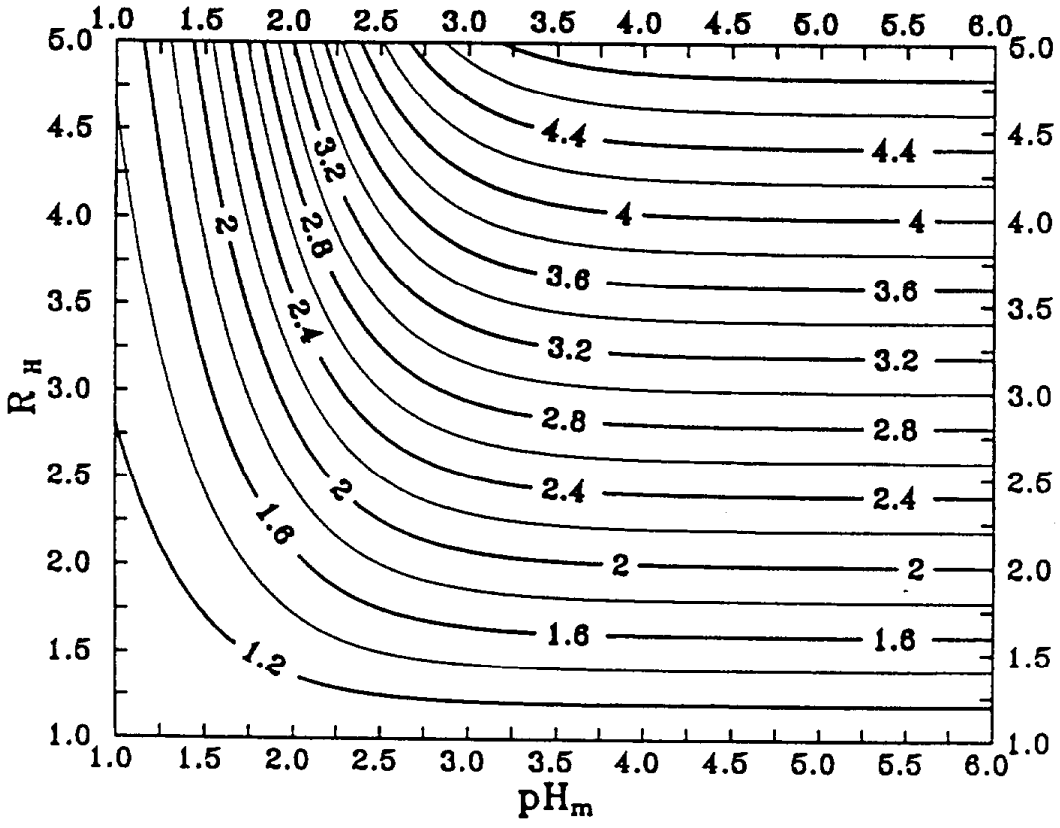

3.3.4.2 Parameters Influencing R_H

The hydrogen ion concentration of the bulk mixture H^+_m lies in the interval $[H^+_{harm}, H^+_{arith}]$. A useful analytical expression for R_H cannot be obtained because equation (11) determining H^+_m is far too complicated. However, some insight can be obtained and an upper limit for R_H can be calculated by studying the ratio of H^+_{arith}/H^+_{harm}. One can show that:

$$R = \frac{H^+_{arith}}{H^+_{harm}} = 1 + \frac{1}{2}\sum_{i=1}^{n}\sum_{j=1}^{n} w_i w_j \frac{(H^+_i - H^+_j)^2}{H^+_i H^+_j} \tag{28}$$

and, therefore, that the ratio of the arithmetic mean to the harmonic mean hydrogen ion concentration increases with increasing pH differences among the different droplet groups. The liquid water content fractions w_i are again the weighting factors in this calculation. The ratio R can be also viewed as the product of the ratio $R_H = H^+_m/H^+_{harm}$ for the acids of the mixture with the inverse of the $R_H = H^+_m/H^+_{arith}$ for the bases of the mixture and is, therefore, an expression of the combined deviation of both the acids and bases from Henry's Law equilibrium.

Equation (28) suggests that the contribution of a group of droplets to the deviation of the bulk sample from Henry's Law depends on the product of its liquid water and the difference of hydrogen ion concentrations between this droplet group and the other droplet groups. So, even if most of the liquid water content of the cloud or fog is concentrated in a narrow size range, one should not neglect the rest of the droplets. For example, let us assume that 90% of the droplets have a uniform hydrogen ion concentration of 1 μM, while the remaining 10% have a hydrogen concentration of 10 μM. Application of equation (28) suggests that in this case $R = 1.73$, which could be roughly viewed as a 70% total deviation from Henry's Law, even if most of the cloud or fog liquid water has the same pH. The above equation also suggests that regardless of the species that control the pH, as long as there are significant hydrogen concentration differences between droplets of different sizes, there is the potential for deviations from Henry's Law.

3.3.4.3 Calculation of R_{aq} Using Experimental Data

Few field measurements of composition differences between droplets of different sizes in clouds or fogs exist (Noone et al., 1988; Munger et al., 1989; Ogren et al., 1989; Heintzenberg et al., 1989). In all these studies, only two size-segregated samples of the cloudwater have been collected and their composition or total solute concentration have been reported. Munger et al. (1989) reported that the hydrogen ion concentration in the fine droplet sample was often a factor of 2 higher than that of the large droplet sample and added that this difference should be considered a lower bound on the actual differences present because of a considerable overlap in the portions of the two droplet spectra. Using these pH values and assuming that all the droplets in each sample had the same composition, equation (28) suggests a value of R equal to 1.13.

Although the collection of two samples is a significant improvement over the collection of just one, mixing of droplets with significantly different compositions occurs in both samples. We shall demonstrate that the knowledge of two pH values is not usually sufficient for the direct calculation of the degree of deviation of the bulk sample from Henry's Law equilibrium.

The measurement of the composition of two size-segregated samples can provide only a lower limit of R, because significant droplet mixing of different compostion had already taken place for each of the two individual samples. This point can be illustrated with a simple numerical example. Assume that a droplet population consists of four droplet groups with equal liquid water contents and the first has an hydrogen ion concentration $H^+{}_o$, the second $5H^+{}_o$, the third $10H^+{}_o$, and the fourth $20H^+{}_o$. These values are slightly exaggerated, but they can still appear under special atmospheric conditions; e.g., high pH and preferential production of sulfate in the last section. For this droplet population $H^+{}_{arith} = 9H^+{}_o$, $H^+{}_{harm} = 2.97H^+{}_o$, and $R = 3.03$. If the first two droplet groups are collected and mixed together, their hydrogen concentration will be between $1.67H^+{}_o$ and $3\ H^+{}_o$, while for the second pair it will be between $13.3H^+{}_o$ and $15H^+{}_o$. Assume that the hydrogen concentration of the two mixtures is the average

of the corresponding limits; that is, $2.33H^+_o$ for the first and $14.15H^+_o$ for the second. If these two groups are collected instead of the original four, $H^+_{arith} = 8.24H^+_o$ and $H^+_{harm} = 4.0H^+_o$, and the ratio has been reduced significantly to $R = 2.06$.

The ratio R is even further reduced if the samplers collect droplets from all four groups with different efficiencies. Let us assume that sampler A collects 100% of the droplets in groups 1, 2 and 3 and 50% of the droplets in group 4, while sampler B collects 100% of droplet group 1, 50% of droplet group 2, 30% of droplet group 3 and 10% of droplet group 4. The sample A will have a hydrogen ion concentration in the interval $[2.64H^+_o, 7.42H^+_o]$, while sample B will be the interval $[1.68H^+_o, 4.49H^+_o]$. Assuming that the hydrogen ion concentration of the samples is the arithmetic mean of the ends of the corresponding intervals, sample A will have a concentration $5.03H^+_o$ and sample B of $3.09H^+_o$ resulting in a ratio R of only 1.06. Therefore, a ratio R of 3.03 can easily be miscalculated as 1.06 if one neglects the fact that the individual samples are also mixtures of droplets of different composition.

Unless sampled cloud or fogwater data have sufficient resolution, even if there are significant composition differences between droplets of different sizes, a quantitative assessment of the effects of these differences on the deviation from Henry's Law is not possible.

3.3.4.4 Calculation of R_{aq} Using Modeling Studies

In view of the lack of suitable ambient data, the calculation of the magnitude of R_{aq} under typical atmospheric conditions requires the use of models that describe the evolution of the size/composition droplet spectrum in a cloud or fog including descriptions of the gas- and aqueous-phase chemical processes.

Using the model developed by Pandis et al. (1990b) applied to a typical fog episode in Southern California, one calculates R values as high as 1.5 for a fog with a pH around 3 (Figure 3.3.2). The R values for this specific episode are relatively low but one should note that, for example, at $t = 135$ min the arithmetic mean of the hydrogen ion concentration differences is 1710 μM, while the harmonic mean is 1170 μM. The

FIGURE 3.3.2. R for the fog episode modeled by Pandis et al [1991].

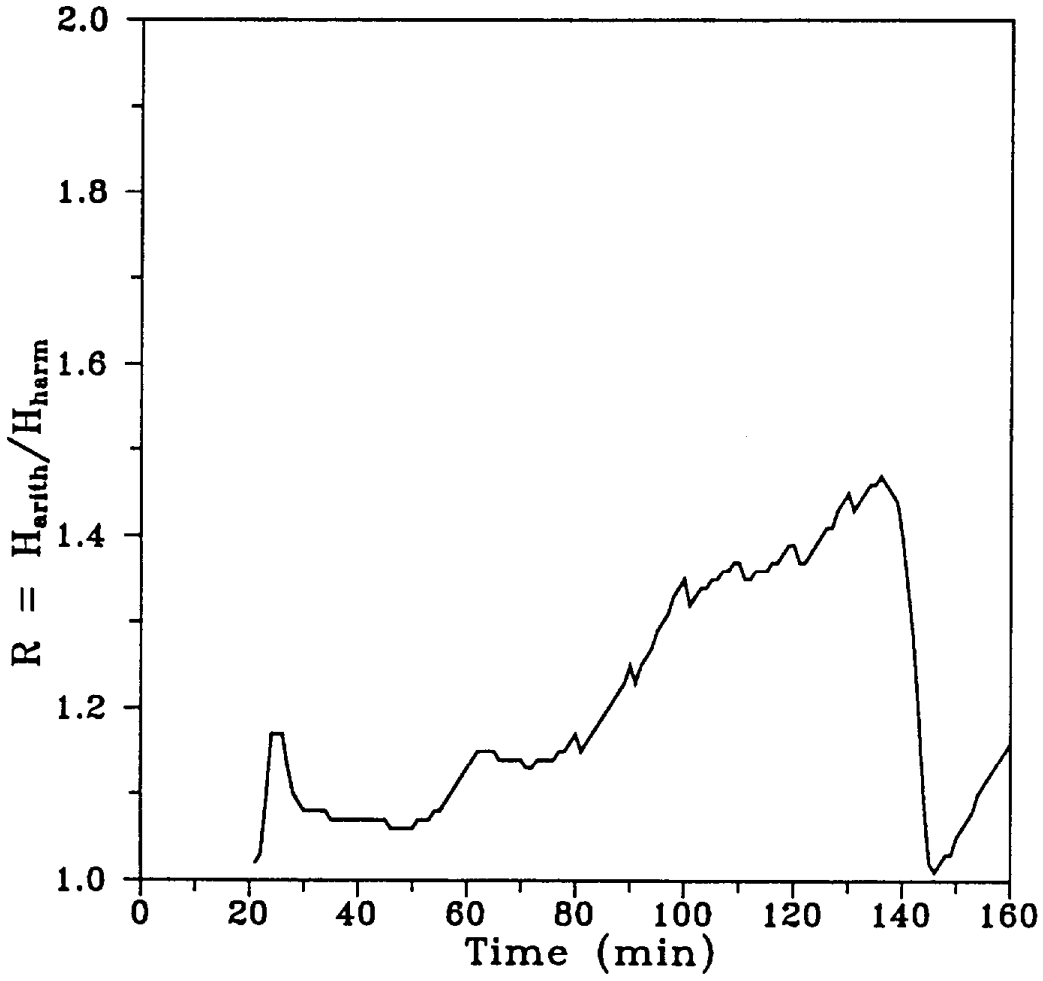

difference of 540 μM is large in absolute terms, but due to the magnitude of the values, their ratio is only 1:5. One expects that in fogs and clouds with higher pH, such large differences will give rise to much higher R values and, therefore, to larger deviations from Henry's Law.

The simulation of Hegg and Larson (1991) indicated hydrogen ion concentration variations from 6 to 100 μM over the droplet spectrum. Values of R around 3 can be easily obtained using the above analysis and assuming that $R_H \simeq R$. For this pH range, Figure 3.3.1 suggests that application of Henry's Law to the bulk mixture results in an overestimation of the aqueous-phase concentrations of weak acids and ammonia by almost a factor of 3.

3.3.5 Atmospheric Implications

Several investigators (e.g., Jacob et al., 1987) have estimated rates of loss of SO_2 in fogs or clouds by using the measured gas-phase concentration of SO_2 and the measured pH of the bulk sample. The S(IV) concentration calculated by using Henry's Law is less than the actual concentration and, therefore, the rate of reaction inferred from this concentration is underestimated. The fact that the observed sulfate production could not be fully explained by the estimated reaction rates is partially due to the application of Henry's Law.

Winiwarter et al. (1988) observed deviations from Henry's Law equilibrium for both HCOOH and CH_3COOH during radiation fog episodes. They reported values of R_K that were generally larger than 1 for HCOOH (especially for pH>5) and generally less than 1 for CH_3COOH. They hypothesized that this behavior is due to the inhomogeneities of pH and chemical composition of the individual droplets. Our results suggest that mixing of droplets results in values of $R_K \leq 1$. While the effect of mixing is an explanation for the CH_3COOH behavior, other explanations of the observed HCOOH behavior are possible.

The measured aqueous concentration and the measured bulk pH have been used for the prediction of the gas-phase concentration. Henry's Law overpredicts the gas-phase

concentration of the species in that case. The measured hydrogen ion concentration of the bulk sample is always less than or equal to the liquid water weighted hydrogen ion concentration of the individual droplets. Attempting to estimate the free acidity of the atmosphere by using the pH of the bulk sample leads to an underestimate because $H^+_m < H^+_{arith}$. The fact that the cloudwater/fogwater bulk samples are supersaturated with respect to the surrounding atmosphere will result in outgassing of weak acids and ammonia from the samples, if such an exchange is allowed. At the same time, the pH of the sample will change.

3.4 HETEROGENEOUS SULFATE PRODUCTION IN AN URBAN FOG

3.4.1 Introduction

The aqueous phase in the atmosphere (clouds, fogs) acts as a physicochemical processor of gases and particles. Water droplets scavenge soluble gases (e.g., HNO_3, NH_3, etc.) and aerosol particles accelerating their removal from the atmosphere. At the same time, the aqueous phase provides a medium for chemical reactions; the most important appears to be the oxidation of dissolved SO_2 (S(IV)) to sulfate (S(VI)) and an associated increase in atmospheric acidity (Pandis and Seinfeld, 1989a). The effect of the aqueous phase on the ambient concentrations of acidic species and on their respective removal rates are problems that still remain partially or completely unsolved.

Modeling studies based on laboratory kinetic data have suggested that significant amounts of sulfate can be produced in the aqueous phase via a variety of chemical pathways (oxidation by H_2O_2, O_3, O_2 catalyzed, etc.) (Schwartz, 1989). The confirmation of these studies by field measurements has been difficult. Detection of the occurrence of sulfate-producing reactions is often hindered by the variability of cloud liquid water content and the temporal instability and spatial variability in concentrations of reagents and product species (Kelly et al., 1989). Continuous sampling of the same air parcel, in a Lagrangian sense, while highly desirable, is difficult to achieve in ambient clouds and fogs.

The effect of urban fogs on the particulate sulfate levels has been the subject of several previous studies with rather inconclusive results. Cass (1977) examined a sample of 62 days with high aerosol sulfate concentrations in Los Angeles and observed that all but one were associated with periods of coastal fog or high relative humidity. Similar observations were reported by Cass (1979) and Cass and Shair (1984). Fogwater measurements by Jacob et al. (1984) in the San Joaquin Valley of California indicated a decrease in the fogwater sulfate loadings in the latter stages of a fog episode lasting

several hours. Pandis and Seinfeld (1989b) simulated a similar extended fog episode in the same area and reported that even if significant amounts of sulfate were produced in the aqueous phase during the episode, the ambient sulfate levels were reduced below those present in the prefog aerosol due to wet deposition. Simulations reported by Forkel et al. (1990) indicated that the net loss of sulfate by sedimentation was higher than its production within a radiation fog that lasted for eight hours. Pandis et al. (1990) reported an increase of the sulfate levels by a factor of two during a two-hour simulated typical Los Angeles fog episode and also observed that the total sulfate concentration (droplet plus interstitial aerosol) started decreasing after the first hour of the fog life.

In the present study, the data collected during an extensive field study are analyzed with three goals: (1) to indirectly detect the existence of heterogeneous sulfate formation in an urban atmosphere; (2) to document the effect of fogwater chemistry on the ambient sulfate levels and acidity; and (3) to theoretically investigate the aqueous-phase chemical pathways that lead to the sulfate formation.

During a period of 13 weeks in the summer and fall of 1987, a comprehensive air pollution data set was collected in the Los Angeles basin during SCAQS (Hering and Blumenthal, 1989). The program focused mainly on gas- and aerosol-phase chemical processes, but sufficient data are available to attempt to quantify the effects of heterogeneous chemistry on the ambient sulfate levels in Los Angeles. In the present work, we shall test the hypothesis that the occurrence of a fog episode near the Southern California coast resulted in a significant increase in the aerosol sulfate levels during the next day, and also that this sulfate increase is principally a result of the aqueous-phase oxidation of S(IV) inside the fog droplets.

To evaluate this hypothesis, we shall start by examining the aerosol sulfate levels at several Los Angeles sites the day after the fog episode. We shall demonstrate that the increase in the sulfate levels at several sites was associated with the arrival of air parcels that passed through the fog layer. The contribution of the gas-phase chemistry to the sulfate concentration will be quantified using a comprehensive gas-phase

trajectory model. Sensitivity analysis of the model to all the main input parameters will be performed, in an attempt to provide an uncertainty estimate on the gas-phase contribution to the sulfate levels. Finally, we shall investigate, by using an appropriate aqueous-phase chemical model, the extent to which the oxidation of S(IV) inside the fog droplets can indeed explain the observations.

3.4.2 Aerosol Sulfate Levels the Day After a Fog Episode

Fog moved into the Southern California coast during the early hours of December 11, 1987. Hoffmann et al. (unpublished data) collected fogwater and measured the fogwater pH in the Long Beach area. According to these available data, the fog episode of December 11, 1987, lasted for around six hours (from midnight to 6 a.m.), with liquid water content values between 0.11 and 0.37 g m^{-3} and pH in the 4.5 to 5.5 range. The fog layer extended a few miles inland.

The aerosol sulfate concentration was measured at six sites in the Los Angeles basin (Figure 3.4.1 [a-d]): Anaheim, Burbank, Hawthorne, Rubidoux, Downtown Los Angeles, and Long Beach (Chan and Durkee, 1989). Five aerosol samples (three four-hour samples during the day and two six-hour samples during the night) were collected at each site every day during the period of December 10-11. During December 10, relatively low aerosol sulfate concentrations were observed at all six sites. The measured sulfate concentrations ranged from 0.56 to 5.37 $\mu g\ m^{-3}$ with maximum measured values of 5.37 $\mu g\ m^{-3}$ (at 9 p.m.) for Anaheim, 1.54 $\mu g\ m^{-3}$ (at 9 p.m.) for Burbank, 2.83 $\mu g\ m^{-3}$ (at 9 p.m.) for Downtown Los Angeles, 4.68 $\mu g\ m^{-3}$ (at 3 a.m.) for Hawthorne, 5.08 $\mu g\ m^{-3}$ (at 12 noon) for Long Beach, and 2.93 $\mu g\ m^{-3}$ (at 9 p.m.) for Rubidoux.

During December 11, the aerosol sulfate levels increased drastically at several locations in the Los Angeles basin. The maximum measured sulfate concentrations were 8.57 $\mu g\ m^{-3}$ (at 9 p.m.) for Anaheim, 7.83 $\mu g\ m^{-3}$ (at 4 p.m.) for Burbank, 12.57 $\mu g\ m^{-3}$ (at 4 p.m.) for Downtown Los Angeles, 15.56 $\mu g\ m^{-3}$ (at 12 noon) for Hawthorne, 16.95 $\mu g\ m^{-3}$ (at 12 noon) for Long Beach, and 3.06 $\mu g\ m^{-3}$ (at 8 a.m.) for Rubidoux. All the locations exhibited significantly increased sulfate concentrations

with the exception of Ribidoux, the inland site.

The trajectory of the air parcel arriving at Anaheim at the time of the sulfate peak (9 p.m.) (Figure 3.4.1a) indicates that the air parcel had spent almost six hours inside the fog layer. The corresponding air parcel for Downtown Los Angeles was inside the fog layer for approximately one hour (5 a.m. to 6 a.m.) (Figure 3.4.1b). The air parcel arriving at Hawthorne at 12 noon on December 11 spent approximately two hours (4 a.m. to 6 a.m.) inside the fog area near Long Beach (Figure 3.4.1c). Finally, the air parcel arriving at Long Beach at 9 p.m. started its trip over the land, remained for the duration of the fog episode just beyond the coast, and returned the next night at the Long Beach site (Figure 3.4.1d).

Analysis of the trajectories arriving at Anaheim, downtown Los Angeles, Hawthorne, and Long Beach indicates that the air parcels arriving at these locations during the maximum sulfate periods all passed through the fog layer. Analysis of the overall windfield over the Los Angeles basin indicated that the air parcels arriving at Rubidoux on December 11 did not encounter fog. The evidence just presented strongly suggests that air parcels passing through the fog layer during December 11 ('wet air parcels') exhibited increased aerosol sulfate levels upon their arrival at a sampling site. Further analysis is required of the contributions of the gas and heterogeneous processes to these observed sulfate levels. The first step in this analysis is the use of a comprehensive gas-phase trajectory model in an effort to explain this sulfate increase by the gas-phase oxidation of SO_2. Two sites have been selected for this detailed analysis– Hawthorne and Downtown Los Angeles–representing, respectively, a site near the coast and one further inland.

3.4.2.1 The Gas-Phase Lagrangian Trajectory Model

The gas-phase Lagrangian trajectory model describes atmospheric chemical reactions, turbulent vertical diffusion, horizontal advective transport and ground-level pollutant deposition. It is based on the numerical solution of the Lagrangian trajectory form of the atmospheric diffusion equation (McRae et al., 1982). Except for the

FIGURE 3.4.1(a). Trajectory arriving at sampling sites in the South Coast Air Basin of California on December 11, 1987 during the period of observed peak sulfate concentration in Anaheim at 2100 PST.

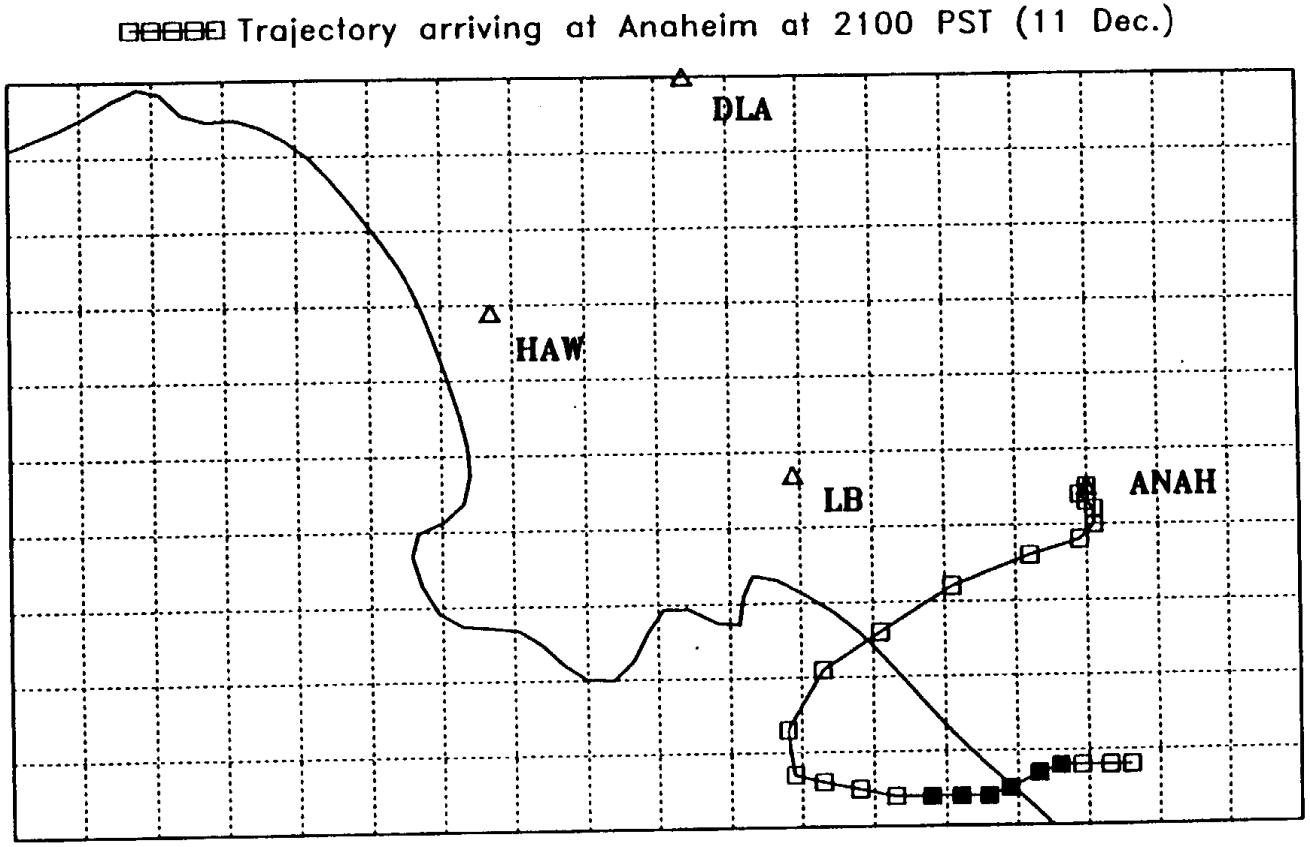

FIGURE 3.4.1(b). Trajectory arriving at sampling sites in the South Coast Air Basin of California on December 11, 1987 during the period of observed peak sulfate concentration in Downtown Los Angeles at 1600 PST.

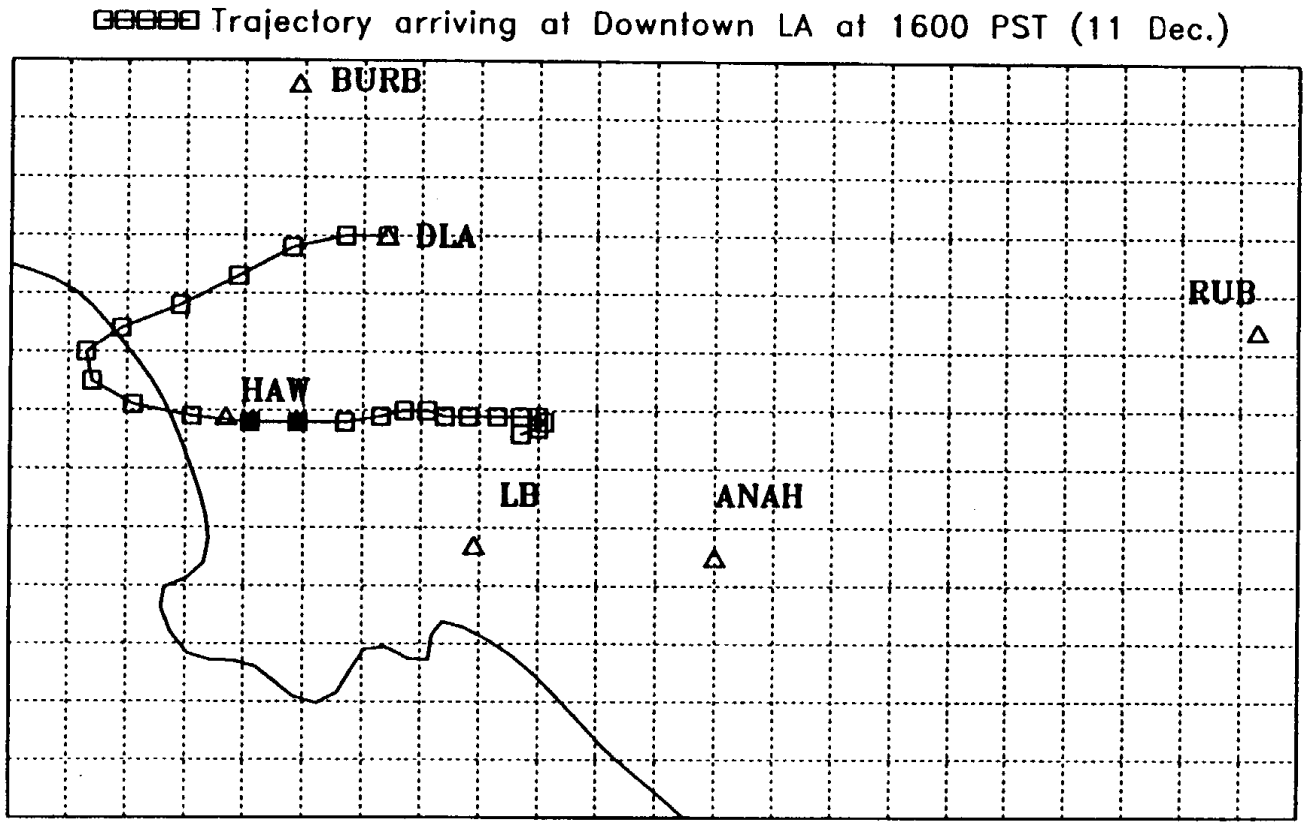

FIGURE 3.4.1(c). Trajectory arriving at sampling sites in the South Coast Air Basin of California on December 11, 1987 during the period of observed peak sulfate concentration in Hawthorne at 1200 PST.

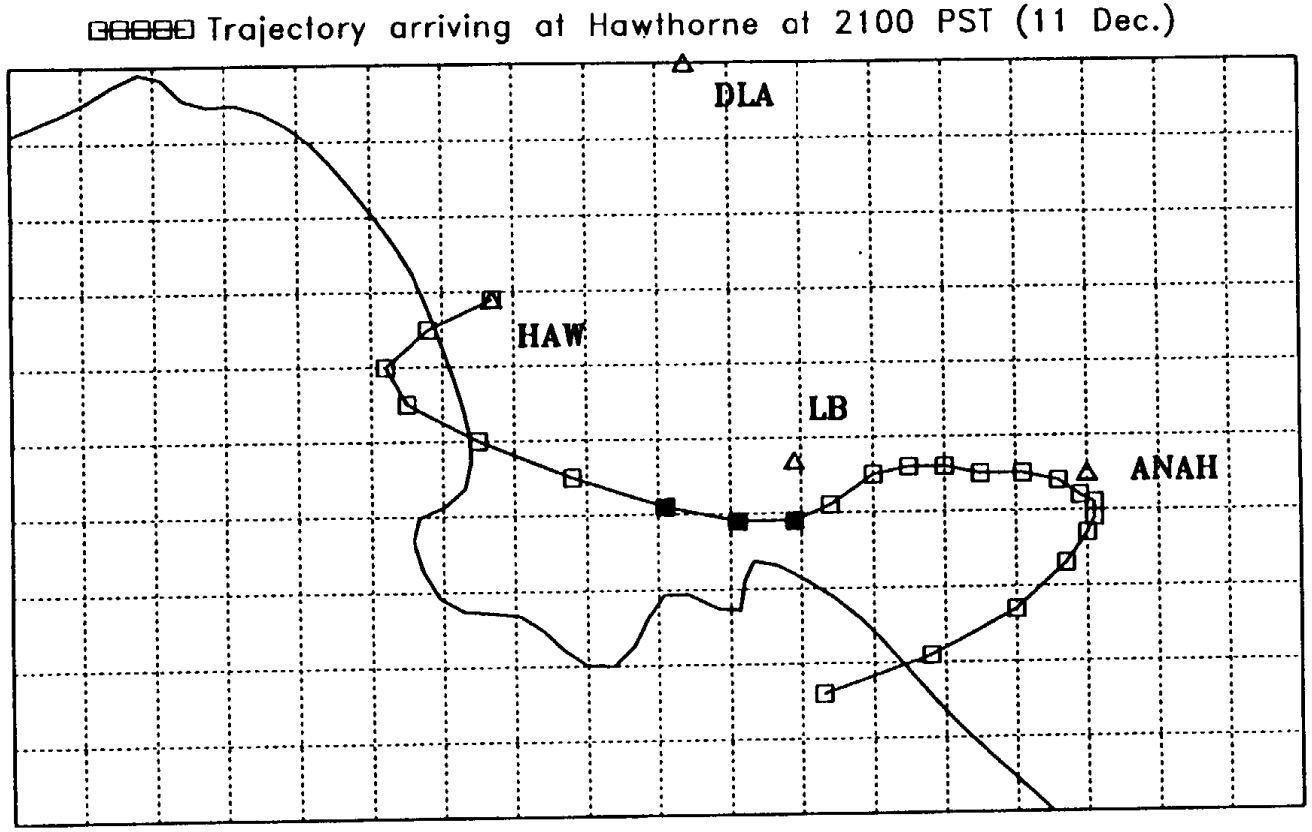

FIGURE 3.4.1(d). Trajectory arriving at sampling sites in the South Coast Air Basin of California on December 11, 1987 during the period of observed peak sulfate concentration in Long Beach at 2100 PST.

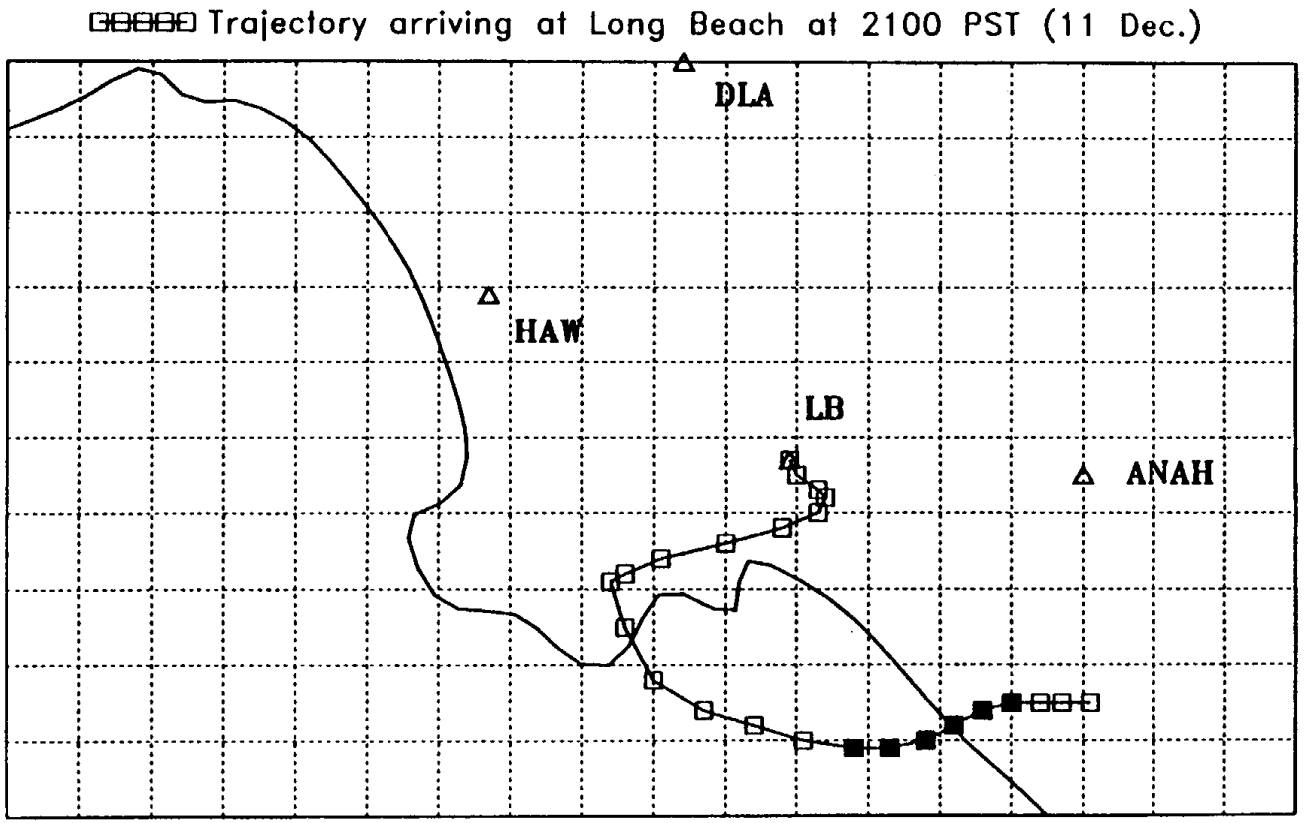

changes mentioned below, the methods employed here are as described by McRae et al. (1982) and Pilinis et al. (1987).

The detailed SAPRC gas-phase chemical reaction mechanism (Carter et al., 1986), with the modifications and extensions of Carter and Atkinson (1988), is used in the model. It contains 154 reactions and 62 species (39 active, seven accumulating, and 16 steady-state species). The photochemical mechanism preparation software of Carter and Atkinson (1988) has been used to prepare the gas-phase mechanism dependent part of the code. A day-specific gridded emission inventory for the December 10-11, 1987 episode provided by the California Air Resources Board (CARB) was processed and used in the model simulations. Detailed gridded air quality and meteorological fields for the 48-hour period were developed by interpolating the raw data applying the method of Goodin et al. (1979). The mixing heights were directly calculated from the measured vertical temperature profiles and then interpolated using the same method.

Similar modeling schemes, in a trajectory and in an Eulerian form, have succesfully predicted sulfate levels in the same region in the absence of a fog episode (Pilinis et al., 1987; Pilinis and Seinfeld, 1988). For each site, the 24 back-trajectories (one for each hour of December 11, 1987) ending at the site were calculated. The duration of each trajectory was 24 hours. The gas-phase trajectory model was then used to simulate the sulfate production, due to gas-phase photooxidation of SO_2 by OH, along the path of each of the trajectories. Five vertical cells were used.

3.4.2.2 Sulfate Concentration at Hawthorne on December 11, 1987

The paths of the air parcels arriving at Hawthorne at 4 a.m. and 8 a.m., and 6 p.m. on December 11, 1987, are depicted in Figures 3.4.2 (a-c) and that arriving at 12 noon in Figure 3.4.1c. The air parcels arriving at 4 a.m. and 8 a.m. at Hawthorne were inland during the period of the fog episode and, while the relative humidity in these parcels was high (around 85%), no fog was created in them. These parcels will be described from now on as 'dry air parcels.' The sulfate levels of these dry air parcels observed upon their arrival at Hawthorne were less than half of the observed maximum

FIGURE 3.4.2(a). Trajectory of air parcels arriving at Hawthorne, California on December 11, 1987 at 400 PST. Filled squares indicate presence of fog inside the air parcel.

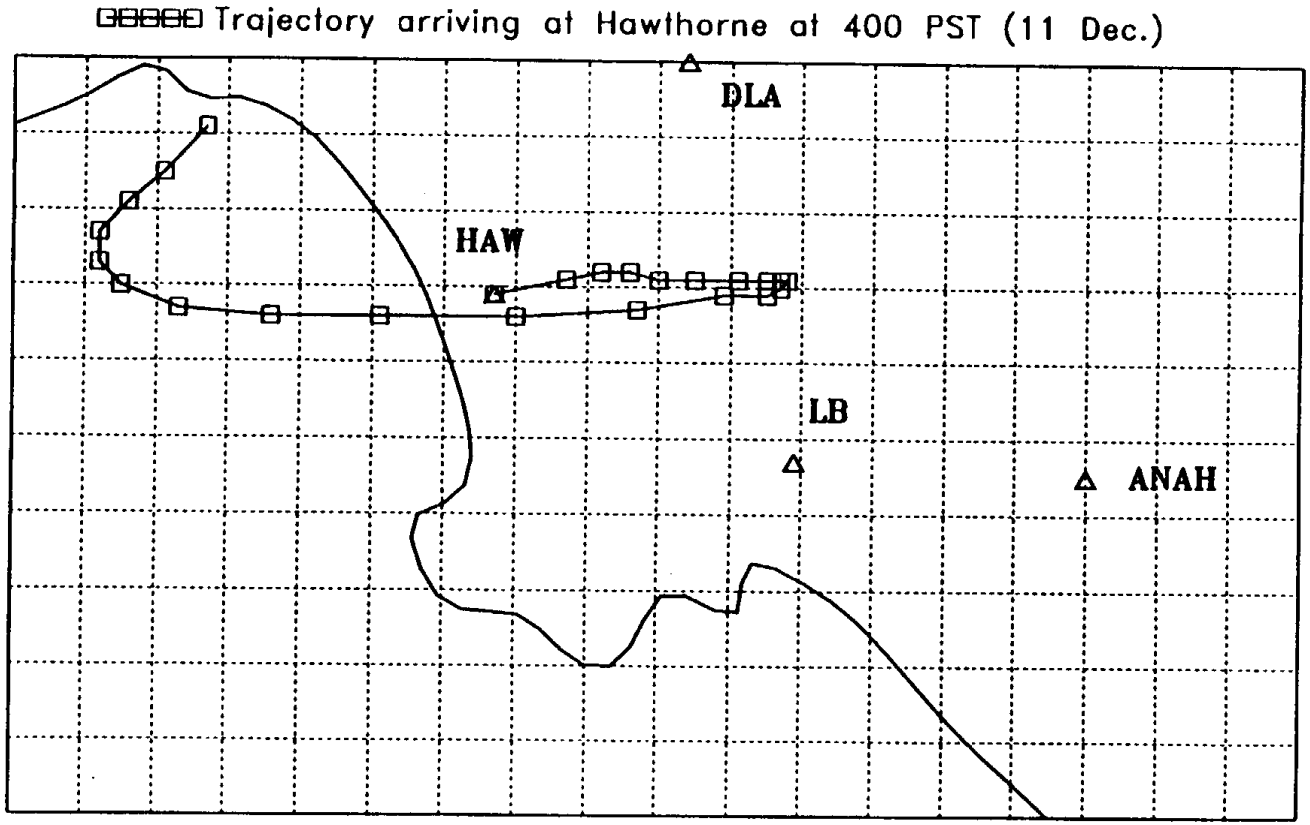

FIGURE 3.4.2(b). Trajectory of air parcels arriving at Hawthorne, California on December 11, 1987 at 800 PST. Filled squares indicate presence of fog inside the air parcel.

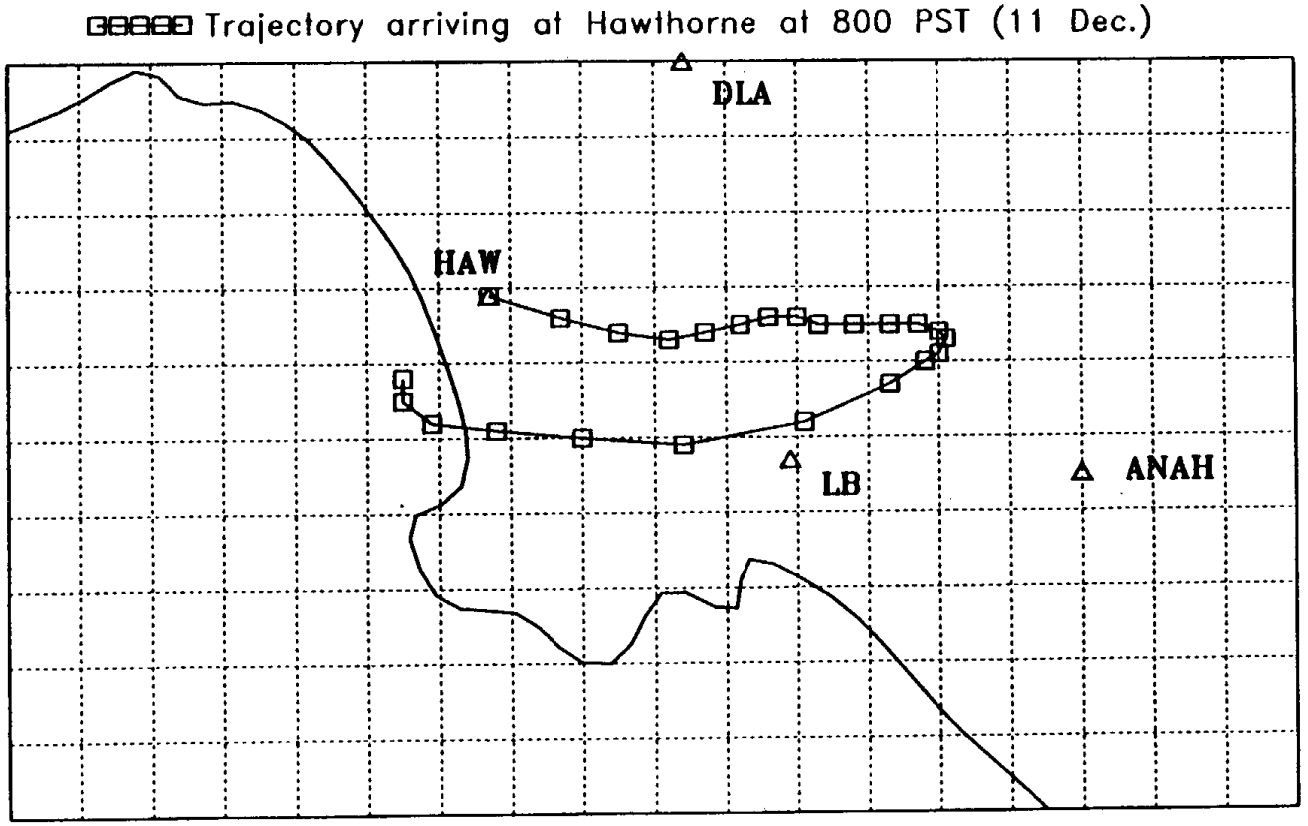

FIGURE 3.4.2(c). Trajectory of air parcels arriving at Hawthorne, California on December 11, 1987 at 1800 PST. Filled squares indicate presence of fog inside the air parcel.

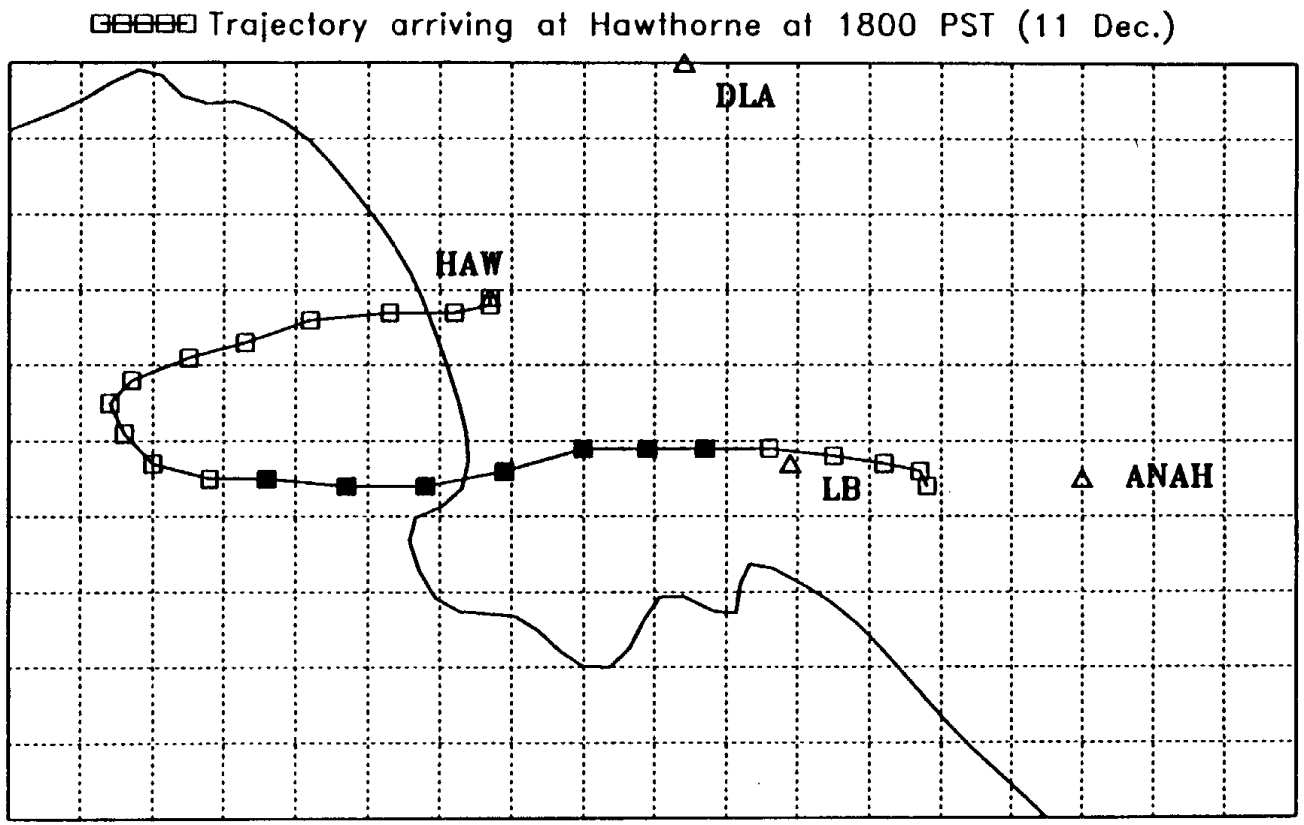

value on this day (Figure 3.4.3). On the contrary, the air parcel arriving at Hawthorne at 12 noon was from (4 a.m. to 6 a.m.) in the fog region ('wet air parcel') and, therefore, aqueous-phase reactions may have contributed to its elevated sulfate levels. The air parcel arriving at 6 p.m. was from 1 a.m. to 6 a.m. as well in the fog region and is, therefore, a wet air parcel.

Application of the gas-phase trajectory model failed to explain the sulfate increase in Hawthorne during December 11, 1987. The sulfate concentrations predicted by these series of simulations are depicted in Figure 3.4.3. The variation in sulfate concentration predicted by the model for December 11 is much smaller compared to the observed one. The sulfate is seriously underpredicted after 1 a.m., when only gas-phase processes are considered. During the period of the maximum observed sulfate, gas-phase production of sulfate can account for only 6.6 of the 15.6 $\mu g\ m^{-3}$ of observed sulfate. During this period, there appears to be an amount of 'excess sulfate' equal to 9 $\mu g\ m^{-3}$. Before continuing the analysis of the sulfate concentrations, it is useful to discuss the other relevant model predictions for this episode.

The model exhibits a tendency to overpredict $SO_2(g)$, especially during the period of the increased sulfate concentrations (Figure 3.4.4). Part of this overprediction is to be expected, as the field data suggest that the model is not able to fully reproduce the conversion of SO_2 to sulfate. One cannot, therefore, explain the existence of 'excess sulfate' by an $SO_2(g)$ underprediction by the model and the problem with the 'gas-phase chemistry only' approach requires further investigation.

The observed ozone levels in Hawthorne during December 11 were very low as a result of the low winter sunlight intensity and the proximity to the coast. The model successfully reproduced the observed ozone levels (Figure 3.4.5). The maximum gas-phase hydroxyl (OH) radical concentration predicted is about 0.05 ppt (roughly 1.2×10^6 molecules cm^{-3}) at 12 noon: a typical low winter daytime OH concentration (Seinfeld, 1986). As a result of the relatively low OH concentrations, the gas-phase oxidation of SO_2 proceeds slowly with a maximum rate of only 0.4%/hr. The total

FIGURE 3.4.3. Observed and predicted aerosol sulfate concentrations, accounting only for gas-phase chemistry, at Hawthorne, California on December 11, 1987. In Test 1, the mixing heights employed were reduced by 50%. In Test 2, the mixing heights employed were increased by 50%. In Test 3, the initial sulfate concentrations were increased by 50%. In Test 4, the sulfate emission rates were increased by 50%. In Test 5, the sulfate deposition velocity was set equal to zero.

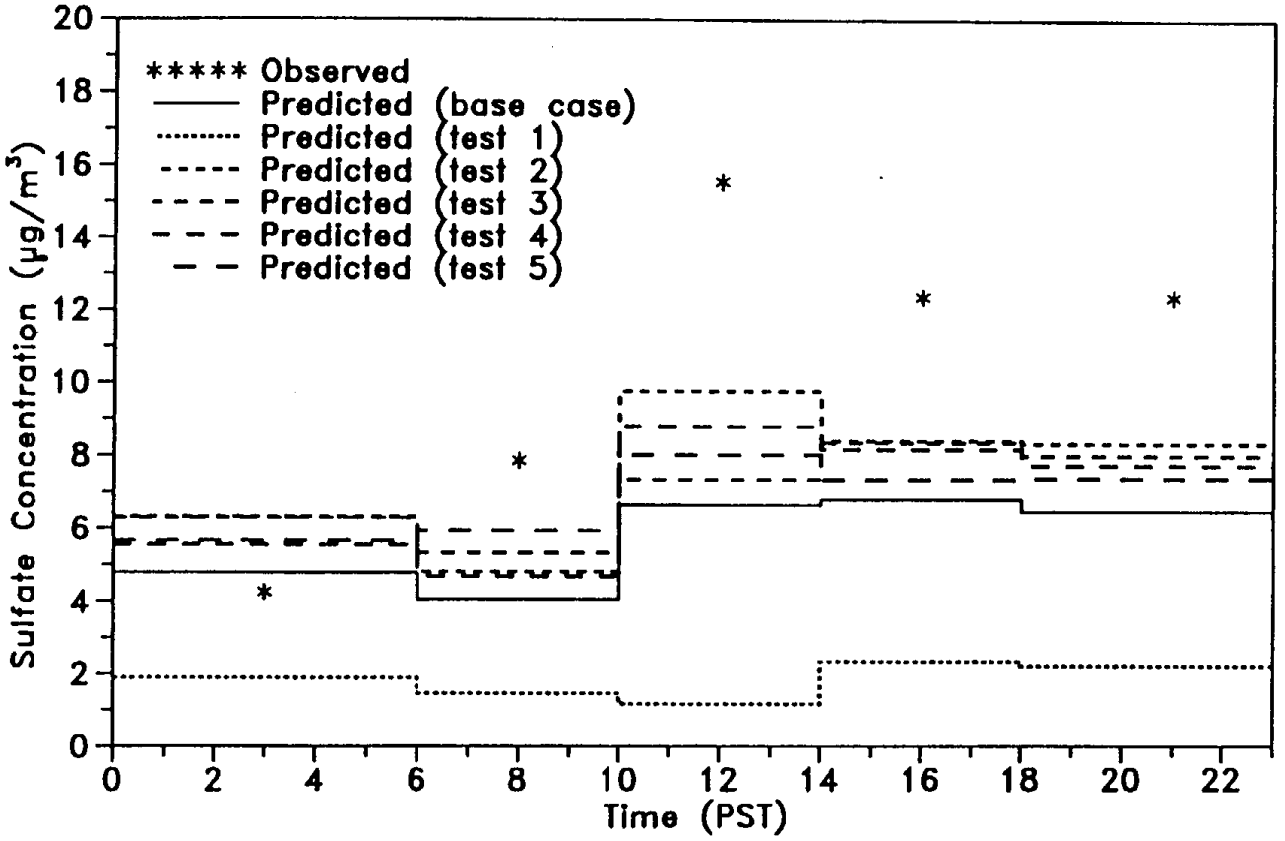

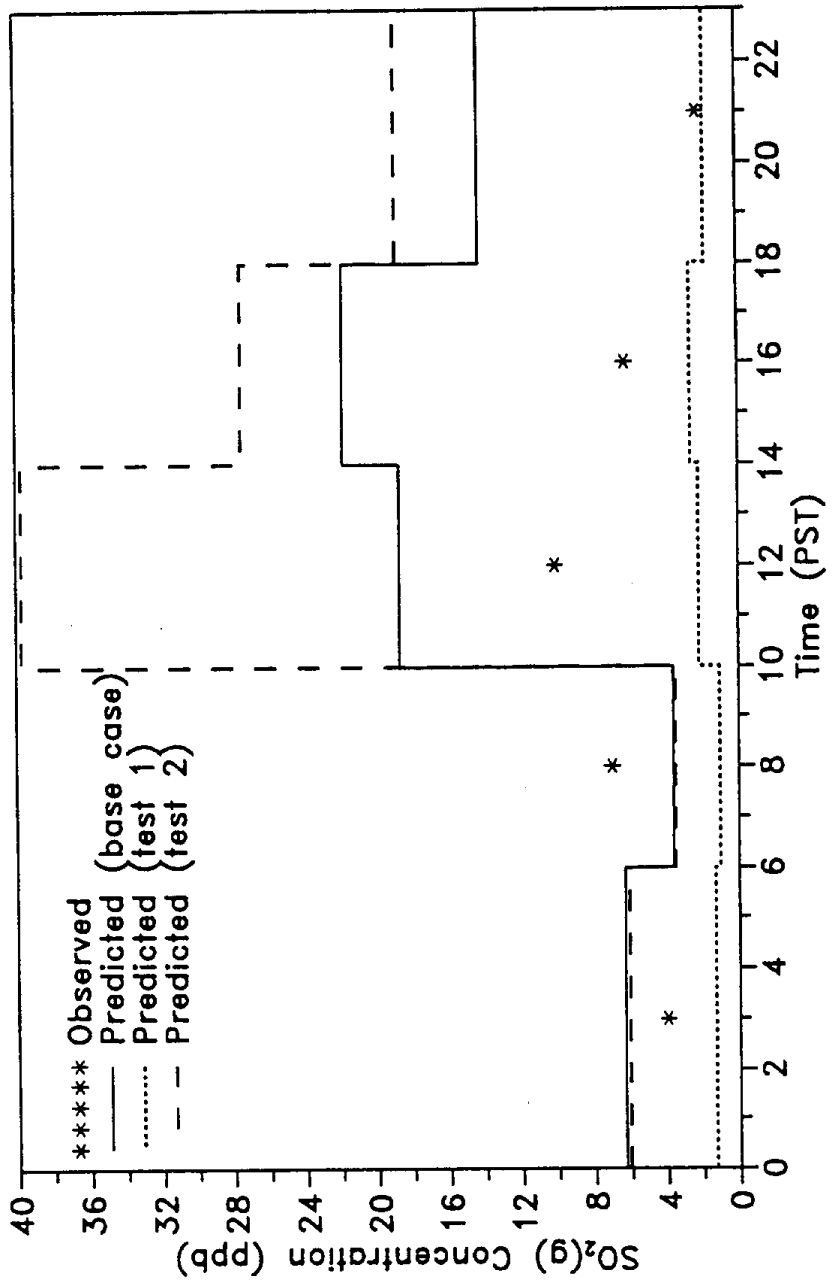

FIGURE 3.4.4. Observed and predicted SO_2 concentrations, accounting only for gas-phase chemistry, at Hawthorne, California on December 11, 1987. In Test 1, the mixing heights employed were reduced by 50%. In Test 2, the mixing heights employed were increased by 50%.

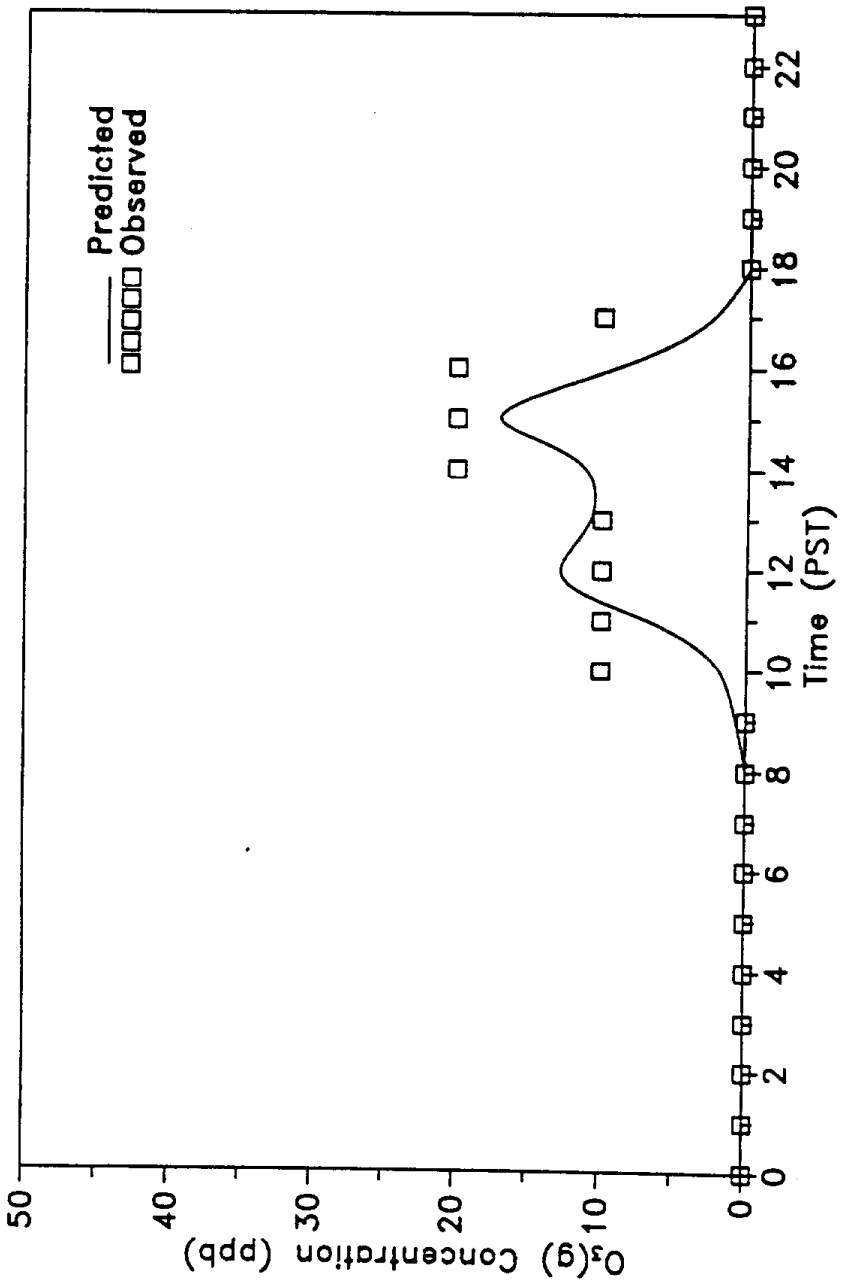

FIGURE 3.4.5. Observed and predicted O_3 concentration at Hawthorne, California on December 11, 1987.

gas-phase sulfate produced during each trajectory has been calculated by

$$S(VI)_{prod} = \int_{t_1}^{t_2} k_r OH(g)(t) SO_2(g)(t) dt \quad (1)$$

with t_1 and t_2 the start and end times of the trajectory, k_r the reaction constant for the $SO_2(g) + OH(g)$ reaction, and $OH(g)(t)$ and $SO_2(g)(t)$ calculated by the model gas-phase concentrations of OH and SO_2, respectively. A total gas-phase sulfate production of around 1.2 $\mu g\ m^{-3}$ per day was calculated.

A trajectory requiring further examination is the one arriving at Hawthorne at 12 noon on December 11. The air parcel starts at 12 noon on December 10 (Figure 3.4.1c) just outside the coast, moves for seven hours in a northeasterly direction, and at 7 p.m. on December 10 passes very close to the SCAQS sampling site at Anaheim. Its relative humidity increases during this period to 65%. The aerosol sulfate concentration measured at Anaheim was 5.3 $\mu g\ m^{-3}$. The model underpredicts that concentration by only 1.5 $\mu g\ m^{-3}$: an indication that most of the discrepancy of 9 $\mu g\ m^{-3}$ between the model predictions and the observations is created during the remaining 17 hours of the simulation, when the fog episode occurred.

3.4.2.3 Sulfate Concentration at Downtown Los Angeles

The above analysis was repeated for Downtown Los Angeles. Again, the model successfully predicted the observed aerosol sulfate levels from just after midnight to 1 a.m., but underpredicted (by as much as 8.7 $\mu g\ m^{-3}$) the sulfate concentration during the afternoon (2 p.m. to 6 p.m.) (Figure 3.4.6). Examination of the corresponding trajectories indicates that the air parcel arriving at Downtown Los Angeles at 4 p.m. spent the previous 24 hours inland (dry air parcel) (Figure 3.4.7a). Another dry air parcel arrives at 12 noon and the model underpredicts its sulfate concentration at Downtown Los Angeles by 2.2 $\mu g\ m^{-3}$ (Figure 3.4.7b). The serious underprediction of sulfate at 4 p.m. (by 8.7 $\mu g\ m^{-3}$) coincides with the arrival of the wet air parcel with its trajectory shown in Figure 3.4.1b (fog occurred in the parcel from 5 a.m. to 6 a.m.). Wet air parcels continued to arrive at the site the rest of the day. The air parcel

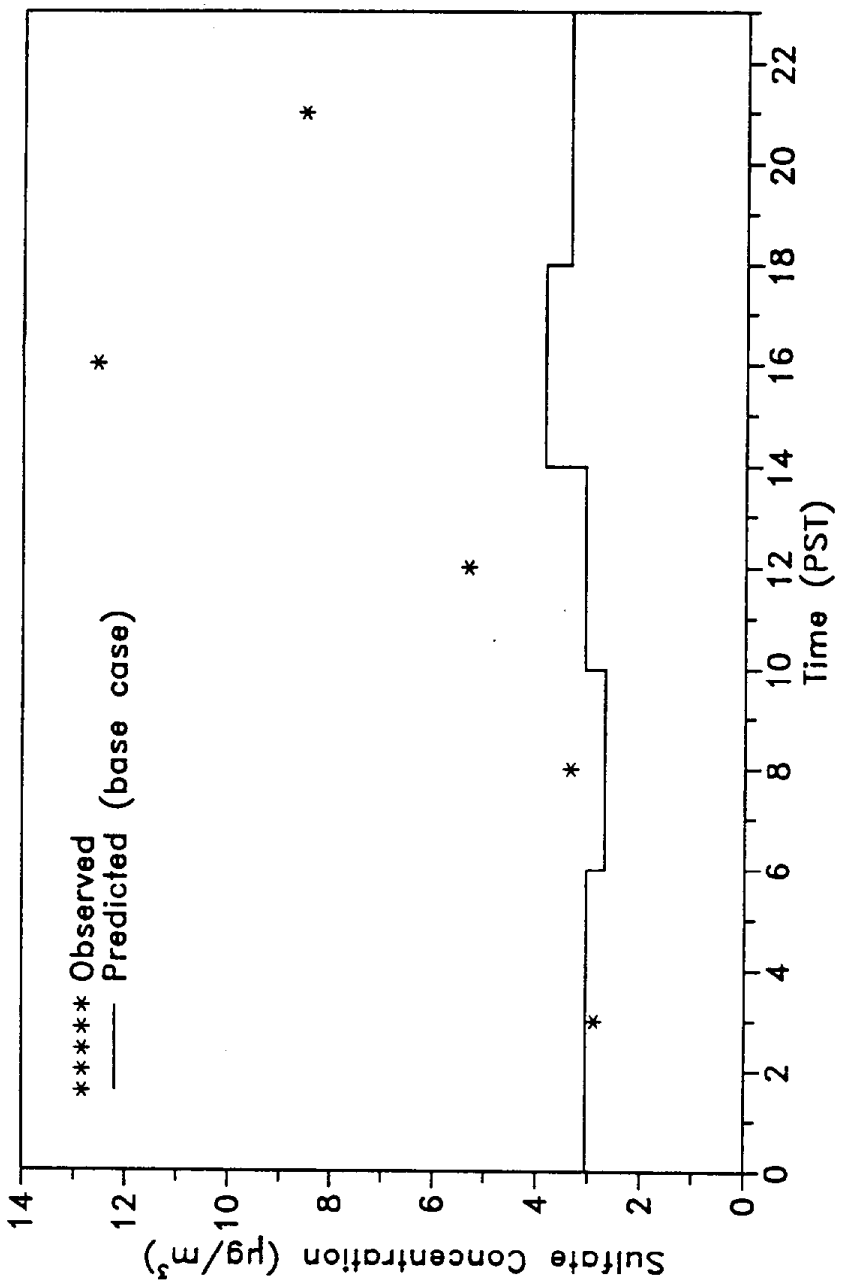

FIGURE 3.4.6. Observed and predicted aerosol sulfate concentrations, accounting for gas-phase chemistry, in Downtown Los Angeles, on December 11, 1987.

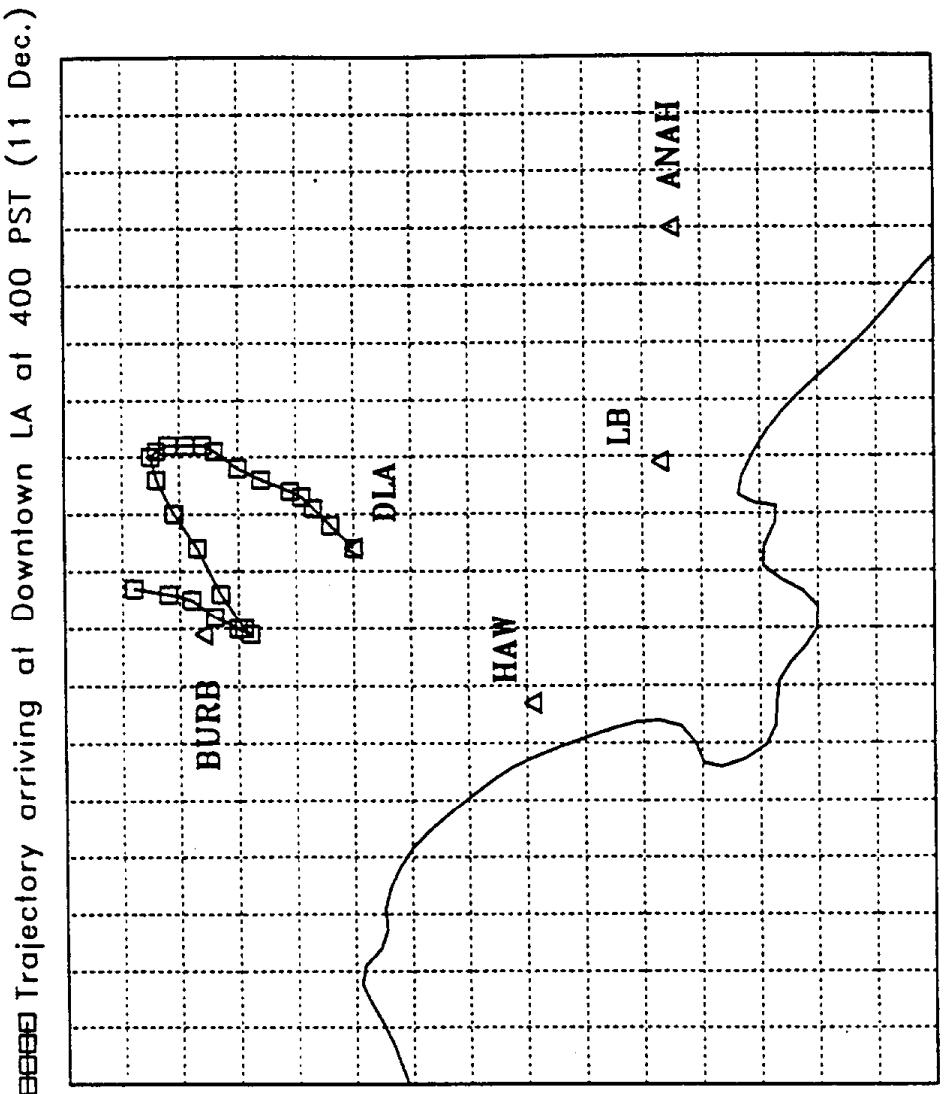

FIGURE 3.4.7(a). Trajectory arriving in Downtown Los Angeles on December 11, 1987 at 400 PST. Filled squares indicate presence of fog inside the air parcel.

FIGURE 3.4.7(b). Trajectory arriving in Downtown Los Angeles on December 11, 1987 at 1200 PST. Filled squares indicate presence of fog inside the air parcel.

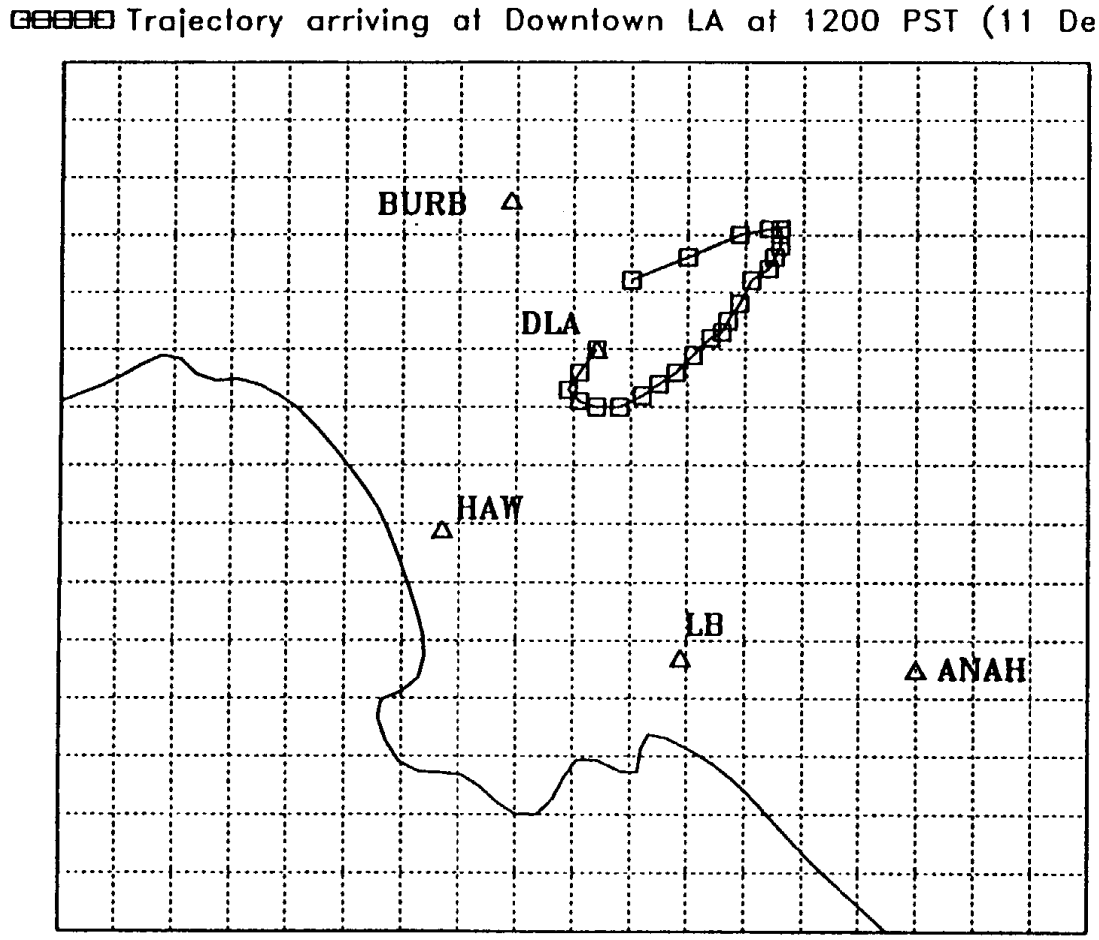

FIGURE 3.4.7(c). Trajectory arriving in Downtown Los Angeles on December 11, 1987 at 2000 PST. Filled squares indicate presence of fog inside the air parcel.

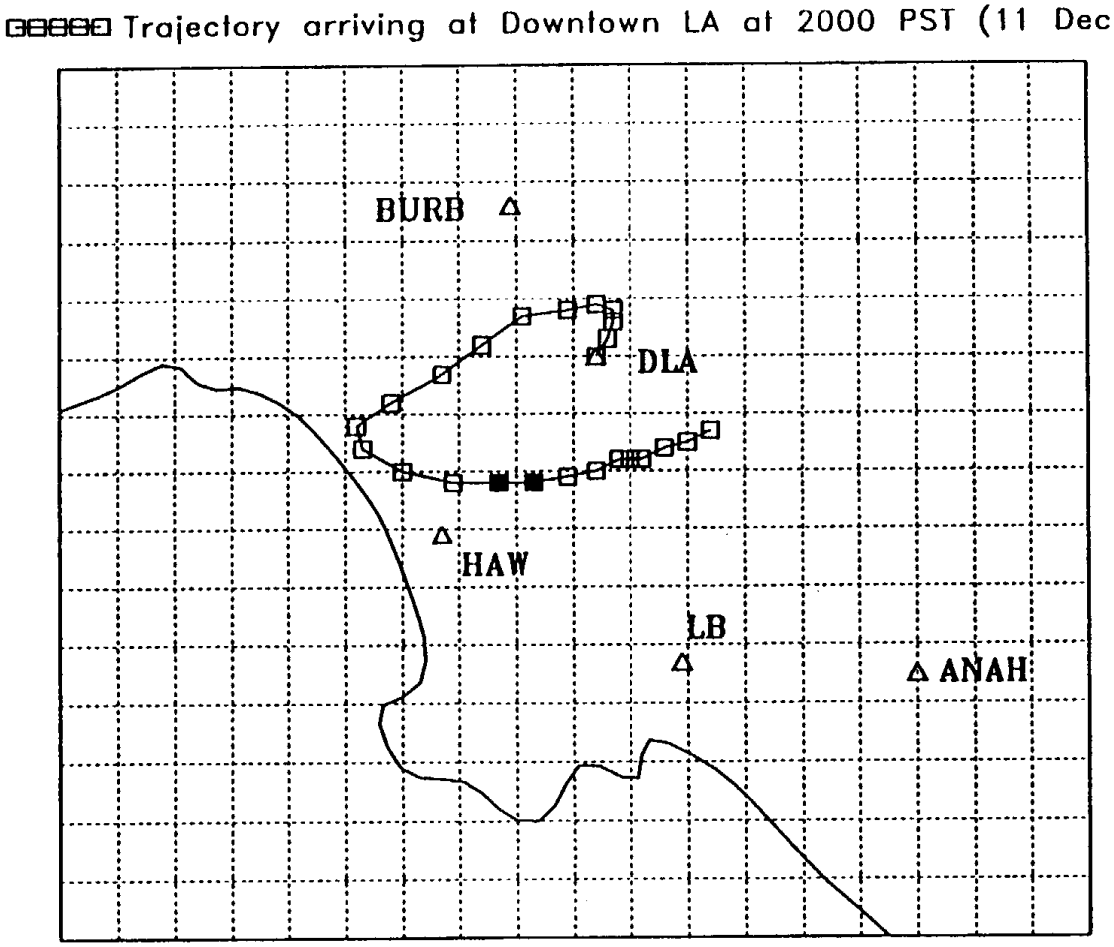

arriving at 2 a.m. spent one hour (5 a.m. to 6 a.m.) in the fog area and then travelled 14 hours before arriving at Downtown Los Angeles (Figure 3.4.7c).

The qualitative similarity of both the observed and predicted sulfate behavior for both sites indicates that the observed discrepancy is not an isolated event resulting from the occurrence of a singular event. Before attributing the inability of the gas-phase model to predict the observed excess sulfate to heterogeneous chemical processes, it is necessary to examine the model's sensitivity to uncertainties in the input parameters used in the above simulations.

3.4.3 Sensitivity Analysis of the Lagrangian Trajectory Model

While the SCAQS data set–from which the necessary inputs to the trajectory model have been taken–is probably one of the most comprehensive sets of its kind available anywhere, one must still carefully examine the response of the model to uncertainties in important input variables. These variables include the mixing heights, sulfate emissions, sulfate initial conditions, and the deposition velocity of sulfate.

3.4.3.1 Mixing Heights

The mixing heights for the Los Angeles basin during December 10 and 11, 1987, were estimated from 89 soundings collected over nine sites. The maximum mixing height over Long Beach, representative of the area covered by the above trajectories, was 410 m for December 10 and 230 m for December 11. On December 11, the height of the inversion was lower than 150 m for 20 hours and lower than 100 m for 14 hours. The mixing heights determine the degree of atmospheric dilution of the primary emissions and, therefore, are expected to influence the sulfate production indirectly. Also, because the SO_2 and primary sulfate are emitted in the area of concern by tall stacks at heights, including the plume rise, comparable to the observed inversion height, the latter will determine if SO_2 is trapped aloft or below the inversion. The effect of both an increase and a decrease of the mixing height on the model predictions will be investigated.

During test 1, the 24 trajectory runs arriving at Hawthorne were repeated with the mixing heights reduced by 50%. This change had, as its main effect, the trapping of fresh SO_2(g) emissions and of primary sulfate aloft and the reduction of their corresponding concentrations near the ground (Figures 3.4.3 and 3.4.4). The sulfate underprediction by the model is exacerbated with the exception of the late evening hours.

The effect of an increase of the mixing height by 50% was investigated in test 2. This change results in SO_2 fumigation for the air parcels arriving between 1 a.m. and 6 p.m. and increases the SO_2 overprediction by the model (Figure 3.4.4). At 12 noon, the model overpredicts the SO_2 concentration by a factor of 4, indicating that this simulation represents an extreme case. Even under these extreme conditions, the model still underpredicts the sulfate concentrations by almost 6 μg m^{-3} as a result of the low gas-phase oxidation rate of SO_2. Further increase of the mixing heights is not expected to influence significantly the sulfate concentrations at noon, because most of the SO_2 aloft has already fumigated to the ground.

The predicted trapping of SO_2(g) aloft during certain periods of December 11, 1987, is supported by a vertical SO_2(g) profile measured at 4:30 p.m. by aircraft performing a spiral over Fullerton (15 km NW of Long Beach). The measured SO_2(g) concentration at 250 m was 12 ppb compared to 2 ppb near the ground.

It must be concluded that the uncertainties in the mixing height cannot account for the observed discrepancy in the predicted versus measured aerosol sulfate levels. The increase of the inversion height that improves the sulfate predictions results in unacceptably high SO_2(g) concentrations.

3.4.3.2 Sulfate Initial Conditions

The initial sulfate concentrations used in the simulations were calculated by spatial interpolation of the measured values. While these interpolated values are expected to be relatively accurate, the sensitivity of the model to the initial aerosol sulfate concentration was investigated by increasing the initial sulfate concentration by 50%, a

value generally exceeding the upper limit of its uncertainty (test 3). Nevertheless, the calculated increase of about 1.5 μg m^{-3} of sulfate cannot explain most of the excess sulfate observed at Hawthorne (Figure 3.4.3).

3.4.3.3 Sulfate Emissions

Uncertainty in the sulfate emission rates is another possible explanation for the 'excess sulfate.' To investigate the effect of these variables we recalculated the 24 trajectories arriving at Hawthorne increasing the sulfate emissions by 50% over the entire modeling area (test 4). The corresponding increase of the sulfate concentrations at Hawthorne varies between 0.6 μg m^{-3} and 2.1 μg m^{-3}. The sulfate emission rates would need to be increased by almost 250% to predict the observed sulfate maximum concentration, a level of increase that greatly exceeds the uncertainty in these emission rates.

3.4.3.4 Sulfate Deposition Velocity

Dry deposition represents a reduction for aerosol sulfate, and considerable uncertainty is associated with the deposition velocities calculated as a function of meteorological conditions and land use. In test 5, in an effort to obtain an upper limit of the aerosol sulfate concentrations, deposition has been eliminated by setting the deposition velocity of sulfate equal to zero. The predicted sulfate aerosol concentration increases by as much as 1.4 μg m^{-3}, still leaving 7.5 μg m^{-3} of excess sulfate remaining at 12 noon.

3.4.3.5 Summary

One could imagine perturbing the NO_x/hydrocarbon mixture in an effort to increase the chemical activity of the system, resulting in higher radical concentrations and therefore in higher production of sulfate in the gas phase. However, an increase of the OH radical concentration by more than a factor of 7 would be necessary to explain the 'excess sulfate.' Such an increase is not achievable with a simple perturbation of the

emissions and it would also cause a significant increase in the predicted ozone levels. We conclude that for December 11, 1987, the day after the fog episode, there is a large concentration of excess sulfate that cannot be explained on the basis of our knowledge of the gas-phase chemistry or the uncertainty in emission rates or mixing heights, etc.

3.4.4 Heterogeneous SO_2 Oxidation in the Aerosol Phase

Heterogeneous aqueous phase of SO_2 can take place either in the aerosol phase or in the fog water. When the relative humidity is below 100%, all the particles are considered as aerosol and the corresponding water as aerosol water. If the relative humidity exceeds 100% and a fog is created, some of the particles become activated to fog droplets while the rest remain in equilibrium with the surrounding atmosphere as interstitial aerosol (Pandis et al., 1990).

If $w_L(t)$ (g m^{-3}) is the liquid water content of the aerosol phase and $r_{aer}(t)$ μg s^{-1} (g water)$^{-1}$ is the rate of production of sulfate in the aerosol phase, then the amount of sulfate produced in the period from t_1 to t_2 (in μg m^{-3}) will be

$$S(VI)_{prod} = \int_{t_1}^{t_2} w_L(t) r_{aer}(t) dt. \qquad (2)$$

If $\overline{r_{aer}}$ is a constant average sulfate production rate, then one gets

$$S(VI)_{prod} = \overline{r_{aer}} \int_{t_1}^{t_2} w_L(t) dt. \qquad (3)$$

The integrated liquid water content along a trajectory path can be estimated using an equilibrium model for inorganic multicomponent aerosols (Pilinis and Seinfeld, 1987). Let us focus on the trajectory arriving at Hawthorne at 12 noon on December 11. The relative humidity along the trajectory path is calculated by spatial interpolation of the measured relative humidities. To separate the contribution of the aerosol and fog production of sulfate, the relative humidity during the fog episode is set at 99% and an 80% aerosol scavenging efficiency is assumed according to the calculations of Pandis et al. (1990). To obtain an upper limit of the aerosol contribution to the sulfate

production, the maximum concentrations of the aerosol species measured along the trajectory path are used throughout the calculation. These maximum concentrations were measured at Anaheim at 7 p.m. on December 10 and were 55.27 μg m^{-3} NO_3^-, 15.34 μg m^{-3} NH_4^+, 5.37 μg m^{-3} SO_4^{2-}, 2.6 μg m^{-3} Cl^-, and 0.91 μg m^{-3} Na^+. The relative humidity along the trajectory path and the calculated aerosol water concentrations are shown in Figure 3.4.8. The liquid water content associated with this aerosol mass in relative humidities less than 100% is low, with a maximum of 0.0015 g m^{-3} for 99%, and is lower than 0.0001 g m^{-3} for most of the day. It is interesting to note that for relative humidities less than 90%, the aerosol liquid water content is less than 0.0002 g m^{-3}. Using the above calculated aerosol liquid water content values, one finds that the upper limit of the time integrated aerosol liquid water content, the integral term in equation 3, along the trajectory path was 7.56 g water s m^{-3}, equivalent to a time average value of 87.5 μg m^{-3}. The production of 9 μg m^{-3} of excess sulfate requires then (equation 3) an average reaction rate of 1.2 μg S(VI) (g water)$^{-1}$ s^{-1} or an average S(IV) aqueous-phase oxidation rate of at least 12.6 μM s^{-1}. This rate cannot be attained at a pH lower than 5.5 by any known aqueous-phase oxidation pathway (Hoffmann and Calvert, 1985). For comparison, the maximum oxidation rate that can be attained by H_2O_2 oxidation (at 1 ppb H_2O_2) is 3.8 μM s^{-1}. The availability of enough neutralizing material to increase the aerosol pH above 5.5 and, furthermore, to maintain these high levels during the production of 9 μg m^{-3} of sulfate, is extremely unlikely.

Knowledge of the aqueous-phase oxidation rates for solutions of such a high solute concentration is incomplete (even at 99% the aerosol solution has a total solute concentration of 1.2 M). Inhibition by the high ionic strength is expected (Martin and Hill, 1987). One must conclude that the aerosol liquid water present could not provide the necessary reactive medium for the production of 9 μg m^{-3} of sulfate in such a short period of time even under the most favorable conditions.

FIGURE 3.4.8. Relative humidity and predicted aerosol liquid water content along the path of the trajectory arriving at Hawthorne, California at 1200 PST on December 11, 1987. During the fog period only the liquid water content of the interstitial aerosol is calculated.

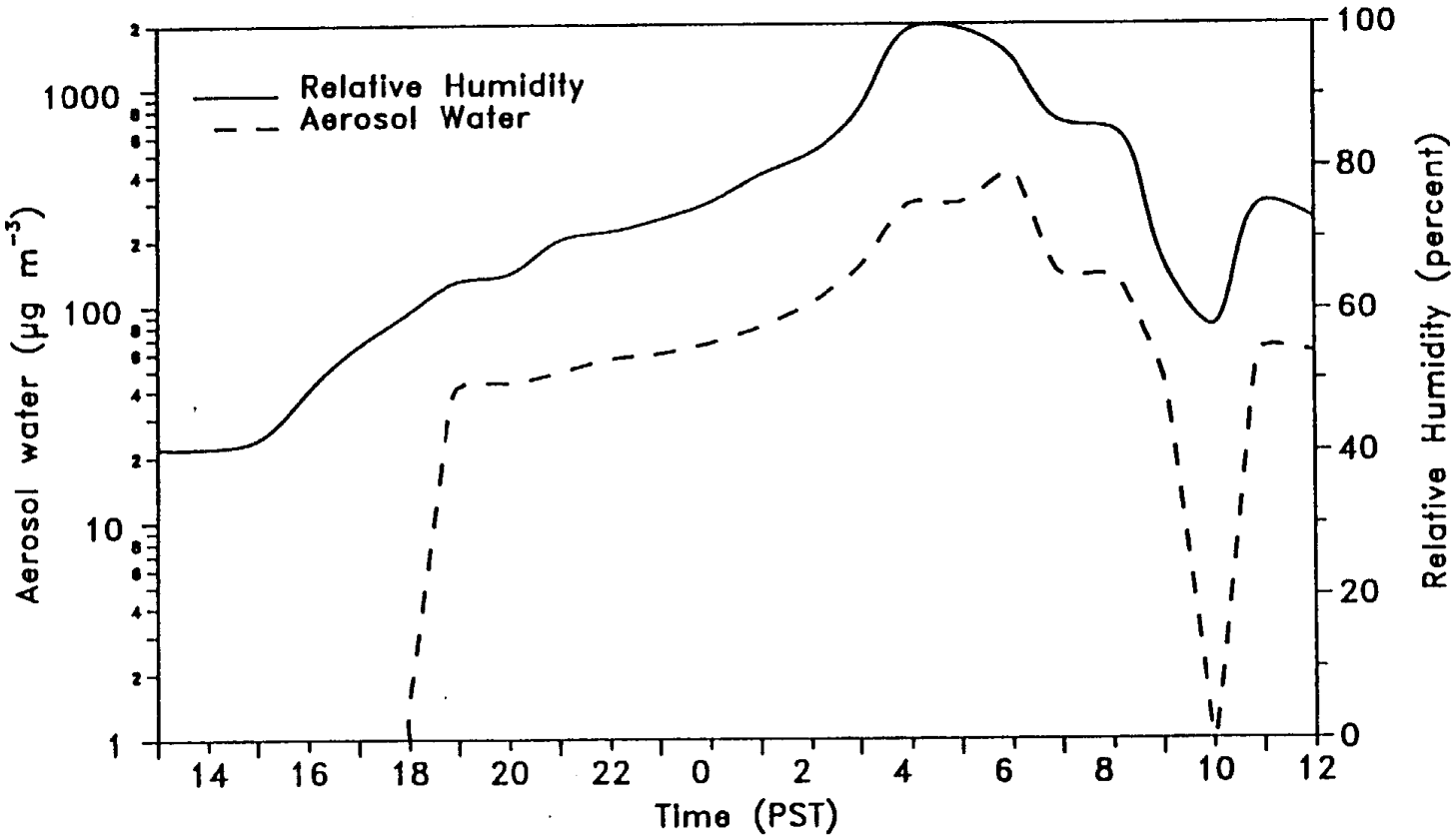

3.4.5 Heterogeneous SO_2 Oxidation Inside the Fog Droplets

Our working hypothesis is that aqueous-phase oxidation of S(IV) inside the fog droplets leads to the increased sulfate concentrations observed during the day after the fog. Unfortunately, the only available reliable aqueous-phase measurements are the liquid water content and the pH of the fog at Long Beach.

To theoretically study the aqueous-phase production of sulfate in the episode of December 10-11, 1987, we have used a mathematical model describing gas-phase chemistry, aqueous-phase chemistry, mass transfer between the two phases and wet deposition. The model is a simplified version of that used by Pandis and Seinfeld (1989b) for the simulation of acid deposition due to fog and employs the aqueous-phase chemical mechanism presented by Pandis and Seinfeld (1989a), which includes 49 individual aqueous-phase species, 17 aqueous-phase ionic equilibria and 109 aqueous-phase reactions. The main differences between the two models are described below. The module simulating the radiation fog development is not required since the fog liquid water content was measured. The fog depositional flux G (g m^{-2} s^{-1}) is calculated as a function of the liquid water content, w (g m^{-3}), according to the expressions suggested by Pandis et al. (1990):

$$G = 0.027w^{1.67} \tag{4}$$

for the growth period (liquid water content is increasing) and

$$G = 0.018w^{1.08} \tag{5}$$

for the dissipation period (liquid water content is decreasing). During the period of constant liquid water content, the deposition flux is calculated by averaging the above two expressions. The fog is assumed to be spatially homogeneous and to occupy the first cell in the trajectory column, with the cell height equal to the fog height. The initial fogwater concentrations are calculated using the aerosol concentrations before the fog event and assuming an 80% scavenging efficiency (Pandis et al., 1990).

3.4.5.1 The Air Parcel Arriving at Hawthorne at 12 Noon

The air parcel arriving at Hawthorne at 12 noon entered the fog area at 4 a.m.. The sulfate concentration predicted by the gas-phase model at this time is 3.9 $\mu g\ m^{-3}$. The fog liquid water content from 4 a.m. to 6 a.m. remains practically constant at 0.15 $g\ m^{-3}$ (Hoffmann, unpublished data) and the fog height can be estimated by the vertical relative humidity profile at around 200 m. The parcel stays in the fog region for approximately two hours. Emissions of NH_3 during this period were taken from the gridded inventory developed for the Los Angeles basin by Russell and Cass (1986).

The model predicts, in agreement with the observations, that the fog pH was relatively high due to the ammonia emissions in the area (Figure 3.4.9). The model underpredicts the fog pH during the first hour of the fog life and overpredicts it during the second hour, but the overall agreement is satisfactory for the purposes of this analysis. The existence of such a high pH leads to several potential pathways for the aqueous-phase S(IV) to S(VI) conversion. The model predicts that approximately 17.5 $\mu g\ m^{-3}$ of S(VI) are produced during the two hours of the fog episode, from which 4.3 $\mu g\ m^{-3}$ are deposited on the ground, with the remaining 13.2 $\mu g\ m^{-3}$ remaining in the aerosol phase after the fog dissipates (Figure 3.4.10). The predicted aerosol sulfate concentration after the fog dissipation (6 a.m.) is, therefore, 17 $\mu g\ m^{-3}$, and is more than sufficient to explain the observed 15.6 $\mu g\ m^{-3}$ of aerosol sulfate upon arrival of the air parcel at Hawthorne.

Initially, most of the sulfate is predicted to be produced by the aqueous-phase oxidation of S(IV) by H_2O_2 (0.8 ppb of H_2O_2 is predicted to exist before the fog episode). Approximately 3.2 $\mu g\ m^{-3}$ of sulfate are produced via this pathway. H_2O_2 is rapidly depleted and after 4:30 a.m. the contribution of this pathway is minimal. The main sulfate production pathway after this point is the oxidation of S(IV) by O_2, catalyzed by Fe^{3+} (aerosol concentration 0.2 $\mu g\ m^{-3}$) and Mn^{2+} (aerosol concentration 0.1 $\mu g\ m^{-3}$). This pathway is assisted by the high droplet pH (Martin, 1984), and contributes approximately 10.9 $\mu g\ m^{-3}$ of sulfate. The oxidation of S(IV) by $NO_2(aq)$

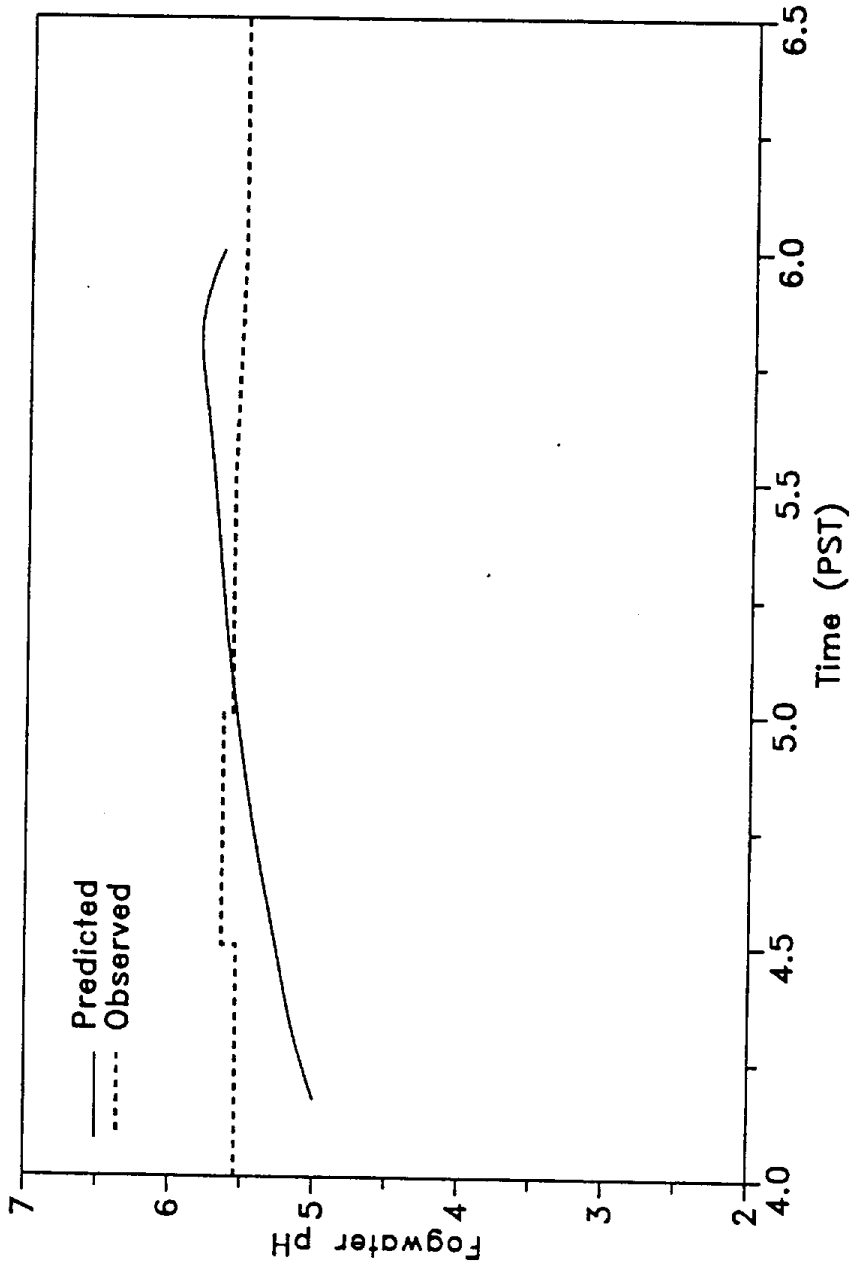

FIGURE 3.4.9. Predicted and observed pH [Hoffman, unpublished data] for the fog episode.

FIGURE 3.4.10. Predicted sulfate balance during the fog lifetime for the 1200 PST Hawthorne trajectory.

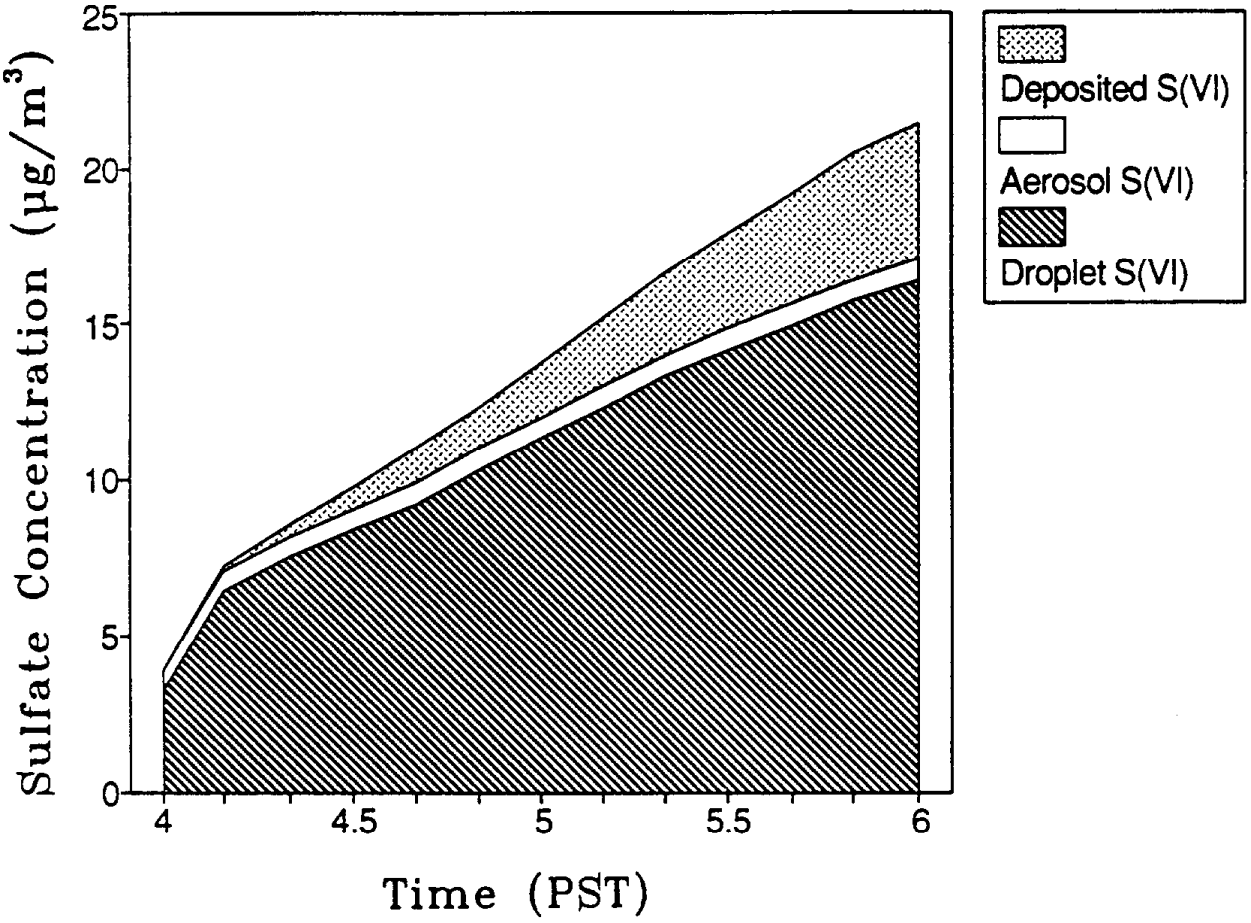

contributes 3.8 μg m^{-3} of sulfate, as the predicted gas-phase concentration of NO_2 is around 135 ppb during the fog episode. A similar observation has been reported by Pandis and Seinfeld (1989b). Oxidation of S(IV) by Cl_2^- and HSO_5^- produce 0.5 and 0.3 μg m^{-3} of sulfate, respectively. Since the ozone concentration predicted by the model during this period is virtually zero, the corresponding contribution of the aqueous-phase oxidation of S(IV) by O_3(aq) is negligible. In spite of the considerable uncertainty associated with the rate expressions of some of the aqueous-phase sulfate forming reactions, our current knowledge of aqueous-phase chemistry can explain the production of the observed excess sulfate.

3.4.5.2 The Air Parcel Arriving at Hawthorne at 6 p.m.

This air parcel passes through the Long Beach area at around midnight, the time fog is forming, stays over land until 3 a.m., and continues its journey inside the fog layer over the sea until 6 a.m.. The main difference between the two air parcels is that this one is not influenced by anthropogenic emissions for three hours, but the fog and wet deposition persists. The sulfate balance for this air parcel is depicted in Figure 3.4.11. The sulfate concentration reaches a maximum of 18.2 μg m^{-3} at 2:30 a.m. and starts decreasing as the wet deposition rate exceeds its aqueous-phase production rate. Its aqueous-phase production decreases signigicantly because the SO_2(g) concentration has significantly decreased and also because the pH decreases. The predicted aerosol sulfate concentration after the fog dissipation is 10.6 μg m^{-3}, while the value measured upon arrival at Hawthorne is 12 μg m^{-3}. The model explains both the maximum sulfate concentration at noon at Hawthorne and its decrease during the afternoon hours.

FIGURE 3.4.11. Predicted sulfate balance during the lifetime for the 1800 PST Hawthorne trajectory.